

SCIENTIFIC & TECHNICAL

REPORT

2019

:csem

IMPRINT

Full report title CSEM Scientific and Technical Report 2019

Editor and publisher CSEM SA
info@csem.ch
T +41 32 720 5111

Publication Frequency yearly
Media printed and electronic
Website www.csem.ch/str2019

Cover page design Contreforme
www.contreforme.ch

Printing Imprimerie Baillod SA, Bevaix (Switzerland)

PREFACE

Dear Reader,

I am pleased to present our 2019 Scientific and Technical Report, which contains a comprehensive selection of the technological advances made by our researchers over the past year in non-confidential research programs and projects.

CSEM is a hub of Swiss ingenuity, enabling and accelerating innovations in advanced, groundbreaking technologies. We are constantly adapting ourselves to encompass the changing nature of the technological landscape and are motivated to innovate sustainable technologies that make a difference.

This year, we are celebrating 35 years of Deep Tech development and transfer to industry—an activity that has accelerated innovation, particularly in the strategic fields of digitalization, precision manufacturing, and sustainable energy. With our partners, we are inspired to draw on our past and present to create disruptive solutions, developing technologies and techniques that can grow the Swiss economy, create jobs, and protect the quality of life of future generations.

Mastering digital, precision, miniaturization, and low-power consumption technologies, we are helping companies go from lab to success by unlocking their Deep Tech potential. Our 500+ employees—passionate about helping our partners achieve success in this rapidly evolving world—are ready to invest more extensively in our smart future than ever before.

Whether you are from industry or are a researcher, we have prepared this report for you. I sincerely hope you will enjoy reading it and that its contributions will engage and inspire you to innovate with us. Let's create the technologies that make a difference, together.

Mario El-Khoury

CEO, CSEM

CONTENTS

PREFACE	1	HIP Conditions: Key Operation for Controlling Mechanical Properties of 3D Printed Ti6Al4V	38
MULTIDISCIPLINARY INTEGRATED PROJECTS—MIPS	9	SURFACE ENGINEERING	39
IntelliDUST—Intelligence in 3D Accelerometer Sensors at Zero-added Power Cost	11	Wafer-scale Manufacturing of Nanoporous Membranes by Mean of Nanosphere Lithography	41
MULTIPLIR—Portable Long Wave Infra-red Camera for Gas Detection	12	Molecular Imprinted Polymer-based Sensor	42
ParticleID—Identification of Particulate Contaminants in Liquids by Neural Network Analysis of Scattering Patterns	13	Improving the Adhesion of Metallic Coatings onto 3D Printed Plastic RF Components	43
PROBIOTICS—an Energy Autonomous Miniature Wireless Sensor Mote Interacting with your Phone	14	Non-visual Effects of Light on Humans: Spectral Tuning and Light Distribution with Freeform Optical Structures	44
Visage—a Miniaturized Face Detection Sensor	15	Non-invasive Optical Oxygen Sensing for Life Sciences and Environmental Monitoring	45
3D- μ FLUIDICS—Automated Long-term Culturing of Organs-on-a-chip	16	Electrically Tunable Nanostructured Color Filter	46
CHAMELEON—Compliant Mechanism with Embedded Sensing	17	Results of Microlens Testing on Back-illuminated Image Sensors for Space	47
HECTIC—Improved SiC Sensor Technology for Harsh Environment and Yield Optimization Strategy for Hermetic Laser Assisted Bonding	18	Freeform Optics for Uniform Wall Illumination	48
LONGECG— Integration of Low-power Sensors in a Textile	19	Hybrid Plasmonic-dielectric Resonant Waveguide Grating for Diffraction with High Color Purity	49
SIOSCAPE—a Novel Silicon-based FlexTech Watch Escapement	20	Patterning Solar Cell Metal Grids on Transparent Conductive Oxides using Self-assembled Monolayers	50
MICROSYSTEMS	21	FluoReader—LED-based Fluorescence Reader with Configurable Color Channels for Flow Cytometry Applications	51
Fabrication of Bolometer Sensors on very Thin YSZ Substrates	24	Development of Scalable Fabrication Methods for High-precision Membranes	52
Geotechnical Inclinometer Sensors in Optical MEMS	25	SenseCard—a Disposable Parallel-sensing Card for Advanced In-vitro Models	53
Micro Heat Pipe: Performance Characterization	26	Automated, Disposable Sample Preparation Cartridge for Complementary Diagnostics	54
Piezoelectric MEMS Transducers, Ultrasonic Transducer for Distance Measurement	27	3MDGen—High Throughput Droplet Generation	55
MEGA—Micro-fabricated Electron Gun for Atomic Clocks	28	Disposable Glass Microfluidics for Nucleic Acids Bioassays	56
Measuring Mechanical Properties at the Scale of Watch Components	29	Automated and High Throughput Tissue Engineering	57
Thermal Management Modeling of High-power Chips and Calibration with Experimental Data	30	Automated Force Measurement System for 3D Printed Muscle Tissues	58
Radiation Hard Glass and Sapphire-based Miniature Hermetic Packages for Space Applications	31	Cotton-based Biosensors—Non-invasive Biomonitoring for Personalized Nutrition	59
Reliability of IR Components for Gas Sensing Applications	32	FoodSmartphone—On-site Biosensor for Pesticides Detection in the Area of Food Safety	60
Metal Matrix Composites by Additive Manufacturing	33	ACEnano—Hydrophobicity, Solubility and Reactivity Monitoring of Nanomaterials	61
Mesoscale Mechanical Performance of SLM Manufactured 17-4 PH	34	An Ultra-thin, Printed Pressure Sensor for Ventilation Monitoring	62
Ti-Al Intermetallic Compound Developing by in-situ Alloying using SLM Process	35	Printed Pressure Sensors: Industrial Case Studies	63
In-situ SLM Alloying for Development of High Strength Supersaturated Alloys	36		
Improved Tribological Properties of Brass through Multi Charge Ion-implantation	37		

PHOTOVOLTAICS & ENERGY MANAGEMENT	65	
Progress towards High-efficiency Perovskite/Silicon Tandem Devices	69	oAFD®—Optical Atrial Fibrillation Detector 98
High Performance Back-contacted Silicon Heterojunction Solar Cells	70	A Contact Microphone for Cardiac and Respiratory Sound Acquisition 99
Technology Platform for High-efficiency Silicon Heterojunction Solar Cells and Modules	71	Customized 3D-printed Seat Cushion for Wheelchair Users 100
Energy Management with Smart Thermostatic Valves	72	
Demonstration of Multi-service DC Microgrid in an Industrial Environment	73	
Evaluation of Battery Technologies for Solar-powered Aviation	74	
SYSTEMS	75	ULTRA-LOW-POWER INTEGRATED SYSTEMS 101
Highly Sensitive Miniature Sensors thanks to Quantum Effects in Atomic Vapors	77	Anomaly and Event Detection in Data Streams in Practice – Gesture Recognition using WiFi 103
Validation of ÉChelle-based Quantum-classical Discriminator of Light	78	First Hardware Platform for Wireless Avionics Intra-communications (WAIC) 104
Laser Head Demonstrator for the Gravitational Wave Observatory in Space	79	Large-scale Demonstration of RF-based Localization of Persons in Cruise Ships 105
Flash Imaging LIDAR for Space Debris Removal Demonstration Mission	80	
Close-up Imager for EXOMARS Mission: from Design to Flight Model	81	End-to-end Security and Privacy in a Heterogeneous Multi-platform Environment 106
Large Angle Flexure Pivot Development for Future Science Payloads	82	Integration of a Passive UHF RFID into a Metallic Package 107
Design Optimization for a Metal Additive Manufacturing Pilot Line	83	Dual-mode Bluetooth Silicon IP in 22 nm CMOS 108
Service-oriented Inference for Crop Classification using Satellite Images	84	60 GHz FMCW RADAR-on-Chip 109
In-line Impedance Spectroscopy for Automated Bovine Milk Analysis	85	Bluetooth Direction Finding 110
3D Lightfield Inspection System for Zero-defects Manufacturing	86	A Frequency Synthesizer for Ultra-low Phase Noise Multi-clock Generation 111
Process Design and Automation for Large Volume Hybrid Manufacturing Robot with High Accuracy and Quality	87	Talbot Effect Increases spaceCoder Resolution by more than One Order of Magnitude 112
ModelStore—A Lightweight System for Storing Neural Network Models	88	MODAL—a Multi-modal Sensing Platform for IoT Applications 113
Ultra-low-power Status Indication Device	89	Handheld Multispectral Imaging Device Designed to Aid Skin Cancer Detection 114
Continuous Non-invasive Blood Pressure Monitoring during General Anesthesia Induction	90	Deep Learning Architectures for Detecting Surface Defects using Multiple illuminations 115
Noninvasive Measurement of Pulmonary Artery Pressure via EIT	91	icyflex-V—a New Ultra-low-power Processor based on RISC-V Architecture 116
Driven Shield for a Robust Heart Bio-potential Monitor for Stress and Wellbeing Applications	92	Binary Weight CNN Hardware Accelerator for ULP Computer Vision 117
MDFD—a Portable Medical Device for Measuring the Electromechanical Properties of Skeletal Muscles through Electrical Stimulation	93	FaceDET—a 1.4 GOPS Face Detection System-on-chip based on Binary Decision Trees 118
Body Fluid Transfer	94	A Miniaturized Motor Control Unit for Space Exploration Missions 119
Obstacle Detection for Visually Impaired and Blind	95	A 20-b Resolution Dual Quartz-based Oscillator Gas-density Readout Circuit 120
Efficient Privacy-preserving Neural Network Inference for Heart Arrhythmia Detection	96	Improving 55 nm Technology System-on-chip Functionality through In-house focused Ion Beam Corrections 121
DeepCardio—Cardiac Arrhythmia Detection with a Neural Network	97	

ANNEXES

123

Publications	123
Proceedings	126
Conferences and Workshops	131
Research Programs	133
Innosuisse – Swiss Innovation Agency	135
European Commission Projects	138
European Space Agency and Swiss Space Office Projects	141
Industrial Property	142
Collaboration with Research Institutes and Universities	142
Teaching	147
Theses	148
Commissions and Committees	149
Prizes and Awards	152

CSEM SA

CSEM is a private, non-profit research and technology organization (RTO) with 35 years of technological transfer experience and know-how in digitalization, precision manufacturing, and sustainable energy technologies. A source of Swiss industrial competitiveness, CSEM offers end-to-end services, powerful R&D capabilities, and world-class engineering prowess—all, of course, “Made in Switzerland”.

The center’s research strategy is built around five main programs:

Microsystems—Dedicated to the development of complete and reliable microsystems solutions using MEMS and additive manufacturing technologies, with packaging and integration concepts.

#additivemanufacturing #AM #mems #3Dprinting #packaging
#hermeticsealing #photonics

Systems—Design, simulation, prototyping, and integration of micro/nano- technologies and advanced algorithms to create (sub-) systems for use within applications such as scientific instrumentation, automation and robotic systems, and wearable and medical devices.

#medtech #automation #wearable #quantumtechnology
#time&frequency #simulation #macroMems #laser #robotics

Ultra-Low-Power Integrated Systems—Addresses the key challenges to, and the technologies required in, developing embedded autonomous smart systems or remote sensing nodes, including deep learning and ultra-low-power electronics and wireless communication.

#smartdata #smartdust #zero-battery #IOT #edgecomputing
#wireless #machinelearning #AI #neuralnetworks #datascience
#smartdust

Surface Engineering—Focused on the functionalization of surface structure and composition (topographical and/or chemical), alongside the optimization of (bio-) chemical, optical and electrical properties. In addition, the program develops related competitive manufacturing technologies that are suitable for use in industrial applications.

#functionalization #biosensing #biosurface #nanocoating
#printedelectronics #nanostructuring #lifesciences

Photovoltaics & Energy Management—Fostering innovation while accelerating the pace of technology transfer in the fields of photovoltaics, energy storage, and systems, to support the Internet of Things, clean tech, and the energy transition.

#smartgrid #storage #energydata #bipv #solarenergy #HJT
#perovskite #thinfilm #scavenging #photovoltaics

MULTIDISCIPLINARY INTEGRATED PROJECTS—MIPS

Harry Heinzelmann

Multidisciplinary Integrated Projects (MIPs) form a horizontal program that mostly builds on technologies developed in the five topical research programs **Microsystems, Surface Engineering, Integrated Systems, Ultra-low-power Integrated Systems, and Photovoltaics & Energy Management**. The goal of the MIP program is to better exploit synergies, and to create solutions by combining several of CSEM's technologies.

Every year CSEM dedicates an important part of its resources to these highly interdisciplinary projects, targeting demonstrators with a high level of maturity (high technology readiness level (TRL)) for novel applications with high market potential in relatively short development times.

Besides typical MIPs, which last 1–2 years, Feasibility MIPs have been introduced, allowing the rapid exploration of new concepts. Another project type, Technology MIPs, addresses long-term co-developments with different technologies.

The MIP program is reevaluated annually and consists of ongoing projects and new proposals in a healthy balance, making it possible to respond quickly to newly emerging market needs. In this way, CSEM's MIPs complement its five topical research programs in an ideal way. The MIP program enables CSEM to offer its industrial clients an even richer portfolio of technologies, beyond the possibilities of its thematic research programs alone.

An overview of 2019 MIPs can be found in the text below; the projects are presented in more detail in the following pages.

Classical MIPs

IntelliDUST—Intelligence in 3D accelerometer sensors at zero added power cost

The processing of data at the sensor node level ("at the edge") is an important feature of future Internet of Things (IoT) applications. The resulting reduction in the sensor data volume transmitted helps to reduce overall energy consumption, which is of increasing relevance in view of the rapidly growing number of deployed sensor networks.

This project has demonstrated that it is possible to implement an intelligent algorithmic layer without significantly impacting the power consumption of the sensor. This is demonstrated for the case of physical activity tracking based on inertial sensors (e.g., 3D accelerometers), an application of considerable interest for wearables with optimized energy autonomy.

MULTIPLIR—Portable long-wave infrared camera for gas detection

Many of the regulated greenhouse gases, such as ammonia (NH_3), nitrous oxide (NO_2), methane (CH_4), sulfur hexafluoride (SF_6), or Freon (fluorinated cooling agents), show characteristic absorption in the infrared wavelength regime. The project MULTIPLIR aims at developing a compact multispectral camera for quantitative gas detection.

The first demonstrator is based on an optical setup with a germanium microlens array matched to an interference filter matrix. The light detection is accomplished with a long

wavelength infrared bolometer. A portable multispectral camera will find applications in gas leakage detection in industrial processing and in fire emergency situations, or during the transport of fuel gas.

ParticleID—Identification of particulate contaminants in liquids by neural network analysis of scattering patterns

Techniques to detect and characterize particulate contaminations in water, such as bacteria, algae, sand, pollen, or micro-plastic particles, are important for water quality monitoring and process control. This project aims at using laser scattering and machine learning for particle identification that is possible without any additional consumables.

Light scattering off individual particles in a capillary tube delivers characteristic scattering patterns that can be classified with dedicated algorithms. The goal of this effort is to achieve competitive speeds for the in-line characterization of concurrent contaminants at the single particle level.

PROBIOTICS—An energy-autonomous miniature wireless sensor mote interacting with your phone

Many applications in the Internet of Things (IoT) domain are demanding sensors with small dimensions and low energy consumption. The project PROBIOTICS is addressing this challenge with the ambition to develop a robust, extremely miniaturized, pin-sized, energy autonomous IoT node combining energy harvesting, storage and management, sensing (e.g., pressure, temperature, acceleration), on-chip digital signal processing, and wireless data transfer.

The small dimensions of $5 \times 3.4 \times 3 \text{ mm}^3$ and the integration of the energy providing PV cell make the resulting sensor node an interesting platform for applications even in environments with reduced light conditions. Demonstrations of indoor status monitoring and theft protection have shown the significant potential of this "smart dust" technology.

Visage—A miniaturized face-detection sensor

People awareness, the automated and timely detection of the presence of people in a given area, offers many advantages, such as improved services, better resource planning, and increased safety in the operation of dangerous equipment. For example, dangerous machinery can be turned off when people are detected within its range of operation.

The project Visage aims at developing a highly integrated system featuring a camera and face detection algorithms. The optical system is optimized for image quality in a small form factor, allowing the whole system to be integrated in a volume smaller than that of a sugar cube.

Technology MIPs

3D- μ Fluidics—Automated long-term culturing of organs-on-a-chip

Organs-on-a-chip (OOC) is a new concept that allows the study of human physiology in an in vitro model. Emerging from lab-on-a-chip fluidic systems, OOCs go further and allow the simulation of cell complexes and entire organs. It is hoped that this

technology will eventually replace animal tests in drug development and toxin testing.

This project aims at developing an OOC system with automated maintenance, so that time-consuming and contamination-prone intervention by lab personnel can be avoided in the future. The cell culturing is supported by continuous sensing of the critical parameters as well as by a regular exchange of the cell medium, all under controlled conditions. The demonstrator system was successfully tested with mouse neurons.

CHAMELEON—Compliant mechanism with embedded sensing

Additive Manufacturing (AM) is a fabrication method that allows 3-dimensional components to be built up in a layer-by-layer process. AM has introduced unprecedented design flexibility and opened the way to toolless, small series and even one-off production. One of the next crucial steps to further advance AM technologies is the integration of functionalities—for example, compliant characteristics, sensors, or actuators—into the fabricated components.

In this project, advanced design is being combined with a wide range of (3D-) printing technologies and surface treatment methods. The resulting metal-based components with embedded functionalities and optimized surface properties will be used in space, aeronautics, and medical applications.

HECTIC—Improved SiC sensor technology for harsh environment and yield optimization strategy for hermetic Laser Assisted Bonding (LADB)

The HECTIC series of projects aims at developing process technologies for silicon carbide (SiC), a material with excellent thermal and chemical properties ideal for sensor applications in harsh environments, including at temperatures of up to 650°C. MEMS SiC pressure sensors have been demonstrated earlier.

In this project, some critical processes need to be improved in order to bring the SiC technology to a higher technology readiness level (TRL). In particular, the quality of ohmic contacts needs to allow low noise measurements, the etching process needs to be more robust, and the yield of the laser assisted bonding process needs to be higher. Finally, the long-term degradation mechanisms need to be better understood.

LONGECG—Integration of low-power sensors into a textile

Portable health monitoring solutions have recently attracted great interest, in particular for regular and long-term monitoring. Key factors for widespread application are the quality of the results and the portability—that latter including the seamless integration of the sensor technology into textiles. The medical grade signal detection of, for example, electrocardiograms (ECG) has, however, been difficult to achieve, mainly due to the complexity of the measurements.

The aim of this year's project is the development of a Holter monitor for medical quality ECG measurements that is comfortable enough to wear over periods of days and weeks. The result is a tightly fitting vest with dry electrodes and integrated electronics, based on CSEM's patented cooperative-sensor technology and an ultra-low-power ASIC that allows weight to be reduced and comfort increased.

SIOSCAPE—A novel silicon-based FlexTech watch escapement

Over the past ten years, the precise mechanical structuration of silicon, on scales from micrometers (MEMS) up to centimeters (MacroMEMS), has allowed the development of innovative watch mechanisms. The project series SIOSCAPE has the objective to design, produce, and characterize silicon-based oscillators and escapements in order to lower the technological risks prior to proposing the technology for industrialization by the Swiss watch industry.

In this project a novel escapement has been designed that makes use of flexure blade pivots for precise and frictionless oscillations. This SIOSCAPE escapement has been paired with a Wittrick oscillator, comprising a total of four monolithic silicon parts. It has been successfully integrated into a watch caliber and subsequently characterized, demonstrating a high power reserve and automatic restarting.

IntelliDUST—Intelligence in 3D Accelerometer Sensors at Zero-added Power Cost

M. Pons Solé, E. M. Calvo, R. Cattenoz, R. Delgado-Gonzalo, S. Emery

Sensors generate raw signals that need processing before providing value. With the advent of new generation of deep-ultra-low power sensors (μW consumption range), the consumption of processing algorithms is becoming dominant and therefore it is limiting for low-power applications. This work shows it is possible to provide the intelligent algorithmic layer without impacting the already negligible consumption of sensors by combining CSEM's algorithmic and ultra-low power know-how. The study is presented for 3D accelerometers sensors and activity tracking processing algorithms.

The power consumption of 3D accelerometers has been continuously decreasing over recent years from more than 100 μW (e.g., ADXL345) to less than 4 μW (e.g., ADXL362) and this trend is still on-going. On the contrary, related processing algorithms running on standard microcontrollers still consume in the order of 100 μW nowadays, impacting overwhelmingly the power budget.

The goal of this work is to bridge this gap for a particular case relevant to the market: physical activity tracking based on inertial sensors (e.g., 3D accelerometers). The booming industry of wearables (e.g., smartwatches, smart-textiles) where reduced consumption leads to extended autonomy and thus increased user comfort would greatly benefit from such results.

CSEM has a long history of algorithm design, development, and implementation in low-power wearable devices relying on inertial sensors. Among them, the following might be highlighted: activity profiling [1], kinetic [2] and gait [3] analysis, energy expenditure [4], fall detection [5] and swimming performance monitoring [6]. The ultimate goal is to add such intelligent algorithmic layers with negligible overall consumption overhead to turn a simple 3D accelerometer into a smart sensor. Five alternatives have been studied and are described below. Table 1 summarizes the results.

Table 1: Activity tracking algorithm consumption and flexibility.

#	Hardware	Supply	Algorithm	Sensor	Flexibility
1	CortexM0	1.8V	90 μW	4 μW	Yes
2	icyflex2	1.0V	16 μW	4 μW	Yes
3	Accelerator	1.0V	1 μW	4 μW	No
4	Accelerator	0.5V	0.1 μW	4 μW	No
5	icyflex2	0.5V	0.8 μW	4 μW	Yes

Option 1 is the reference design and uses an ARM's Cortex-M0 microcontroller embedded into a Nordic BLE transmitter (NRF51822) to run the activity tracking algorithm software. Power consumption is estimated to 90 μW . Option 2 uses CSEM's low-power icyflex2 microcontroller [7] implemented in standard 55 nm bulk technology (at 1 V nominal voltage). Power consumption is estimated to 16 μW and is still too high when compared to the 4 μW sensor consumption. Option 3 is to design a dedicated hardware accelerator for the activity tracking algorithm using the same standard 55 nm technology. Power consumption reduces to 1 μW , which is already lower than the sensor consumption. It could already be interesting depending on the application power budget. Option 4 is to go one step further for the dedicated hardware accelerator design and use sub-threshold voltage design on a specially tailored MIFS Deeply Depleted Channel (DDC) [8] 55 nm technology (at 0.5 V supply voltage). The power consumption is estimated to 0.1 μW , more than one order of magnitude lower than the sensor. Option 5 is based on the sub-threshold technology and conditions of option 4 but the algorithm is executed on an icyflex2 microcontroller [9]. In this case, running the algorithm draws 0.8 μW , similar to that of the dedicated hardware accelerator at nominal voltage, but with the advantage of having the flexibility of a microcontroller. The algorithm can thus be tailored to the application needs or refined during the product lifetime.

As expected, dedicated hardware accelerators show the lowest power for adding higher level intelligence such as activity tracking to a 3D accelerometer with up to 100-1000x power gain compared to the reference design, marginally impacting the sensor power budget. However, thanks to CSEM's know-how in sub-threshold design, comparable power levels are obtained when implementing the algorithm on an icyflex2 general purpose microcontroller, yielding the best of the power-flexibility trade-off.

- [1] R. Delgado-Gonzalo, *et al.*, "Learning a Physical Activity Classifier for a Low-power Embedded Wrist-located Device," IEEE BHI (2018).
- [2] M. Bertschi, *et al.*, "Accurate Walking and Running Speed Estimation Using Wrist Inertial Data," IEEE EMBC (2015).
- [3] R. Delgado-Gonzalo, *et al.*, "Real-time Gait Analysis with Accelerometer-based Smart Shoes," IEEE EMBC (2017).
- [4] R. Delgado-Gonzalo, *et al.*, "Human Energy Expenditure Models: Beyond State-of-the-art Commercialized Embedded Algorithms," DHM (2014).
- [5] C. Moufawad el Achkar, *et al.*, "Real-time Fall Detection Using Smartwatches," EU Falls Festival (2018).

- [6] R. Delgado-Gonzalo, *et al.*, "Real-time Monitoring of Swimming Performance," IEEE EMBC (2016).
- [7] J.-L. Nagel, *et al.*, "The icyflex2 Processor Architecture", CSEM Scientific and Technical Report (2009).
- [8] K. Fujita, *et al.*, "Advanced Channel Engineering Achieving Aggressive Reduction of VT variation for Ultra-low-power Applications," IEEE IEDM (2011).
- [9] M. Pons, *et al.*, "A 0.5V 2.5 $\mu\text{W}/\text{MHz}$ Microcontroller with Analog-Assisted Adaptive Body Bias PVT Compensation with 3.13nW/kB SRAM Retention in 55 nm Deeply-Depleted Channel CMOS," IEEE CICC (2019).

MULTIPLIR—Portable Long Wave Infra-red Camera for Gas Detection

G. Voirin, C. Kündig, N. Cantale, B. Timotijevic, N. Niketic, R. Ischer, M. Krieger, L. A. Dunbar

Combining a long wave infra-red bolometer, germanium microlens array and an interference filter matrix we create a compact portable multispectral system suitable for direct quantitative gas detection. Many regulated gases have absorption line in the long wave infra-red, e.g., NH₃, methane, SF₆, N₂O, and Freon. Applications include helping firefighters locate dangerous gas leakages such as ammonia, gas leakage monitoring in industry and specifically those dealing with compressed gases, such as fuel gas control on Liquefied Natural Gas carrier ships or Low-Density PolyEthylene production with hyper compressors.

Detection in the thermal infrared wavelength region has applications in environmental testing, agriculture, life science and medical markets. The rapid market expansion can be attributed to the recent advances in Long Wave Infra-Red (LWIR) technologies, in particular the apparition of cost-effective LWIR bolometers cameras and the invention of IR glass which allows inexpensive LWIR optics for high volume applications.

Many gases and materials have direct spectral signatures in the LWIR, for example greenhouse gases or ammonium sulfate. By attributing and quantifying these absorptions or reflections lines we identify and quantify these elements.

In this project, CSEM combines thermal imaging, filters and signal processing techniques to visualize and identify materials using their infra-red spectral signatures. This is useful to monitor gas leakage, gas emissions or to distinguish materials. One use case was to help firefighters detect ammonia, which is highly toxic and common in modern building's cooling systems. In such cases it is important for the firefighters to locate the ammoniac leakage to be able to isolate and seal it quickly. Other industrial use cases are when gas leakage monitoring can avoid large air pollution, monitoring in cargo ships for loss during transport, decrease greenhouse gas contributions or minimize explosion risks in industrial sites.

CSEM is developing a multispectral optical system in the LWIR, composed of up to 35 spectral wavelengths. A bolometer with 1024x768 pixels is used as the detector. Each wavelength forms its own spectral image in a narrow spectral band given by passing through a dedicated filter (Ref to patents: WO2018115320 & WO2018113939). This results in 35 imagelets with a resolution of about 150x150 pixels.

As alternative to commercial interference filters, CSEM is developing Fabry-Perot filters based on porous metallic mirrors that will lead to cheaper filters when produced in large quantities with microfabrication technologies and processes (patent pending).

The optical system was reproduced using optical simulation software (ZEMAX). An image simulation and a typical quality parameter (Modulation transfer function MTF) are presented on Figure 1. A picture of the 35 imagelets is presented on Figure 2.

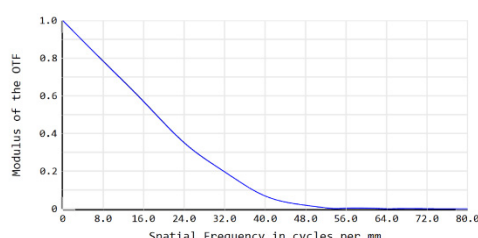


Figure 1: Image simulation and MTF quality parameter.

Using the absorption spectrum of the gases of interest and the filters transmission spectrum, image processing software is currently being developed to locate and measure specific gases and materials.

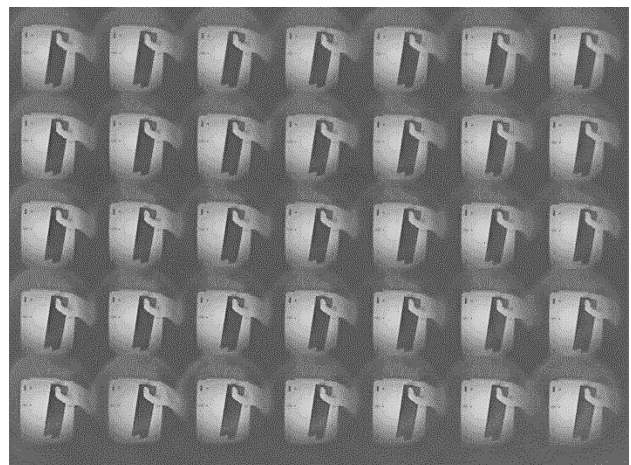


Figure 2: Example of an image with 35 imagelets.

The system has been tested with different gases (N₂O, SF₆, NH₃) using a gas cell with IR transparent window. The cell was filled with a target gas at different pressure. Imagelets at different wavelength were recorded. As expected, the absorption of the gas at the specific wavelength can be directly visualize on images (Figure 3 left). Software identifies the gas and estimates its absorption (Figure 3 right).

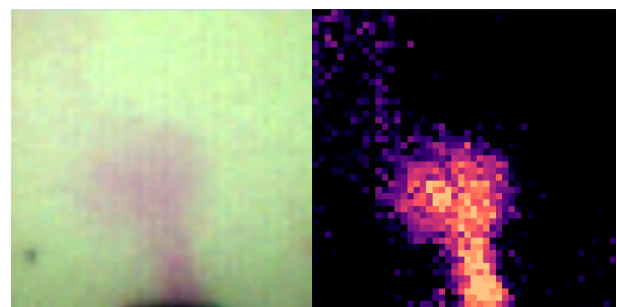


Figure 3: Visualization of NH₃ vapors coming out from a bottle: left composite image (left), concentration map (right).

Using the latest technology of thermal imaging and filters, it was possible to demonstrate the feasibility of visualizing a gas with a specific absorption in the Long Wave Infra-Red. Detection in the range of dozens ppm.m for gas like SF₆ can be reached. The system is portable and can be adapted to different gas panel by changing the microarray of filters.

This project was executed in the frame of CSEM's MIP program, and CSEM would like to thank the Swiss Confederation and the Canton of Neuchâtel for their financial support.

ParticleID—Identification of Particulate Contaminants in Liquids by Neural Network Analysis of Scattering Patterns

P. Cristofolini, M. A. Kirschmann, P. Jokic, S. Cattaneo

Techniques to identify, measure and count particles in a flow of liquid are becoming widely used in water quality monitoring and industrial process control, but they are still expensive to operate or of low specificity. CSEM is developing a simple, autonomous system to identify particles one-by-one, which harnesses the power of artificial intelligence and needs no extra consumables. The system is based on laser scattering of single particles and classification of the resulting scattering patterns with a purpose-trained neural network.

Natural water contains many particulate contaminations, like bacteria, algae, sand, pollen and micro-plastic particles. These contaminations are tested in regular intervals by water authority bodies to ensure the high standards for drinking water are met. Also in process control it is of high importance to monitor particulate contamination concentrations in process liquids and waste water. In order to identify and quantify particles in a mixed suspension, it is necessary to measure each particle one-by one, or to separate particles by type and size before measuring them as an ensemble. Systems for mixed particle identification currently on the market are complicated and human operated (flow cytometers), of low specificity (particle counters and size analyzers, impedance spectrometers) or targeted to a very special task only (electrochemical monitoring sensors, contamination warning systems).

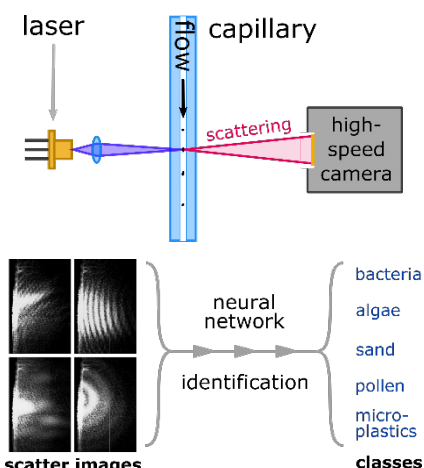


Figure 1: (top) Liquid with suspended particles is run through a narrow capillary. A laser crosses the capillary and produces 2D scattering patterns that are recorded by a high-speed camera. (bottom) The recorded scatter images are analyzed by a neural network to identify the particles, by assigning them to one of the pre-trained classes.

CSEM is working on a new system for autonomous in-line monitoring and counting of multiple particle types in liquids. The system is depicted in Figure 1 top. Liquid containing suspended particles is run through a capillary and a focused laser illuminates the capillary perpendicularly to the flow direction. When a particle crosses the laser beam it scatters some of the laser light and produces a 2D scattering pattern. These patterns are recorded by a high-speed camera and transferred to a PC for identification. A pre-trained artificial neural network (NN) is used to identify the particle class (bacterium, sand, micro-plastic, etc.) automatically (Figure 1 bottom). The beauty of the NN-approach is that it can pick up features from the scattering patterns, and how they change as the particle flows thought the laser light, that cannot be detected with other means. The system can be trained for very specific applications, like monitoring the concentration of particles with a specific size and shape, or counting the number of micro-plastic particles in a mixed sample.



Figure 2: Image of the first prototype setup.

The system currently uses an off-the-shelf capillary and an inexpensive laser diode, together with the "FastEye" high-speed camera developed in-house by CSEM, equipped with an onboard FPGA processor. With this low-cost system (compared to competing products) we could achieve single particle scatter imaging at 2'000 frames per second for particles with diameter 1 to 25 μm . The measurement volume is very small at 0.5 nL and the system was able to analyze liquid at a rate of 200 $\mu\text{L}/\text{min}$. In a measurement campaign we have recorded a training dataset with 1'000 events per class (PS spheres: 1, 2, 4.5, 5, 10 μm diameter; yeast). A subset of these images was used to train the NN, then the NN was used to classify the entire dataset. The scattering events were sorted by intensity of the scattering signal. For events with strongest signal the classification results were very good for each class (91.7% average), and also for weaker events the classification worked very well. The NN was successful in distinguishing 4.5 μm from 5 μm polystyrene spheres, which attest that the system can achieve a size resolution of < 0.5 μm .

One of the target applications is water quality monitoring. We have dissolved baker's yeast in water and measured it with our system. The NN was able to pick out the yeast cells from polystyrene particles of comparable size (4.5, 5 and 10 μm) with remarkably high accuracy of 86% for the strongest events. In addition, we were able to record video sequences of yeast cells as they traversed the laser beam. A rotation of the scattering pattern was visible, indicating that video sequences contain valuable additional information that can be used to better identify particles.

As a next step, it is planned to test this system a much wider selection of particles found in the environment (different bacteria, algae, pollen, river water, micro-plastic) to see how well the system works with natural samples. Furthermore, it is envisaged to embed the NN classification directly on the FPGA of the FastEye camera, thus making the system a truly autonomous intelligent particle monitoring solution, much smaller and cheaper than existing solutions on the market.

PROBIOTICS—an Energy Autonomous Miniature Wireless Sensor Mote Interacting with your Phone

D. Ruffieux, J. Bailat, P.-A. Beuchat, S. Biselli, J. Brossard, M. Dadras, C. Denizot, D. Domine, M. Fretz, R. Jose James, Y. Liechti, Y. Marozau, P. Nussbaum, P. Stadelmann, S. Zabihzadeh, L. Zahnd

This multidisciplinary project aims at demonstrating a miniaturized energy-autonomous wireless sensor node that is powered with a 3-segment PV-cell and a solid-state battery. Despite its $5 \times 3.4 \times 3 \text{ mm}^3$ size, it is able to interact with tablets, mobile phones and the cloud while harvesting its own energy.

IoT, digitalization and industry 4.0, three fashionable keywords that share a common requirement: achieve seamless data transfer between sensors, a network of distributed intelligence and the cloud with its unlimited computing resources. While power-plugged, bus interconnected sensors might be deployed relatively easily, wiring is costly, voluminous, lengthy and heavy (meaningful for planes, cars) and quite hard to deploy a posteriori preventing flexibility, re-configurability. Although wireless data transfer has gradually eliminated the data routing wire requirements over the last thirty years (mobile phones, WiFi, Bluetooth/BLE), one issue remains: how to cut the last wire, the power plug without getting trapped into the battery replacement/recharge maintenance hurdle?

Energy harvesting is obviously part of the answer but of utmost importance is energy usage optimization through proper architecting and management. Among the different energy sources available widely, harvesting sunlight or even indoor lighting with compact photovoltaic diodes already fulfills the powering requirements for many use-cases. Remembering the hand-held, solar-powered calculators of the late seventies, but considering the humongous performance improvement brought meanwhile by CMOS scaling, may one design a miniaturized wireless sensor node capable of 365 d / 24 h monitoring and seamless interactions with the cloud via mobile phones, tablets?

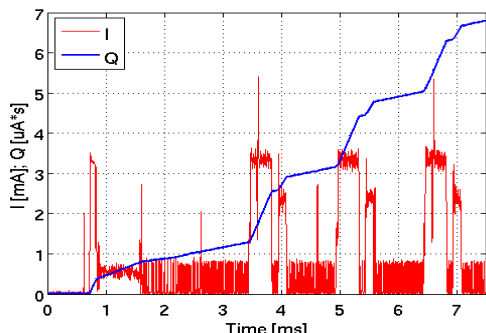


Figure 1: Current profile of a BLE advertisement beacon with RSL10.

The key requirements to build an energy autonomous wireless sensor may be summarized as follow: 1) maintain network synchronization over idle periods with an ULP timing source that is precise enough to organize timely periodic wake-ups so as to perform correlated sampling or exchange data wirelessly among spatially distributed sensor nodes; 2) use smart ULP sensors permitting context-level hierarchical or threshold-triggered sensing autonomously; 3) perform edge processing, *i.e.*, compute at node level to extract higher-level information and minimize the energy cost of transmitting excess data; 4) secure cloud access while dissipating as little energy as possible locally, either via a dedicated local hub gateway, or even better taking advantage of an already widely deployed, standardized, communication infrastructure; 5) manage and optimize the energy harvesting, storage and distribution so as to guarantee the best possible sensing performance and quality of service at any time.

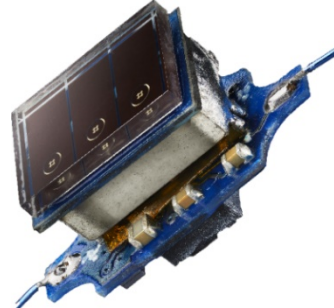


Figure 2: Photograph of the miniature wireless sensor node.

Requirements 1, 3, 4, 5 may all be satisfied with a modern IoT system-on-chip (SoC) such as On Semiconductor's RSL10, one of the lowest power circuit available on the market that relies on CSEM BLE IP. Figure 1 shows the current consumption of the SoC while transmitting BLE beacons consecutively in the three advertisement channels after the system resumes following a timer interrupt. A quiescent current consumption of 250 nA including leakage is reached in timekeeping mode. The charges drawn from a 3 V supply reaches 7 $\mu\text{A}\cdot\text{s}$ per beacon, 55% of which is used for the 3×35 bytes transmission, 17% to potential acknowledge reception should a master attempt to bond with the device, 28% for the MCU to execute the IRQ code. Within the first 3 ms, the MCU starts the radio XTAL, restores the system clock, performs a battery voltage measurement using the on-chip ADC, turns on the different power management blocks and updates the data to be transmitted, before triggering the modem and returning idle. One gets sub- μA current with 1 beacon / 10 s.

As a smart sensor illustrative of 2, the BMA400, a novel 3-axis accelerometer developed by Bosch, was selected. With a current consumption of 150 nA, 850 nA, 4 μA , 15 μA respectively in off, motion activation, step analysis and full accelerometer modes, this sensor incorporates low-power digital accelerometers able to perform, in an autonomous way, (in)activity detection and recognition, orientation detection (tilt), step counting as well as tap/double tap detection. As such high-level context signals are all mapped to dedicated IRQs, both data transfer between the sensor / system MCU and the computational load, are greatly reduced, yielding substantial power savings.

The resulting miniature sensor node is shown in Figure 2. Excluding the antenna, the mote measures $5 \times 3.4 \times 3 \text{ mm}^3$, while including a 200 $\mu\text{A}\cdot\text{h}$ battery and a 3-segments PV-cell forming the power pack. Even when the latter was placed on a west facing window in winter time, 50 $\mu\text{A}\cdot\text{h}$ could be harvested daily on average, despite foggy days. This is enough to power the complete sensor node and monitor window tilt, opening/closing and perform glass break detection. One could imagine other applications such as piece of art, asset surveillance or even lapel pin or earrings remote controls using (double)tap functions.

Field tests are under way paving the way towards a cloud of ubiquitous motes that one may merely drop to the cloud!

Visage—a Miniaturized Face Detection Sensor

P. Nussbaum, M. Fretz, R. Krähenbühl, E. Türetken, E. Azarkhish, P. Jokic

Bringing face detection into a single low-cost and low-power component opens up new perspectives in products requiring safety or people awareness, as it can control simple functions such as access control, standby operation etc. Here a system-on-chip supporting an accelerated machine-learning algorithm with state-of-the-art optics and packaging have been devised to meet this challenge.

This component should be low-cost and contain a highly integrated system with an optic, imager and the System-on-Chip (SoC) that should not take up more than $\frac{1}{2}$ cm³. In such a system the packaging will encapsulate the compact lens, that must nevertheless provide a crisp image with a small track length, the SoC with the dedicated face detection algorithms.

Packaging

A global concept for the encapsulation of all the components has been sketched in Figure 2:

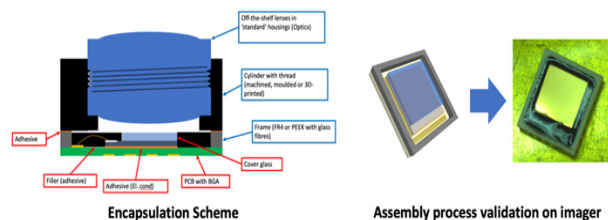


Figure 2: Encapsulation approach (left) and first tests on imager only (right).

The assembly process has been validated on a simpler encapsulation (imager only) the next step is to include the optics. The final system encapsulation includes the Visage SoC.

Optics

A commercial off-the-shelf (COTS) lens meeting the requirements of Visage has been procured, to provide a basis for comparison and to speed-up early prototyping. This version is more compact with a track length of 6 mm, see Figure 1, but is likely to give more blur.

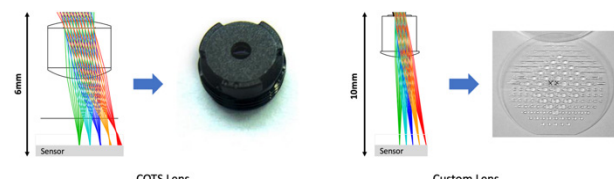


Figure 1: COTS lens (left) and CSEM lens (right).

A custom version has been designed and assembled for release in time with initial project planning. This version has a longer track length, *i.e.*, 10 mm, but is designed to deliver crisper images than the COTS lens (resulting spot size on imager of 8 μ m vs. 17 μ m) over a twofold increased focal depth range. Integration into the packaging and characterization will be completed in 2019.

Algorithms selection and training

Two algorithms capable of achieving good accuracy for face detection while fitting with the exceedingly small memory footprint (1 Mbytes) have been identified. The first is a modified AdaBoost Binary Decision Tree (BDT) algorithm that has been thoroughly optimized for Visage and the second is based on a Convolutional Neural Network (CNN) in an attempt to ultimately quantify to a binary neural network.

A data set containing more than 1 million images with uniformly distributed face sizes, locations, rotations and random distortions has been compiled to train and test the algorithms. Tests on unseen images showed 96% accuracy at less than 1% false positive rate. The operation of the detection algorithm is illustrated in Figure 3.

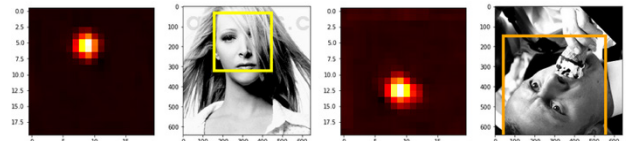


Figure 3: Probability distribution map of a face in the scene (orange blob) and the resulting face location in the source images.

System-On-Chip (SoC)

The integrated circuit supporting the machine learning accelerator has been structured around a Risc-V CPU which manages the whole system and drives the external communications (imager and detection output), see Figure 4.

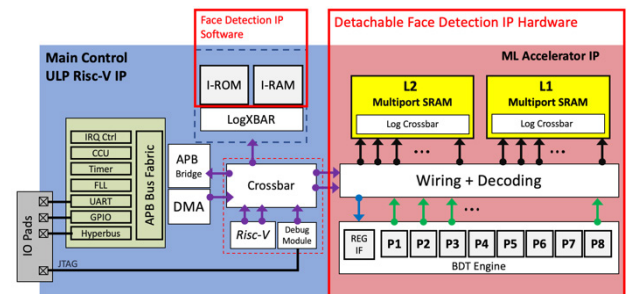


Figure 4: SoC Architecture.

The machine learning accelerator shown by the right part in the bloc diagram occupies 90% of the silicon area due to the size of the required memory. A first floorplan of the SoC can be found on the right side, showing an overall surface of 3 mm².

2019 Demonstrator

A first version of the demonstrator is presently being assembled. It is based on the Vision-in-Package (VIP) platform running the latest version of the BDT algorithm developed for the Visage project.

The setup implements a fully functional LED torch lamp controlled by the VIP and powered by batteries. The objective is to test the concept at the system-level and appraise the performances obtained when achieving the expected safety feature (dimming when beaming to a face).

The final component, which will be comprised of the packaged custom optics, SoC will be released in Q2 of 2020.

3D- μ FLUIDICS—Automated Long-term Culturing of Organs-on-a-chip

S. F. Graf, S. Berchtold, T. Volden, S. Boder-Pasche, S. Heub, N. Glaser, M. Zinggeler, F. Kurth, H. Chai-Gao, G. Weder, V. Revol

Organ-on-Chip (OoC) is by nature a very diverse field covering topics that range from developmental biology, microfabrication, tissue engineering, organoids, and organ-specific models to regulatory aspects and disease modelling. The development of OoC follows six steps: (1) organ-level functions to be mimicked, (2) design & bioengineering, (3) qualification & bio validation, (4) standardization, (5) production, upscaling & high throughput, and (6) adoption by pharma community. Nowadays, the main challenge is to develop technologies allowing to standardize as well as parallelize and increase the robustness of OoC. A first response to this challenge is our maintenance system which automatically exchange culture media over long periods. We have successfully demonstrated its potential on mouse neurons during a 3-week differentiation period.

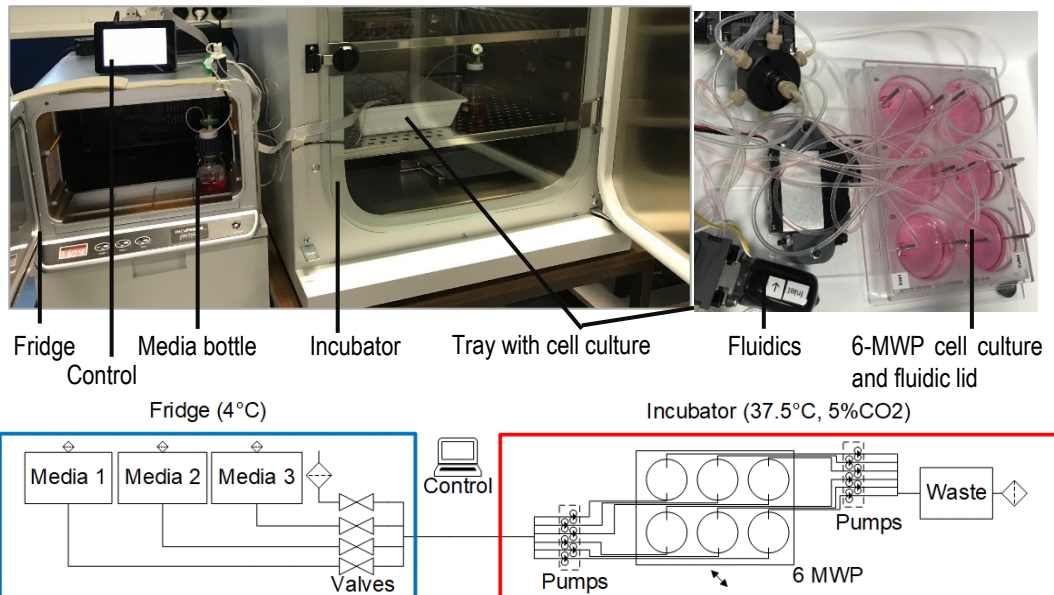


Figure 1: Automated culturing system with the buffer stored in the fridge and the cell culture in the incubator.

Micro-well plates ranging from 6 to 1536 assays have become a standardized platform in analytical research and clinical diagnostic laboratories including handling by robots. This international standard is increasingly adopted by Organ-on-Chip (OoC) systems for high throughput screening. There are two common denominators: base-plate and lid. All OoC systems, regardless of the biological model, require continuous maintenance as well as bio-sensing for analysis. For this purpose, we have designed a maintenance system and successfully demonstrated it with mouse neurons over the 3-week differentiation period.

Our maintenance system (Figure 1) pumps fresh media directly from a bottle stored in the fridge while the cells are kept in the incubator. The fluidic lid sitting on the well plate helps to refresh culture media. The frequency of media exchange can be chosen by the operator and is then performed fully automatically. The setup is designed, such that the operator still has the freedom to check the cell health on a microscope.

To validate our setup we have cultured mouse neurons over the 3 week differentiation period in a 6-well plate and performed an automated media exchange every second day. In a first step, the well plate is automatically tilted and about 2 ml of the 4 ml working volume is removed. In a second step, the well plate is moved back into the horizontal position and 2 ml of fresh buffer is added. From time to time, the operator also moved the setup on to a microscope to check the cell health. Finally, Figure 2 shows the successfully cultured mouse neurons and its control. Both images show the presence of neurons (red), astrocytes (green) and cell's nucleus (blue) as it would be expected. The initial sterility has been achieved by autoclaving and ethanol

sterilization. Furthermore, bottles have been equipped with filters. In a mass product, these sterilization steps will be replaced by gamma sterilization.

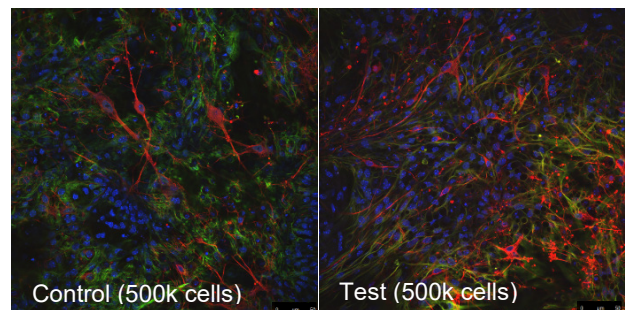


Figure 2: Immunocytochemistry stainings of mESC-derived neuronal cultures on glass. Neurons are stained with β -III Tubulin antibody (red). Astrocytes are stained by GFAP antibody (green). DAPI stains the nucleus of the cells (blue). Images were acquired on an Axiovert microscope with 40x oil objective.

After the successful test with mouse neurons, we will test our system with human neurons. Furthermore, we are going to implement an electro-chemical sensor to monitor the cell behavior with, e.g., glucose consumption. The operator will then receive a direct feedback of the cell health without moving the cell culture on a microscope.

This work was supported by the Swiss Confederation and MCCS (Micro Center Central Switzerland). CSEM thanks them for their support.

CHAMELEON—Compliant Mechanism with Embedded Sensing

S. Lani, N. Hendricks, O. Chandran, H. Saudan, L. Kiener, F. Cosandier, N. Marjanovic, J. Schleuniger, J. Kaufman, R. Jose James

Structural health monitoring for preventive maintenance, control feed-back of moveable mechanisms, integrated actuation and adaptive objects necessitate a heterogeneous integration of numerous technologies. In order to bring Additive Manufacturing (AM) beyond state-of-the-art technologies of topology optimization, it is important to develop concepts and technologies allowing such functionalities while keeping the versatility and flexibility advantages of AM. Hence, CHAMELEON aims at developing technologies to manufacture metal-based 3D parts with embedded functionalities such as compliant mechanisms, electrical/pneumatic feedthroughs, sensors and actuators by combining advanced design, ink-jet printing (IJP), aerosol jet printing (AJP), polymer casting, laser powder bed fusion (LPBF) and surface post treatment. The main applications will focus on markets already using AM in production (space, aeronautic, and medical) that are requesting additional functionalities.

AM is taking more and more importance for the production of high-end components in application like space, aeronautics and medical fields. Such industries have critical needs for which AM has appealing features. Among them, they benefit very much from a manufacturing technology able to produce components with complex geometries that is suitable for moderate production volume as well as weight reduction thanks to topology optimization. However most of today's applications, for which AM is used, is for manufacturing "passive" elements with no functionality except providing a mechanical structure. To grow the market attractiveness of AM, it is important to develop technologies to bring new functionalities while keeping the advantages of flexibility and versatility of AM. Hence, CSEM is investigate the opportunity to combine 3D with 2D printing to obtain 3D compliant mechanisms with embedded sensors in order to elaborate complex AM-based Mechatronics devices.

Within the past years, CSEM has achieved the following milestones using LPBF AM technology:

- Minimum feature size reduced by a factor of more than two with stainless steel, aluminium and titanium alloys (reaching 100 µm features size with stainless steel).
- Compliant mechanism made by AM opening new design, mass reduction and reduced assembly steps.
- Embedded electrical wiring by combination of LPBF, polymer casting, and machining with the demonstration of a new slip ring rotor with RUAG Slip Rings SA®.
- Demonstration of various 2D printed sensors by IJP and AJP

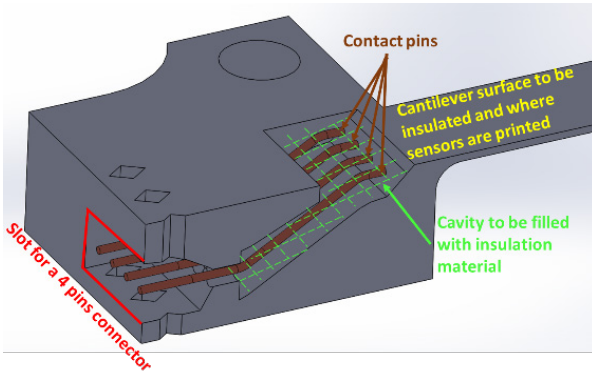


Figure 1: Cross section of the testing cantilever structure CAD design.

In this project we have used and optimized the above building blocks. Moreover, to demonstrate a complex mechatronics device, we have additionally successful demonstrated:

- The integration of built-in electrical wires and connecting interfaces to avoid wires soldering steps. The dielectric insulator has been made by polymer casting technique (see Figure 1).

- Laser smoothing of the metal surface to achieve <700 nm Ra surface roughness in order to provide a good quality surface for sensors printing.
- Ink jet printing (IJP) and aerosol jet printing development (AJP) to deposit electrical insulator layer and strain gauges on AM-flexure elements (see Figure 2). The measured gauge factor (GF) is 2 with silver based AJP gauge wires which is in-line with expected value with such technology.

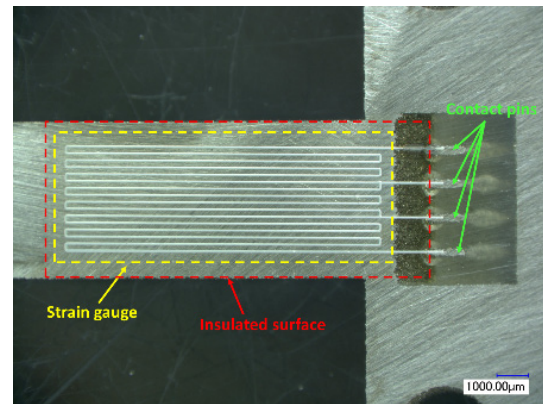


Figure 2: Printed strain gauge and insulation by Aerosol jet printing on a 300 µm-thick flexure element.

The demonstrator is currently under fabrication and consist of a ±5 mm-stroke XY stage with a laser mounted on its output platform. The high precision linear motion will be achieved by integrated 300 µm-thick flexure elements including built-in electrical wires to supply the laser source and to provide an interface for the printed strain sensors. The total structure will represent a volume of about 80x50x80 mm³. The actuation of the demonstrator will be external.

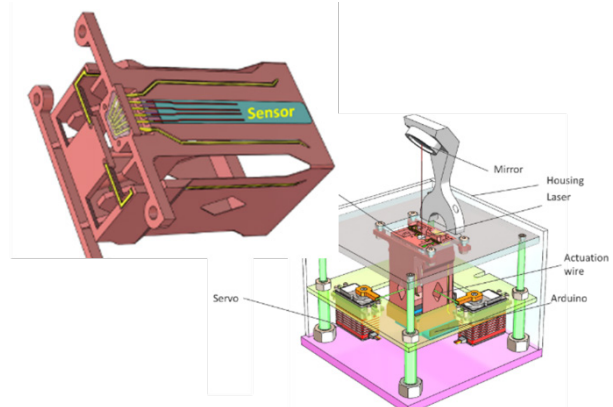


Figure 3: Final demonstrator consisting of the 3D printed XY-stage with embedded sensor and external actuator. A laser pointer is integrated to the moving platform to illustrate the capacity of the demonstrator.

This work is supported by the state of Neuchâtel, the MCCS (Micro Center Central Switzerland) and state of Basel Land.

HECTIC—Improved SiC Sensor Technology for Harsh Environment and Yield Optimization Strategy for Hermetic Laser Assisted Bonding

G. Spinola Durante, A. Hoogerwerf, R. Jose James, K. Krasnopski, M. Fretz, S. Ischer, M. Despont, O. Dubochet, M.-A. Dubois, S. Mohrdiek

Last year, CSEM technology development has shown its potential for SiC MEMS pressure sensor manufacturing for harsh environments. Towards achieving a high TRL required by the industry, both challenging front-end and back-end process steps needed to be improved in quality and long-term reliability. In this respect, at the front-end level, effort was made to reduce the level of electrical noise in SiC MEMS contacts. A second step was taken to upgrade the SiC etching equipment to improve overheating issues, etching uniformity and productivity. At the back-end level, a new clamping fixture enabling chip edge temperature measurement, together with a thermal multi-physics model developed in Comsol®, was implemented to improve the yield of the laser-based (LADB) hermetic sealing of the SiC back-plate. At last, approaches are investigated to overcome the degradation mechanisms observed at 600°C in air for 500h^[1].

Silicon carbide (SiC) has excellent chemical and thermal characteristics to make it the material of choice for sensing in harsh environments. CSEM has therefore developed SiC pressure sensors that can operate at temperatures of up to 650°C^[1,2]. The promising results of this development have led us to continue working on maturing these sensors aiming to achieve a Technology Readiness Level of 4 (TRL 4) that is sufficiently high to attract the interest of the industry.

The issues to be addressed to mature the technology are the following:

- Improve quality of ohmic contacts to SiC for realizing low-noise piezo-resistance in the MEMS pressure sensor.
- Upgrade equipment for Deep Reactive Ion Etching (DRIE) of SiC to achieve a more robust etching process.
- Improve our understanding of the Laser Assisted Bonding (LADB) process to increase its yield.
- Avoid degrading mechanisms after 500 hours at 600°C in air.

The cause of the electrical noise in the ohmic contacts was investigated and it was found that gas diffusion that occurred during the wafer fabrication degraded the contacts, as can be seen by the dark voids in the Focused Ion Beam (FIB) made cross-section of the contacts shown in Figure 1. Modifications were made in the fabrication process flow to prevent the gas diffusion from taking place. As a result, the electrical noise of the contacts was reduced by two orders of magnitude.

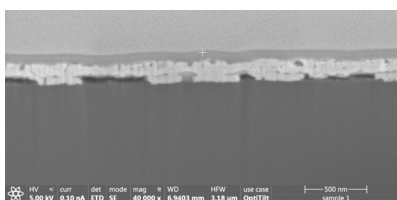


Figure 1: FIB-made cross section of a noisy electrical contact to SiC.

The DRIE etching of SiC improved with the purchase of a Plasma-Therm Corial 210IL DRIE etcher. Especially the improved clamping mechanism of this machine allows a better cooling of the wafer during etching and allows a better resistance

^[1] G. Spinola Durante, et al., "HECTIC2—SiC-based MEMS Pressure Sensor Development", CSEM Scientific and Technical Report (2018), p. 18.

^[2] A. Hoogerwerf, et al., "Silicon carbide pressure sensors for harsh environments", Transducers 19, Berlin (DE), 2019.

to thermally induced wafer bow. A selectivity of 100:1 with respect to the etch mask material has been achieved.

At the back-end level, a process with highly localized heat and minimal damage to the chips, to achieve low-stress, hermetic and reliable laser assisted bonding (LADB) is performed. To improve process yield, more insight in the thermal field is necessary. Therefore, a new clamping fixture has been developed to enable laser bonding (Figure 2), while closely monitoring with a thin-wire thermocouple (0.25 mm diameter) the chip edge temperature. A test showed that the SiC chip edge reached ~300°C within 3 seconds of laser exposure. This is expected due to SiC substrate absorbing ~20% of laser power and confirmed by Au80Sn20 preform melting when placed on top of the SiC chip.



Figure 2: Fixture to apply pressure on SiC chip for LADB hermetic sealing. The arrow shows direction of the hidden thin-wire thermocouple.

Simulations also enable to estimate temperatures directly in the bonding metal ring, where no other method can be applied. The simulation model temperature field will be calibrated with the experimental values from the fixture thermocouples (Figure 2). In Figure 3 non-calibrated simulation results are shown, featuring only laser power absorbed in the metal ring^[3].

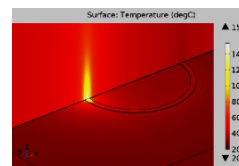


Figure 3: Cross-section of Comsol thermal model (non-calibrated) to show laser induced temperatures on the sealing ring and on the SiC chip.

As an outlook on the long-term reliability in air up to 650°C improvement activity, CSEM is focusing on different potential solution areas: high-quality protection coatings, dedicated diffusion barriers and accelerated testing strategy.

^[3] G. Spinola Durante, et al., "Laser Assisted Bonding (LADB) Thermal Modeling with COMSOL Multiphysics®" Comsol Conference in Cambridge (UK), Poster presentation, 2019.

LONGECG—Integration of Low-power Sensors in a Textile

A. Fivaz, M. Crettaz, J. Wacker, O. Chételat, B. Bonnal, K. Badami, M. Pons Solé, S. Emery

Actual portable bio signals health monitoring solutions are not wearable in the modern sense, i.e., like usual clothes. Clinical measurements such as ECG (Electrocardiograph) require numerous electrodes. Moreover, according to a panel of consulted doctors, many patients would benefit from daily long-term monitoring. Unfortunately, the available solutions able to acquire medical ECG are far from being adapted to such a daily use. Therefore, there is a corresponding lack in the prevention of heart illnesses due to limited observability for reasons such as comfort and usability, and, more importantly, because of the disagreements and irritations due to the long-term use of adhesive gel electrodes and straps. CSEM developed the technology of 'cooperative sensor' to address the integration of sensors with dry electrodes in garments and is further pushing toward system integration into textiles. This paper presents the ongoing activities and the expected achievements to be obtained through the realization of a first demonstrator that will be available in 2020 for first testing.

The diagnosis of different heart conditions (e.g., arrhythmias and other conduction abnormalities) requires long-term monitoring of the electrical activity of the cardiovascular system with an ambulatory electrocardiogram (ECG) device, so-called Holter devices. To capture a complete image of the health state of the heart, in particular in the attempt to capture rare and fleeting events, ECGs should be recorded for periods as long as possible (weeks to months). In recent years, a number of miniature Holter devices has been brought to the market that are relatively simple to use but have only a limited number of leads and, more importantly, are not comfortable to wear over long periods, mainly due to the adhesive of the gel electrodes and straps, the cables to the electrodes, the resulting handling and maintenance, and the weight and size of the electronics.

Consequently, CSEM is developing a 12-lead Holter monitor comfortable to wear even during long periods. In contrast to most other ambulatory ECG recorders (including patches), dry, adhesive-free active electrodes are used and integrated in a tight-fitting vest together with the electronics. To achieve this, the system is built via CSEM's patented cooperative-sensor technology that allows connecting a large number of active electrodes only with a 1-wire bus while preserving ECG signal quality at least to the level of conventional devices. With respect to previous developments, the wearing comfort is further enhanced by reducing the size and the weight of the cooperative sensors thanks to an ultra-low-power ASIC. This allows, for the first time, to power the active electrodes of the cooperative sensors remotely via the same 1-wire bus used for the measurement of ECG. The current return is achieved by the body itself. Even though the wire needs to be insulated for correct operation, a failure of insulation due for instance to tear and wear or to the presence of body fluid (e.g., sweat) is safe since the powering current is limited to a value below the maximum allowed by the medical standard IEC 60601-1. The vest is washed together with its embedded sensors — only the recorder and its battery have to be removed. A high wearing comfort of the sensor garment is finally achieved by using recent technologies from the sport textile industry.

The ASIC is housed in each of the sensors (see Figure 1) and is optimized for ultra-low power and for meeting the best ECG signal quality compatible with medical use, in particular in motion and in environments disturbed with electromagnetic noise. The ASIC includes the following building blocks: (a) a power-management unit responsible for harvesting power from the recorder and for providing a clean power supply to the other circuits of the ASIC; (b) a low-noise wideband unity-gain buffer to address the high-impedance contact with the skin; and (c) a digital logic for sensor synchronization and time-sharing. Up to 10 sensors are embedded in the textile garment (see Figure 1).

The textile garment has to fulfill three major functions: 1) it shall connect the sensors and the recorder via a 1-wire bus; 2) it shall apply the sensors with slight pressure on the skin at defined spots; and 3) it shall be comfortable to wear. To achieve these objectives, we are working with sport fashion designers on a highly stretchable seamless apparel with printed conductive tracks. An additional challenge comes from the fact that body shapes vary a lot from one person to another. Since the positioning of the sensors and their skin contact is of high importance, easily adaptable garments are developed, to which healthcare professionals can attach the sensors so that their positions and preload can easily be custom-fitted to any body type. The drawing shown in Figure 1 depicts a solution based on a wrapping garment with a freely adjustable waist circumference. Moreover, as the cooperative sensors have only one connection to the 1-wire bus, printed conductive pads on the vest allow healthcare professionals to freely pin the sensors to the right spots and thereby achieving fine adjustment of electrode position.



Figure 1: Drawing of the developed vest showing the sensors, conductive tracks, and pads allowing custom fine positioning of the electrodes as well as the ASIC embedded in the cooperative sensors.

In conclusion, this development brings textile solutions and electronics integration to achieve usability and comfort for the long-term measurement of ECG of outpatients.

SILOSCAPE—a Novel Silicon-based FlexTech Watch Escapement

F. Barrot, G. Musy, O. Laesser^{*}, R. Winiger^{*}, F. Cosandier, L. Giriens, E. Dominé, Y. Petremand, M. Amine, S. Ischer, P.-A. Clerc, S. Pochon, F. Rigoletti.

Using micro-manufacturing techniques inherited from the microelectronics industry, it is possible to batch process with a micrometric precision, centimeter scale silicon parts featuring extremely fine mechanical functions. High precision mechanical watch can particularly benefit from this approach which fosters the emergence of novel ideas and allows their concretization at the watch scale. CSEM has always played a pioneering role in this field and aims at becoming the Swiss Competence Center for the design, manufacturing, assembly, and characterization of hybrid silicon based innovative watch micro-mechanisms. In the Frame of the SILOSCAPE MIP, a novel escapement has been invented, designed, produced and integrated in a watch caliber; its functionality has been validated through a first characterization campaign.

Silicon is amagnetic, corrosion free and characterized by an ideal elastic behavior, a high fracture strength and a low density. Using microfabrication techniques inherited from the microelectronic industry (DRIE), it can be batch processed in 2.5D with a micrometric precision for the production of large quantities of centimeter scale mechanical parts that can comprise several levels and fine mechanical functions such as flexure blades. It is because of to the combination of all these interesting features that silicon has progressively opened up new opportunities for the design and production of novel and innovative watch mechanisms.



Figure 1: Assembly of the SILOSCAPE escapement in a watch caliber.

In the late 90's CSEM was a precursor in this field^[1], paving the way for a new trend that is now followed by several key players in the Swiss watch industry. Since then CSEM has kept carrying on its pioneering work by pushing back the frontiers of the micromechanical structuration of silicon and by improving its mastery of the production of such delicate parts^[2,3,4].

The oscillator and the escapement are the most delicate and high added-value technical parts of a mechanical watch. For the past ten years, CSEM has proposed several original designs of mechanical watch oscillators and, in a close partnership with Vaucher Manufacture Fleurier, integrated at the watch level, the very original FlexTech and silicon-based Genequand^[5] escapement, the very first in its kind. The SILOSCAPE escapement is the last FlexTech based escapement designed and produced by CSEM (Figures 1 and 2).



Figure 2: SILOSCAPE escapement (right) integrated in a watch caliber (left).

Like the Genequand escapement, the SILOSCAPE escapement is based on the use of flexure blade pivots, replacing conventional ruby pivots and allowing very precise and frictionless oscillations of the guided components. Paired with a Wittrick oscillator and comprising a total of four monolithic silicon parts, from the escapement wheel to the oscillator, this original escapement is assembled by a mixed of wafer level and manual assembly technics. The SILOSCAPE escapement features a high-power reserve (typically three times higher than conventional Swiss anchor escapements) and, when subject to external perturbations causing it to halt, it can instantly restart by itself using the torque provided by the escapement wheel, behaving therefore similarly to the classical Swiss anchor escapement. As far as its isochronism is concerned, it is expected to be comparable to a Swiss anchor escapement but a fine tuning mechanism is required to set it properly; this mechanism is directly integrated in the escapement itself so that, in the end, no additional part is required.

The experimental tests carried out on the first prototypes allowed the validation of the intrinsic auto-starting specificity of the SILOSCAPE escapement. A design update is still required to better tune/compensate the isochronism; a solution has been found and is ready to be implemented on the next run of parts. The next steps required to fully validate the last main design iteration are: a shock analysis leading to a specific anti-shock design, the integration of all these updated parts in a watch caliber and a full characterization campaign similar to the procedure followed by watch makers when they want to validate a new design prior to its industrialization.

^{*} External key contributors: "Olivier Laesser" and "Winiger Horloger"

^[1] A. Perret, "Le silicium comme matériau dans la fabrication de pièces mécaniques", SSC, 2001.

^[2] S. Jeanneret, et al., "Procédés de micro-fabrication avec application horlogère, développements récents", SSC, 2008.

^[3] O. Dubochet, et al., "L'hybridation du silicium: vers une simplification de l'intégration decomposants silicium dans les mouvements horlogers", SSC, 2015.

^[4] M. Despont, et al., "Tic-Tac" made in Silicon", SSC, 2019.

^[5] F. Barrot, et al., "Un nouveau régulateur mécanique pour une réserve de marche exceptionnelle", SSC, 2014.

MICROSYSTEMS

Michel Despont

The use of microsystem technology continues to grow, fueled by the need for ever-smaller, lower-power, smart devices. Integration of different technologies and miniaturization are at the heart of CSEM, and its Microsystems program aims to bring innovation through the development of new micro-manufacturing technologies, the use of MEMS technology, and the introduction of advanced packaging concepts.

The microsystems market, according to different studies, enjoys a healthy 13–14% CAGR and is approaching a market size of 15 billion dollars. Microsystems are used almost everywhere in devices that sense and monitor our environment and control actions in our daily lives. As an example, today's cars can make use of dozens of integrated sensors and actuators for monitoring and controlling engine functions as well as for safety, navigation, and passenger comfort. Similar trends can be seen in portable devices such as smart phones, with a dozen sensors incorporated into the most recent models. Moreover, global technology trends like the Internet of Things (IoT), Smart City, Industry 4.0, or personalised medicine require a massive use of connected sensors and promise large new markets for ultra-miniaturized microsystems for applications in, for example, building automation, healthcare and life sciences, consumer and home automation, transportation, industrial and environment monitoring security, and retail and logistics. All of these applications are looking for autonomous, low-power, small-form-factor, and low-cost sensor and actuator devices.

A large part of the microsystems market is taken by large companies such as ST Microelectronics, Bosch, or Texas Instruments, targeting mainly the consumer and automotive markets and exerting strong efforts in process standardization in order to cope with the permanent cost pressure of such applications. Beyond these mass markets, a large fraction of sensors and actuators are fabricated in moderate volumes for specialty, but high added value, markets. The fabrication of these moderate volumes of microsystem devices requires customization and necessitates the significant know-how of multiple disciplines, such as fabrication technology, packaging, material science, and reliability. Hence, although the fabless model may be gaining some momentum, providers of MEMS-based microsystems are mostly relying on the Integrated Device Manufacturing (IDM) model, and use their own, dedicated, manufacturing facilities.

Swiss industry, and in particular its SMEs, has recognized the potential of developing specialty microsystem-based products as a strong differentiator and is present in many niche markets, successfully competing on a global level. For SMEs in particular, it is crucial to fill the pipeline of innovation from fundamental research to the industrialization of new technologies in order to be able to continue to offer innovative products. CSEM has a track record in bringing microsystems technologies to the market, and is uniquely positioned to be an essential partner in bringing ideas to market for many Swiss high-tech SMEs active in the domain of highly miniaturized microsystems. Moreover, CSEM is looking at cross-disciplinary solutions—benefiting from nanotechnology, bioscience, and material science—in order to deliver innovations in MEMS and enable new microsystems.

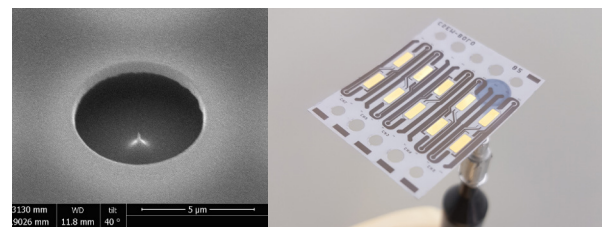


Figure 1: (left) Micro-fabricated electron gun for space applications; (right) 5-channel bolometer sensor integrated on an YSZ sheet (25 x 33 x 0.02 mm³).

MEMS play a major role in the Microsystems program, and this role will be supported by increased efforts to develop advanced manufacturing and integration technologies. In particular, recent advances in digital manufacturing open new opportunities to create and optimize MEMS devices and microsystems. CSEM strongly believes that "traditional" MEMS technologies will be augmented by these new manufacturing technologies to provide new functionalities and deliver the versatility required for fast market introduction.

Packaging, meanwhile, no longer serves mainly as a "device protection" and increasingly integrates added functionalities. These include an interface to the outside world (optical paths, electrical leads, actuators ...), environmental compatibility (biocompatibility, withstanding high temperatures, etc.), or built-in sensors or quality monitoring features (antennas, pressure sensitive surfaces, etc.). This makes the border between the package and the device fuzzier. Hence, it is essential to elaborate a common strategy with regard to developing—under one roof—new processes, new devices, and new packaging that will enable the creation of novel microsystems. With its Microsystems program, CSEM aims to create an environment that is adapted to the new challenges of microsystems and that benefits Swiss industry.

Looking back over recent years, the Microsystems program has seen significant progress related to the development of micro-components for mechanical watches and integrated optoelectronic devices. Although those topics are of great importance to Swiss industry, the technology spectrum being developed within the program must address a broader range of applications. The program has therefore, over the last few years, incorporated several new initiatives in order to diversify into new application fields, including instrumentation, aerospace, and medical devices, all of which are important markets for Swiss industry.

Hence, at CSEM, the microsystems strategy is oriented along several lines of action, encompassing design, microfabrication, and packaging technologies. They are:

- 1) Innovation for mechanical watches, at the crossover point of high-performance materials, advanced manufacturing, and innovative designs.
- 2) Excel in microsystem technology for harsh environments, for a broad range of applications ranging from medical to aerospace.
- 3) Develop key technologies in the field of infrared sensing and imaging.

- 4) Enhance the technology portfolio in optical MEMS and optoelectronic device assembly.
- 5) Life-interacting microsystems for applications in medtech and engineered environments for biological model.

Long-term objectives

The global objective of the Microsystems program is to establish MEMS devices, advanced micromanufacturing, and packaging technologies for CSEM's partners and to offer to Swiss and international industries a full product-development platform from feasibility demonstration of new device ideas to industrialized, qualified fabrication processes including the production of MEMS in small volumes. Therefore, the activities of this program are aimed at continuing to excel and to build up new competences in microsystems technology—in particular for application fields such as watch technologies, scientific instrumentation, optoelectronics, and medical device technology—with a strong focus on packaging, reliability, and cost reduction for demanding applications.

Content

The Microsystems program strategy has been organized into three activities—namely, (1) *MEMS Devices*, (2) *Functional Packaging*, and (3) *Advanced Micro-Manufacturing*.

The *MEMS Devices* activity deals with the development and industrialization of specific MEMS in a wide spectrum of applications. The global objective of this activity is to maintain a state-of-the-art platform capable of developing and fabricating reliable MEMS products, from prototypes to small volume production or for technology transfer. This platform, at the service of Swiss SMEs and industries, consists of a fully equipped MEMS fabrication clean room, a reliability laboratory, and an R&D infrastructure focusing on the pursuit of advanced and novel MEMS-based devices. Today, development is underway in the fields of watches and timekeeping, instrumentation and aerospace, and health, biotech, and lifestyle. These are domains in which Swiss industry is highly successful at a global level and which have a large impact on the Swiss economy.

For industrial applications, reliability is of the utmost importance and CSEM's reliability and microstructure characterization capabilities are a powerful tool for supporting process development aiming at eliminating defect- and stress-generated failure modes and performance limitations. The continuous improvement and systematic documentation of development and production process flows within ISO-9001 ensures the successful exploitation of the technology platforms developed. This enables a systematic approach to MEMS development, from feasibility demonstration, via prototyping, to industrialization.

The *Functional Packaging* activity focuses on (i) the development of new integration platforms for CSEM's customers, and (ii) the realization of new products based on these platforms. The chosen approach allows CSEM to serve a large number of customers in different application fields and markets. The activity's primary objectives are the integration of active MEMS dies, sensors, and actuators into prototype systems and products for different applications and markets. The activity addresses today's global packaging challenges in sensor platforms for medical and environmental monitoring, the integration of

measurement solutions for harsh environments, and optoelectronics. The integration of microsystems continues to be a key element of many future high-technology application areas. Hybrid integration technologies—from embedded silicon in polymer to M(O)EMS—find broad uses in markets such as healthcare and energy. Combined with hermetic sealing and embedded self-testing, they open up additional applications for sensors in harsh environments, such as in the medical field. In addition, miniaturization in optoelectronics continues to be an innovation driver, from devices to architecture.

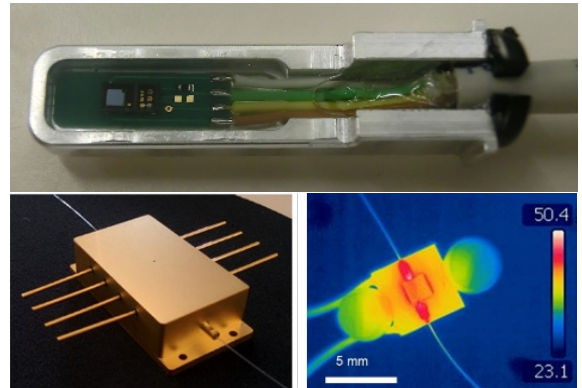


Figure 2: (top) PCB with mounted LED/PD encapsulated with optically transparent epoxy; (bottom) fiber-coupled, packaged waveguides with effective heat dissipation.

The goal of the *Advanced Micro-Manufacturing* activity is to answer the need of the Swiss industry to fabricate small-dimension components (typically $<1 \text{ cm}^3$) that can take advantage of a 3D aspect and that would not be achievable using existing technology such as clean room microfabrication (MEMS and CMOS). The envisaged solution is to develop a new combination of manufacturing technologies to improve the performance of microsystems. The core technology is based on additive manufacturing (AM), a worldwide “big trend” linked to digitalization, IoT, and industry 4.0. This technology brings with it more flexibility and can increase the complexity of systems. However, it is still lacking user confidence, and still needs to be developed in order to achieve the small dimensions and structure quality required for its use in microsystems. The combination of its skill sets in material, microfabrication, surface engineering, and characterization is allowing CSEM to tackle the challenge of combining different technologies and to make these new manufacturing technologies available to Swiss industry. Hence, CSEM's attention is focused on two points: (1) the process optimization of 3D-printing technology for the fabrication of small structures made of functional materials, and (2) heterogeneous integration of 3D-printing technologies with other microfabrication technologies (in particular with MEMS).

Needless to say, the Microsystems program will continue to work closely with the other CSEM programs (Surface Engineering, Ultra-Low-Power Microelectronics, Systems, and Photovoltaics & Energy Management) to create unique solutions for our industries. One of the major USPs of CSEM, we will continue to cultivate this multidisciplinary approach to answer the needs of our customers.

Highlights

Structural-health monitoring for preventive maintenance, control feedback for moveable mechanisms, integrated actuation, and adaptive objects necessitate a heterogeneous integration of numerous technologies. In order to take additive manufacturing (AM) beyond the state of the art of topological optimization, it is important to develop concepts and technologies that allow such functionalities while keeping the versatility and flexibility advantages of AM. CSEM is paving the way toward AM/printed-based mechatronics technology by combining 3D printing with 2D printing. A demonstrator has been fabricated consisting of a ± 5 mm-stroke XY stage with a laser mounted on its output platform. High-precision linear motion will be achieved by integrated 300 μm -thick flexure elements including built-in electrical wires to supply the laser source and to provide an interface for the printed strain sensors. The total structure will represent a volume of about 80x50x80 mm^3 .

The use of carbon nanotubes (CNTs) has skyrocketed in recent years; yet research reveals that when inhaled, this material could replicate a cancer in humans most commonly associated with asbestos. Helping to identify and quantify this nanomaterial, Stat Peel, the University of Geneva, and CSEM have collaborated to develop a workplace-compatible sensing solution to detect workers' exposure to airborne CNTs. CSEM's unique expertise and knowledge in MEMS process technology and surface engineering at the nano scale was instrumental in achieving this outcome. The development, industrialization, and production of the solution under the same roof was able to offer Stat Peel a shorter time-to-market for their innovative products while avoiding time-consuming, risky, and costly technology transfer to a third-party manufacturer.

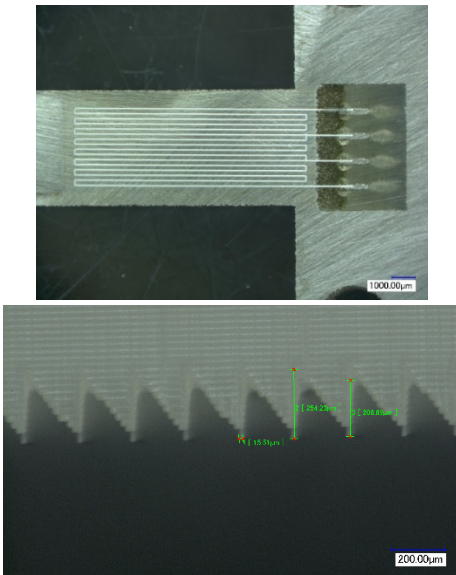


Figure 3: (top) Embedded strain sensors and interconnect to an AM metal cantilever; (bottom) polymer mold made by stereolithography with 15 μm features for the fabrication of gratings.

ITER is a 35-country development program that aims to build the world's largest tokamak, a magnetic fusion device that has been designed to prove the feasibility of fusion as a large-scale and carbon-free source of energy based on the same principle that powers our Sun and stars. Thanks to its unique combination of microfabrication technologies and know-how, its flexibility with regard to working with non-conventional materials, and its certified ISO 9001:2015 environment, CSEM has been selected to develop a bolometer array on a self-supporting substrate to measure high energy particle flux. The fabricated devices used a 20 μm -thick yttrium stabilized zirconia (YZB) substrate with specific processing steps such as double-side patterning, temporary bonding technology, and laser trimming of sensing resistance.

Fabrication of Bolometer Sensors on very Thin YSZ Substrates

M.-A. Dubois, P. Surbled, D. Faralli, O. Dubochet

In the frame of ITER, the international consortium developing the world's largest Tokamak to prove the feasibility of fusion as a large-scale and carbon-free source of energy, CSEM is manufacturing the bolometer-sensors necessary to monitor the plasma during operation. Despite the fact that these devices need be manufactured on very unusual substrates—20-micrometer thick yttrium-stabilized zirconia—standard microfabrication technologies have been used owing to the development of dedicated handling tools and a suitable temporary bonding process.

In the quest for sustainable energy production, an international joint experiment has been launched, called ITER. The goal is to build a magnetic fusion reactor which will be capable of delivering net energy for the first time, paving the way to the power plants of tomorrow. The device consists in a toroidal vacuum chamber in which a very high temperature plasma is formed and confined. This plasma will host the fusion reactions between deuterium and tritium nuclei and produce energy in the process.

In order to control the extreme conditions necessary for the reactions to take place, a very large battery of monitoring systems has to be developed. One of them is the bolometer diagnostic, which consists of about 100 5-channel bolometer sensors, the purpose of which is to measure the profile of total radiated power emitted by the plasma in the part of the electromagnetic spectrum situated between X-rays and infrared. Each sensor is basically a thin membrane, with on one side a metallic radiation absorber, and on the other side thin film resistors. The latter are connected in a Wheatstone bridge, enabling the detection of any temperature variation through the monitoring of the resistance value.

Prototypes of bolometer sensors are fabricated at CSEM (Figure 1). A first challenge is linked to the type of substrate material to be used: The 20- μm thick membranes must be made of YSZ (yttrium-stabilized zirconia), which is extremely brittle. The $100 \times 100 \text{ mm}^2$ YSZ thin foils cannot be processed as such by the regular pieces of manufacturing equipment. It is thus necessary to temporarily bond them on carrier wafers that can be handled by the different machines. A bonding process compatible with all the fabrication steps has thus been developed, together with the necessary tooling to manipulate and release the thin substrates.

During the manufacturing sequence, the bonding and release of the YSZ foil must be done twice, since processing is performed on both sides. On the first, the resistors are fabricated, which requires the sputtering of a platinum film, and its subsequent patterning by photolithography and dry etching. On the second side, the absorbers are realized by electrodeposition of gold in photoresist molds, which entails first the deposition of different adhesion, barrier, and seeding layers. The choice of materials and processes to apply is critical as the devices must survive thermal cycling. Long-term stability of the interfaces between YSZ and the absorbers must be ensured. Another challenge for the manufacturing of the bolometer sensors is the thickness of the absorbers, which is more or less comparable to that of the YSZ substrate. Stress management in the different layers is hence of utmost importance in order to obtain a flat device after the final release. As a last step, the substrates are cut by laser, which enables not only the dicing into individual sensors, but also the punching of round holes necessary for the mounting of the membranes into the measurement system.

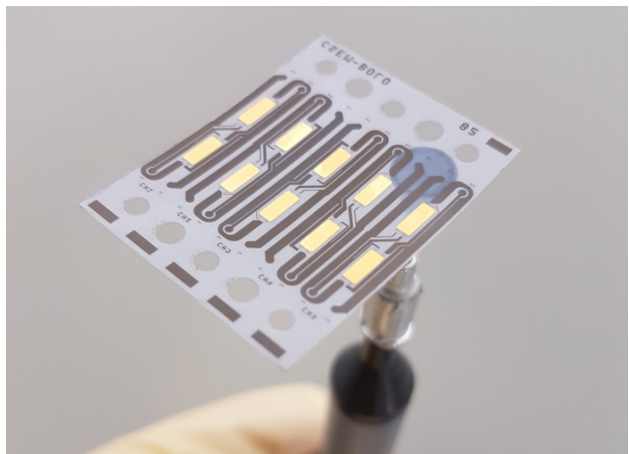


Figure 1: 5-channel bolometer sensor ($25 \times 33 \times 0.02 \text{ mm}^3$).

The finished devices must meet stringent specifications. In addition to surviving harsh conditions (thermal cycling at 400°C), electrical stability of the Wheatstone bridge is mandatory. The value of each resistor is hence measured at 4 temperatures, and the temperature coefficient of resistance (TCR) is derived from the measurements. In case the absolute value of any individual resistor is out of specification, laser trimming is applied on the Pt meander to tune resistance. Special features have been included in the device layout for that purpose, enabling a modification of the electrical path length (Figure 2).

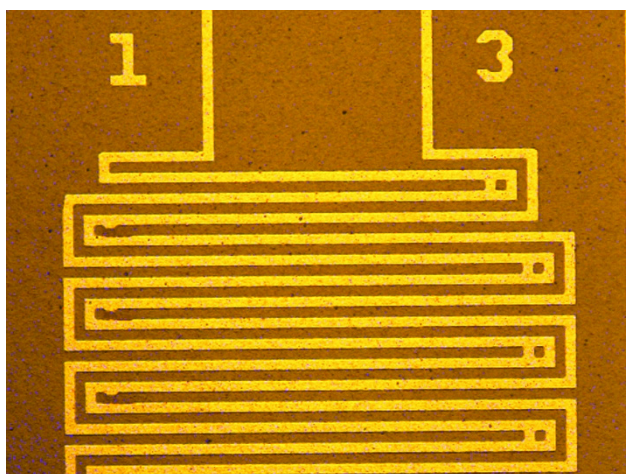


Figure 2: Detail of meanders with laser-trimmed features on the left.

This development is commissioned by the European Joint Undertaking for ITER and the Development of Fusion Energy (or F4E, Fusion for Energy).

Geotechnical Inclinometer Sensors in Optical MEMS

B. Timotijevic, Y. Petremand, M. Luetzelschwab, D. Z. Bayat, N. Niketic, M. Despont

We have designed, fabricated and tested small and cost-effective tilt meter sensors for structural health monitoring using simple and inexpensive MEMS technology and fiber-to-chip assembly. The packaged devices show excellent linear response and angular resolution as low as 0.014 mm/m (14 μ rad).

Inclinometers are used in a variety of monitoring applications in civil and geotechnical engineering. Together with strain, displacement and pressure, tilt is one of the most important indicators of structural health and performance. Currently, the most used tilt sensors are based on electrical sensors, which suffer from significant limitations for uses where electromagnetic disturbances are present, for example in proximity of train lines or in structures subject to lightning strikes. The maximum cable length is also limited for electrical sensors, which poses a problem for the monitoring of very large structures, in particular dams and dykes.

Optical fiber sensors are typically used to address those limitations thanks to their insensitivity to electro-magnetic interference and the ability to transmit information over long distances. Some optical fiber inclinometers have been developed in the past but are typically bulkier and more expensive than the conventional sensors and offer inferior performance. Existing fiber optic tilt sensors are based on conventional mechanical concepts with mechanical pendulums applying strain to a sensing optical fiber. Because of the fiber rigidity, large masses are required in the pendulum and this makes the sensors bulky and expensive.

In collaboration with Smartec SA we have developed the inclinometer concept which is based on a miniature, MEMS seismic mass that moves when the sensor axis rotate in respect to the earth gravity vector (Figure 1). The mass movement induces a variation of a Fabry-Perot (FP) cavity gap. The tilt meter sensor extracts the information on the gap by analyzing the optical spectrum coming from the FP cavity formed by a fixed optical fibre and a movable MEMS mirror. Thus, the sensor measures the inclination through calculation of the FP gap.

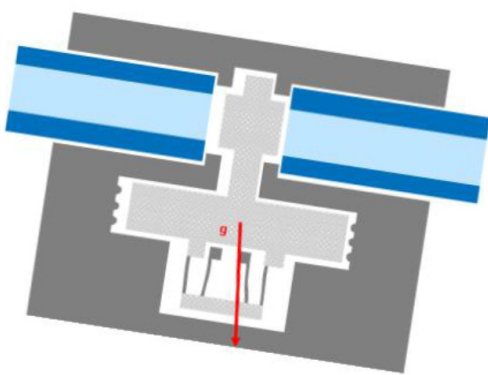


Figure 1: A concept for a Fabry-Perot optical MEMS inclinometer.

A module based on a single Fabry-Perot cavity is already sufficient for most of the applications. However, in some cases a module based on a dual Fabry-Perot cavity (as shown in Figure 1) is required; in presence of thermal expansion a single cavity module would not be sufficient to discriminate a gap variation due to module rotation or due to thermal dilation. With two cavities operating in opposition when the module is subjected to rotation and operating in synchronous for thermal expansions, the two contributions can be separated.

Following COMSOL simulations (mechanical performance) and ZEMAX simulations (optical performance), the microfabrication of the sensing chip is performed following a simple 3-mask process based on silicon-on-insulator wafers, standard photolithography, dry etching and HF release steps. An example of a fabricated chip is shown in Figure 2.

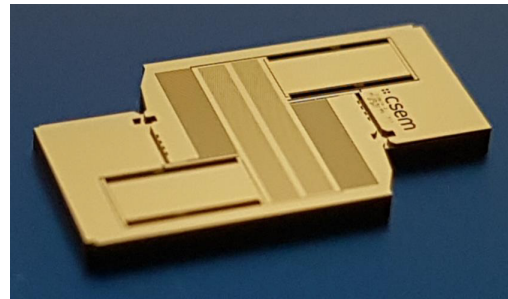


Figure 2: Fabricated silicon inclinometer chip from SOI wafer.

Custom designed supports made in PEEK material are used to house the silicon chip and to attach the multi-mode optical fibres (62.5 / 125 / 250 μ m). The non-hermetic assembly procedure has been performed on a 5-axis stage while actively monitoring the intensity and quality of the optical signal exiting the fibres.

The inclinometer prototypes are tested in laboratory conditions after preliminary stress, shock (500g) and thermal cycling tests (-40°C - 80°C), which did not affect the sensor performance. The typical calibration curve of a packaged chip is plotted in Figure 3. It shows a relation between the FP gap distance and the chip tilt. The sensors are designed to work in a max $\pm 5^\circ$ range. The values simulated in COMSOL and experimental results are in excellent agreement, giving the highest sensitivity in a range around 14.5 μ rad/nm. Considering that the developed read-out module can detect 1 nm displacements, this value translates to 14.5 μ rad angular resolution (0.014 mm/m). The obtained sensitivity is far below the target performance set by the client to 100 μ rad, typically stated for state of the art optical fibre inclinometers.

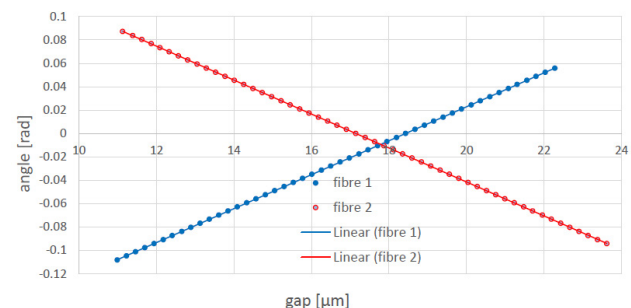


Figure 2: The linear fitting of the inclinometer calibration curve.

The inclinometer devices are currently undergoing additional field testing and characterization as a preparation for the device 2nd level packaging and industrialization.

The authors would like to thank Innosuisse for their financial support (Project No 18646.2PFNM-NM).

Micro Heat Pipe: Performance Characterization

T. Frei, A. Hoogerwerf, A. Mapelli •, D. Alvarez Feito •, M. Despont, V. Gass •*

The silicon-based micro oscillating heat based on a dual-diameter design showed an improvement of thermal conductivity compared to the un-patterned substrate. The orientation independence was demonstrated for several fluids at different power inputs.

High energy physics (HEP) experiments and space missions impose stringent thermal management requirements. Single-phase and two-phase microchannel cooling represents an attractive solution for the thermal management of silicon pixel detectors [1] and high-performance electronics [2]. Two-phase cooling systems exhibit a better temperature uniformity and a minimal load-driven temperature variation over their single-phase counterparts. Integration of these micro channels at chip level can increase the cooling efficiency by reducing the thermal pathway between the heat source and the heat extractor. Fluidic connections and interconnections for micro channel cooling circuits remain a great challenge in particular for HEP and aerospace applications.

New modularity concepts with potential simplification of maintenance and re-workability procedures are enabled by creating two separate cooling loops. The primary cooling loop refers to the main cooling circuit, while the secondary cooling loop is formed of one, or more, micro heat pipes which are thermally and mechanically coupled to the primary loop.

Micro heat pipes come in various configurations and among them micro Oscillating Heat Pipes (μ OHPs) [3] have been identified as the most promising technology to offer two-phase cooling [4]. A μ OHP consists of a wickless meandering of channels partially charged with a fluid. High thermal conductivity, fast thermal response and reduced thickness are the main characteristics of the μ OHPs.

The heat pipe's orientation affects its thermal performance as gravity influences it. This is also true for μ OHPs with single hydraulic diameter channels. However, the dual-diameter design, as shown in Figure 1, allows orientation-independent operations when the maximal capillary driving pressure forces exceed the frictional pressure drop [5]. Figure 1 also shows a microfabricated prototype of μ OHP with 400 μm deep micro channels etched in silicon and closed by a glass lid. It relies on a dual-diameter design with channel widths of 400 μm and 225 μm .

Figure 2 illustrates the thermal performance of the designed μ OHP for various orientations with three different working fluids (isopropyl alcohol (IPA), acetone and C_6F_{14}) charged at 50% with the condenser's temperature set at 20°C. The thermal performance of the microfabricated device is displayed as a function of the heat input, fluid type and its orientation in four different directions. First, the addition of liquid and micro

channels increases the equivalent thermal conductivity compared to a plate of glass and silicon with the same dimensions. Second, the equivalent thermal conductivity is dependent on the input power and on the fluid filling and type.

The performance in the worst orientation, when the heater is above the condenser and the μ OHP is filled with acetone, is dependent on the power input: seven Watts of heating have to be supplied to activate the oscillations. Similarly, each fluid has a threshold above which the oscillations start and lead to an increase in thermal performance.

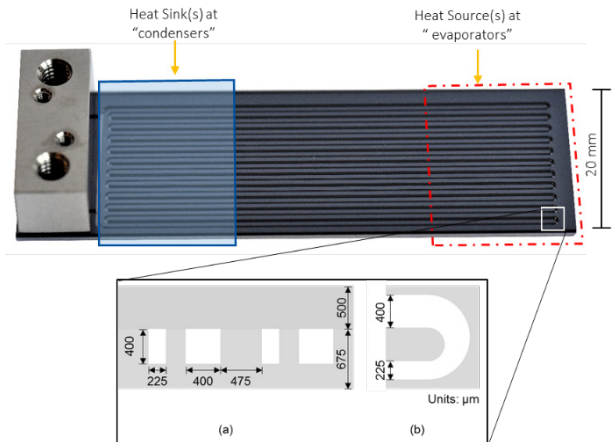


Figure 1: Prototype of the dual-diameter μ OHPs. The connector is thermo-compressed to the glass using a gold-gold bond. It is used to connect the filling system. Schematic diagrams of a (a) partial cross section of micro channels with geometrical parameters and of a (b) dual-diameter turn seen from the top.

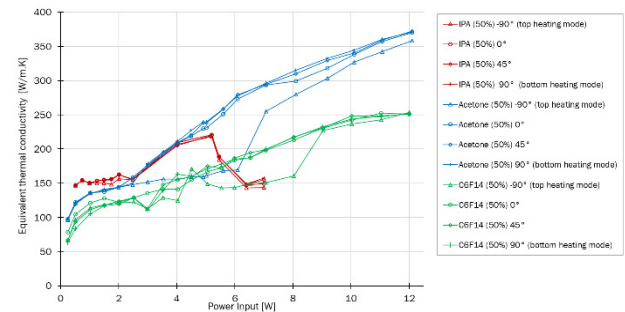


Figure 2: Apparent thermal conductivity in function of power input for one μ OHP charged with IPA and acetone at various orientations for channels 400-225 μm wide and 400 μm deep tested with the condenser's temperature set at 20°C.

- CERN, 1211 Genève, CH
 - Swiss Space Center, EPFL, 1015 Lausanne, CH
- [1] A. Mapelli, A. Catinaccio, J. Daguerre, H. van Lintel, G. Nuessle, P. Petagna, P. Renaud, Nuclear Physics B (Proc. Suppl.) 215 (2011) 349–352.

- [2] B. Agostini, M. Fabbri, J.E. Park, L. Wotjan, J.R. Thome, B. Michel, Heat Transfer Engineering 28 (2007) 258-281.
- [3] T. P. Cotter, 5th International Heat Pipe Conference (1984).
- [4] L. L. Vasiliev, Applied Thermal Engineering 28(4) (2008) 266-273.
- [5] G. H. Kwon and S. J. Kim, Int. J. Heat Mass Transfer 89 C (2015) 817-828.

Piezo MEMS Transducers, Ultrasonic Transducer for Distance Measurement

T. Overstolz, D. Faralli, M. Amine, S. Ischer, G. Bergonzi, K. Schurch, Y. Pétremand, M.-A. Dubois, O. Dubochet, S. Nicolay

CSEM is developing a miniaturized piezoelectric micromachined ultrasonic transducer chip for industrial applications in distance and proximity sensing.

Ultrasonic distance and proximity sensors for industrial automation have basically been built for decades with transducers made of a piezoelectric disc and a matching layer. The latter is used to increase the amplitude of the piezoelectric disc in order to transmit enough sound energy into the air. One speaks also of adaption of acoustic impedance from the hard piezo ceramics to the soft air. The sound is very much attenuated then in the air path, reflected by a target and finally received by the very same transducer. The sensor switches between transmitter and receiver mode. The main advantages of ultrasonic sensors over other sensing technologies are:

- Sensing independent of material, surface, color, size
- Works under dust, dirt, fog, and difficult lighting conditions
- Detection of transparent and bright objects
- Wide measuring range from mm up to 5m

MEMS-based ultrasonic transducers have gained attention in the last 10-15 years in particular through academic research. Currently two technologies have been established, known as capacitive micromachined ultrasonic transducers (CMUT) based on electrostatic actuation, and piezoelectric micromachined ultrasonic transducers (PMUT) based on thin film piezoelectric actuation. Our development is based on PMUT technology since CSEM has a lot of expertise in this domain.

The scientific goal of this project is to have rugged ultrasonic proximity sensing at least for 50 mm distance. Typical applications are target detection in automated production and packaging machines and robots as well as level measurement in narrow cavities such as, e.g., medical test tubes or liquid medicine containers (ampoules). Furthermore, consumer goods such as coffee machines (filling level adjusted to coffee cup) and professional laser printers (web guide control) would benefit from low-cost miniature ultrasonic sensors once the technology is mature.

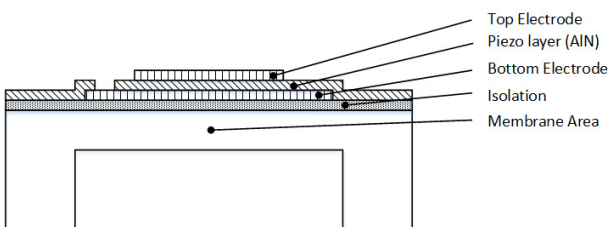


Figure 1: Schematic cross-section of the MEMS transducer device.

The focus in this project is not only on high sound pressure but also on very sensitive reception and few crosstalk within a MEMS unit. The main challenge with MEMS-based ultrasonic transducers to be addressed in this project is related to the reduced transmission power due to reduced transducer size, compared to bulk piezoelectric discs. The lack of transmission power has to be compensated by a very efficient conversion of input power to ultrasound emission, and on the receiver side by a highly increased sensitivity. Both aspects have been investigated and optimized by COMSOL multiphysics modeling.

A schematic cross section of the basic MEMS transducer / receiver element is shown in Figure 1. The fabrication process is relatively simple and requires only 4 mask layers. The transducer element consists of a bimorph membrane formed by a passivated silicon membrane and a polycrystalline piezoelectric AlN layer with top and bottom electrodes. When applying a voltage between top and bottom electrodes, the polycrystalline piezoelectric AlN layer is subject to dimensional changes in lateral (horizontal) direction. The bimorph of AlN layer and silicon results finally in a vertical buckling of the membrane when excited.

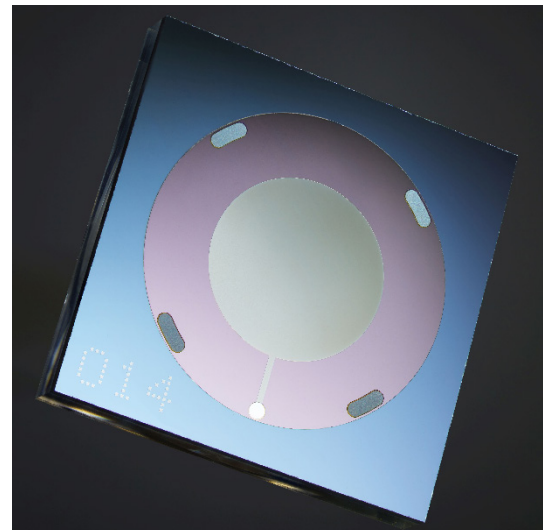


Figure 2: Picture of the MEMS chip. The outer dimensions are 5x5 mm², and the membrane has a diameter of 3.5 mm.

A picture of the device is shown in Figure 2. The MEMS chip measures 5x5 mm², and the membrane has a diameter of 3.5 mm. Measurements based on an optical white light profilometer show a membrane displacement of 1 µm at a resonance frequency around 154 kHz and a driving voltage of 50 V. Currently the device is being characterized by the implementation partner. Preliminary results show a sensitivity well beyond the target value.

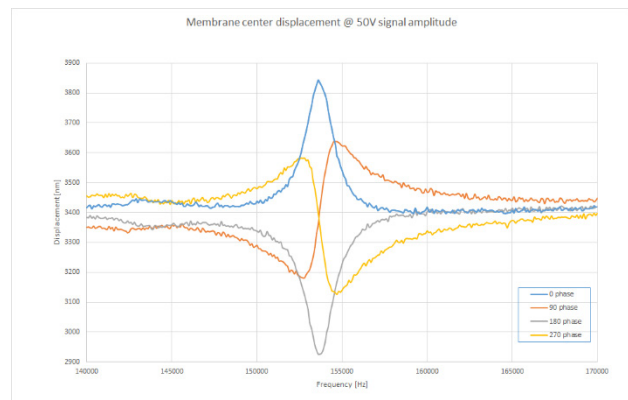


Figure 3: Preliminary measurements using a white light optical profilometer show a membrane amplitude of 1 µm at a resonance frequency close to 154 kHz.

MEGA—Micro-fabricated Electron Gun for Atomic Clocks

D. Faralli, M. Dadras, S. Ischer, F. Droz, M. Despont, D. Bayat, S. Unterhofer

A cold electron emitter is fabricated as an alternative to standard hot-filament emitters. The device is a "Field Emitter Array" based on the known effect of the increase of electric fields in proximity of a sharp tip. A dense array of tips is fabricated using platinum silicide and integrated with a gate electrode done with the same material. The cold emitters will be used in the next generation of atomic clocks, where the use of hot filament emitters has a number of drawbacks. The samples will be assembled in a dedicated flange for testing of the emissivity in a UHV system, down to 10^{-10} mbar.

Atomic clocks by "trapped Hg ions" are being developed for next generation of space and ground applications, due to their potential for superior stability over long period of time. An essential element of these clocks (Figure 1) is the electron gun, which is operated periodically to ionize the Hg atoms present in the resonant chamber. The standard "hot filament" electron guns have a number of drawbacks such as high-power consumption, very slow on/off switching response, form factor, weight and noise (thermal and magnetic).

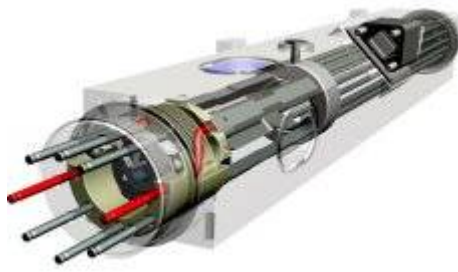


Figure 1: Draft of an "Hg trapped ion" atomic clock [1].

It is known that electron emission can be achieved at room temperature (cold emitters) by using the "tip effect", i.e., the enhancement of electric field at a sharp tip. An array of tips can be micro-fabricated and integrated with a gate electrode to achieve electron emitted current in the order of 1-100 μ A.

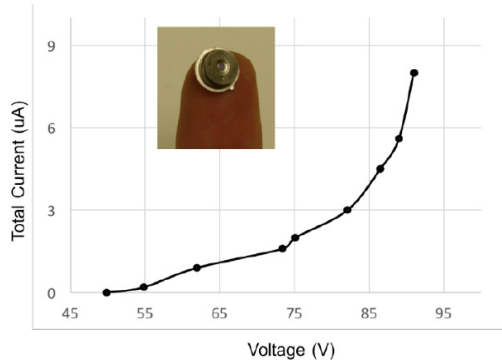


Figure 2: Picture and V/I characteristic of a Field Emitter Array [2].

In Figure 3 the cross section of a Field Emitter is shown. The cathode/tip is fabricated on the substrate and is separated from the gate electrode by an insulator. At a threshold voltage of 20-40 V the emission starts, and the electrons generated are collected by the anode, which is placed in the ion trap.

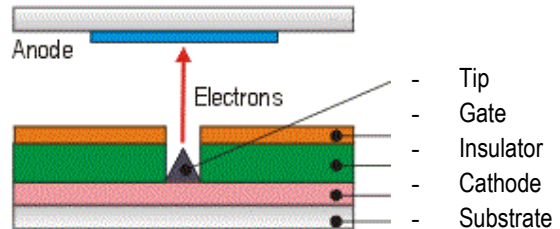


Figure 3: Schematic cross-section of a typical field emitter.

The emitted current is given by a Fowler-Nordheim relation:

$$I = J \times \alpha = A \times V_g^2 \exp(-B/V_g)$$

where V_g is the voltage between Gate and Cathode and A, B parameters that depend mostly by the tip material work function and sharpness as well as the gate geometry.

In this project we use platinum silicide as material for the tips and for the gate electrode, due to its low work function, low resistivity and excellent resistance to electromigration.

The tips are initially formed on the silicon substrate using an isotropic dry-etch process followed by thermal oxidation for sharpening. A platinum layer is sputtered and annealed @700°C for silicide formation. A self-align process is used to pattern both tips and gate electrode.

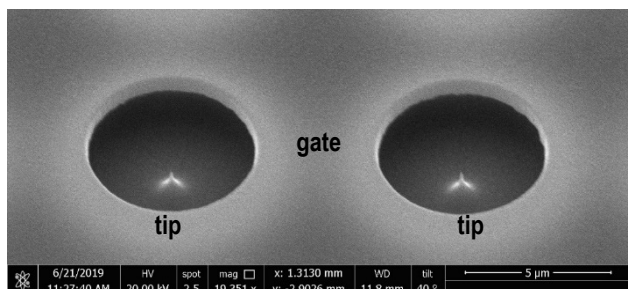


Figure 4: SEM picture of two tips from MEGA technology.

In Figure 4 an example of the micro-fabricated tips and gate electrode is shown. Arrays at different size and density have been designed, ranging from 1.000 to 40.000 tips.

The device will be assembled in a dedicated vacuum flange and mounted in a UHV vacuum system to characterize the current emission as a function of the V_g voltage at different vacuum level, down to 10^{-10} mbar.

The project is supported by the MdP18 program, coordinated by the Swiss Space Center and funded by the Swiss Space Office of SERI (State Secretariat for Education, Research and Innovation).

[1] G. K. Gulati, et al., "Miniatured and low power mercury microwave ion clock", abstract IFCS 2018, May 21-24, 2018.

[2] G. K. Gulati, et al., "Miniatured and low power mercury microwave ion clock", abstract IFCS 2018, May 21-24, 2018.

Measuring Mechanical Properties at the Scale of Watch Components

V. Pejchal, O. Sereda, M. Dadras

Mechanical properties of materials are often considered as size independent. However, once the size of a component gets smaller at some point this assumption does not hold anymore [1]. For example, as the size of a material sample gets smaller, features that had a very little effect at macroscopic scale – grain size relative to the sample size, surface roughness, individual voids, and other defects – start to play an important role and may significantly influence the mechanical properties. The length scale at which the response of most materials becomes size dependent is influenced by several factors (class of material, microstructural factors) but, as a rule of thumb, it becomes significant between one millimeter and several tens of micrometers. This so-called mesoscopic scale lies between the macroscopic and microscopic one corresponding very much to the scale of watch components.

In MEMS, watch components and more general in any component with the characteristic size between several tens of micrometers and one millimeter, the effect of surface quality on mechanical behavior is significant [2]. Defects that are often introduced during the sample preparation, treatment, and handling are disproportionately larger than in the case of macroscopic samples relative to the sample cross-section. Therefore, characterization and understanding of material behavior at mesoscale is crucial for improving the performance of watch and mesoscale components in general.

This problematic has been addressed by ASRH in the framework of a joint industrial project. As a project partner, CSEM promoted the technology transfer and implemented novel and unique characterization capabilities to investigate and improve mechanical properties of materials for mesoscale components. In particular, a mesoscale tensile test bench shown in Figure 1 was developed to characterize Young's modulus, yield strength, ultimate tensile strength, and ductility of mesoscale material samples with cross-sections of 100 µm to few millimeters in the longer axis and applied force from 1 N up to 400 N. Alongside, a mesoscale compression test bench has been developed with similar technical specifications shown in Figure 2.

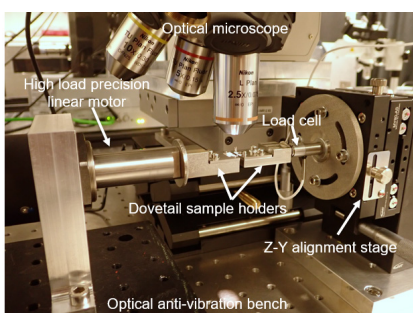


Figure 1: Mesoscale tensile test bench.

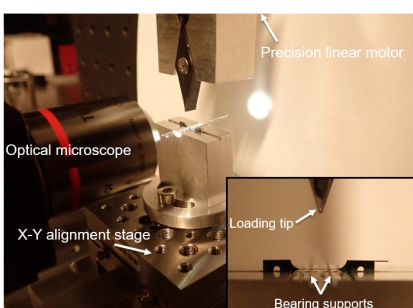


Figure 2: Mesoscale compression test bench in 3-point bending setup.

Both tensile and compression test benches can be precisely aligned using optical microscopes and micrometer precision stages. The set-up is optimized for high throughput testing when large amount of samples has to be tested to obtain statistically relevant data for example in the case of brittle materials. The setups are controlled by custom-made Labview code that enables to perform tests while acquiring optical microscopy images. These images are then used in a Digital Image Correlation (DIC) software to calculate deformation of tested samples thus enabling to construct the whole stress-strain curve.

Figure 3 below shows an example of characterization of a 3D printed stainless steel mesoscale specimen. Each point in the obtained stress-strain curve represents one image taken during the test while image acquisition is being synchronized with the force acquisition. Deformation measurement via image acquisition and DIC has several advantages and is especially well suited for small scale tests as any deformation measurement that requires contact with the tested sample is difficult to implement and may itself influence results.

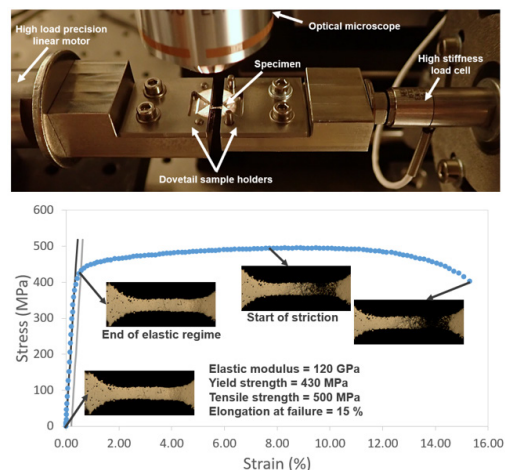


Figure 3: Specimen in the tensile test setup. Images taken during the test using optical microscope are used in DIC to calculate deformations.

Thanks to the novel state-of-the-art characterization capabilities, CSEM is working on understanding the behavior of mesoscale components and improving their performance as the acquired data are used to have a better material selection (e.g., supplier) and better selection of the component manufacturing processes. For example, CSEM is using this platform to develop high-precision 3D printed parts with mesoscale size features as the mechanical behavior of such parts shows significant sensitivity to the process related defects and microstructural features.

[1] J. Krebs, et al., "Cast aluminium single crystals cross the threshold from bulk to size-dependent stochastic plasticity," *Nature Materials*, vol. 16, p. 730, May 2017.

[2] J. Prokop, et al., "Mechanical testing of micro samples produced by a novel LIGA related process chain," *Microsystem Technologies*, vol. 17, no. 2, pp. 281–288, Feb. 2011.

Thermal Management Modeling of High-power Chips and Calibration with Experimental Data

G. Spinola Durante, M. Lutzelschwab, R. Jose James, K. Krasnopolksi, M. Fretz, A. Hoogerwerf

The presented work follows previous activities in the area of thermal management of high-power semiconductor devices [1]. The goal of this activity is to carefully estimate the thermal conductivity of the die-attach layer, based on a realistic package model with a thermo-electric cooler. For a proper estimation, an inverse thermal problem is solved with a fully multi-physics FEM model simulated in Comsol® and calibrated to fit thermistors experimental data. The key aspect is to find an accurate and time-efficient strategy to reduce the possible impact of material parameter uncertainties on simulation results. Good agreement was reached with the proposed method on a packaged heater test-chip assembled with AuSn die-attach.

The thermal management of high-power semiconductor devices is generally critical and targets the lowest maximum junction temperature in operation to achieve longest component lifetime. A higher thermal conductivity of die attach material is always beneficial to reduce the chip temperature. New advances in die-attach materials for high power chips are nowadays based on silver-sintering technology.

The goal of this activity is to set-up a reliable procedure to extract the die-attach thermal conductivity from thermal simulations with accurate models calibrated with experimental data, including convection and radiation losses and the thermo-electric cooler.

The package configuration consists of a heater test-chip, suited for both heating and built-in temperature sensing, directly mounted with an AuSn die-attach layer on an AlN-substrate. The substrate is fixed to a Cu-W heat-spreader and controlled in temperature by the underlying thermo-electric-cooler (TEC). This is then mounted into a typical optoelectronics butterfly package. Finally, the package is connected to a water cooled aluminum plate by means of a thermal conductive paste (Figure 1).

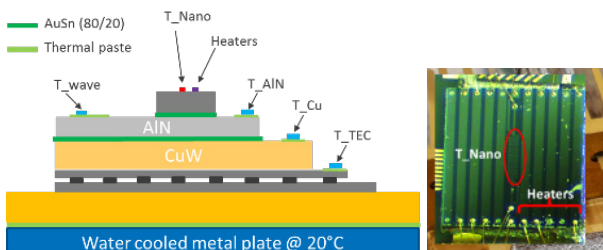


Figure 1: (left) Package configuration cross-section; (right) zoom on the heater test-chip assembled for die-attach evaluation purposes.

When simulating the thermal problem, a numerical accuracy of 3.2 K (~0.1% deviation on Temp. max. of 320 K) is achieved. Temperature deviations, on the contrary, between simulation and measurements are often well above 5 K.

To address these topics, we have identified two main strategies. At first, we calibrate the individual physics/component in the thermal model when possible with experimental data, if not at least with specification data verified by the component supplier.

The second step is to significantly reduce simulation time for each set of parameters from 75 min to around 7 min by adjusting solver settings, grid resolution and, while still retaining numerical accuracy.

Concerning the calibration of the package model, a basis for accurate modeling is to run parametric analysis (optimization) to estimate the die-attach thermal conductivity by matching experimental and simulated readings from the thermistors (Figure 1).

Comparison to experiments dataset #1 with full model are plotted in Figure 2. The resulting fitted curves are generated assuming a constant heat of 10.1 W on the Nanotest chip and by varying the thermo-electric cooler power from 0 W to 75 W. The temperature curve is accurate to within 2.17 K between simulated and measured test-chip on-board temperature sensor (T_{Nano}). This agreement has been achieved by calibrating the TEC and its thermal interface parameters.

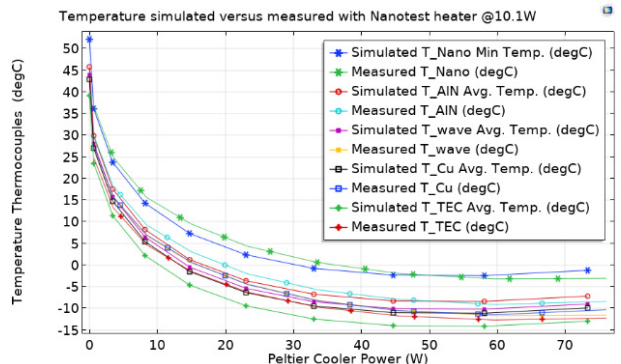


Figure 2: Thermistors temperature measured versus simulated with varying thermo-electric cooler power. Test-chip heater fixed at 10.1 W.

The non-linear multi-physics model fitted with dataset #1 was also used to predict correctly another experimental dataset #2, when keeping power constant at 60 W for the thermo-electric cooler and increasing the test-chip heating power from 0 W to 25 W. The results showed a good agreement, with a maximum deviation between simulated and measured on-board test-chip temperature of 1.14 K only. The defined procedure and modeling results so far achieved are therefore quite promising to enable calibration of thermal models.

As an outlook, we can use this approach to advance CSEM's contribution in the industry with relevance to areas involving silver sintering and other high thermal conductivity die-attach material properties verification. CSEM has conducted these investigations partially in the framework of the EU-consortium MIRPHAB [2] and partially in the recently started EU-project Heatpack [3].

[1] G. Spinola Durante, et al., "Thermal Management Solutions for mid-IR Optoelectronics Packages", CSEM Scientific and Technical Report (2017) 36.

[2] MIRPHAB is an all-services integrated Pilot Line for the development of MID-IR photonics sensors in Europe.
<http://www.mirphab.eu/>

[3] HEATPACK is an EU-Project Consortium developing "High thErmAl efficiency componENts PACKages for space".
<http://www.heatpack.eu/>

Radiation Hard Glass and Sapphire-based Miniature Hermetic Packages for Space Applications

R. Jose James, G. Spinola Durante, V. Revol, J. Kaufmann, K. Krasnopolzki, S. Mohrdiek

Electronics to be used in space are routinely subjected to harshest environmental conditions imaginable, but at the same time require a very long lifetime. Thus, hermetic packaging of electronics has been not a choice but a requirement for space applications. The limited space available in space applications points to miniaturized solutions instead of using conventional hermetic sealing options which are often bulky. A novel technique to hermetically seal optical components was tested and proven for reliability in space relevant atmospheres.

Extremely harsh environments to which components in space applications need to endure, like high-g acceleration, extreme levels of vacuum, exposure to chemicals and various gases and vapors, dust particles, large temperature gradients and variations, large variations in humidity as well as rough mechanical shocks asks for a rugged electronics packaging. Therefore, hermetic packaging of electronics is not a choice but a requirement for space applications. When the electronic component to be sealed is an optoelectronic device with a primary function of transmitting or receiving light, the lid should be transparent. The need for a transparent lid like glass reduces the choices for sealing to adhesive bonding, which gives only a near hermetic seal. Other conventional hermetic sealing methods could be used with a more complicated lid made by brazing of a glass lid on to a metal frame for example. These methods can hardly be miniaturized and are restricted to specific metals due to thermal expansion mismatch concerns. Specifically some of these metals can also cause hydrogen pollution in the package cavity, which leads to high radiation sensitivity of the component.

A novel low temperature laser based hermetic sealing technique using glass and sapphire was tested in this project. This sealing technique was used to hermetically seal a Vertical Cavity Emitting Laser (VCSEL) array and a micro-lens array, which are aligned to each other. This system is intended to be used in an optical transceiver application. The micro-lens array was used either to collimate or focus the light beam to the desired spot size for subsequent coupling to an optical fiber

Four different designs options, covering 3 different transparent materials for the housing and 3 different light handling options were selected for manufacturing. One design is with a stack of 2 parts bonded together and the other three designs are made with a stack of 3 parts bonded together (Figure 1).

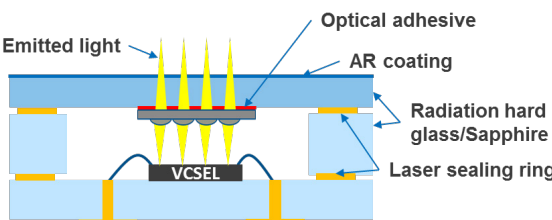


Figure 1: Schematic of one of the 3 stack designs.

The laser sealing process was developed for all the 4 designs to achieve a hermeticity level of less than 10^{-10} mbar*l/s and a shear strength of greater than 190 MPa for sapphire and more than 93 MPa for the glass packages. A total number of 36 samples were manufactured according to the geometries in Figure 2 and screened for hermeticity and functionality. The samples were also subjected to accelerated thermal shock tests to screen for any infant failures before the actual reliability tests.

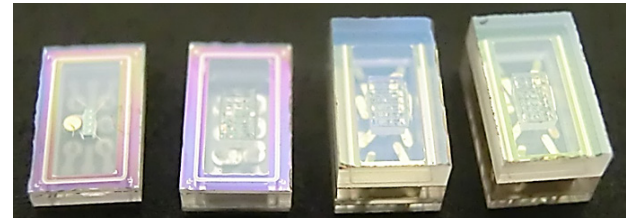


Figure 2: Manufactured samples of 4 different designs.

The parts were subjected to stringent reliability tests like resistance to glass cracking as listed in Table 1. The maximum temperatures of the tests were less than the maximum allowed operating temperature of the VCSEL to avoid any possible degradation of the VCSEL performance.

Table 1: Reliability tests conducted and the standards used.

Reliability Test name	Test standard reference	Test parameters
Vibration	MIL-STD-750 method 2056	20 Hz - 2g _N 80/1000 / 2000 Hz - 20g _N 4 minutes/axis/sweep dir.
Mechanical shock	MIL-STD-750 method 2016	100x 1000g, Tau<1ms
Moisture resistance	MIL-STD-750 method 1021	10 cycles with 3h dwell time
Temperature cycling	MIL-STD-750 method 1051	Condition B (-40°C+100°C), 1000 cycles
Resistance to glass cracking	MIL-STD-750 method 1057	10x dipping in boiling & cold (0°C) water
High temperature storage	JEDEC-JESD22-A103D	100°C for 1000 hours.

After reliability testing, the parts were inspected for hermeticity using helium bombing tests and for VCSEL electro-optical functionality. The hermeticity tests showed a very good yield for all the parts ($< 1 \times 10^{-9}$ mbar*l/s). The optical output power of the samples did not show any measurable change before and after the reliability as can be seen in Figure 3.

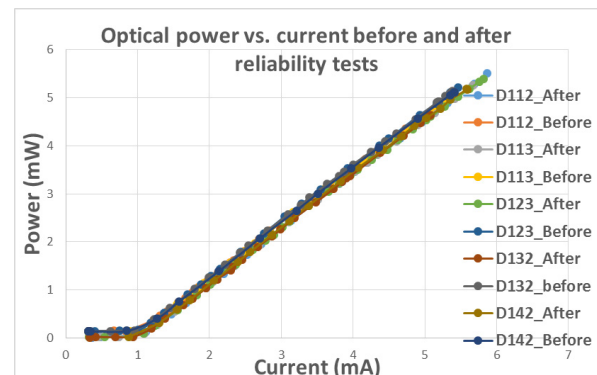


Figure 3: optical output power vs. current for one of the designs.

As a result, the technology has achieved a technology readiness level of 4 for space applications and is generally suitable for a wide range of applications in harsh environments.

We acknowledge European Space Agency for the technical and financial support provided in the project.

Reliability of IR Components for Gas Sensing Applications

I. Marozau, O. Sereda, A. Janaszek, C. Kistner

New reliability stress-testing standards and procedures were established for qualification of IR components, which find their applications in various domains, such as energy, transportation and health diagnostics. The functional lifetime was calculated based on accelerating aging models and test results. The broad variety of components and their application domains required a special care to adapt the reliability evaluation tests and procedures. Performed failure mode analysis allowed the understanding of the failure root causes. The investigations were carried out in collaboration with the IR source and detectors manufacturers within the framework of an EU project (MIRPAHB). This project focuses on the development of a pilot line for providing a unique chemical detector spectroscopic system by combining mid-infrared sources, photonic circuits and detectors in a standard packaging. One of the major challenges in such a pilot line is to establish a common procedure for qualification of various components from different manufacturers in order to ensure their lifetime and compatibility in a common package.

The aim of MIRPAHB project is to set up an all-service integrated pilot line for the development of mid-IR photonics gas sensors from the IR components available in Europe. Mid-IR spectroscopy of molecular vibrations enables accurate and precise determination and quantification of various gases based on their spectroscopic response (Figure 1).

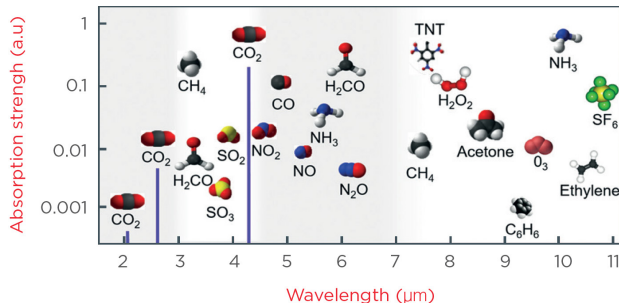


Figure 1: Absorption wavelengths and strengths of various gases.

The pilot line concept implies a selection of the proper source, detector and other components from the available list. Various components can be combined in the final system, similar to the Lego building blocks. This allows fine-tuning of the wavelength window and sensitivity to design the most suitable system for each specific customer application.

The pilot line aims to achieve the TRL 8 to 10, which requires complete qualification of the final devices. In order to assure the necessary lifetime of the final system, there shall be a common qualification methodology for constituent components of the system. CSEM in partnership with the IR component manufacturers has established such a methodology. The approach is based on the analysis of the component integration level, and specific stress factors and environmental conditions that act on the system during its operation. Based on this analysis, we have defined 4 component integration levels (Figure 2):

- Level A: bare chip
- Level B: chip on a carrier (e.g., sapphire or AlN plate)
- Level C: chip mounted on a thermoelectric cooler (TEC) without packaging
- Level D: chip mounted on a TEC and hermetically sealed

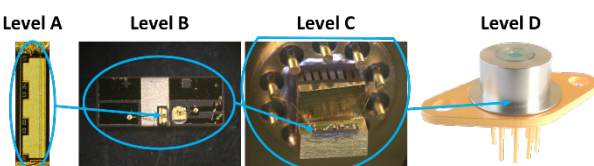


Figure 2: Integration levels of IR components (example: mid-IR laser).

Depending on the component integration level and the expected operation conditions (normally T=25°C and RH~40-50%) the following corresponding reliability stress-tests shall be performed:

- Temperature-accelerated lifetime test (levels A, B, C, D)
- Temperature cycling test (levels A, B, C, D)
- Temperature-humidity bias test (level D)
- Mechanical shock test (level D)
- Mechanical vibration test (level D)

The developed stress-test procedures reflect different possible system use conditions by defining test load severity levels. This allows to qualify the components and to estimate their expected lifetime for the defined use conditions using the Arrhenius law for T-accelerated lifetime tests:

$$R(T) = \gamma_0 \exp\left(\frac{-E_a}{kT}\right)$$

The failure assessment is based on the measurements of certain electrical and optical characteristics of the tested components before and after the test. Figure 3 shows an example of the I-V characterization curves of an IR detector subjected to temperature-accelerated lifetime test. The device has passed the test at 125°C for 1000 h without a failure. Using the Arrhenius law, the component lifetime can be calculated: ~100 years at the use temperature of 25°C and ~20 years at the use temperature of 45°C.

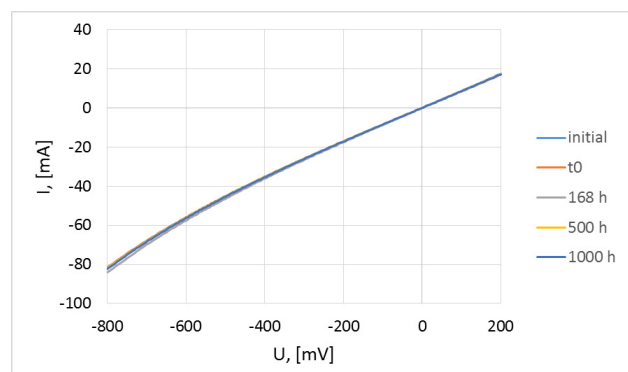


Figure 3: I-V characteristics of an IR detector subjected to T-accelerated lifetime test. A close overlap of the curves indicates no device failure.

Verification of the developed methodology and test procedures was accomplished by carrying out the tests on real devices. Necessary adjustments to the test conditions were made based on the results of the test campaign. The finalized test procedures will serve as test standards for qualification of newly developed IR components for their use in the pilot line.

Metal Matrix Composites by Additive Manufacturing

V. Pejchal, V. Hoqui, O. Sereda, M. Dadras

Metal Matrix Composites (MMCs) are materials that combine a continuous metallic matrix with a second reinforcing phase, typically made of ceramic, with a goal to create a new material with properties unavailable using either of the individual constituents. One of the characteristic features of MMCs is that the reinforcement bears a significant fraction of the applied load, thus offering enhancements in strength and stiffness simultaneously [1]. An attractive class of MMCs are light metals such as aluminum reinforced with hard and stiff ceramic particles such as alumina providing stiff yet lightweight composite. One of the main drawbacks of MMCs is their poor machinability. Therefore, very near-net shape manufacturing techniques such as additive manufacturing (AM) by selective laser melting (SLM) represents one of the potential ways of producing MMCs. The high specific stiffness of MMCs combined with AM topology optimization creates added synergy in producing metallic composites that offer high strength and stiffness while being lightweight.

One of the main challenges in manufacturing MMCs via SLM is the fact that the wetting of Al_2O_3 by molten aluminum is very poor, raising the question if it is possible, using SLM, to achieve good bonding between the aluminum matrix with the reinforcing particles – the key prerequisite of achieving strong and tough MMC. Therefore, a preliminary study focused on the investigation of the AlSi12 – Al_2O_3 interface quality was first performed. Selectively laser melted material samples made using powder beds of aluminum alloy AlSi12 (particle size 20-60 μm) mixed with 2.5vol% of Al_2O_3 particles (particle mean size 10 μm) were prepared. Figure 1 shown below represents one cross-section view from a 3D FIB volume reconstruction of a representative volume of the 3D printed MMC. It shows a continuous AlSi12 matrix with two separate Al_2O_3 particles and a void in the right bottom corner. The figure clearly shows that the AlSi12 – Al_2O_3 interface may be locally very good, despite the fact that molten aluminum does not wet Al_2O_3 . This is enabled by the so-called Maragoni convection that appears in the melt pool caused by local temperature gradient and chemical concentration difference [2]. A vigorous Maragoni convection disrupts the native oxide layer of AlSi12 particles and stirs Al_2O_3 particles in the molten metal. Thus, due to the resultant capillary forces the liquid metal surrounds and wets Al_2O_3 particles.

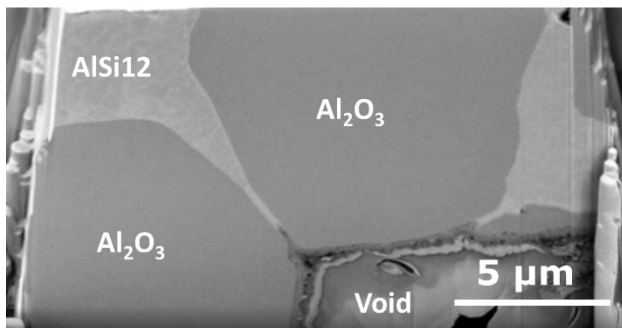


Figure 1: A cross-section view from 3D FIB volume reconstruction of a representative volume of the 3D printed AlSi12/ Al_2O_3 MMC.

Showing that SLM may lead to good AlSi12 – Al_2O_3 interface, the work focused towards increasing the volume fraction of Al_2O_3 up to 15vol% and optimize the SLM parameters to minimize the total porosity. To this end, a large parameter window of laser power and speed was explored using Design of Experiment rules, keeping the powder layer thickness constant (30 μm). Single laser-track walls (4x4 mm) were manufactured as shown in Figure 2. A good quality single laser-track walls with continuous and homogenous morphology as shown in Figure 2 were observed only for the highest energy densities.

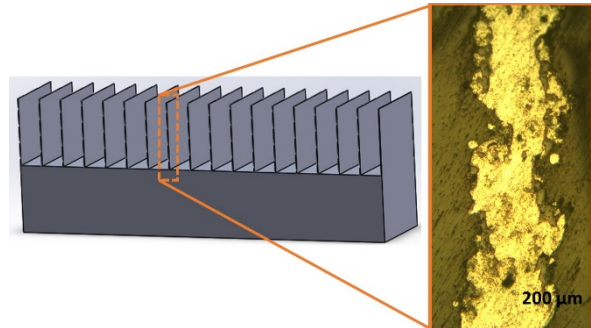


Figure 2: Design of single laser-track walls manufactured and the best quality observed wall with 15vol% of Al_2O_3 is shown.

Laser parameters that led to the printing of continuous laser tracks were subsequently used to print 10 mm^3 cubes while varying the hatch distance. The hatch distance overlap near 50% provided the so far best obtained result for 15vol% Al_2O_3 MMC. Figure 3 shows the resulting microstructure that exhibited less than 10% porosity and reinforcing particles with good bonding to the AlSi12 matrix. It was observed that during the process, Al_2O_3 particles were melted and some even recombined to form larger particles compared to the particles present in the feedstock.

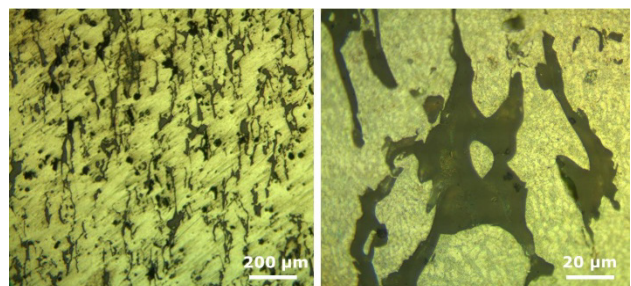


Figure 3: Microstructure of 15vol% Al_2O_3 of 3D printed MMC using the so far optimized laser parameters and 50% hatch distance overlap.

In conclusion, we show that SLM is a promising technology for manufacturing MMCs. In combination of the Maragoni convection and optimized printing strategy, the poor wetting between Al_2O_3 and molten aluminum may be overcome providing good matrix-reinforcement bonding. So far we were able to produce particle reinforced MMCs with as much as 15vol% of Al_2O_3 particles with porosity lower than 10% in as-built condition without any post-treatment. Aluminum-based MMC with 15vol% of Al_2O_3 reinforcement has a potential to have 25% higher specific stiffness compared to metallic alloys. The further work focused on applying Hot Isostatic Pressing (HIP) to further decrease the porosity is ongoing.

[1] N. Chawla, K.K. Chawla, Metal matrix composites, Springer, New York, 2006.

[2] J. Berthier, Micro-Drops and Digital Microfluidics, A volume in Micro and Nanotechnologies, Elsevier, 2013.

Mesoscale Mechanical Performance of SLM Manufactured 17-4 PH

O. Chandran, S. Lani, V. Pejchal, H. Saudan, L. Kiener, M. Dadras, O. Sereda

Compliant mechanisms can achieve macroscopic linear or rotary motions without friction and wear, while ensuring extremely high fatigue performances [1]. Such compliant properties originate in the use of fine lamellas with thickness ranging from 100 μm to 400 μm , traditionally manufactured using Electrical Discharge Machining (EDM). With the design freedom offered by Selective Laser Melting (SLM), the printing of fine structures represents a field of growing interest, for which the impact of the process inherent high surface roughness on the mechanical properties is not yet clear, especially for mesoscale samples. In this study, we report on the fabrication and mechanical performances of such structures printed in 17-4 PH.

Selective Laser Melting (SLM) is an additive manufacturing process in which a laser selectively melts a powder bed, layer after layer, thus reconstructing a Computer Aided Design (CAD) file. Four process parameters are generally admitted as having the greatest impact on the process stability and part quality: the laser power, the laser scanning speed, the scanning strategy and the layer thickness [2]. To assess the mechanical properties of mesoscale SLM structures (400 μm in this case, Figure 1), an optimization of the process parameters was carried out with the objective of reaching a high density part. The main steps are as follows: (1) definition of an appropriate process window; (2) measurement of the meltpool dimensions and corresponding hatch overlap; (3) iteration based on density measurement and minimum line width until a satisfactory density with respect to the bulk material is reached.

Once the process parameter window was optimized, a tensile structure with a 400 μm wide reduced section was manufactured and tested on a CSEM developed mesoscale tensile machine. The classic tensile test curve is then reconstructed using the data of a high precision load cell and Digital Image Correlation performed on sample images captured during the test (Figure 1).

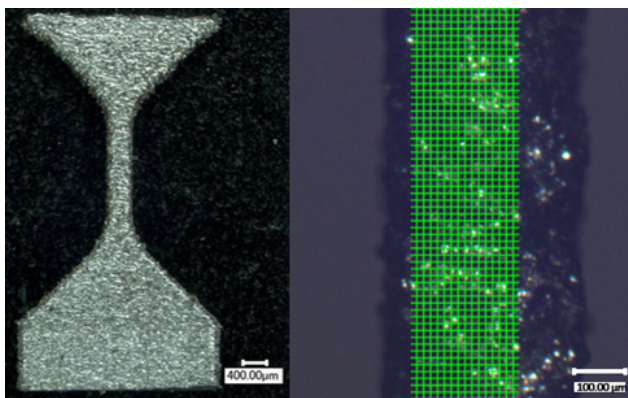


Figure 1: Image of the mesoscale tensile structure (left), grid used for the DIC on images recorded during the test (right).

The mesoscale mechanical property obtained (UTS) is presented after a solution annealing and age hardening (H925) and compared to the mechanical performance of SLM printed macroscale samples (tested according to ASTM E8/E8M). With an UTS of 1307 MPa (± 13 MPa) for the mesoscale sample and 1345 MPa (± 2 MPa) for the macroscale sample, no significant difference is measured between both sample sizes. When compared to conventionally manufactured macroscale tensile sample, the SLM printed structures, regardless of size have a slightly lower UTS (reference sample [3]: UTS=1379 MPa)

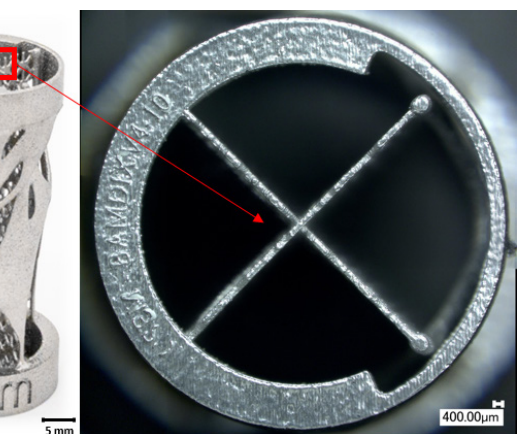


Figure 2: Lamellar pivot designed and manufactured at CSEM (left), 400 μm wide interlocked compliant lattice (right).

In conclusion, a SLM process was developed for the manufacturing of thin wall samples (400 μm) of 17-4 PH maraging steel. The UTS of 1307 MPa obtained for the mesoscale sample is comparable to that of macroscale parts, a result currently used for the design of compliant structures, such as lamellar pivots (Figure 2).

[1] L. L. Howell, S. P. Magleby, B. M. Olsen, eds. Handbook of Compliant Mechanisms. Wiley; 2013.
doi:10.1002/9781118516485.

[2] J. P. Choi, G. H. Shin, M. Brochu, et al., Densification behavior of 316L stainless steel parts fabricated by selective laser melting by

variation in laser energy density. Mater Trans. 2016;57(11):1952-1959. doi:10.2320/matertrans.M2016284.

[3] MatWeb YS for MI. AK Steel 17-4 PH® Precipitation Hardening Stainless Steel, Condition A. Matweb.
<http://www.matweb.com/search/DataSheet.aspx?MatGUID=20362bbf0a7f45b8ae59b19a9425239e>. Accessed September 23, 2019.

Ti-Al Intermetallic Compound Developing by in-situ Alloying using SLM Process

M. Dadras, V. Pejchal

Intermetallic compounds are considered as materials having the properties between those of metals and ceramics. Their strength, Young's modulus and yield stress are higher than metals but lower than ceramics. However, their ductility is lower than that of metallic alloys and better than for most of ceramics. Ti₃Al having low density and high oxidation resistance with high mechanical properties at high temperature is suitable for aerospace applications. However, manufacturing of parts having complex shape is a limitation for application of such materials. Selective Laser Melting (SLM) opens new horizon for manufacturing of near net-shape parts made of difficult-to-form materials. However, one of the limitations of this process at present is availability of the powder. In-situ alloying of conventional Ti6Al4V powder was explored at CSEM to obtain Ti₃Al based alloy.

Intermetallic compounds were largely studied to explain their mechanical resistance and improve their ductility [1,2,3,4,5,6]. Ti₃Al intermetallic compound having low density, high temperature mechanical properties and high oxidation resistance is used in aircraft engines and airframes [6]. High yield strength of Ti₃Al is explained by its Do19 ordered structure and lack of a significant number of dislocations which have Burgers vectors with a c-component.

As nearly all intermetallic compounds, manufacturing of complex-shape parts is a challenge if not impossible for Ti₃Al compound because of its low malleability and machinability. More than 80% of Ti₃Al produced parts are fabricated by machining with production cost about ten times more than aluminum alloys. SLM permits to fabricate parts having complex shapes and could be a solution for fabrication of intermetallic compounds. However, this manufacturing process suffers from limitation of alloyed powder availability. In-situ alloying is a method which can overcome this limitation and permits to develop intermetallic-based materials.

Present investigation focused on developing the process for manufacturing the Ti-Al intermetallic by in-situ alloying. Ti6Al4V powder was used as the base material which was blend with 6wt% of pure Al. The mixed powder was used as the feedstock for developing the process of in-situ alloying using SLM process.

BSE micrograph and XRD spectrum (Figure 1) of as fabricated material shows presence of at least two phases, hexagonal α' and orthorhombic α'' .

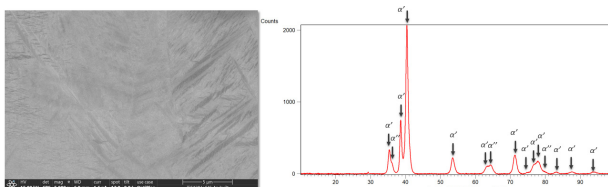


Figure 1: As built microstructure and XRD pattern. The main phases detected are, hexagonal α' and orthorhombic α'' .

- [1] P. Ravindran, H. Fjellvag and O. Eriksson, PACS numbers: 61.50.Ks, 71.15.Nc., 71.20.Eh.
- [2] V.Y. Gertsman, O. Dremailova, Journal of Materials Science, 41 (2006) 4490-4504.
- [3] D.G. Morris, M. Dadras, M.A. Morris, Journal de Physique III, 3 (1993) 429-434.

More detail investigation by Transmission Electron Microscope (TEM) and corresponding EDS analysis shows (Figure 2) presence of ordered TiAl based phase.

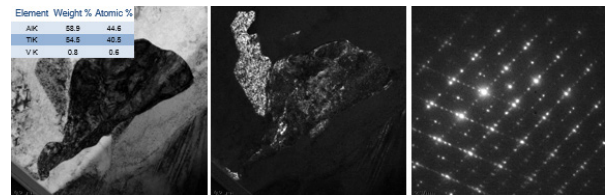


Figure 2: TEM micrographs and diffraction pattern corresponding to ordered structure.

As built samples were heat treated at 900°C 1 hr under Ar atmosphere. The main objective of the treatment was on the one hand to homogenize the alloy and on the other hand to precipitate the Ti₃Al phase.

Figure 3 shows the XRD spectrum and TEM micrographs confirming intermetallic Ti₃Al ordered structure formation.

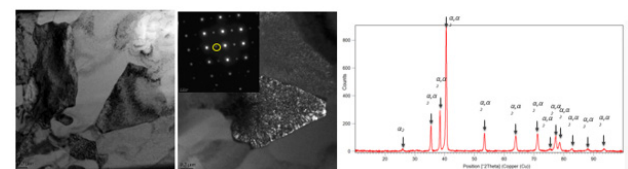


Figure 3: TEM micrographs, corresponding diffraction pattern and XRD pattern shows presence of Ti₃Al ordered structure in annealed samples.

Microhardness was measured on samples before and after the heat treatment. Measurements show that microhardness increases from 390 HV for Ti6Al4V to 460 and 487 for Ti6Al4V+ 6wt%Al as-built and annealed, respectively.

In conclusion, in-situ SLM alloying permits to fabricate the intermetallic Ti-Al when the powders are not commercially available. Process optimization permits to control the microstructure and improve the mechanical properties. Further investigation to characterize the mechanical properties and relate them to the microstructure and process is planned.

- [4] D. G. Morris, M. M. Dadras, M. A. Morris, Acta metall. mater. vol. 41, No. 1, pp. 97-111, 1993.
- [5] T. Ito, T. Fukui, AIP Conference Proceedings 1946, 020008, 2018.
- [6] H. Kusamichi, Y. Murakami, H. Kimura, O. Izumi, Metallic Taitanium and Its applications, Nikkan Kogyo Shinbun LTd, Chuo-Tokyo 1989.

In-situ SLM Alloying for Development of High Strength Supersaturated Alloys

M. Dadras, V. Pejchal, S. Unterhofer, O. Chandran, S. Biselli, O. Sereda

The improvement of mechanical properties is a continuous need for nearly all applications. The mechanical properties of alloys are related to their microstructure and one of the well-known method for alloy strengthening is solid solution hardening which increases the shear stress for dislocation movement. The limitation of this method is the maximum solubility of solute atoms in a matrix which presented by equilibrium phase diagrams. Rapid solidification permits to overcome this limitation. However, the main restriction of this method is the design limitation to obtain near-net shape parts. Selective Laser Melting is process in which by controlling printing strategy, it would be possible to control the cooling rate of molten pool and be able to put more solute atoms in matrix. The present investigation focused on the in-situ development of Cu-Sn alloy using 15wt% Sn with the potential to replace Cu-Be alloy. The printed parts showed the microstructure not achievable by classical elaboration and the UTS near 500MPa.

Improving the mechanical properties of alloys is a continuous challenge in scientific and technical worlds. It is well known that the mechanical properties of alloys are related to their microstructure. Solution hardening is a well-known mechanism of improving and controlling the strength of alloys^[1]. In this regard, increase the alloy strength is given by

$$\Delta\tau = Gb\varepsilon^2\sqrt{c}$$

where " $\Delta\tau$ " is increasing the shear stress for dislocation movement, "G" is shear modulus, "b" is burger's vector, " ε " is lattice strain due to the solute and "c" is concentration.

Alloy strengthening by solute solution has the limitation defined by the maximum solubility of solute atoms in the matrix and generally presented by equilibrium phase diagrams^[2]. Rapid solidification was used to overcome this limit and add more solute atoms in the matrix^[3,4,5]. The main limitation of this method is the design limitation of the final shape of a functional part, while SLM technology allows to overcome it.

By correctly establishing the SLM printing strategy it would be possible to control heating and cooling rate and approach the classical rapid solidification conditions. This would permit in one hand to put more solute atoms in the matrix and overcome the limit of solubility and on the other hand fabricate directly near net-shape parts.

The present study focused on in-situ alloying of Cu-Sn by SLM. Equilibrium Cu-Sn phase diagram^[3] shows the maximum of solubility of tin in copper of 15.8 wt% at 520° which decreases to 1.3 wt% at 200°C. Cu 10 wt%Sn powder was used and mixed with 5wt% pure Sn powder. The process was developed and optimized to obtain the sample with density more than 98%. The alloy could fill in one hand the compromise between strength and conductivity (Figure 1) and on the other hand potential to be comparable with Cu-Be alloy.

The chemical composition measured Cu + 13.8 wt%Sn. The microstructural observation (FIB/TEM) shows (Figure 2) presence of very fine microstructure with the lamella having the thickness of about 20 nm in the matrix with grain size about 400 to 600 nm large. The EDS analysis showed that the fine lamella contains about 33.4 ± 1.6 wt%Sn and the grains having the

chemical composition of 11.6 ± 0.8 wt%Sn. The phase analysis of X-Ray pattern (Figure 2) showed presence of two crystalline phases: α Cu (saturated to 11.6 wt%Sn) and δ of Cu44Sn11 confirming manufacturing the phases which is not possible based on equilibrium phase diagram at RT.

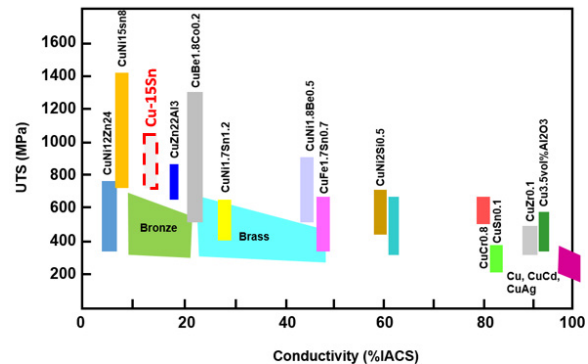


Figure 1: Strength and electrical conductivity (IACS) of Cu based alloys^[6]. The goal of investigation was to achieve the UTS about 950 MPa and IACS about 18% nearly comparable to Cu-Be alloy.

Tensile test samples were prepared by the optimized SLM process. The mechanical properties found with the maximum tensile strength about 500MPa and the ductility less than 2%. The presence of some unmelted particles and microcracks could explain the low ductility of the sample.

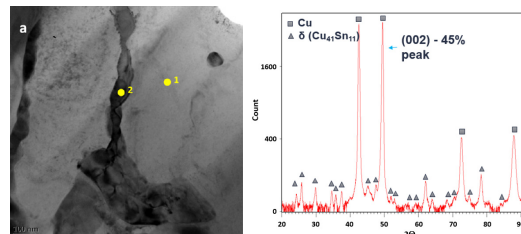


Figure 1: TEM micrograph, matrix "1" presents 11.6 ± 0.8wt% and phase "2" 33.4 ± 1.6wt% of Sn. Phase identification (right) reveals presence of two phases: α of Cu and δ of Cu44Sn11.

The primary objective of this feasibility study was to show potential of the in-situ alloying combined with the freedom in the design aspects for the final part fabrication for high strength non-conventional alloys.

^[1] H. Suzuki, (ICSMA 7), 7th Int. Conf. on the Strength of Met. Alloys, Montreal, 12–16 August 1985, pp 1727-1744.

^[2] P. Joshua, Mechanical Properties of materials, Springer, pp 236-239, 2013.

^[3] T. B. Massalski, H. Okamoto, Binary Alloy Phase Diagrams, ASM International 1990.

^[4] M. Dadras, D.G. Morris, Scrip. Mat., Vol. 38, 1998, 199-205.

^[5] C. Biselli, D.G. Morris, Mat. Sci. Eng, A148, 1991, 163.

^[6] C. Biselli PhD, UniNe, p 32, 1993.

Improved Tribological Properties of Brass through Multi Charge Ion-implantation

K. Vaideeswaran, O. Sereda, C. Yamahata •, S. Biselli, C. Spoerl •, M. Dadras

The improvement of the tribological properties of a wide range of materials through ion implantation has been previously demonstrated^[1,2]. In comparison to single charge ion implantation, Multi-Charged Ion Implantation (MCII) provides for a more uniform penetration of ions over a wide range of depths through the simultaneous implantation of ions with different energy levels associated with different charged ions (e.g., N+, N2+, N3+ and N4+ in the case of nitrogen)^[3]. In this study, the MCII technique has been optimized for application to brass (free machining and lead-free). As a result, more than two-fold reduction of the coefficient of friction (COF) and a 100× reduction in the wear has been achieved. Process optimization realized by fine microstructural investigation. Such improvements are of great interest for industries using brass components in precision-mechanisms, such as watchmaking.

The project aims at optimizing the MCII technique in order to modify the surface microstructure through the implantation of nitrogen ions into free machining brass (CuZn39Pb3), resulting in a reduced coefficient of friction (COF) and lower wear. Metallographic observation of the alloy showed the presence of three phases: α FCC brass, β BCC brass, and Pb particles.

The process parameters of the MCII technique (implantation bias, implantation dose) were optimized in order to obtain a reduced COF that remains stable over long sliding distances. As a result of the optimized parameters for implantation of free-machining brass, the COF was not only reduced from ~0.7 to <0.3, but was also shown to be stable for over 400 m of sliding (see Figure 1). The resulting wear track profiles from these experiments were analyzed to obtain the resulting wear rate. The free machining brass surface implanted with nitrogen MCII results in a 100× lower wear in comparison to unimplanted reference surface. Application of the optimized parameters to implant lead-free brass (CuZn37, see Figure 2) surfaces resulted in a 2.5× reduction of the COF, demonstrating the applicability of the process to lead-free brass.

The low wear observed in the implanted brass sample surface is related to the surface hardening during implantation. Grazing-Incidence X-Ray Diffraction (GI-XRD) studies after implantation showed no peaks corresponding to any crystalline nitrides. These results corroborate well with other studies^[4] and imply that the surface hardening is not achieved from a second phase formation. Transmission Electron Microscopy (TEM) observations of the implanted sample show a microstructure modification over a depth of about 70 nm from the surface (see Figure 3 left). Two modified layers are clearly observed: a "porous" layer (named "b") and a layer with very fine crystallite size (named "c"), the latter being distinguished in dark field TEM micrograph (see Figure 3 right). Through elemental analysis, presence of N was clearly detected in the inner layer (named "b").

These observations suggest the occurrence of recrystallization of the brass grains at the surface as a result of the kinetic energy transferred from the implanted ions. The presence of nanocrystalline grains in layer "c" as well as the "pores" observed in layer "b" impede dislocation movement, resulting in a higher wear resistance of the layer.

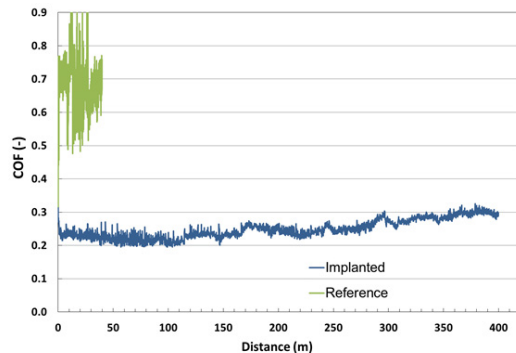


Figure 1: For an applied force of 5 mN, the COF was reduced from >0.7 for the reference (unimplanted) to <0.3 for the implanted Cu39ZnPb3 sample.

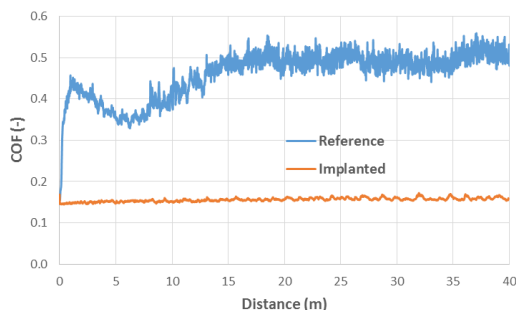


Figure 2: Application of optimized MCII to lead-free brass also results in the lowering of the COF by a factor of 2.5.

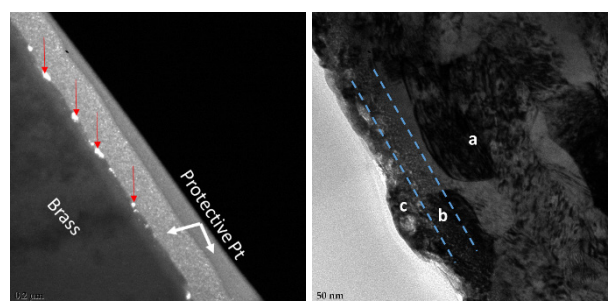


Figure 3: (left) Bright field TEM micrograph showing the microstructural modification of the implanted surface (right) Dark field TEM micrograph showing nanocrystalline brass in layer 'c'.

This project was funded by the Swiss Commission for Technology and Innovation (now Innosuisse) under the project number CTI No.25480.1 PFNM-NM.

• IDONUS Sarl, Rouges-Terres 61, 2068 Hauterive, Switzerland

[1] D.M. Gordin, J. Mat. Sc.: Mat. in Med., 2012, 2953-2966.

[2] C. Pierret, PhD Thesis, Caen Univ. (France), 2012.

[3] S. Thibault, PhD Thesis, Caen Univ. (France), 2009.

[4] M. Cavallier, PhD Thesis, Caen Univ. (France), 2014.

HIP Conditions: Key Operation for Controlling Mechanical Properties of 3D Printed Ti6Al4V

V. Pejchal, S. Zabihzadeh, F. Reinert, O. Sereda, M. Dadras

Selective Laser Melting (SLM) is a process used for near-net shape fabrication of complex parts. The process consists of metal powder melting and rapid solidification resulting in complex microstructure and formation of defects such as micropores. Ductility and especially fatigue resistance are sensitive to presence of defects such as micropores. Hot Isostatic Pressing (HIP) is a well-known process that permits to compact the material and in the case of SLM manufactured parts eliminate the micropores. A common project with ProtoShape GmbH and Bern University of Applied Sciences has been launched to develop full-chain SLM process fabrication for Ti6Al4V alloy for aerospace applications. Present investigation focused on improving the mechanical properties of SLM manufactured parts by HIP post treatment.

Ti6Al4V alloy is a well-known alloy for aerospace application as it offers low density and high mechanical properties. SLM process enables nearly unlimited freedom in design, which permits to fabricate parts with improved performance or design novel unique components. Preliminary investigations focused on topology optimization and microstructure were reported earlier [1].

Table 1: Mechanical properties of samples in as printed and after post treatment compared to commercial alloy.

	Commercial alloy (aged)	As manufactured	HIP (a)	HIP (b)
$\sigma_{0.2}$ (MPa)	1020-1080	833	1273	1000
σ_{max} (MPa)	1100-1270	1310	1290	1080
ϵ (%)	8-13	5.3	2.0	18.4

The present study focused on establishing full-chain process development for SLM manufacturing of Ti6Al4V alloy to obtain homogenous material with mechanical properties be as good as the commercial alloy. Table 1 summarizes mechanical properties measured for as-build samples as well as after HIP treatment. For comparison the properties of the commercial alloy in aged condition are also presented [2]. The process optimization permitted to obtain samples with the density of 99.9 % and well-controlled microstructure. In as-built SLM samples, the yield stress is about 20% lower than for the commercial aged alloy (833 MPa instead of 1050 MPa) and the ductility is about half of the commercial alloy (5.3% instead of about 10%). The maximum tensile strength is comparable to the commercial alloy (1310 MPa). The variation of mechanical properties according to build direction (X, Y and Z) were below 15%. The microstructure of as-built samples investigated by SEM and TEM (Figure 1) showed that the sample is nearly fully martensitic α' phase.

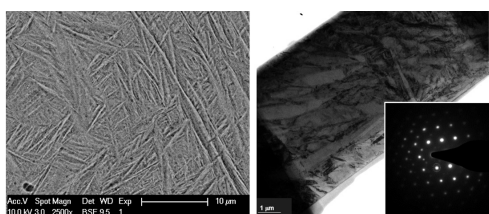


Figure 1: SEM and TEM micrographs of as-built SLM sample. The microstructure is fully martensitic α' phase.

Samples prepared using optimized SLM parameters were HIP treated (900°C and 2000 bar). The main objective of HIP treatment was to remove microporosity and enhance properties. HIP process (Table 1) improved $\sigma_{0.2}$, however, the ductility varied between 2 to 18% according to HIP cycle. Detailed analysis showed that in the case of low ductility HIP(a), the microhardness of samples was higher near sample surface compared to the bulk

(Figure 2). Ductility of Ti6Al4V alloy is very sensitive to oxygen content as presence of oxygen during heat treatment forms a brittle alpha case layer at the surface [3]. Increase of the near-surface microhardness is consistent with the presence of a brittle alpha case that causes the significant drop in ductility for HIP(a) cycle. Thus, obtained results lead to the conclusion that the atmosphere in the chamber during HIP(a) cycle contained oxygen enough to influence the sample properties.

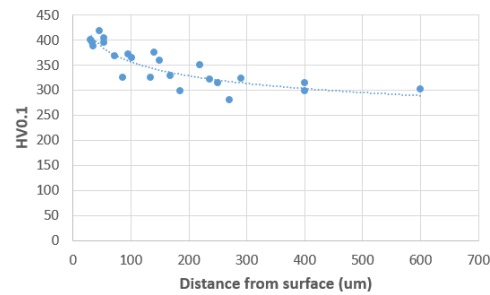


Figure 2: Microhardness variation in the HIP(a) treated sample along the cross-section. The variation is consistent with the presence of brittle alpha case layer rich in oxygen.

The microstrucure and XRD analysis showed that after HIP post-treatment two-phase $\alpha + \beta$ microstructure was achieved (Figure 3).

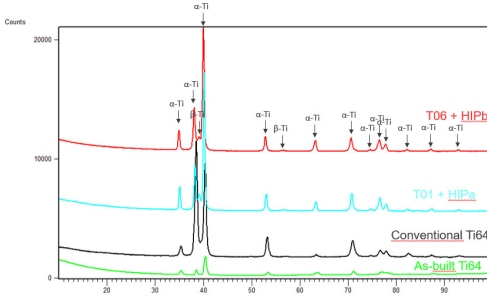


Figure 3: Microstructure and XRD diffractograms after HIP treatment. The main phases detected are α - and β -Ti.

The study established the full-chain process to achieve the mechanical properties of SLM Ti6Al4V manufactured samples comparable to the commercial material. To prevent poor ductility it is important to control oxygen content during HIP treatment. The current project gives full manufacture process for reliable SLM implementation into mass production for aerospace application.

Commission for Technology and Innovation (CTI) is acknowledged for its partial financial support.

[1] S. Zabihzadeh, V. Pejchal, S. Biselli, et al., CSEM Scientific and technical Report (2017) 42.

[2] Metals Handbook, Vol.2, ASM International 10th Ed. 1990.

[3] S. Birhan, Licential Thesis, Lulea University of technology, 2014.

SURFACE ENGINEERING

Helmut F. Knapp

The **Surface Engineering** program addresses controlling surface structure and composition (both topographical and chemical) and developing related manufacturing technologies that enable the fabrication of engineered surfaces at large scales and a competitive cost, making them applicable in an industrial environment. These topographical and chemical properties determine effects such as surface adhesion, wettability and friction, optical reflectivity and color, electrical conductivity, and (bio-) chemical affinity. In addition to elaborating scientific knowledge in the design and understanding of functional surfaces, the **Surface Engineering** program also develops higher level integration pathways that enable CSEM to develop components or devices in which surface properties are a critical factor. Solutions for industry can be offered at all levels of this value chain.

Within the program the development and fabrication of nano-structured surfaces and nanoporous films with added functionality is addressed, as is the design and realization of nano-optical components based on nano-engineered surfaces. Furthermore, biochemical functionalized surfaces are developed for use in (affinity) sensors and as cell and tissue support substrates, including in microfluidics and sample handling instrumentation. Finally, a flexible and broad material and process technology base is established for the printing of components and hybrid systems for the fast and low-cost employment of flexible devices.

In short, the program focuses on research into and the development of engineered surfaces and interfaces by controlling their nano- or micro-structured topography and their surface composition using processes compatible with large-scale manufacturing, all in order to design and optimize their (bio-) chemical, optical, and electrical properties to improve the performance of the respective components and integrated devices.

Long-term objectives

The global long-term objectives of the **Surface Engineering** program are twofold.

First, the program aims at strengthening those areas where CSEM's offering is unique and valuable for Swiss industry. These areas include the development of surfaces and functional coatings with properties that are optimized for specific applications. Highly specialized components and instrumentation for handling and analyzing cells and other biological matter and technologies for printing electrical and optical components on flexible substrates are also developed.

Second, it is of the utmost importance that, given the ongoing trend of miniaturization, the technologies used to optimize surface properties and a state-of-the-art understanding of surfaces are both available at CSEM. Surfaces are key to the improved performance of components and systems and thus also affect all other technology programs of CSEM.

Content

The **Surface Engineering** program is based on three activities:

The activity *Nano Surface Engineering* addresses functional nanocoatings with unique properties and micro-/nano-manufacturing technologies for the cost-effective production of nanostructured surfaces, as well as the engineering and production of micro-/nano-photonic components. While the first two topics remain focused on origination and up-scalable replication methods as well as sol-gel materials with controlled porosity and surface functionalization, the last topic includes methods for the small-scale production of optical components by printing and additive manufacturing, including the emerging field of free-form optics.

The activity *Bio Surface Engineering* deals with interfaces and instrumentation for handling and measuring biological entities. In bio-interfaces, surface functionalization and structuring are optimized for their application in cell supports and other cell-handling components. In bio-sensors, sensors are developed for biochemical sensing by electrochemical and optical methods for applications in *in vitro* and *in vivo* diagnostics and environmental sensing. Finally, bio-instrumentation is being developed for the handling, treatment, and analysis of biological samples, ranging from molecules to small model organisms.

The activity *Printable Electronics* addresses the development of materials and processes for the functional printing of layers and structures onto 2D and 3D substrates in order to generate functional components and to combine such printed components with conventional surface-mounted components into fully functional hybrid systems. A particular emphasis is put on flexible substrates and potentially large-scale printing processes including sheet-to-sheet and roll-to-roll printing.

These three activities have strong mutual synergies, for example in the development of printed electrochemical sensors that are specifically functionalized for applications in environmental or biochemical sensing, for the development of cell culture supports with optimized surface topography and chemistry and integrated electrochemical sensors for monitoring, or for plasmonic sensing for high-sensitivity, label-free analytics.

Beyond that, the work carried out in the **Surface Engineering** program is a critical enabler for a number of projects in other research programs, including surface treatment for hermetic sealing solutions in functional packaging, the design of novel optical filters and masks that can be directly designed onto vision sensors, or surface roughness optimization in intermediate adsorption layers for increased conversion efficiencies in amorphous silicon PV cells.

Highlights

The following reports describe some of the work elaborated during the last reporting period in the **Surface Engineering** program.

Specifically, the *Nano Surface Engineering* activity has progressed in the up-scaling of micro- and nano-structured components with respect to larger surfaces and higher yield. The

examples shown are nanoporous silicon or polymer membranes for various filtering effects in sample treatment or sensing solutions and microlens arrays for improved light collection on image sensors. Also, new optical effects were established with either static or tunable properties for improved color effects or illumination properties using either plasmonic structures or free-form optics. Finally, new sensors were realized relying on either functionalized mesoporous films or molecular imprint polymers.

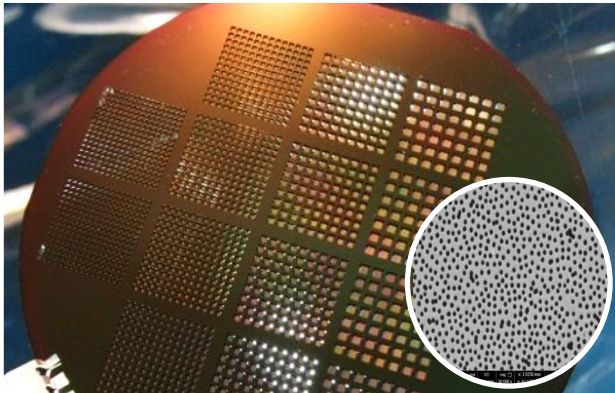


Figure 1: Waferscale production of highly homogenous, nanoporous, ultrathin silicon membranes.



Figure 2: Tunable color filter based on a plasmonic metasurface and liquid crystals.

The *Bio Surface Engineering* activity has put enhanced effort into providing instrumentation for more reliable and automated fabrication, handling, and monitoring of 3D tissue models. These models have become increasingly important for drug development and personalized medicine. Additionally, the technology bricks developed for this purpose are also useful for the field of regenerative medicine. CSEM has progressively been building up a strong network in all of these domains with Swiss and European players in the field from academia, start-ups, SMEs, and also big pharma. Several of the following reports and the MIP 3DuFluidics deal with the automation of the engineering/monitoring of tissues and cell cultures. Nevertheless, CSEM also continues to develop *in vitro* sensing solutions for applications in *in vitro* and companion diagnostics, food safety, or environmental monitoring. Finally, microfluidics and liquid-handling approaches for the controlled, precise handling of small volumes remain a focus at CSEM.

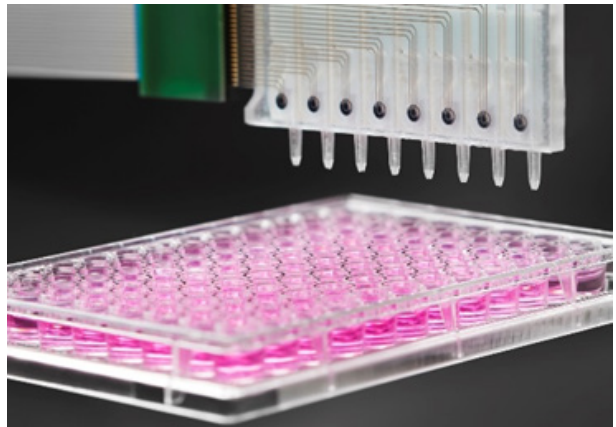


Figure 3: SenseCard for precise, low-volume, in-line glucose measurements from organ-on-chip cultures.

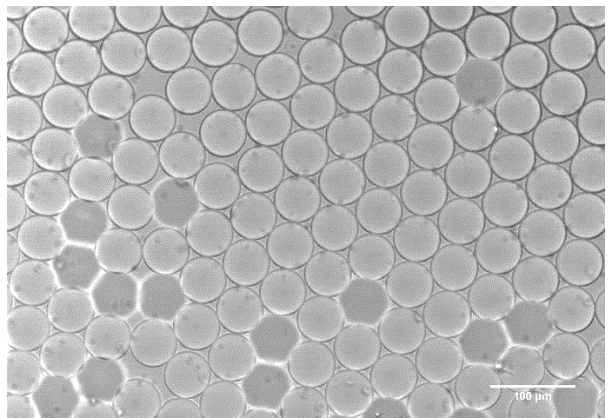


Figure 4: Highly monodisperse droplets generated in high throughput with a microfluidic droplet generation device.

Last but not least, the *Printed Electronics* activity, as the youngest of the activities in the program, has been able to progress toward fully functional components and devices. This is made possible by the understanding and control of the printed materials and printing processes. Examples in this year's report range from a medical application for ventilation monitoring to robotics, where a haptic experience for a robotic hand is realized by the printing of pressure sensors on flexible foils.



Figure 5: Pressure sensor arrays printed on flexible foils for conformal coverage on robot grippers for haptic experience.

Wafer-scale Manufacturing of Nanoporous Membranes by Mean of Nanosphere Lithography

N. Blondiaux, M. Crenna, T. Overstolz

We report on the manufacturing of nanoporous membranes used as highly selective, high flowrate filters for a CNT detection device. The main objective of this work was to decrease manufacturing costs, streamline the process flow used for membrane fabrication by using nanosphere lithography. With this approach, the size and distribution of the pores was defined by using nanoparticle monolayers as a template for the manufacturing of ultrathin silicon nitride nanoporous membranes. This represents a cost-effective alternative to standard lithography techniques for this case study. In this project, we mainly focused on the upscale and automation of the nanosphere lithography process to 100mm wafers and investigated different characterization means to improve quality control during the membrane fabrication.

During the past 10 years, CSEM has been manufacturing a broad range of micro and nanoporous membranes using silicon-based materials for various applications. Specific microporous membranes have for instance been developed to fabricate Fabry-Perot optical filter^[1]. Membranes presenting sub-micrometer pores were manufactured and over-molded in a plastic cell-culture insert to investigate the growth of biological barrier cells using TEER measurement^[2]. Nanoporous membranes have also been developed and optimized to achieve selective molecular filtration^[3] and were also found to improve the kinetics of a bioassay^[4].

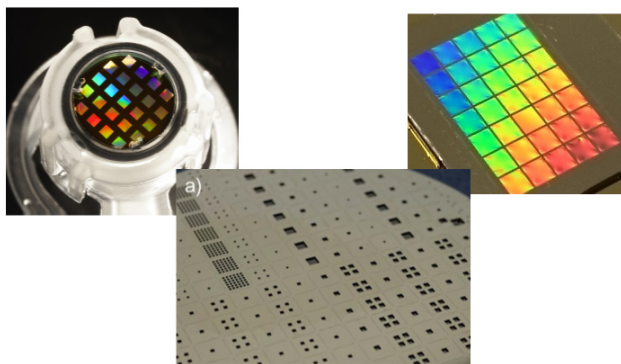


Figure 1: Examples of micro, submicro and nanoporous membranes manufactured at CSEM.

On a process standpoint, the manufacturing of micro and submicroporous membrane relies on well-established microfabrication steps. However, in the case of nanoporous membranes, existing lithography techniques are either too expensive (DUV, E-beam) or do not have sufficient resolution to fabricate nanopores. For that, CSEM has been developing cost-effective alternatives for surface-nanopatterning by means of polymer self-assembly and nanosphere lithography. These nanopatterns have been successfully used as templates in standard clean room process-flows to generate sub-100nm pores in ultrathin silicon nitride membranes.

The main task of this project was to streamline the process flow for nanoporous membrane fabrication by focusing on nanosphere lithography. For that, a specific process was developed to deposit monolayers of commercially available nanoparticles at a wafer scale. The process was automated to improve the quality of the deposition and wafer-to-wafer process reproducibility.

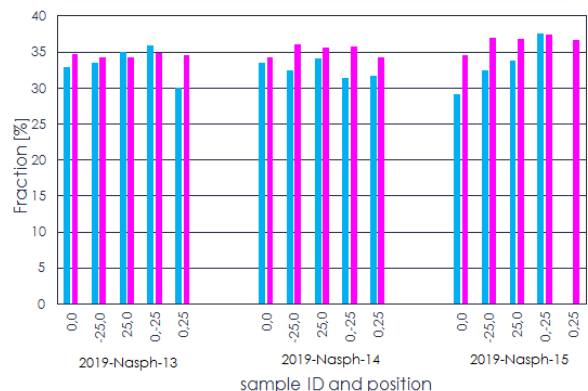


Figure 2: Comparison of quality control for membrane porosity (homogeneity and reproducibility). SEM characterization (blue) and ellipsometry (pink)

On a quality-control point of view, ellipsometry was evaluated to characterize the monolayers with a high-throughput and compared with standard SEM characterization. Membranes are currently manufactured using 100 mm wafers. However, the objective is to further decrease manufacturing costs by upscaling this process to 150 mm wafers.

One application of such nanoporous membranes is their use in a highly sensitive carbon nanotube (CNTs) detection device^[5]. In this system, which was developed in collaboration with the company Statpeel, the porous membrane is a key element acting both as a filter to collect CNTs and as a sensing element for their detection among other dusts.

- [1] B. Timotijevic, A. C. Hoogerwerf, N. Niketic, Fabry-Perot MEMS Optical Filters in 2 – 20 μm Wavelength Range, CSEM Scientific and Technical Report (2017) 26.
[2] G. Voirin, et al., Integration and Interconnection of MEMS Membrane into a Multiwell Plate Insert by Overmolding, CSEM Scientific and Technical Report (2017) 34.

- [3] F. Montagne, N. Blondiaux, A. Bojko, R. Pugin, Molecular transport through nanoporous silicon nitride membranes produced from self-assembling block copolymers Nanoscale, 2012, 4, 5880.
[4] G. Andreatta, A. Fanget, R. Pugin, Ultrathin Silicon Nitride Membranes for Improved Biosensing Kinetics, CSEM Scientific and Technical Report (2014) 66.
[5] D. Schmid, et al., System for Airborne Nanofibers Exposure Monitoring, CSEM Scientific and Technical Report (2016) 50.

Molecular Imprinted Polymer-based Sensor

X. Bulliard, G. Voirin, M. Crenna, R. Pugin, S. Steiner*, J. Binder*, A. Kuczaj*, J. Hoeng*, M. Pesavento **

Molecular Imprinted Polymers (MIP) are developed as sensitive and selective layers for the detection of melamine and nicotine in liquid solutions. The MIP layer can be deposited on different transducers, for example in this study on electrochemical electrodes (EC) for nicotine detection and on Quartz Micro Balance (QCM) for melamine detection. The results show that this technique is particularly adapted for the detection of analytes at rather low concentrations and, thanks to its high selectivity, to the differentiation of targeted molecules from molecular analogues.

The demand for highly specific and sensitive sensors is continuously increasing for the detection of targeted molecular compounds, such as pollutants, contaminants, toxic gases, biological markers. To this end, MIP is a promising approach as with this technique, the MIP detection layer can be specifically designed for being selective to the target analytes. For the formation of a MIP, a polymer layer composed of a monomer with a specific functional group is mixed with the target analytes during production. After reticulation, the target analytes are dissolved leaving cavities in the polymer layer with a specific shape, size and functionalities. The MIP layer becomes therefore highly and selectively sensitive when re-exposed to the target molecule.

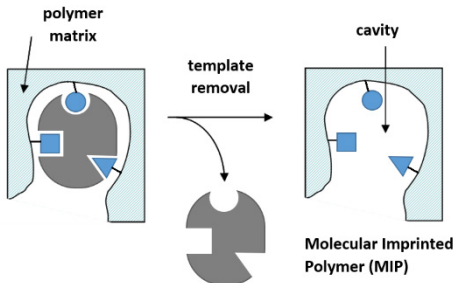


Figure 1: Principle of MIP detection.

For the production of MIP layers, the polymer monomer is mixed with a cross-linker, an initiator, the target molecule that serves as the porogen, and a common solvent. After solubilization, the MIP solution can be deposited by spin coating or by dispensing on the transducer substrate. Curing of the layer occurs then by thermal heating or by UV exposure. The cured MIP layer is finally washed with a solvent to remove the target molecule (porogen). In this study, two different MIP layers have been designed for respectively melamine and nicotine detection.

For signal reading, a large range of transducers can be adapted to the MIP layer, such as electrochemical (EC) electrode, optical systems, or quartz microbalance (QCM). In this study, QCM and EC transducers were used for nicotine detection and QCM was used for melamine detection.

For the detection of melamine, the MIP layer was deposited by spin coating on QCM. Figure 2 shows the results for different concentrations of melamine in solutions, from 0.1 g/L to 1 g/L. The curve with a smaller amplitude corresponds to the Non-Imprinted Polymer (NIP) as a reference. For the NIP, the same polymer layer was used without adding the template nicotine molecule.

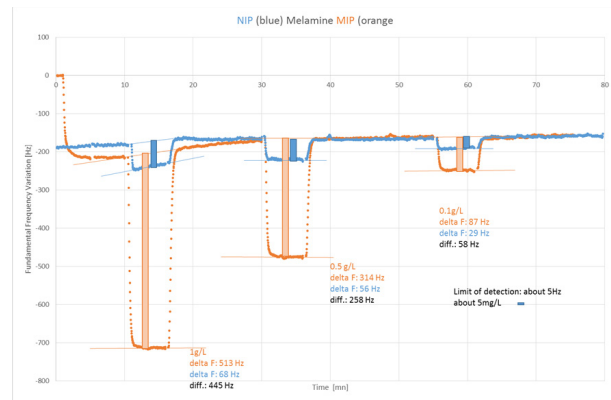


Figure 2: Melamine detection for a MIP deposited on QCM. The curve with the smaller amplitude corresponds to the NIP (Non-Imprinted Polymer).

For nicotine detection, the MIP was deposited on EC electrodes or on QCM by dispensing. The MIP on EC electrodes was particularly adapted to detect low level of nicotine in water solution, down to 1 ppm. An additional series of measurement on QCM showed the high selectivity of nicotine MIP by comparing the signal obtained with other molecules, as shown in Figure 3. In this figure, the measurement was done with anabasine solutions and nornicotine solutions, for which no signal could be observed, in contrast to the nicotine solution, which shows a strong response.

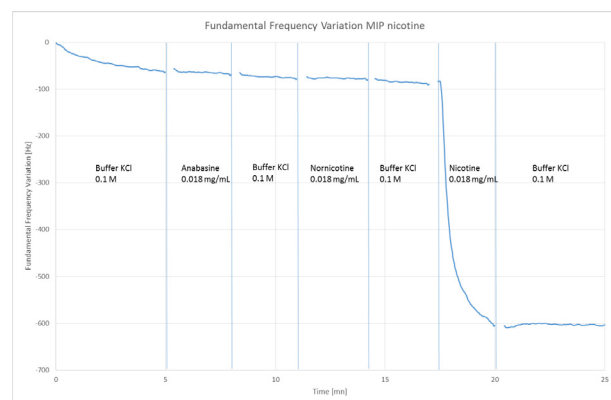


Figure 3: MIP detection of nicotine on QCM. Comparison with the signal obtained with anabasine and nornicotine.

In conclusion, MIP is a suitable approach for the specific detection of analytes with a high level of selectivity. It is not limited to the two cases used in this study, i.e., melamine or nicotine, but can be extended to a wide range of other molecular compounds.

* Philip Morris International R&D, Quai Jeanrenaud 5, CH-2002 Neuchâtel, Switzerland

** Department of Chemistry, University of Pavia, Via Taramelli 12, 27100, Pavia Italy

Improving the Adhesion of Metallic Coatings onto 3D Printed Plastic RF Components

G. Andreatta, O. Chandran, A. Grivel, S. Lani, M. Billod •, E. de Rijk •

Adhesion of coatings and metal layers on plastic parts is critical part of numerous industrial processes in the field of microelectronics (PCBs) and communication such as RF components and THz antennas. SWISSto12 has developed a game changing patented technology based on 3D printing that opens a new world of solutions for radio frequency applications. Currently, the metallization of plastic parts requires toxic and complex etching processes to obtain good adhesion. However, we were able to significantly enhance the adhesion of electrolessly plated metals on 3D printed parts by combining our unique processes for grafting polymers on plastic parts with additive manufacturing methods.

"Three-dimensional printing makes it as cheap to create single items as it is to produce thousands and thus undermines economies of scale. It may have as profound an impact on the world as the coming of the factory did... Just as nobody could have predicted the impact of the steam engine in 1750—or the printing press in 1450, or the transistor in 1950—it is impossible to foresee the long-term impact of 3D printing. But the technology is coming, and it is likely to disrupt every field it touches [1]."

Through polymer metallization, the specific properties of 3D-printed plastic and polymeric parts, such as light weight, design flexibility and complexity are enriched by the addition of properties usually associated with metals such as reflectivity, abrasion resistance, electrical conductivity and a variety of decorative effects^[2]. Electroless or chemical plating has emerged as a low-cost tool enabling the production of high quality samples at room temperature, especially suitable for polymeric substrates, which would not withstand the high temperature required for vapor deposition strategies^[3].

When the metallization of polymer substrates is required, the mechanical cohesion between the deposited film and the substrate (adhesion) is a significant challenge. Current methods include mechanical roughening of the surface, which is not adapted for the kind of complex design, small shapes and high-resolution features available thanks to 3D printing, or chemical etching, usually with a chromium-based etchant. The latter produces large amounts of highly toxic waste and is not always efficient on certain types of 3D printed polymers. Moreover, because of the future European ban on chromium wastes, that efficient process needs to be replaced.

We have developed a process based on the covalent grafting of an interfacial polyelectrolyte layer between the plastic surface and the metal layer, replacing the rough interface obtained by usual pretreatments methods (e.g., chromic acid treatment or mechanical roughening). The process uses the *in-situ* formation of catalytic nanoparticles and increases the final adhesion between the plastic surface and the final metal layer through interdigitation between the materials. Figure 1 schematizes the principle of our method. The process is versatile, based on insertion chemistry activated by heat or UV light.^[4]

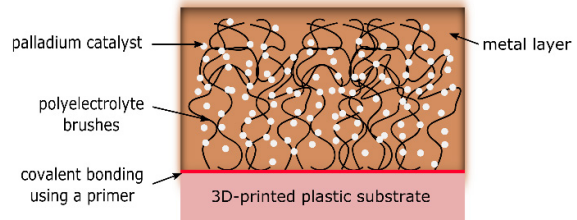


Figure 1: Surface preparation by covalent binding of polyelectrolytes onto 3D-printed plastics and subsequent metallization by electroless plating.

The results obtained on a sample printed with high resolution stereolithography (SLA) are shown in Figure 2.

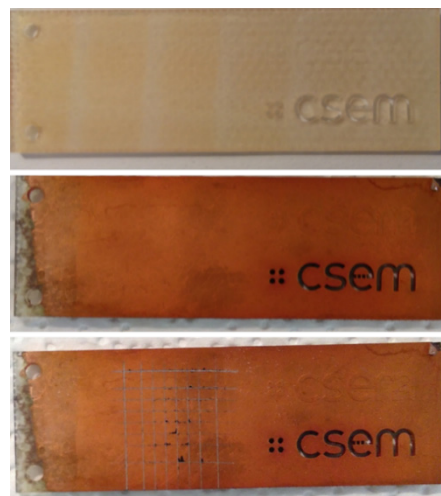


Figure 2: (top) 3D printed plastic sample by stereolithography (SLA); (middle) the same sample after the metallization process; (bottom) the same sample after the adhesion test.

High resolution, smooth, and complex 3D surfaces can thus be metallized with very high adhesion and the process is compatible with a wide range of plastic surfaces. The process is currently tested on the complex 3D shapes of RF components and validated for the wide temperature range over which it needs to operate.

CSEM and SWISSto12 would like to thankfully acknowledge the financial support of CTI (now Innosuisse) during this project.

• SWISSto12 SA, Renens, Switzerland www.swissto12.com

^[1] The Economist, Leader, February 10th, 2011.

^[2] A. Garcia, T. Berthelot, P. Viel, A. Mesnage, P. Jégou, F. Nekelson, S. Roussel, S. Palacín, "ABS Polymer Electroless Plating through a One-Step Poly(acrylic acid) Covalent Grafting" *Appl. Mater. Interfaces* 2 (2010) 1177.

^[3] O. Azzaroni, Z. Zheng, Z. Yang, W. T. S. Huck, "Polyelectrolyte Brushes as Efficient Ultrathin Platforms for Site-Selective Copper Electroless Deposition" *Langmuir* 22 (2006) 6730.

^[4] Patent filed during the Innosuisse collaboration with SWISSto12.

Non-visual Effects of Light on Humans: Spectral Tuning and Light Distribution with Freeform Optical Structures

T. Aderneuer, O. Fernández, R. Ferrini

Nowadays most people spend the majority their day inside, where they are exposed to artificial lighting, which are mainly provided by LED luminaires. Light is the most important "Zeitgeber" for the circadian rhythm of our inner clock^[1]. It triggers non-visual effects such as alertness, cognitive performance and sleep. Sunlight, upon which humans have evolved, changes its spectrum and intensity through the day. In accordance, many studies have investigated the non-visual effects of the spectrum and the intensity of light on humans. Sunlight is also dynamic in its direction. It is known that the distribution of non-visual photoreceptors in the retina is non-uniform. This shows the potential to develop professional lighting with respect to non-uniform illumination. The project aims to produce optimized illumination patterns for non-visual effects using freeform optical structures.

Analysis of metameristic lighting

Light is known to influence humans' circadian rhythms through the so-called ipRGCs (Intrinsically photosensitive retinal ganglion cells) whose sensitivity peaks at 460-484 nm wavelength (*i.e.*, blue-shifted compared to that of the visual photoreceptors). This effect is nowadays exploited using color-tunable lighting solutions that attempt to mimic the color correlated temperature, CCT, of sunlight throughout the day.

The CCT is also a fundamental parameter from a visual perspective. In several applications is preferable to keep it fix at a predetermined value (typically 4'000K). We have investigated the possibility to influence circadian rythems by tailoring the spectral power distribution, SPD, of the light at a preset CCT, *i.e.*, using metameristic light stimuli. Metamers are optical stimuli that are spectrally different but chromatically equivalent (*i.e.*, perceived as same color). An additional constraint was implemented namely a Color Rendering above 80.

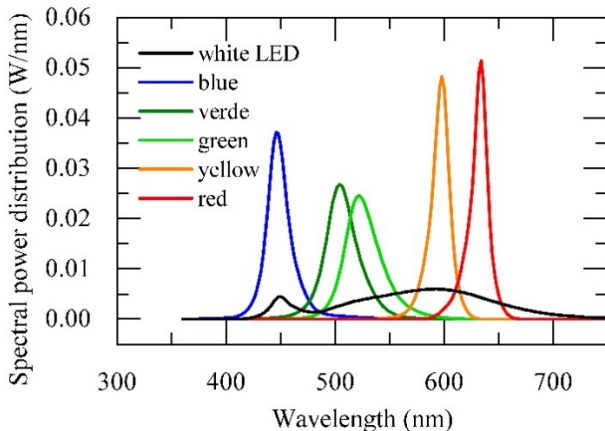


Figure 1: SPDs of the five-colored narrow-band LED (red (624 nm), yellow (594 nm), green (530 nm), verde (505 nm) and blue (455 nm)) and a white LED of 3600 K, which are combined in different ratios.

For this goal, different SPDs were generated by mixing the SPD of several commercially available narrowband (colored) and broadband (white) LEDs (shown in Figure 1). The SPDs were optimized for non-visual effects with the constraint of CRI>80. In order to quantify the non-visual effects, we use the so-called circadian stimulus (CS)^[1,2], which quantifies melatonin suppression (melatonin is the hormone that regulates our sleep-

wake cycle). We show that the particular choice of LED combination, namely a broadband white LED and few narrowband colored LED can be used in lighting application to trigger non-visual circadian effects as well as maintaining required visual color rendering quality

Freeform optical structures

Angular light distribution is a fundamental parameter in classical (*i.e.*, visual) lighting design and several studies have indicated its importance from a non-visual perspective. Therefore, the possibility to realized customized light distributions is very attractive for visual and non-visual applications. Freeform optical components, designed with no constrains in symmetry, enable fully customized light distributions. Several methods exist to design macroscopic freeform lenses for imaging and non-imaging applications

On the other hand, optical microstructures are, compared to the macroscopic counterparts, much lighter and lower volume. And hence, much easier to integrate and manufacturable using cost-effective processes. However, the design of freeform optical microstructures faces several challenges which currently limits their application to for example collimated sources and relative simple distribution such as square/rectangular uniform illuminance.



Figure 2: Left: Hexagonal target irradiance pattern. Middle: Designed freeform optical microstructures. Right: Irradiance pattern produced by the designed solution as predicted using raytracing software ZEMAX.

We are developing algorithms for the design of freeform optical microstructures based on the ray mapping concept. The preliminary results, (an example given in Figure 2) show the promising results achieved so far and indicate that further development is still needed in order to design high-quality lighting solution.

[1] C. Cajochen, et al., "Circadian and light effects on human sleepiness–alertness." Chapter 2 in Sleepiness and Human Impact Assessment, Springer, (2014).

[2] M. Rea, et al., "Modelling the spectral sensitivity of the human circadian system," Lighting Research & Technology 44, 386–396 (2012).

Non-invasive Optical Oxygen Sensing for Life Sciences and Environmental Monitoring

S. Heub, R. Ischer, A. Grivel, X. Bulliard, G. Voirin, R. Pugin, M. Despont, G. Weder

Oxygen is one of the most often monitored parameters in research, medicine and industry. CSEM has developed a new generation of non-invasive optical oxygen sensors based on a dual hierarchical porosity that significantly improve the response of the sensing layer. This contactless sensing technology is available in various systems such as objective-like device for microscopes or fiber-based for further implementation in existing setups.

Oxygen is involved wherever there is life and, therefore, control of oxygen level is of particular importance in the biotech, pharma and medical sciences. The portable systems paired with smartphones are especially attractive for environmental applications.

Traditionally, oxygen concentration is measured electrochemically, while more recently optical sensors have become more widely used. The working principle of these optical sensors is based on selective quenching of fluorescent dyes in the presence of oxygen. One of the biggest challenges for oxygen sensing is to maintain efficiency, stability and accuracy under different conditions of temperatures, humidity levels, or salts concentrations for liquid environments.

CSEM's patented sensing solution is based on the functionalization of thin mesoporous silica-based films with selective dye indicators^[1]. A dual hierarchical porosity is created by infiltrating the first coated mesoporous porous layer with a second microporous layer made of a dye containing sol-gel material (Figure 1). This dual hierarchical porosity is essential to improve the response of the sensing layer in the life sciences, both in terms of selectivity and sensitivity. The stability of the sensor is also drastically improved.

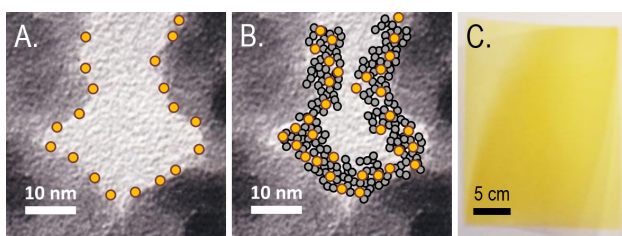


Figure 1: SEM micrograph of the sensing layer based on silica nanoparticles showing the difference between the incorporation of dyes either in a single level (A) or dual level (B) of porosity. The yellow dots represent the dyes encapsulated in the nanoporous structure of the sol-gel matrix (grey dots). The sensing layer is deposited on A4 sheets (C).

The methods of production of these hierarchical sensing layers vary in function of the size and location of the oxygen sensors. The slot die coating is used for large areas (A4 sheet) whereas printing techniques such as aerosol jet printing is required for patterns with high resolution.

Typical sensor performances in temperature of 37°C with relative humidity of 90% are the following:

- Working range 0.1% - 21% O₂
- Accuracy 0.1% at 2% O₂
- Precision ±0.3%
- Shelf life 12 months

An extra compact system has been designed and produced in a format very similar to a microscope objective (Figure 2). The reader can be directly mounted on microscopes used routinely in the life sciences. The oxygen sensor are biocompatible, can be sterilized and disposable, and placed to the inner surfaces of any transparent plastics, glassware or bioreactor. The microscope facilitates alignment between sensor and reader while ensuring a stable and constant optical environment for reliability.

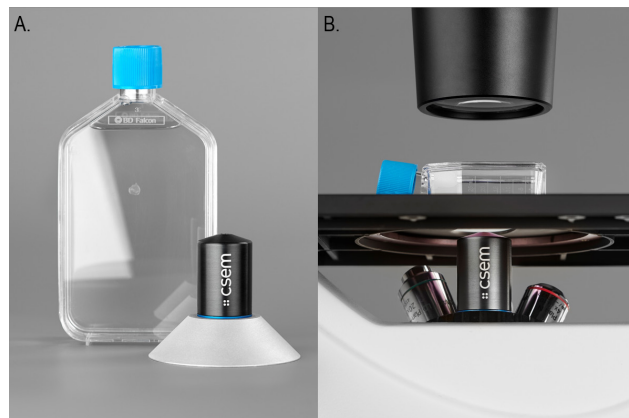


Figure 2: Contactless sensing system for microscopes showing the sensor placed in a disposable plastics (A), and the reader installed on an inverted microscope (B).

A fiber-based system was developed to monitor oxygen in incubation chambers (Figure 3). This innovation allows on-site gas monitoring with minimal invasiveness thanks to an optical fiber that is simply connected to the desired environment to be controlled.



Figure 3: Overview of a gas sensing system for incubation chambers (A). The oxygen sensor on its support is inserted on the optical fiber (B), screwed (C) and pushed in the incubation chamber with gas control (D).

The oxygen sensing solution is highly customizable. Power supply on battery, wireless communication or e-reading on mobile devices are also available on these systems.

^[1] E. Scolan, B. Wenger, R. Pugin, "Optical sensor for detecting a chemical species", EP3184994A1, 2015.

Electrically Tunable Nanostructured Color Filter

B. Gallinet, L. Driencourt, J. Disser, F. Geister, R. Ferrini, D. Kazazis*, Y. Ekinci*, F. Federspiel**, R. Frantz**

Plasmonic nanostructures with a strong and spectrally narrow birefringence have been developed. Strong color effects depending on the polarization have been observed, which could have applications in optoelectronic devices such as displays or multispectral imagers.

Surface plasmon resonances in metallic nanostructures enable the confinement and manipulation of the electromagnetic field well below the diffraction limit, thus opening new paradigms for optical devices. In addition, subwavelength resonators are able to act on the phase of the light, making them essential building blocks for metasurfaces. This project aims to the development of a colored optical retarder and its integration in optoelectronic devices. This is achieved by design and fabrication of plasmonic nanostructures showing a strong and spectrally narrow birefringent effect that yields a color effect which can be actively controlled by, e.g., liquid crystals.

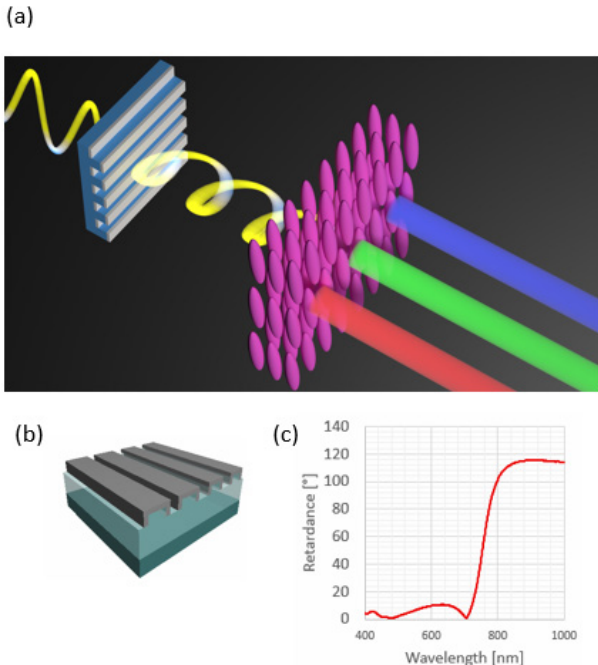


Figure 1: (a) Plasmonic retarder between a polarizer and a liquid crystal-based polarization analyzer, allowing to generate a variety of colors as a function of the voltage applied to the liquid crystal cell. (b) Plasmonic phase retarder made of a deep subwavelength array of silver nanowires. (c) Measured phase retardance between polarization along and across the wires.

The basic working principle of the device is shown in Figure 1. A plasmonic phase retarder can generate different colors in transmission when placed between crossed polarizers and the output polarization is rotated [1]. The plasmonic phase retarder consists of a periodic array of deep-subwavelength metallic nanowires. The light polarized across the nanowires (TM) excites a plasmon resonance. A first entrance polarizer prepares the incident light in a polarization state oriented at 45° from the nanowires orientation. A phase retardation between TM and TE

* Paul Scherrer Institute

** Rolic Technologies Ltd.

polarization yields an elliptically polarized light in transmission. A polarization analyzer based on liquid crystal cells allows to project the transmitted light onto a polarization state whose orientation depends on the applied voltage. Interferences between the different birefringent contributions lead to a color effect in transmission.

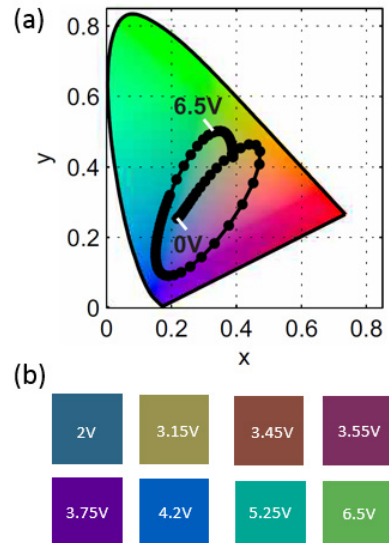


Figure 2: (a) CIE plot of color range spanned by the system. White: colors obtained by mechanical rotation of an analyzing polarizer. Black: colors obtained by increasing the voltage applied to the liquid crystal cell from 0 V to 6.5 V. (b) Colors at particular voltages.

A broad variety of colors can be spanned upon application of a voltage in the range between 2 V and 6.5 V (Figure 2). In particular, red is obtained from the plasmonic structure, blue from the LCC and green from the combination of cyan and yellow from the plasmonic structure and the LLC, respectively. Other colors such as violet, magenta, yellow, cyan, turquoise and different tones of white are generated at intermediate voltages. Overall, an area above 70% of the color gamut of standard RGB filters is generated with a single filter. This spectral selectivity is added in transmission without any loss in the image resolution. Compared to liquid crystal tunable filters, the resonance spectral width of the transmitted light is decreased from 180 nm to 120 nm in the green range. The presented approach is foreseen to be implemented in a variety of devices including miniature sensors or smart-phone cameras to enhance the color information, ultra-flat multispectral imagers, wearable or head-worn displays as well as high resolution display panels.

Funding from Nano-Argovia is gratefully acknowledged.

[1] L. Dömpelmann, A. Luu-Dinh, B. Gallinet, L. Novotny, Four-fold color filter based on plasmonic phase retarder, ACS Photonics 3: 190–196, 2016.

Results of Microlens Testing on Back-illuminated Image Sensors for Space

F. Zanella, G. Basset, C. Schneider, A. Luu-Dinh, I. Marozau, S. Fricke, A. Madrigal, D. Van Aken*, M. Zahir**

CSEM has been mandated by the European Space Agency (ESA) to lead an activity with the objective to design, manufacture and test the application of microlenses on a back thinned Back-Illuminated CMOS Image Sensor (BI-CIS) under space environment conditions. The validation had to address the microlenses technology, their design, materials and involved processes.

Earth observation and scientific exploration missions rely on image sensors *i.e.*, cameras. One way to increase the quantum efficiency (QE) in Front-Illuminated CMOS Image Sensors (FI-CIS) is to add microlens arrays (MLA) which will direct light preferentially into the photosensitive volumes of the pixels. Because Back-Illuminated CIS (BI-CIS) already have almost 100% active surface (100% fill-factor), adding microlenses should not increase the QE significantly. However, they could enhance performance by reducing the parasitic light sensitivity (PLS) and improving the modulation transfer function (MTF) by focusing the light on the center of the photodiode well. The work reported so far on MLA deposition on BI-CIS were only addressed on consumer imaging products for the consumer electronics market where the pixel pitches are below 5 µm whereas space image sensors exhibit usually larger pixel pitches. Additionally, MLA foundries addressing this market are looking for large to very large volumes which is not compatible with space applications. Assessing the microlenses in the space environment is thus required for any integration on image sensors for space applications.

For this study the CAE302 “ELOIS” BI-CIS from Caeleste was selected on which the MLA was deposited. Indeed, this BI-CIS was developed with ESA and tested for space environment. The ELOIS sensor has 2048x256 pixels with 15.5 µm square pixels. This radiation tolerant BI-CIS was designed to use as hyperspectral imager in the wavelength range 350 – 900 nm. The ELOIS sensor exhibits (without MLA) a QE above 90% in most of the visible range and a MTF around 0.556 – 0.593 which is close to the theoretical limit (≈ 0.6). More specifications are available in ELOIS’ datasheet^[1].

The 3 main achievements of this study are:

- Successful replication of microlenses on **packaged** BI-CIS, see Figure 1. Indeed, the BI-CIS had first to be electro-optically characterized in order to deposit microlenses only on screened BI-CIS. Therefore, a dedicated process was developed by CSEM. According to CSEM’s knowledge^[2] this is actually a first, at least in Europe.
- BI-CIS performance improved due to microlenses: the PLS was improved by a factor 1.8 whereas the MTF and QE improvements were less significant. However large improvements are expected to happen on front-illuminated CIS as well as for MTF and QE.
- Robustness through space evaluation campaign: Total Ionization Dose, mechanical shocks ↔ vibrations, outgassing, thermal step stress, moisture and thermal cycling passed successfully. A challenge remains with the long-term UV stability of the microlens material.

* CAELESTE CVBA, Mechelen, Belgium
** ESTEC, Noordwijk, The Netherlands

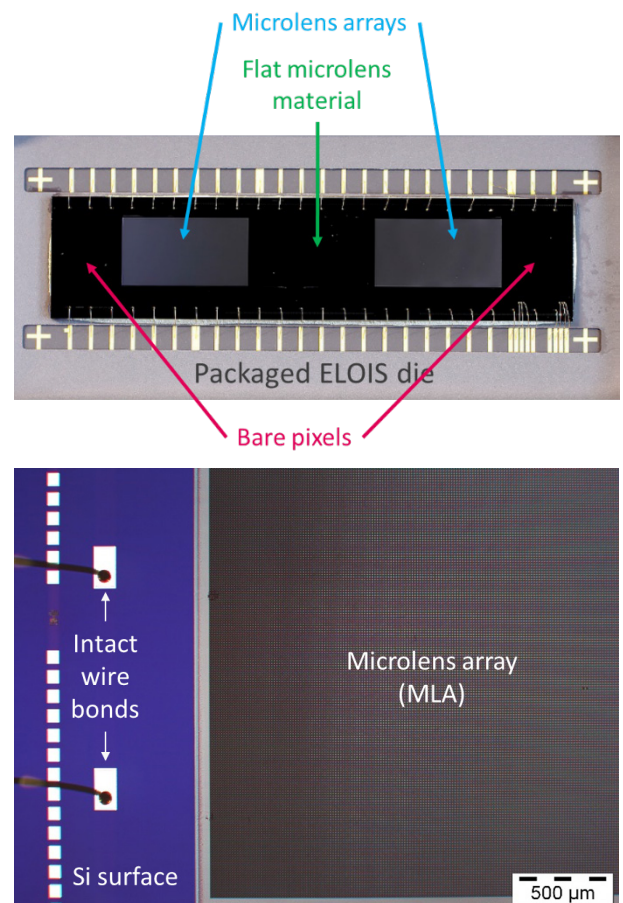


Figure 1: Microlens deposition on packaged BI-CIS from Caeleste.

Since CSEM can address any medium to very large pixel imagers (CIS, CCD, SPAD...), future space missions such as Earth observation and scientific exploration could benefit of the use of integrated MLA. This is especially the case for front-illuminated imagers but also for back-illuminated ones. At this stage, CSEM recommends the integration of microlenses only on imaging systems equipped with a UV filter, hence for missions imaging in the visible or near-infrared. In the meantime, CSEM continues screening new microlens materials having long UV stability while keeping all others highly robust properties. This in addition to moving back to CSEM’s standard wafer or die processing (instead of packaged imagers) will hence increase the Technology Readiness Level (TRL).

These results clearly demonstrate the suitability of pixel-level microlens to improve imagers in a variety of cases in the space environment.

CSEM thanks ESA for funding this activity (TRP T123-501QT).

[1] <http://caealte.be/wp-content/uploads/2018/04/datasheet-ELOIS.pdf>

[2] Based on the feedback from customers and end-users.

Freeform Optics for Uniform Wall Illumination

O. Fernández, T. Aderneuer, R. Ferrini

Freeform optical components have the potential to re-distribute light extremely precisely since their surface can be optimized for nearly all incident rays. This property has been exploited to create uniform illumination of non-symmetric shapes. Here we demonstrate that freeform optical components can be exploited further, to achieve off-axis, asymmetric and precisely non-uniform light distributions which are impossible with standard axially invariant components. Furthermore, we also report on potential strategies to transform macroscopic freeform components into freeform microlens arrays, FMLAs, hence exploiting the high potential for the continuously increasing demands for device miniaturization and their compatibility with cost-effective large-area manufacturing.

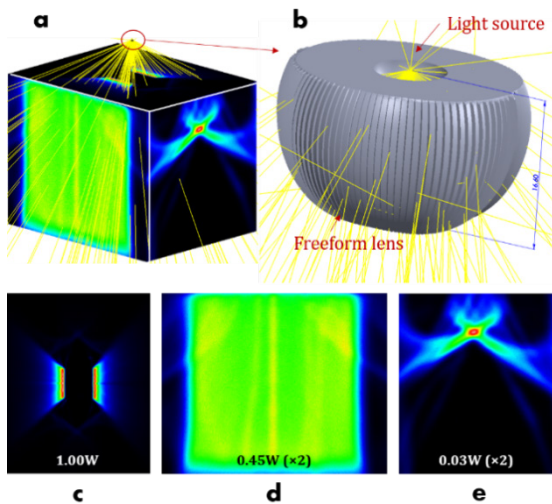


Figure 1: a) Uniform Irradiance distribution achieved using a freeform lens; b) designed at CSEM. The Irradiance distribution are presented and quantified in -c, -d and -e.

Freeform lenses: Uniform vertical illumination

The horizontal Illuminance is only an adequate criterion for working environments where the working plane is horizontal. However, in today office spaces many tasks include non-horizontal surfaces which influence worker's visual and physiological assessment. Indeed, our perception of brightness is mainly determined by what we see in our field of view and hence, by the vertical Illuminance levels. For example, increasing wall Illuminance leads to more stimulating rooms and lower preferred desktop illumination. In shop-retail applications, rack-lighting solutions that lit shelves uniformly produce more attractive product presentation and facilitate the shoppers to survey the range. It is also known that highly uniform luminance levels on walls enhance the impression of room spaciousness and increases visual clarity making well-lit shopping malls more attractive to customers than poorly illuminated ones.

Specifying vertical Illuminance distribution as the merit function for lens design is highly inconvenient from the perspective of a lens designer. Especially for freeform optics, it is more convenient to specify the horizontal Illuminance distribution instead. Vertical Illuminance distributions can nevertheless be dealt with by reversing the problem. From the specific geometric of the problem the position and k-vector of each ray can readily be calculated. The wall source, defined by the collection of emitting points and their k-vectors, is then ray-traced and the Illuminance distribution over the horizontal upper plane obtained and finally used as the (equivalent) horizontal target. The calculated freeform lens was ray-traced using ANSYS SPEOS optical simulation software. The results, presented in Figure 1, clearly indicate that the Illuminance over the target walls is fairly uniform compared to that produced by the bare (Lambertian) light

source. In addition, the total power hitting the (two) walls is 90% of the power emitted by the source compared to the very modest figure of 28% obtained with the uncorrected light source.

Freeform microlens arrays, FMLA

There is a strong need for precise light management in continuously miniaturized devices and systems and the standard freeform macro-optical solutions/industry will only be able to partially address the current and future challenges and requests for solutions featuring miniaturized optics.

CSEM has developed a design method based on the complex arrangement of relatively simple individual microstructures (such as, e.g., microspheres, micoprisms, microaspheres, etc.). A big advantage of this method is its compatibility to large-area light sources. An extended collimated light source illuminates the FMLA (Figure 2 top left) and produces a batwing intensity distribution (Figure 2 bottom left). As a result, the far-field Illuminance is much more uniform than that produced by a Lambertian source (see the Illuminance distributions shown in the right part of Figure 2).

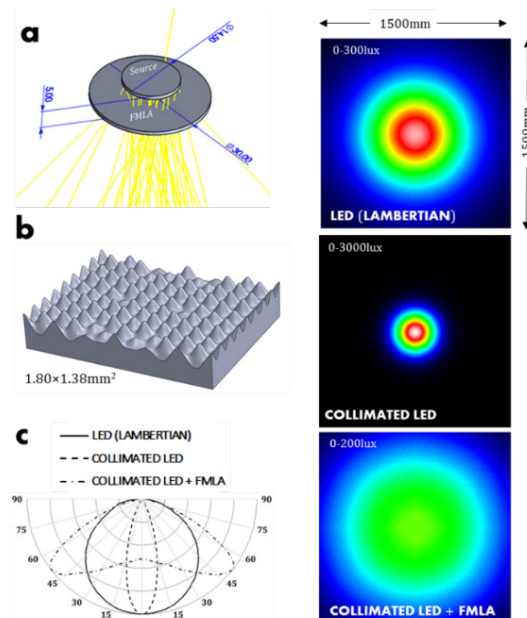


Figure 2: CSEM FMLA for uniform lighting. (left) FMLA 3D CAD model (top) and normalized (polar) luminous intensity distribution, LID (bottom; the Lambertian and the LID of the collimated incoming light are shown for comparison); (right) The corresponding Irradiance distributions over a 1'500x1'500 mm² planar detector located 1'000 mm away from the source; those produced by a Lambert and the collimated incoming beam are shown for comparison.

This work was supported by the InnoSuisse project freeform lens and microlens arrays for high-quality lighting systems (FreeMLA) (33436.1 IP-ENG) in collaboration with INKA – Institute of Polymer Nanotechnology, FHNW University of Applied Sciences and Arts Northwestern Switzerland.

Hybrid Plasmonic-dielectric Resonant Waveguide Grating for Diffraction with High Color Purity

B. Gallinet, G. Quaranta, O.J.F. Martin*

A hybrid dielectric-plasmonic waveguide grating enabling highly color-selective first order diffraction is reported. This work shows the promising use of hybrid structures for designing highly integrated optical devices such as spectrometers or optical security features.

Plasmonic waveguides and resonant waveguide gratings have been a subject of extensive research for a few decades. In particular, filtering has been achieved thanks to the extraordinary optical transmission effect, implemented for imaging and spectral imaging devices. In parallel, resonant waveguide gratings have been used for their filtering and coupling properties into thin film waveguides. The search for full control of polarization, amplitude and phase of the electromagnetic field from planar surfaces remains of high interest, especially for the development of highly integrated photonic systems. Here, we report on a hybrid dielectric-plasmonic resonant waveguide grating which enables highly color-selective first order diffraction in a multimode light guide.

The system investigated in this work is sketched in Figure 1a. A periodic sub-wavelength grating is patterned on a glass substrate and coated with a silver film and silica. The silver layer supports a surface plasmon mode, which is altered by the presence of the thin silica film into a hybrid dielectric waveguide-plasmon mode. At a given wavelength, the incident light is diffracted by the grating and coupled into the waveguide mode. It is released in the substrate by means of a Fano-like interference, as shown in the rigorous coupled wave analysis calculations in Figure 1b.

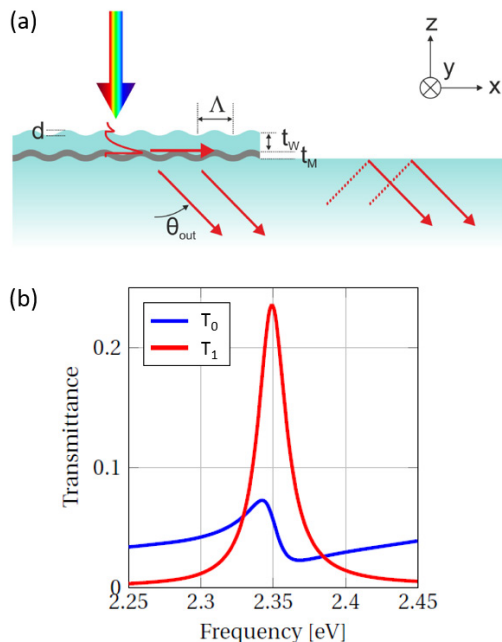


Figure 1: (a) Wavelength selective coupling in a highly multimode light guide using a hybrid plasmonic-dielectric resonant waveguide grating. The incident light is coupled by grating diffraction into a hybrid surface plasmon-dielectric waveguide mode and released into the substrate. (b) The interference between the direct diffracted light and the light coupled into a waveguide mode yields a Fano interference in the zeroth and first order of diffraction.

In the first transmitted order, an isolated peak at the resonance wavelength with a very weak amplitude at other wavelengths is observed, a signature of the resonance effect. In order to achieve high color purity, the coupling from free space to the waveguide should be small, which implies a low grating corrugation depth. The grating depth and silver coating thickness are chosen to achieve the critical coupling condition, thus optimizing the diffraction amplitude in the first order of diffraction while minimizing the contribution of the zeroth order, a potential source of noise.

The grating fabrication has been performed with electron beam lithography into a silicon wafer, which has been used as a replication template for UV-nanoimprinted lithography on glass. After silver and silica coating, the first order diffraction efficiency in the substrate has been measured as a function of the wavelength and the incidence angle (Figure 2). Figures 2b and 2c show the outcoupling angle and amplitude corresponding to the diffracted peak, respectively. As the incidence angle is varied, the resonance wavelength is shifted.

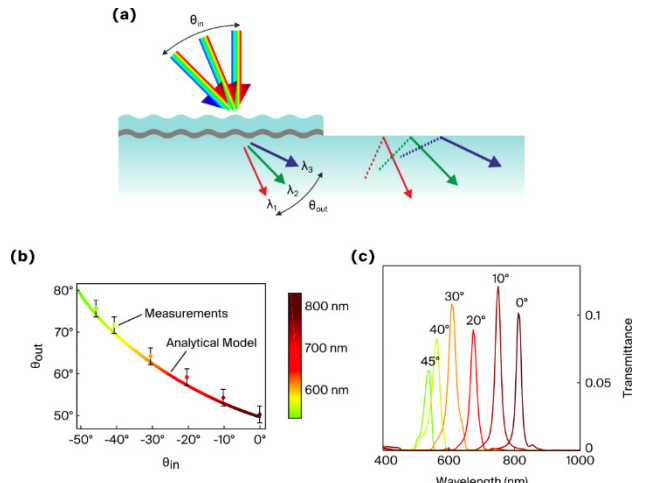


Figure 2: (a) Diffracted angle and wavelength related to the diffraction peak as a function of dielectric waveguide thickness and the period. (b-c) Separation of incident white light with a large range of incidence angles into a set of quasi-monochromatic diffracted beams, comparison between measurements and analytical model.

In particular, a white light beam with large angle divergence would be transformed into a set of angularly separated quasi-monochromatic light beams using this device (Figure 2a). In fact, both functionalities of angular and spectral filtering are performed using a single sub-micrometer interface. The diffracted light can be coupled into a light guide or directly harvested by a photodiode array. Applications in highly compact spectrometers or spectral imagers are foreseen. Alternatively, optical security features with original color effects could be designed using this approach.

* Ecole Polytechnique Fédérale de Lausanne

Patterning Solar Cell Metal Grids on Transparent Conductive Oxides using Self-assembled Monolayers

G. Andreatta, A. Lachowicz, A. Faes, N. Blondiaux, C. Allebé, M. Despeisse

The conductor grids of heterojunction (HJT) solar cells are typically made of screen-printed silver paste with significant costs. They are limited in curing temperature to less than 250°C to prevent silicon passivation damages. However the low curing temperature causes a higher resistivity of the paste compared to high curing temperature^[1]. Copper plating is thus seen as a cost-effective alternative to screen-printed silver. The technological challenges consist in reaching precise patterned structures without parasitic-ghost plating, which demonstrate a high adhesion to the cell TCO, a low contact resistance, a high line conductance, as well as minimum shading (<30 µm line width)^[2,3]. We propose here a novel concept based on self-assembled monolayers (SAMs) in order to obtain patterned copper lines on TCOs. Since SAMs utilize an extremely small amount of material, this approach could achieve plating selectivity with ultra-low costs.

Self-assembled monolayers (SAMs) have attracted enormous interest for a wide variety of applications in micro- and nanotechnologies. We apply commercially available fluorosurfactants to form hydrophobic SAMs on transparent conductive oxides (TCO). Our concept is shown in Figure 1. The cost of such layers is estimated to be approximately significantly lower than currently available processes with different molecules such as thiols or silanes. Moreover, we might not require stripping of the SAM at the end of the process^[4].

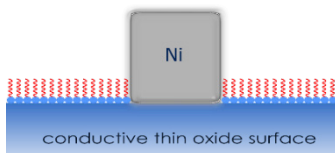


Figure 1: Schematics showing self-assembled monolayers (SAMs) used as a masking layer for electroplating of nickel, then copper on thin conductive oxides.

A spraying method was developed to produce perfluorinated alkylphosphonic acids self-assembled monolayers on pyramid-textured and polished silicon coated with indium tin oxide (ITO) surfaces. On textured substrates, superhydrophobic behavior was observed as shown on Figure 2.

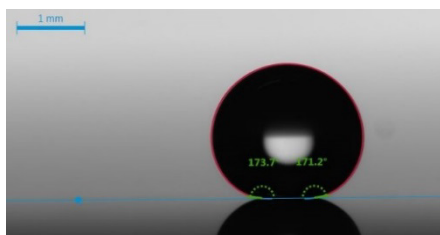


Figure 2: Water droplet behavior on pyramid-textured ITO surfaces.

The dynamic water contact angle measurements show very small hysteresis between the advancing and receding contact angles. This demonstrate the high quality of the self-assembly of molecules on the surface. We also observed that the self-assembled monolayer provides ITO with a resistance to highly acidic electrolytes electroplating solutions. Figure 3 shows the etching effect of the solution. When the surface was not exposed,

a smooth white image is observed. Bare ITO was visibly attacked and completely etched by the solution. On places where the ITO is removed, a blue color appears on the microscope images. Microstructures are observed, showing that the SAM presents weaker spots that are more readily attacked by the acidic solution.

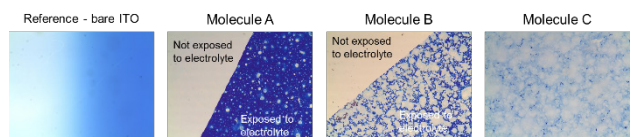


Figure 3: Microscopic images of the etched ITO after 10 minutes dipping in a highly acidic electroplating solution.

The process flow for production of HJT solar cells requires a first layer of nickel to be electroplated on the TCO in order to provide sufficient adhesion for the copper lines. Figure 4 shows the patterned nickel lines obtained in a mild (pH=4.4) sulphamate nickel electroplating bath. The SAM was patterned by a directional oxygen plasma through a silicon hard mask.

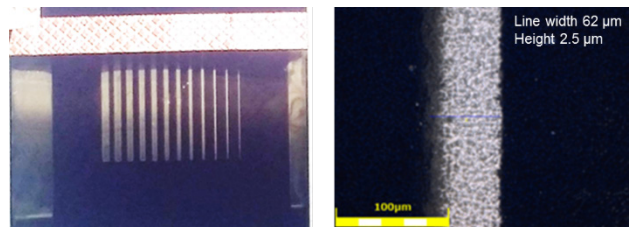


Figure 4: (left) Picture of sample after nickel electroplating using a SAM as resist; (right) Scanning confocal microscopy image taken on the thinnest line of picture shown left.

We are thus able to use the SAM as a resist for electroplating nickel. However, some ghost-plating is observed on the surface where the SAM remained after the plasma treatment. We plan to improve this by strengthening the organization of the SAM. We also will investigate further the quality of the SAMs, patterning methods and the use of SAMs for copper electroplating in the future.

We would like to thank CEA-INES for providing substrates and the Swiss National Science Foundation for its financial support.

[1] J. Lossen, M. Matusovsky, A. Noy, C. Maier, M. Bähr, Pattern Transfer Printing (PTPTM) for c-Si Solar Cell Metallization, Energy Procedia 67 (2015) 156–162.

[2] A. Faes, A. Lachowicz, A. Bettinelli, P. Ribeyron, J. Lerat, D. Munoz, J. Geissbühler, H. Li, C. Ballif, M. Despeisse,

Metallization and interconnection for high-efficiency bifacial silicon heterojunction solar cells and modules, (2017).

[3] A. Lachowicz, J. Geissbühler, A. Faes, J. Champliaud, F. Debrot, E. Kobayashi, J. Horzel, C. Ballif, M. Despeisse, Copper plating process for bifacial heterojunction solar cells, Proc. 33rd Eur. Photovolt. Sol. Energy Conf. Exhib., 2017: pp. 1–4.

FluoReader—LED-based Fluorescence Reader with Configurable Color Channels for Flow Cytometry Applications

P. Cristofolini, G. Orawez, Z. Halvorsen, S. Cattaneo

Fluorescence measurements are widely used for measuring chemical or physical properties of cells and particles in solution. CSEM is developing a configurable, cost-effective and sensitive fluorescence reader for flow cytometry applications and fluorescent readout of microfluidic assays.

Fluorescence (FL) is the spontaneous emission of light by a substance that has absorbed (in most cases) light of higher frequency. Many minerals, molecules, proteins, DNA and living organisms fluoresce under ultraviolet illumination. In life sciences, fluorescence staining is a much-used technique to visualize tissue structure and metabolic or physiological processes with high specificity and spatial resolution. For this purpose, fluorescent marker molecules are introduced into cells and accumulate in specific cell compartments due to physiological or osmotic transport, or due to the unique chemical binding properties of the fluorescent stain.

Stained cell are often used in flow cytometry (FCM), a powerful technique to screen tens of thousands of cells per second for specific chemical or physical properties, like the presence of a specific protein, metabolic or physiological state and reproductive activity. FCM is widely used in biotechnology, cancer research, genetic engineering and water quality monitoring. It relies on a simple working principle: cells suspended in water are aligned in a single row and flow through a focused light beam that excites fluorescence in the cells. The faint fluorescence light is collected, filtered in different spectral regions and measured electronically. These fluorescence signals are often combined with scattering signals and analyzed in multi-dimensional plots, where cells with different properties separate into clusters whose size can be used for statistical analysis of the cell population.

A typical flow cytometer is benchtop-sized, and its detection system requires several sets of expensive components: high power lasers with special emission wavelengths, matching spectral filters with very sharp edges and extremely sensitive photon detectors with large gain (photomultiplier tubes). In the project FluoReader a standalone fluorescence reader is being developed with two excitation sources (cyan and orange) and three detection channels (Figure 1):

- green: SYBR green stain for discriminating biological cells for abiotic particles
- red: DiBAC stain for bacterial metabolic activity
- NIR: propidium iodide stain for bacterial viability

The measurement configuration was chosen to be in reflection (Figure 1), so that samples can be excited and measured from the same side. This does not limit the sample options to a transparent measurement cell, so that the readout from non-transparent surfaces becomes possible. The reader has exchangeable excitation and detection modules that can be fitted with laser diodes or LEDs. The use of high-power LEDs allows to easily customize the excitation wavelength to the measured stain at a very reasonable cost. For detection, multi-pixel photon counters (MPPCs, arrays of silicon photomultipliers) are used instead of expensive conventional photomultiplier tubes to count single fluorescence photons one-by-one. The housing measures 174 x 122 x 56 mm and is fully 3D printed, with alignment

features for the optics and a 3D positioning stage for microfluidic chips. Special care has been taken to reduce stray light, especially for the LEDs, due to their large emission angle. For the laser diode option, a 25 mm diameter eccentric mount was developed, which allows seamless positioning of the laser diode in xyz in a range of ± 1 mm for exact alignment with the optical axis of the reader. Electronic readout is carried out on an oscilloscope interfaced with MATLAB. At a later stage the oscilloscope will be replaced with a dedicated microcontroller that processes the data onboard.

The fluorescent reader can be used to measure fluorescence properties of static and in-line samples. It is ideally suited for the fluorescent readout of microfluidic chips and in-line flow cytometry. It is planned to benchmark the reader in single cell detection against commercial FCM systems and to use it for fluorescent readout of the in-house developed Inca slide assays.

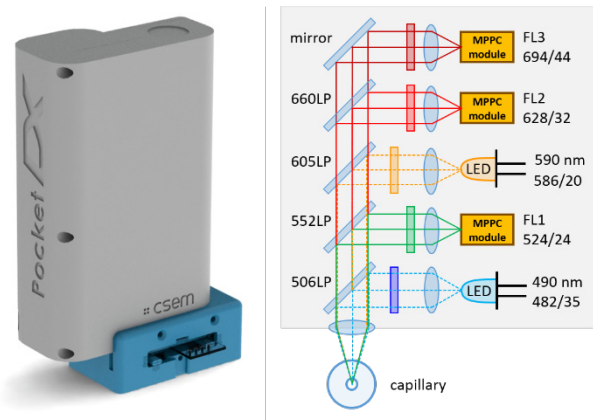


Figure 1: (left) Rendered view of the reader with microfluidic slide holder; (right) Optical sketch with spectral properties of filters and light sources.

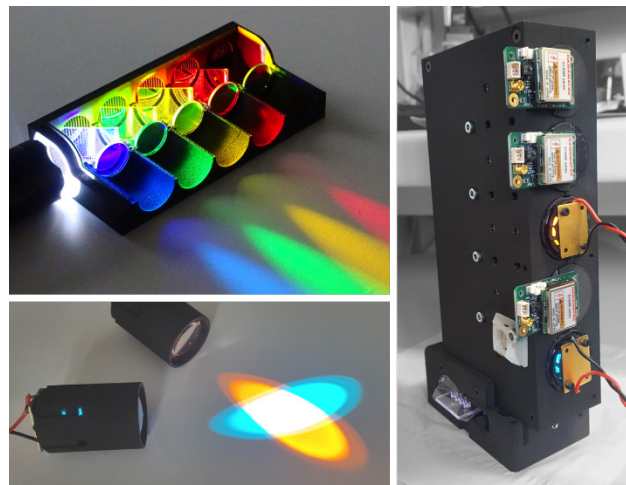


Figure 2: (top left) Optical setup with mounted spectral filters separating the light for the respective emission/detection channels; (bottom left) LED modules with cyan and orange light; (right) Reader equipped with light sources and detectors.

Development of Scalable Fabrication Methods for High-precision Membranes

M. Zinggeler, A. Luu-Dinh, C. Schneider, A. Lücke, D. Schlup, T. Offermans, G. Basset, I. Zhuraminsky, S. Fricke

Microfiltration membranes play an important role in various applications and processes. However, the currently available track-etched polymer membranes suffer from their random structure and statistical hole diameter, while standard precision membranes are typically stiff and brittle and are made using expensive silicon semiconductor processes. In response to these challenges, scalable and cost-effective fabrication processes for large area and flexible high-precision membranes were developed. The processes allow the fabrication of the membranes from a variety of different metals and polymers and can be customized for various applications.

Microfiltration membranes are an integral part of many systems and processes, where they are mainly used to filter or up-concentrate cells or micro-particles, with polymeric track-etched membranes representing the current industry standard. However, these types of membranes struggle with several drawbacks: Their pores suffer from uneven distribution, vary in terms of their diameter and they randomly overlap. Additionally, they have severely limited pore density (porosity) and their geometry is bound to being cylindrical in shape, which is unfavorable in many cases. High-precision membranes based primarily on silicon semiconductor processes have long been recognized as alternative technologies capable of overcoming the limitations of track-etched membranes – but they also come with a catch, as the used materials are typically stiff and brittle and they present a significantly increased cost per unit membrane area, when compared to track-etched membranes.

In response to these challenges, we have developed scalable and cost-effective fabrication processes for large area and flexible high-precision membranes. These fabrication processes overcome the issues associated with polymeric track-etched & high-precision membranes by combining and improving their best features – and as an additional bonus, the processes also allow the fabrication of the membranes from a variety of different metals and polymers.

In our process, microstructures are first prepared using standard lithography methods. The generated structures are then transferred into a suitable metal by electroplating which either yields the desired metal membrane (Figure 1) or a metal tool. The metal tool is then used in an embossing approach for the fabrication of polymer membranes (Figure 2). While this process is currently performed on small scale using a sheet-to-sheet method, it has a high potential for later upscaling to roll-to-roll production.

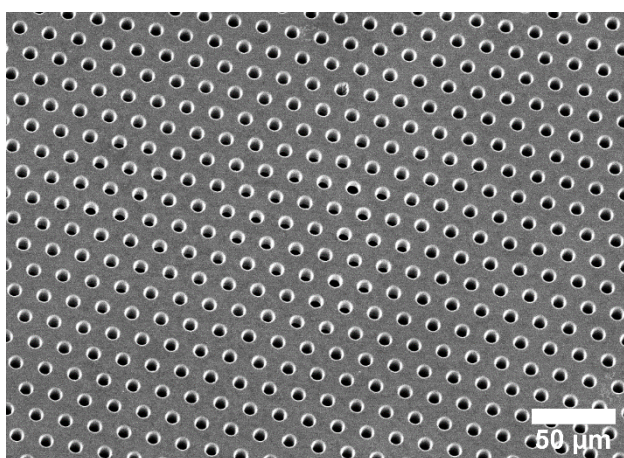


Figure 1: Metal membrane example (SEM micrograph).

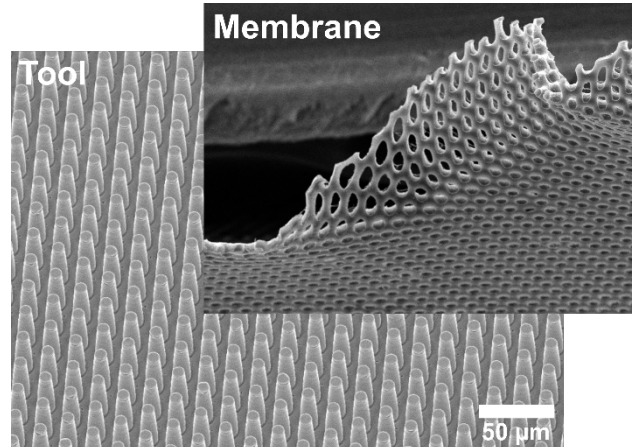


Figure 2: Example of a metal tool and the generated polymer membrane (SEM micrographs).

In the shown examples high-precision membranes with 7.2 μm cylindrical pores, 23% porosity and 20 μm thickness were realized which are designed for the isolation of circulating tumor cells (CTCs) from the blood of cancer patients. However, the membranes are not limited to filtration applications but could be used as a key component in diagnostic devices or organ-on-chip systems. In addition to tailor-made micro-pores, the surface chemistry and nano-topography of the membranes can be tuned for specific purposes.

Key advantages:

- Precisely shaped and aligned pores
- Tunable surface properties
- 2-4 times higher porosity than industry standard
- Scalable and cost-effective processes

Possible application fields:

- Cell isolation and analysis
- Point-of-care diagnostics
- In vitro models and organ-on-chip
- Biological sample preparation
- Downstream processing

SenseCard—a Disposable Parallel-sensing Card for Advanced In-vitro Models

S. F. Graf, N. Schmid, T. Volden, N. Glaser, K. Petropoulos, S. Boder-Pasche, H. Chai-Goa, S. Paoletti, G. Weder, V. Revol

Due to increasing regulatory constraints and lack of physiological relevance of animal tests, there is an increasing demand for in vitro microsystems mimicking organ-level functions. Cell-on-a-chip approaches have proven their versatility and strength to reproduce the cell/tissue/organ microenvironment. While academia and SMEs have so far mainly been working on proving the biological relevance of their systems, they are now looking for solutions to monitor the cellular response, to get functional read-outs and to facilitate the use of such systems. With our SenseCard we provide a simple solution to sense molecules like glucose in such cell cultures.

The emerging market of organ-on-a-chip and 3D cell culture is mainly looking for a comprehensive solution, which allows to verify the validity of their systems for drug screening or toxicology. Therefore, many methods can be used for determining the concentration of molecules in the cell culture. However, methods based on optical readout (fluorescence, luminescence, or colorimetry) typically require relatively large amounts of sample. Others, based in molecular recognition and marking / or separation using magnetic beads, are not adequate for quantitative concentration measurements and are typically implemented for single-use positive / negative detection of target molecules. Electro-chemical sensors are on the other hand particularly well suited for measuring the concentration of molecules in an accurate, quantitative way, from a small sample-volume and can be re-used several times if the sample is efficiently evacuated and renewed without cross-contamination between successive measurements.

CSEM's SenseCard combines the strength of the electro-chemical sensors and parallel fluidics. It allows to perform 8 parallel measurements simultaneously with up to 40 cycles within 6h. This allows to closely monitor the cell culture without the need of many manual steps like dilution. Furthermore, with the recalibration possibility, SenseCard does not suffer from potential offset due to the culture media matrix effects.

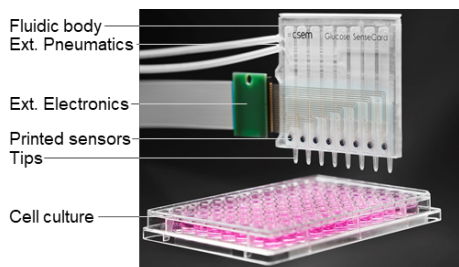


Figure 1: SenseCard on top a well plate containing a cell culture.

The current SenseCard (see Figure 1) holds 8 electro-chemical sensors in a row fitting on top of a standard 96-well plate. With pneumatics, 5 μ l of culture media is aspirated into each of the 8 sensor chambers in parallel (simultaneously). To enable the parallel aspiration, a fluidic body was designed with appropriate restrictions to compensate for manufacturing tolerances. Meaning, after each channel a restriction is placed which dominates the flow resistance in this channel. With this feature it is possible to aspirate 8 samples of the culture media with one single pull-stroke of a pipette. During the aspiration, the sensor chamber is filled and the excessive liquid (not in contact with the sensor) can be returned to the cell culture with one single push stroke on the pipette. After the measurement, the analyzed samples are moved to the on-card waste with another single pull-stroke. Before the first measurement, a 3-point-calibration should be performed to tune the electronics for the applied culture media. Additionally, after each measurement, a wash cycle and ideally a one-point-calibration step follows to verify the cards function.

The complete fabrication process is optimized for low-cost mass production. The sensor's electrodes together with the electrical connections can be roll to roll (R2R) printed onto a heat stabilized PET foil. The subsequent electro-chemical functionalization can be handled with automated dispensing equipment. Finally, the fluidic body can be injection molded and the assembly completed with a lamination step. The complete assembly is finally sterilized via gamma radiation.

In Figure 2 we present results taken with the electro-chemical sensors functionalized for glucose. In a first step, three different glucose concentrations (0.5 mM, 1 mM and 5 mM) were used for calibration. In a second step, daily measurements over a period of 4 days have been performed in a 3T3 cell culture. Due to the sensor operational stability of 6h, every day a new sensor was calibrated and used for the culture media measurement. The calibration curve shows a good linearity while the culture results show, that the glucose consumption is rapidly increasing after the first day due to the fact that the cells proliferate constantly.

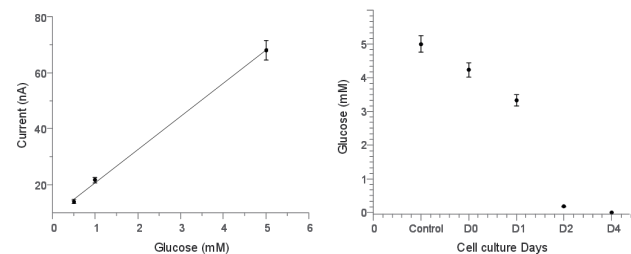


Figure 2: Electro-chemical sensor calibrated (left) and tested in cell culture over several days (right).

The patent pending SenseCard provides a solution which allows the operators to focus on their cell culture instead of the tedious work of diluting and pipetting. The gamma sterilized SenseCard with 8 parallel sensors generates results within a half a minute and can be calibrated to the applied cell culture media with or without serum. Due to the design, the measured samples are directly disposed in the card's waste. Furthermore, the rest of cell culture is never in direct contact with the sensor to prevent any contamination also by the sensor. Finally, the reuse of the SenseCard for up to 40 measurement cycles ($40 \times 8 = 320$ measurements) and its operational stability of 6 hours allows to closely monitor the cells behavior during one day.

In a next step, the card will be used to monitor 3D cell cultures and might be equipped with on-card washing buffer to further reduce manual steps. Depending on user needs, we continue the development of additional electro-chemical sensor functionalization for, e.g., lactate or others.

The Swiss Confederation and MCCS (Micro Center Central Switzerland) supported this work for which we are thankful.

Automated, Disposable Sample Preparation Cartridge for Complementary Diagnostics

S. F. Graf, S. Berchtold, T. Volden, V. Revol

Within the European Project BIOCDx^[1], a Point-Of-Care (PoC) solution has been developed to measure the concentration of four biomarkers in the pg to ng range per ml out of whole blood. A single drop of blood from a needle prick is enough to obtain a complete signature indicative of cancer progression. The current system is developed as a complementary diagnostic to allow patient stratification and support therapy monitoring for prostate and breast cancer. The CSEM contributed to this success by developing a disposable cartridge and associated liquid actuation module that enable to run and monitor the complete workflow. With our solution the patient's whole blood sample is automatically preprocessed to plasma and metered for the subsequent optical measurement and finally collected in the on-cartridge waste before the disposal. All reagents are prefilled in the cartridge and all liquids remain entirely in the cartridge, avoiding contamination risk.

In the consortium of the European project BIOCDx CSEM has developed a solution consisting of a point of care (PoC) instrument (Figure 1) and a pre-filled disposable cartridge (Figure 2) previously reported in^[2,3]. The cartridge contains a photonic sensor containing 8 asymmetric Mach Zehnder Interferometers (aMZI) from Lionix International. To detect the bio-markers, antibodies are deposited on the aMZI. For a first demonstration, the cartridge was customized to process whole blood from a liquid biopsy and detect a protein signature for breast and prostate cancer.

The user-friendliness was increased by reducing the manual steps to a minimum. Meaning, the user receives the packaged, self-contained cartridge and inserts it into the instrument. Then the sample (currently a drop of blood) is loaded into the cartridge and the sample port is closed. The instrument then prepares (I) the cartridge, (II) the detector, and (III) filters the sample before it is (IV) analyzed. Finally, the operator reads the result and disposes the cartridge in which all liquids are contained in the waste compartments to prevent any contamination.



Figure 1: BIOCDx instrument, developed jointly with LRE medical.

As soon as the cartridge is inserted into the instrument, the on-cartridge syringes, valves and sensor on the backside are interfaced with the actuators. On the front side of the cartridge, five flow sensors are monitoring the transition from air to liquid as shown in Figure 2 and enable to monitor the progression of the liquid columns in the microchannels and detect air bubbles. The flow front sensors are positioned (I) after each syringe to monitor their initialization and (II) before the two wastes to verify the correct flow directions. A final sensor is positioned in the metering loop to detect air bubbles during the priming procedure and to direct them into the bypass waste. The example at the bottom right in Figure 2 shows that the metering loop (position S3) is wet

at the start time of recording and dry up at time index 1850 when air passes the sensor S3. At time index 2350 the metering loop is wet again, and the air gone. With a delay of about 50 units which corresponds to Δs which is the distance between S3 and S4 the entry to the bypass waste (position S4) gets dry and wet again. Meaning the air bubble has traveled through the metering loop to the bypass waste. The two signals are inverted due to the different backgrounds and can be handled as such in the software.

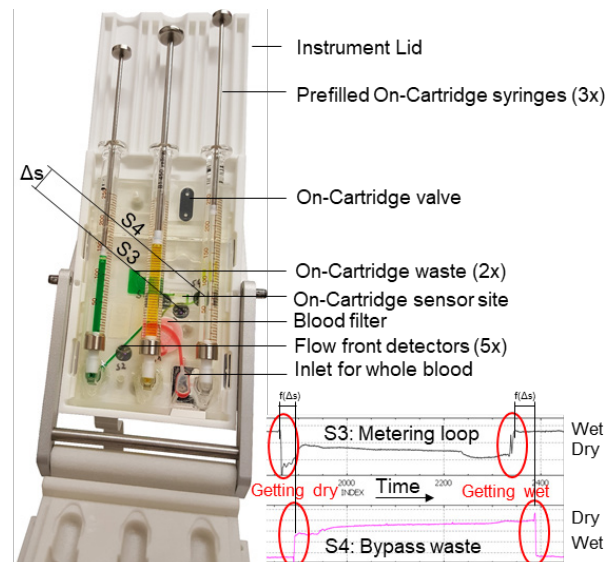


Figure 2: (left) Cartridge in instrument lid; (right) Flow front detector signal showing an air bubble moving from the metering loop to the bypass waste.

The main part of the cartridge is currently injection molded while glass syringes are still used enabling fast design iterations and easy preparation on site. In a next step, the available solution will be validated in a small clinical study to detect breast and prostate cancer. Simultaneously, a new cartridge design with embedded syringes will be done to enable mass production.

In future work, this technology might be adapted to work with other body fluids such as urine or saliva.

This work was supported by the Swiss federation, MCCS Micro Center Central Switzerland, and the European Commission (H2020-732309 BIOCDx). CSEM thanks them for their support.

[1] BIOCDx is a European Project with ID 732309, "A miniature Bio-Photonics Companion Diagnostics platform for reliable cancer diagnosis and treatment monitoring", <http://biocdx.eu/>

[2] S. F. Graf, et al., "Analysis Cartridge for Companion Diagnostics", CSEM Scientific Report (2017) 60.

[3] S. F. Graf, et al., "Liquid Biopsy - A disposable Cartridge to Measure Proteins from Whole Blood", CSEM Scientific Report (2018) 45.

3MDGen—High Throughput Droplet Generation

Z. Halvorsen, V. Revol, N. Schmid

A high throughput microfluidic device to produce highly uniform micro-droplets has been developed. Micro-droplets with a narrow size distribution have applications in the fields of pharmaceuticals, cosmetics, diagnostics and the food industry. The narrow size distribution of emulsions increases their stability and allows a high degree of control over volumes, payload and tailored release of encapsulated substances.

Micro-emulsions could be formed when two or more immiscible liquids like water and oil are mixed, so that one liquid forms droplets in the other liquid and stabilizes with the help of an added surfactant (amphiphilic molecules that act as an emulsifier). This technology can be used for protection from heat, moisture and oxidation as well as to increase the stability of compounds, to mask undesirable tastes and to improve the release properties of compounds like target delivery in food and pharmaceutical industries.^[1,2]

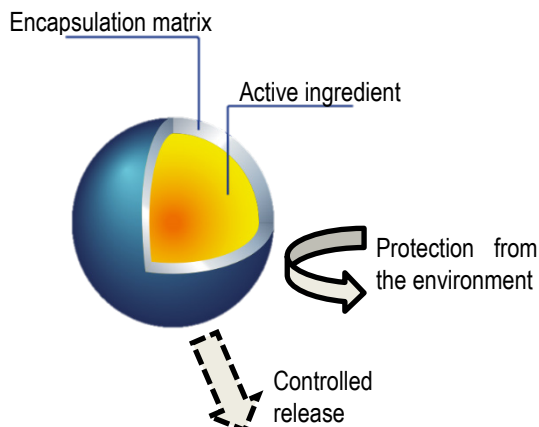


Figure 1: Motivation for encapsulation of active compound.

In this project we fabricated a membrane emulsification device, similar to the grooved microchannel (MC) array developed by Prof. Mitsutoshi Nakajima^[3] to manufacture emulsions with narrow size distribution, which provides a very high control over the drop formation. Water in oil or oil in water single emulsion drops were manufactured by changing the surface chemistry of the microchannel to hydrophobic or hydrophilic, respectively. The coefficient of variation of the drop size is as low as 3%

Poly (lactic- co-glycolic acid) (PLGA) is well established as a biodegradable polymer carrier for drug encapsulation and drug-depot delivery. In order to have a high degree of control over beads degradation rate and ultimately drug release, highly monodispersed beads are required. Conventional methods of PLGA particles synthesis with high shear force mixing generates beads with a very wide range of diameters, which is not desirable and size selection for the emulsion particles is also limited.

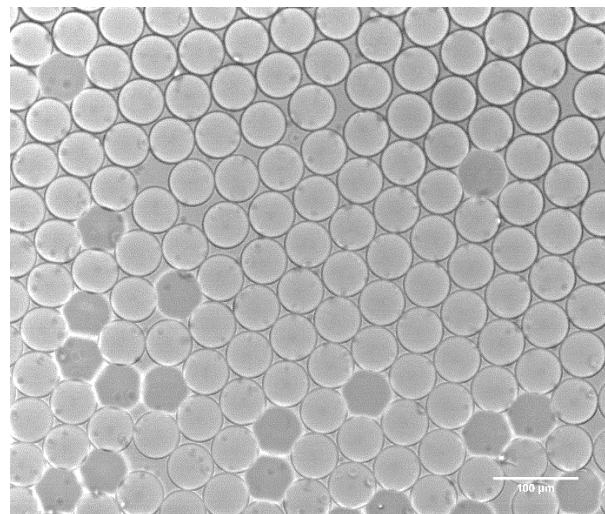


Figure 2: Highly monodisperse water in oil droplets generated with membrane emulsification device, droplet size around 50 μm (droplet size is tunable with nozzle geometry).

Oil-in-water emulsions were produced using a membrane emulsification microfluidic device. The surface of the channel was made hydrophilic. The aqueous continuous phase contains 2 wt. % poly (vinyl alcohol) (PVA, Mw 31,000–50,000, 98%–99% hydrolyzed, Sigma-Aldrich) in DI water and the dispersed phase contains (PLGA, Mw 40,000–75,000, 65:35, Sigma-Aldrich) in dichloromethane (DCM). Oil in water droplets were collected and PLGA microcapsules were ultimately solidified by evaporation of DCM at ambient temperature.

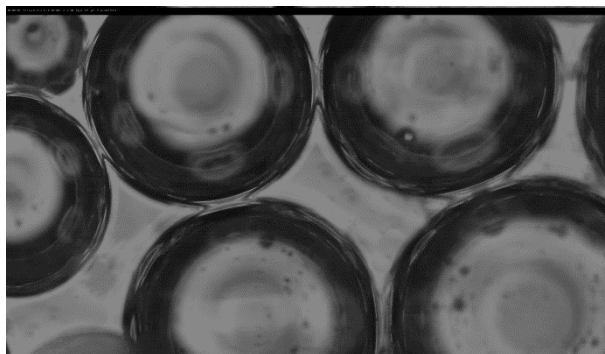


Figure 3: Optical images of monodisperse PLGA encapsulated oil in water emulsion prior to solvent evaporation and conversion to solid PLGA microsphere.

[1] L. Corrêa-Filho, et al., "Advances in the Application of Microcapsules as Carriers of Functional Compounds for Food Products." *Applied Sciences*, vol. 9, no. 3, Sept. 2019, p. 571 doi:10.3390/app9030571.

[2] M.R.I. Shishir, L. Xie, C. Sun, X. Zheng, W. Chen, Advances in micro and nano-encapsulation of bioactivecompounds using

biopolymer and lipid-based transporters. *Trends Food Sci. Technol.* 2018, 78, 34–60.

[3] N. Khalid, et al., "Formulation Characteristics of Triacylglycerol Oil-in-Water Emulsions Loaded with Ergocalciferol Using Microchannel Emulsification." *RSC Adv.*, vol. 5, no. 118, 2015, pp. 97151–97162., doi:10.1039/c5ra18354e.

Disposable Glass Microfluidics for Nucleic Acids Bioassays

S. Heub, G. Voirin, R. Pugin, M. Despont, T. Bauert*, A. Tzannis*, G. Weder

Despite plastic's favored use in microfluidic consumables, the superior optical and chemical properties of glass mean it should be the material of choice. Undesirable damage to pre-immobilized biomolecules caused by some bonding methods have so far limited the use of glass. In collaboration with IMT AG, CSEM is developing new cost-effective glass solutions to maintain biomolecule integrity.

Glass advantages over plastics are acknowledged in the microfluidics community. However, the costs associated with device manufacturing often limit its use in bio-applications. Although micro-structuration and surface functionalization (typically by dip-coating or vapor deposition) are both available at the wafer scale, glass channel sealing remains costly. Existing industrial-scale solutions are not suitable for the life sciences as the processing conditions are not compatible with pre-immobilized biomolecules (e.g., high temperature for fusion or anodic bonding, O₂/CF₄ plasma for direct bonding). Methods using an adhesive inter-layer seem promising but typically lack standardization in the application of the adhesive [1] and remain limited to the laboratory scale.

A glass microfluidic device was fabricated based on the patented design of the IncaSlide [2]. It consists of a meandering channel including an array of 384 cylindrical positive microstructures (bumps). The chip fabrication process is shown in Figure 1. A total of 13 chips (25x75 mm) per 8-inch wafers are produced (Figure 2). After spotting the oligonucleotides on the bump array of wafer 2, a homogeneous layer of adhesive is transferred onto Wafer 1 without wetting the channel walls. Wafers 1 & 2 are then aligned and brought into contact. The adhesive is cured by exposure to UV light.

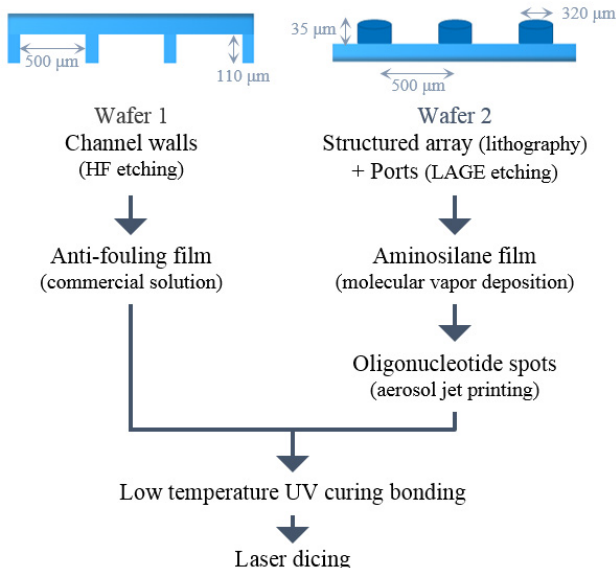


Figure 1: Fabrication process of the microfluidic microarray device.

Injection of a fluorescent solution in the channel enables to assess the sealing efficiency (Figure 3A). We demonstrate that the sealing is stable for at least 4 months without any leakage. Our method allows a reproducible application of the adhesive

without spreading in the channels after curing. Besides, the integrity and functionality of the spotted biomolecules are verified at the end of the fabrication process (Figure 3B). The pre-immobilized target oligonucleotide is still visible (green spots) and pairs properly with the probe (red spots) after bonding and hybridization. We also demonstrate that there is no non-specific binding of other probes on the spots and at the glass/adhesive interface (data not shown). The immobilized biomolecules maintain their reactivity and specificity after the whole fabrication process.

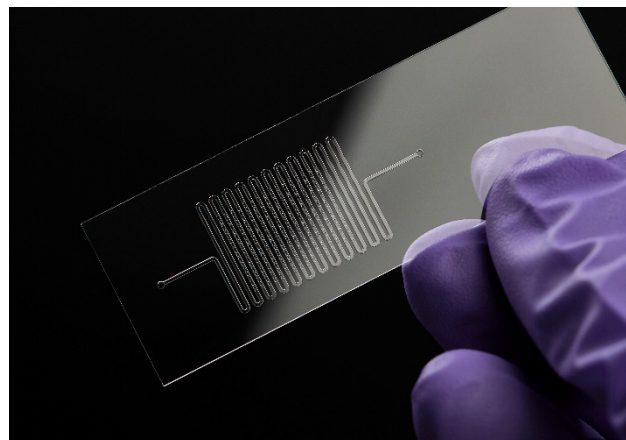


Figure 2: Picture of the sealed glass microfluidic microarray device.

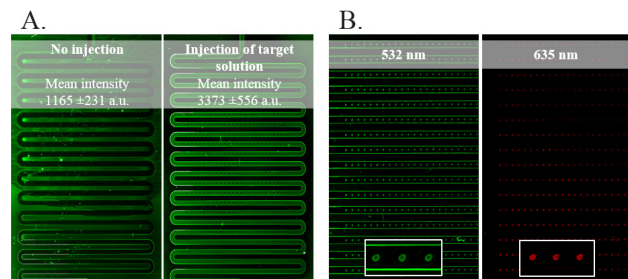


Figure 3: Example of fluorescence images obtained before and after injection of a fluorescent solution in the channel, 4 months after sealing (A) and results obtained after bonding and hybridization of the pre-immobilized target (B).

In this study, we demonstrate for the first time wafer-level integration of structured bio-functionalization by UV-bonding for sequencing applications. This work pushes further wafer-scale glass bonding and opens the way to cost-effective precision glass consumables for life science applications, such as high throughput sequencing, but also in vitro diagnostics and cell handling.

* IMT Masken und Teilung AG

[1] Y. Temiz, R.D. Lovchik, G.V. Kaigala, E. Delamarche, "Lab-on-a-Chip Devices: How to Close and Plug the Lab?", *Microelectronic Engineering*, 132, 156-175, 2015.

[2] F. Crevoisier, F. Heitger, H. Siegrist, H. Chai-Gao, "Apparatus and Platform for Multiplex Analysis", EP2397224A1, 2011.

Automated and High Throughput Tissue Engineering

V. Revol, G. Weder

The engineering of tissue substitutes and their application for *in vitro* drug testing and on human patients has become a reality. However, pharmaceutical industry and medical doctors are still struggling with problems of scalability for high throughput screening and lack of standardization for human implantation. CSEM is developing microsystems, automated tools and physiological environments for standardized tissue engineering.

Tissue engineering names the use of a combination of cells, engineering materials and suitable biochemical and physico-chemical factors to produce artificial tissues mimicking or replacing biological functions. With impressive progress in the last 5 years, tissue engineering has the potential to become a standard tool for drug discovery to assess the safety and/or efficacy of new compounds. Functional engineered 3D tissues have been proven to have a better predictive power compared to 2D cell culture or even animal models. Beyond drug discovery applications, tissue engineering holds promise to be used in regenerative medicine to replace organs (e.g., skins, retina, liver...) made of patient cells with re-implantation. While remarkable progress has been realized in laboratory condition, this breakthrough technology has difficulties to reach the market due to the complexity of the manual processes involved.

Current obstacles for tissue engineering are tackled by combining autonomous self-assembly of cells in functional tissues and biomimicry to provide physiological conditions. Automated cell handling, sorting and seeding as well as microscale technologies such as bioprinting, microfluidics and micro-environments represent the technological bricks to build complex systems for *in vitro* testing or standardized tissue engineering platforms for implantation. CSEM supports biotech companies to transfer manual laboratory process to a scalable and automated manufacturing process. Two project examples are the development of multi-materials bio-printing and a skin-tissue producing machine

In vitro testing

RegenHU based in Villaz-St-Pierre is the market leader in bioprinting instruments with hundreds of users worldwide (Figure 1). Bio-printing is the method of choice to engineer complex 3D-structured tissues. By adding biological materials, layer after layer, a 3D arrangement of cells can be obtained. This initial positioning is essential to create the microenvironment in which the cells will migrate and differentiate to create the tissue. Recent examples of the use of this technology are the fabrication of skeletal muscle tissue^[1] or even of a complete miniature heart^[2]. CSEM supports its partner regenHU with its expertise in liquid handling and microfluidics to improve the ease-of-use of the technology while increasing the functionalities to create more complex tissue structures.

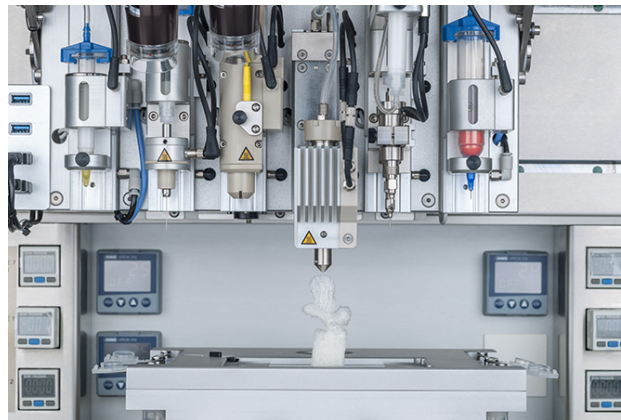


Figure 1: 3D discovery bioprinting platform from regenHU.

Artificial skin

The biotech start-up CUTISS has developed denovoSkin™ – a bio-engineered personalized, permanent skin graft. A small biopsy of healthy skin is harvested from the patient. The biopsy is processed to isolate epidermal and dermal cells. The cells are expanded *in vitro*, and thereafter used in combination with a hydrogel to create a dermo-epidermal skin graft. denovoSkin™ is now ready to be transplanted on the patient's wounds (Figure 2). Together with Cutiss, CSEM is now developing a cutting-edge technology that will enable to automate the production of the skin graft – thus decreasing costs, ensuring robustness and scaling up the process. Two main challenges are addressed. First, a disposable carrier is being developed, where the complete skin bio-engineering process is performed while ensuring sterility. Secondly, scaling up for the production of up to 100 skin grafts per patient in parallel requiring novel liquid handling processes that are investigated in the project.

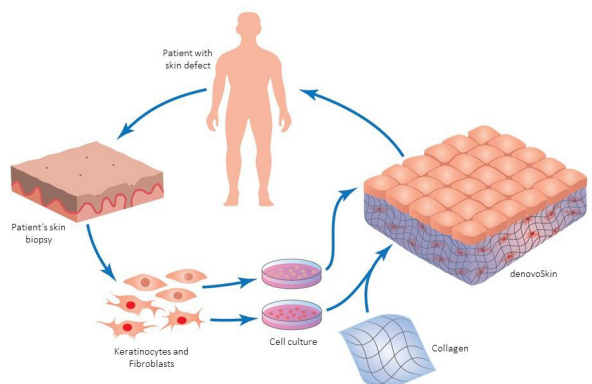


Figure 2: DenovoSkin™ engineering process from autologous skin graft.

^[1] J. Goldowsky, V. Revol, Automated force measurement system for 3D printed muscle tissues, CSEM Scientific and Technical Report (2019) 18.

^[2] N. Noor, et al., 3D Printing of Personalized Thick and Perfusionable Cardiac Patches and Hearts, Advanced Science, Vol. 6 (11), 1900344 (2019).

Automated Force Measurement System for 3D Printed Muscle Tissues

J. Goldowsky, V. Revol

Despite a huge medical need for treatments of degenerative muscle diseases in our aging societies, there are today no approved pharmaceutical therapies. Key for successful drug development are biologically relevant predictive tissue models. Recent progresses in bio-printing allow today to bio-engineer functional human 3D skeletal muscle tissue models in a 24-well plate^[1]. However, there is no solution on the market for combined electrical stimulation and force readout for efficiently allowing to use such muscle tissue models in drug screening and analyze the effects of compounds on muscle maturation, calcium signaling and contractility. The developed approach uses flexible posts which are displaced when the muscle tissues contracts. Each of the 24 wells of a well-plate can be located below the measurement optics while being stimulated by the integrated electronic pulse stimulation generator and kept at stable environmental conditions with the help of a stage top incubator. By integration of these key features the system allows the automatic screening of novel compounds to eventually address musculoskeletal diseases.

The growing worldwide demand for high throughput solutions for quantitative evaluation of the effects of novel compounds onto skeletal muscle tissues is not addressed by the current market offer. Especially there is no automated solution on the market for combined electrical stimulation and force readout that allows the efficient use of 3D printed muscle tissue models in drug screening.

Based on this market need, Life Imaging Services (LIS), Novartis, Weidmann Medical Technology, ZHAW and CSEM started a collaboration to develop a system capable of measuring the forces created by 3D printed muscle tissues. To be able to readout forces created by the muscle tissues, a specialized insert with two posts is placed in the wells of a well-plate. The muscle tissue is printed around the posts and differentiated over a period of approximately 10 days.

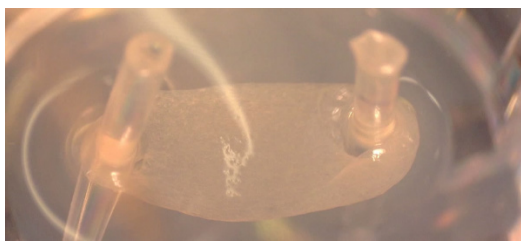


Figure 1: Picture of the muscle tissues printed around two posts.

Once the muscle tissue is fully developed it can be stimulated by the systems integrated electrical stimulation generator. By contracting the muscle bends the flexible post of the insert. The movement of the post is related to the force the muscle tissue applies on the post.

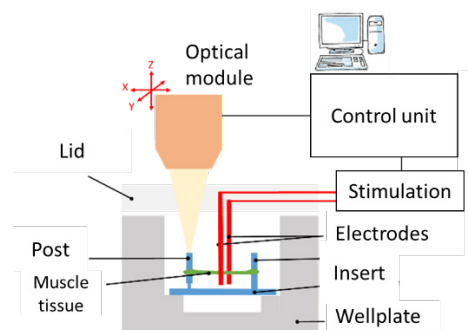


Figure 2: Schematic representation of automated force measurement system based on well-plate inserts that translates the muscles force into post displacement.

An image processing algorithm performs the GPU based image calculations in real-time for framerates up to 70 fps, to give the operator an instant feedback about the muscle's performance. The system is able to detect movements of the post as small as 1 µm.

The integrated stage top incubator (STI) developed by LIS enables the control of temperature, moisture and CO₂ concentration, in order to keep the muscle tissue viable during longer experimental procedures. Additionally, the entire system setup is temperature controlled due to the presence of an outer casing thus avoiding fogging of the STIs transparent lid which would render the optical displacement measurement unusable.

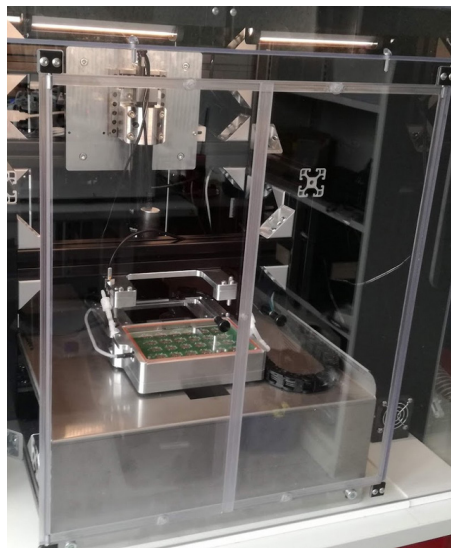


Figure 3: Automated force measurement system for 3D printed muscle tissues developed by the partners of the ongoing InnoSuisse project.

The integrated electronic pulse stimulator has been developed within the frame of the ongoing InnoSuisse project as commercially available pulse generators are bulky and do not offer the required flexibility to drive each of the well-plates 24 channels with an independent pulse profile.

The integration of the electronic pulse stimulation generator, stage top incubator, XY-positioning system, a temperature-controlled measurement chamber, measurement optics and processing algorithms into a complete and automated measurement system render the systematic screening of novel compounds possible.

[1] S. Laternser, H. Keller, O. Leupin, et al., A Novel Microplate 3D Bioprinting Platform for the Engineering of Muscle and Tendon

Tissues. SLAS Technol Transl Life Sci Innov. 2018;23(6):599-613.
doi:10.1177/2472630318776594.

Cotton-based Biosensors—Non-invasive Biomonitoring for Personalized Nutrition

D. Migliorelli, Y. Tang, H. Chai-Gao, K. Petropoulos, F. Kurth, S. Generelli

Personalized nutrition is a future tool for large scale health management. Tools to define personal dietary needs have to be simple of use and robust. CSEM is working in this direction exploring new materials for optimized sensing solutions. Cotton-based screen printed electrodes (SPE) and nanocellulose (NC) based hydrogels as functional layers are given as examples.

Personalized optimization of nutrition is one of the pathways medicine is taking to maintain an optimal health management and prevent diseases in the large population. To be implemented to its best, this approach will need some feedback loop: a simple, robust system for the identification of individual dietary needs. Urine and saliva biomarkers monitoring is foreseen as one of the potential tools to help the correct health management at home or at a medical doctor's cabinet. In this framework, CSEM has been working for years in the development of novel point-of-care technologies. In recent years, innovations in substrate material and design for printed sensors fabrication have been in focus. Cotton and cotton-derived materials have been selected as ideal candidates, because of the versatile nature of the materials, as well as low cost, wide availability and renewable sourcing. Cotton's high porosity makes this material very effective to adsorb liquids, and this feature can be useful in liquid transport but as well as a filter. Cotton being 99% cellulose based can be easily functionalized to achieve a chemical composition for an optimized, tailored sample manipulation.

For example, non-woven cotton tissues have been used as substrate for sensor fabrication (H2020 project grant agreement 761145 - MANU-SQUARE). Briefly a hydrophobic wax barrier was printed on the cotton surface to make it impermeable and then electrodes printed by using screen printing technology (Figure 1). Subsequently the electrodes have been modified to achieve pH sensitivity. A comparative characterization of standard polyester based pH sensors and cotton-printed pH sensors. The sensors were characterized by using cyclic voltammetry (CV) and electrochemical impedance spectroscopy (EIS) as electrochemical techniques. Even though the unmodified SPEs show a better performance, in terms of electrons transfer and charge transfer resistance when polyester has been used as substrate, nevertheless once they are modified with pH sensitive material (Figure 2) the performance of both is comparable.

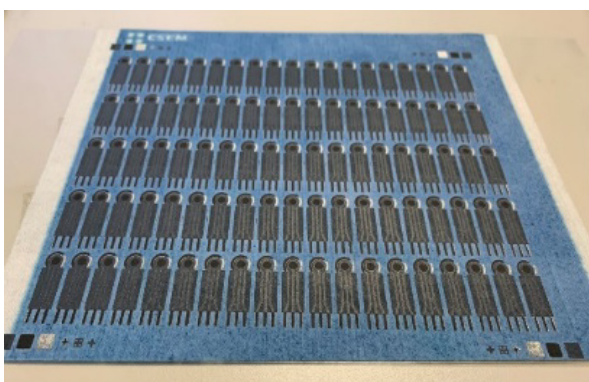


Figure 1: pH sensors printed on a cotton substrate.

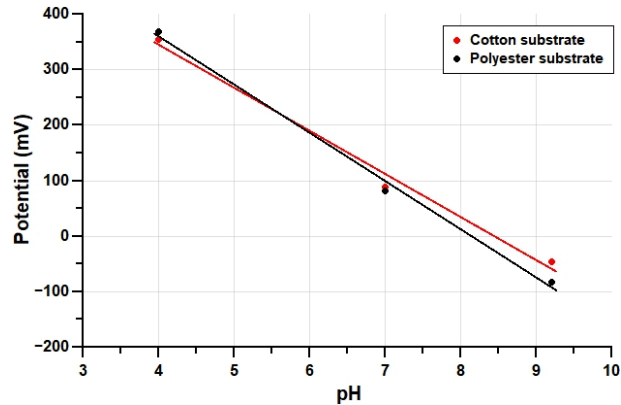


Figure 2: Response at 3 different pH (4.01-7.00-9.18) made by using pH sensors printed both on cotton and polyester.

Nanocellulose, a derivative of cotton, is another interesting material whose properties of porosity, microstructure, surface energy can be tailored to optimize for example the anchoring and transportation of biomolecules (*i.e.*, antibodies, enzymes). Its peculiar characteristics can be summarized in:

- Excellent mechanical properties
- Good biocompatibility
- Tailorable surface chemistry
- Tailorable optical properties

Commercial cellulose nanofibrils have been chemically and mechanically treated in order to produce scaffolds (see Figure 3) for optimized liquid transport and sensitivity in the biosensor's domain.

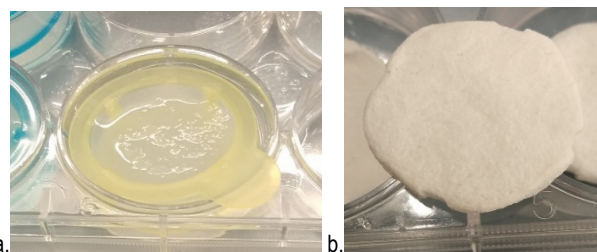


Figure 3: (a) Mixing of the nanofibrils and reagents for cross-linking; (b) Finished nanocellulose scaffold.

The synergic effect of the cotton-based substrate to be used as a material for the SPE fabrication together with the application of NC hydrogels able to capture and transport specific biomolecules will be applied in the development of improved, simple and quantifying sensing solutions for the use out of the analytical laboratory.

FoodSmartphone—On-site Biosensor for Pesticides Detection in the Area of Food Safety

D. Migliorelli, K. Kopper*, L. Mühlbach, R. Galvea*, P. Marco*, S. Generelli

Pesticides are primarily used in the agricultural sector but also in forestry, horticulture, amenity areas and in-home gardens. The widespread and intensive use of pesticides induces negative cascading effects on ecosystems. Herein we report on the fabrication and characterization of an electrochemical sensor for detection of different pesticides in food samples on a smartphone.

Herbicides are the most common type of pesticide found in streams and ground water within agricultural areas. The most common herbicides in agricultural streams were atrazine which was found in about two-thirds of all samples from agricultural streams. Consumer concerns on food safety and society awareness of chemical contaminants, in the environment have increased in the past few years. As a consequence, more restrictions in the use of chemical products have been imposed at national and international levels.

Electrochemistry (EC) could potentially be a good addition to the standard method for quality control. Potentiostats nowadays are small portable devices furthermore relatively cheap. Moreover, if carbon screen printed electrodes (SPE) are used as transducer the cost per analyses can be drastically reduced making them the perfect candidates for on-site analysis.

CSEM in collaboration with CSIC^[1] has characterized and developed a carbon black (CB) based biosensor for the detection of atrazine in the area of food safety. The nanomaterial CB is highly attractive for this application since it has been reported to have comparable or even better performance than graphene-oxide and carbon nanotubes, in terms of electron transfer constant, redox reversibility and background currents^[2]. CB is also quite inexpensive (~1 €/kg for CB versus ~100-1000 €/kg for graphene^[3] depending on the quality and ~1000 €/g for CNT^[4]).

SPE modification with CB has been done both by drop-casting directly onto the working electrode (WE) and by mixing CB into the printing ink. All the electrochemical characterization tests have been done by using cyclic voltammetry (CV) and electrochemical impedance spectroscopy (EIS). The first technique (CV) was used to evaluate the sensors in terms of electron transfer and current signal; the second one (EIS) in order to evaluate the charge transfer resistance at the WE surface.

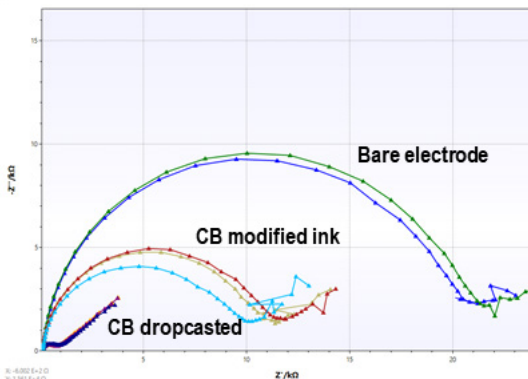


Figure 1: Nyquist plots of the EIS analysis of the different SPEs using 1 mM $[\text{Fe}(\text{CN})_6]^{3-/4-}$ in 0.1 M KCl solution as redox probe.

After the electrochemical characterization, the drop-casted electrode, which showed the best electrochemical characteristics was selected and used as the transducer for an atrazine assay using magnetic beads as a platform for the immunoassay (ELIME format, see for example^[5]). The electrochemical response curve towards atrazine seen in Figure 2 was recorded using chronoamperometry as detection technique.

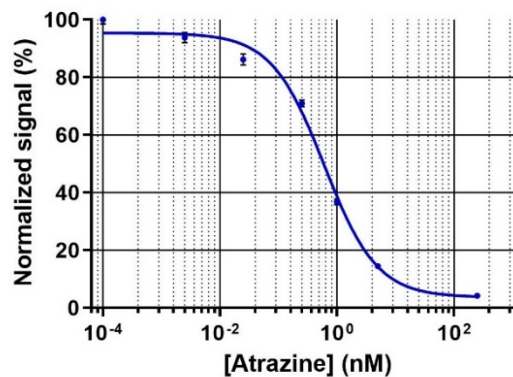


Figure 2: Calibration curve for atrazine.

Figure 2 shows that the achieved IC₅₀ (0.83 nM) fulfils the requirements of the EU regulations (maximum residue level (MRL) for Atrazine in cereals is 0.05 mg/kg), which is important from the view of the real sample analysis.

* Nanobiotechnology for Diagnostics research group (Nb4D). IQAC- CSIC, 08034 Barcelona, Spain

^[1] This project has received funding from the European Union's Horizon 2020 research and innovation programme under the Marie Skłodowska-Curie grant agreement No 720325.

^[2] R Cinti, et al., *Electroanalysis* 27: 2230-2238; 2015.

^[3] R. Ciriminna, et al., *Chem Commun* 51:7090–7095, 2015.

^[4] R. Smajda, et al., *Phys status solidi c* 7:1236–1240, 2010.

^[5] D. Romanazzo, et al., *Biosens Bioelectron.*; 25(12):2615-21 25: 2615–2621, 2010.

ACEnano—Hydrophobicity, Solubility and Reactivity Monitoring of Nanomaterials

D. Schmid, L. Burr, P. Cristofolini, F. Kurth, G. Orawez, S. Cattaneo

Engineered nanomaterials are being produced in exponentially increasing quantities, due to their unique physical and chemical properties and the improved performance of final products, and therefore spur technological and economic progress. A comprehensive risk assessment of these new materials is crucial to create new adequate regulations. In the frame of the European ACEnano project, CSEM is developing innovative techniques for the characterization of nanoparticles. In particular, CSEM focuses on three key properties of nanomaterials, namely their surface hydrophobicity, solubility and reactivity.

The European project ACEnano is improving nanomaterial risk assessment by developing a widely implementable and robust tiered approach to nanomaterials physicochemical characterization, which will simplify and facilitate contextual (hazard or exposure) description and its transcription into a reliable nanomaterial grouping framework [1]. Among the key properties of nanomaterials are surface hydrophobicity, particle solubility and particle reactivity, for which there is a substantial lack of techniques for reproducible assessment.

Within the frame of ACEnano, the rose Bengal assay, and more generally, the dye partitioning method (the main technique for nanomaterial (NM) surface hydrophobicity assessment) has been tested for automation using a field-flow fractionation (FFF) system. The technique was chosen for its potential to combine partitioning coefficient assessment and size distribution measurement to refine the hydrophobicity of the NMs as a function of their size.

We demonstrated that this method is limited by the nature of the hydrophobic interaction, which is a weak and reversible affinity binding and leads to dye losses by contact with the FFF membrane. Therefore, the FFF-dye partitioning assessment method is not suitable for hydrophobicity assessment. However, this study raised several useful key points to consider for the dye partitioning method for surface hydrophobicity measurement such as the influence of the dye on the NM stability, the impact of the NM on the dye (e.g., chemical degradation) and the general strong influence of the pH on the results.

CSEM investigated two alternative approaches, based respectively on hydrophobic interaction chromatography (HIC) with elution investigation in hydrophobic columns and on 2D surface analysis with CSEM's waveguide interrogated optical sensor (WIOS) instrument^[2]. These approaches showed very promising results that will be published in a peer-reviewed journal.

For both NM solubility assessment and reactivity monitoring, CSEM developed a simple and low-cost automated mixing and colorimetric measurement system for 24 parallel assays, based on a SLAS/ANSI standard-sized disposable custom-designed microfluidic chip (well plate) as well as a standalone unit for pneumatic actuation and readout, into which the chip is placed. Nanomaterials in solution and solvents/reactants of interest can be pipetted manually or by robot into the well plate, where they are automatically and rapidly mixed 1:1 (<0.4 s) and incubated in-plate.

For solubility assessment, NMs are mixed in the system with a solvent and then the chip is placed on a plate shaker, from where an auto-sampler feeds the mixtures into an external inductively coupled plasma mass spectrometer (ICP-MS) for analysis of concentration and particle size distribution (in single particle operation mode), as depicted in Figure 1.

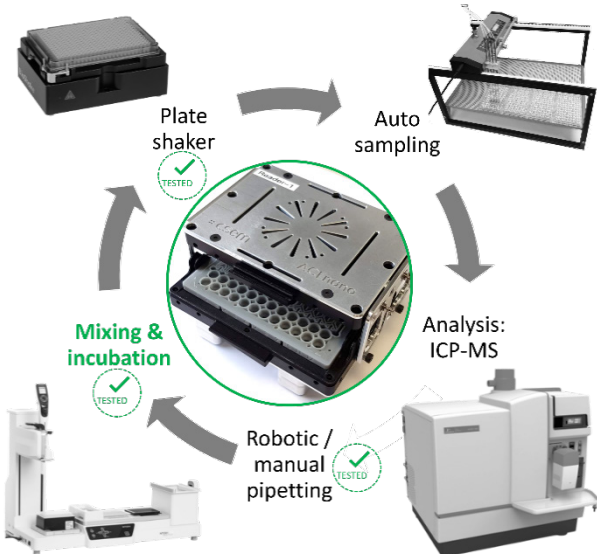


Figure 1: CSEM's automated sample preparation system (microfluidic chip inside the control unit) at the core of a new nanomaterial solubility assessment.

For reactivity monitoring, the control unit's 24 optical readout channels were used, compatible with a colorimetric assay for determining catalytic reactivity developed by Wageningen Food Safety Research (former RIKILT)^[3]. For this assay, the control unit mixes and incubates the nanomaterials in the chip with a dye and reducing agent, and also determines the reactivity colorimetrically.

Both, the microfluidic chip and control and readout unit are currently being characterized at CSEM, while the ICP-MS solubility analysis method is being further developed by our consortium partners.

The ACEnano project is a collaboration between 28 European, Chinese and Korean consortium partners (www.acenano-project.eu) and received funding from the European Union's Horizon 2020 research and innovation program under grant agreement No. 720952. CSEM thanks them for their support.

[1] www.acenano-project.eu

[2] J. Adrian, S. Boder-Pasche, J. Diserens, S. Sánchez-Baeza, H. Gao, M. Marco, G. Voirin, "Waveguide interrogated optical immunosensor (WIOS) for detection of sulfonamide antibiotics in milk, Biosens. Bioelectron. 2009, 24, 3340-3346.

[3] C. Corredor, M. Borysiak, J. Wolfer, P. Westerhoff, J. Posner, "Colorimetric detection of catalytic reactivity of nanoparticles in complex matrices", Environ. Sci. Technol. 2015, 49, 3611-3618.

An Ultra-thin, Printed Pressure Sensor for Ventilation Monitoring

N. Glaser, F. Zanella, J. Disser, F. Geister, T. Erb •

A thin, printed pressure sensor is manufactured on a polymeric film and mounted on a tubus for tracheal ventilation monitoring. The prototype developed with the University Children Hospital Basel showcases the potential of a sensor-equipped tube towards lung controlled ventilation to prevent ventilation induced lung damages.

In current ventilation settings, the overpressure for the air volume to be pushed into the lungs is estimated at the respiration machine. Especially for patients with damaged lungs or fragile patients like children, care must be taken to avoid severe damage of the lungs. An actual pressure measurement close to the lung could substantially improve the situation as it would allow for a gentler and more natural intubation. The sensor-equipped tubus will allow for an airway pressure measurement directly in the trachea. Such a system would be a paradigm shift from machine triggered to an actual lung triggered respiration support. A sensor that detects the remaining spontaneous breathing capacity, e.g., of stationary patients, would sustain and gently support natural breathing.



Figure 1: A printed pressure sensor for ventilation monitoring close to the lung 1 behind the balloon of the intubation tube.

Here we report the prototype of an ultra-thin, <0.2 mm thick, printed pressure sensor. Electrodes are screenprinted and micro-structured with an elastic dielectric to fabricate a very sensitive, capacitive pressure sensor consisting of a sandwich of two thin foils (Figure 2, patent pending.)

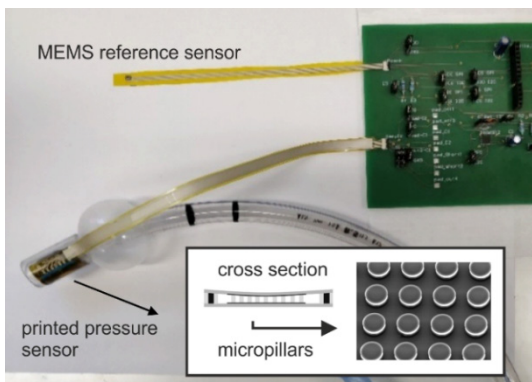


Figure 2: The prototype setup. A reference sensor and the printed sensor are mounted on an intubation tube and then put into a lung model to record different respiration cycles.

A thin layer of PDMS is casted onto the screen-printed electrodes and subsequently imprinted to form micro-domes that deflect under small pressure. A second, thin elastic foil is glued on top to encapsulate the sensing chamber for relative pressure measurements. The long leads to the two electrodes are protected with a printed shielding layer.

The printed sensor is fabricated only with high-throughput compatible technologies, in volume production the costs may range in the single-digit Swiss francs range for this smart add-on.

Even the smallest available off-the-shelf MEMS sensors are too thick to be integrated into a smaller intubation tube as illustrated in Figure 3.

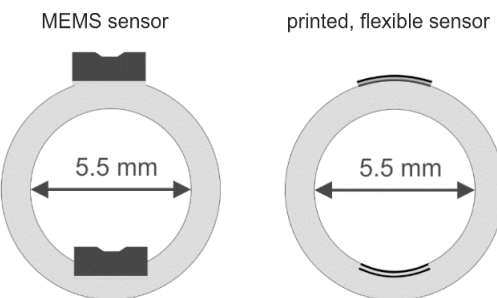


Figure 3: Cross section of a tube. Integration advantage of a thin, flexible sensor printed on polymer film.

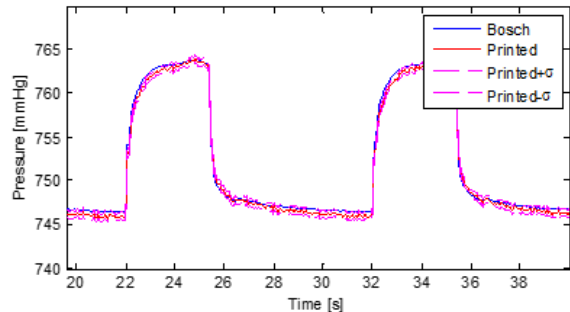


Figure 4: An example of the recorded respiration cycles. Here 1-sigma (deviation) of the pressure sensor is 0.42 mmHg. Recorded at UKBB.

The thin sensor film was successfully integrated on the tip of an endotracheal tubus. Such a sensor may be mounted on the inside or outside of small tubes. We realized a small PCB with a fast-capacitive readout to interface our newly developed sensor. The capacitive signal amplitudes in the range of 0.5 to 2 pF were recorded at a minimum 40 Hz to accurately display respiration cycles as seen in Figure 4. In parallel, the PCB recorded the signal from a Bosch reference pressure sensor which was placed inside the lung model as well. An artificial lung model was used with a plastic tube that modelled the trachea with an inserted sensor-equipped endotracheal tubus. All respiratory cycles could be perfectly recorded with the printed sensor. The amplitude, of the sensor is stable over the full measurement period of 10h.

Characteristic	Results
Dynamic range	-50 to 150 mmHg
Acquisition speed	21-61 Hz
Sensitivity	15-30 fF/mmHg
Resolution	0.4-0.9 mmHg
Footprint	12 x 18 mm
Drift	1.2 mmHg/8h
Amplitude stability	<0.1 fF/mmHg/8h

Supported by Innosuisse grant 27100.1 PFLS-LS.

• UKBB, Universitäts-Kinderspital beider Basel

Printed Pressure Sensors: Industrial Case Studies

N. Marjanovic, J. Disser, F. Zanella, N. Glaser, P. Duchamp*, A. Wallbaum*, V. Callegari**

Recently large-scale printed pressure / force sensors are intriguing electronics community because of their unmet properties, i.e., flexibility, tunability, large area, cost-effective fabrication and high integration potential. CSEM deals with printing technologies for more than a decade mastering printing materials and substrates, devices and systems and its functionalities. Here we are presenting two printed pressure / force sensor prototypes showing their functional tunability and high system integration potential in robotic and smart shelf applications. The prototypes are realized in collaboration between CSEM and F&P Robotic AG and Turck duotec SA, respectively. Both cases demonstrate the advantages of an innovative hybrid system integration approach – integration of large area printed components and standard electronics. Thus, a new developed systems contains best of both worlds, i.e., (conventional) high-density SMD electronics and (emerging) large area printed electronics.

Recently printed pressure / force sensors rise significant interest among the electronics community because of its high flexibility and high system integration potential. In a nutshell, CSEM's screen printed pressure sensors consists of two flexible polymer foils; one with interdigitated electrodes and the other one with patterned resistive paste. After fine layer thickness tuning, though thickness/resistance adjusting, foils are assembled. The interface with the external electronics is provided through the connectors suitable for overmolding. This way, hybrid integration between printed and conventional electronics is established.

Robots have been working in the industrial production for decades, however they have been doing this in an isolated environment i.e., with no humans around. In recent years, the field of collaborative robotics has gained a lot of attention and robots started working alongside their human co-workers. This change demands the robots to be aware of their surroundings in a much more comprehensive way. The Swiss SME F&P Robotics AG has been aware of this challenge in their customers' industry and is producing service robots and technology assisting, helping and facilitating activities from people's daily lives. Through the integration of flexible pressure sensors into the robotic fingers, F&P Robotics AG strives to improve its products further.



Figure 1: Pressure sensors for robotic grippers (F&P Robotic case).

The realized fingers shown in Figure 1 consists of 20 pressure sensor pixels which are printed on a flexible and stretchable foil. CSEM conducted the design of the sensors, their fabrication by screen printing and their characterization. The resulting pressure sensor is thin (below 400 µm thickness), flexible, easy to customize and has a sufficiently large active area in order to provide pressure mapping information (i.e., position of the pressure stimulus) over the contact surface of the robot finger. The sensor is molded on the 3D printed "bone" and is interfaced with the robot electronic hardware. In this configuration the sensor is sensitive to forces between 0.1 N and 10 N. The novel technology will allow F&P Robotics AG to become a game changer in this industry by providing robots equipped with cost-effective and large area printed pressure sensors which add sensing functionalities, manipulating and correction capabilities.

* F&P Robotics AG, Switzerland

These demonstrators will open new market opportunities for the collaborative robot from F&P Robotics AG, especially in the human environment and food handling segments.

On the other hand, multifunctional smart shelves are envisioned to be effective solution used in various domains, e.g., in shops where they can easily serve as indicators for products missing. Less pressure indicates that the product is removed or half empty – so called "out-of-the-shelf case", another application case is "track-and-trace", where the missing item triggers a warning alarm, if not returned on the original place after a certain time.

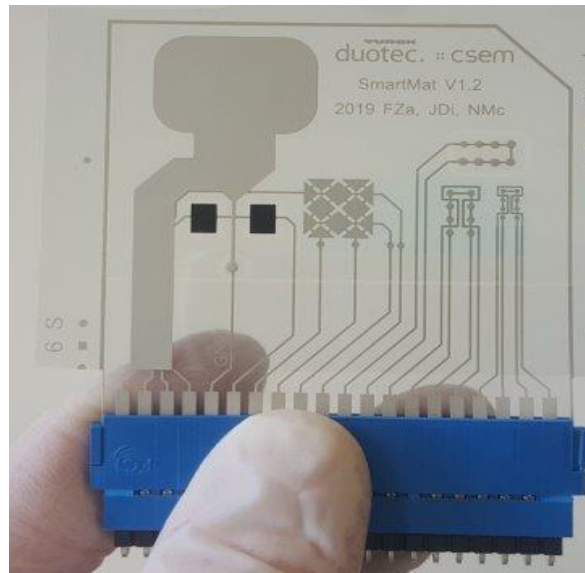


Figure 2: Pressure sensors (test features) for smart shelves (Turck duotec case).

In Figure 2, printed test features contain printed pressure / force sensors, touch sensors and process integration test features (from left to right). The test features are further processed by Turck duotec SA to integrate the standard electronics interface and overmold the electronics including parts of the sensor foil. The full system is characterized electronically before and after environmental stress tests.

The shown cases demonstrated:

- Printed sensors tunability, from high to low/medium sensitivity, and
- High integration potential

CSEM and its partners are pursuing this integration approach, to offer new innovative products to the market.

This work was partly funded by Innosuisse (Project No. 30156.1 IP-ICT). CSEM thanks them for their support.

** Turck duotec SA, Switzerland

PHOTOVOLTAICS & ENERGY MANAGEMENT

Christophe Ballif

The world seemed to wake up in 2019 with respect to climate change and biodiversity issues. Without doubt, the young people and students marching in the streets created an enhanced awareness and raised the attention of the media to an unprecedented level. With a single and simple slogan: "Please just listen to science".

Rightly so: A new IPCC report was released, with even more alarming warnings and confirming the need to act quickly. In the latest advanced simulations from leading French groups,^[1] scientists show that global warming could lead to an average global temperature rise of up to 7°C by the end of the century if we pursue a business-as-usual approach. This is around 2°C higher than the figure from the 2014 IPCC report. Beyond ravaging a large part of the world ecosystem, driving the migration of hundreds of millions of people, it will also have a direct impact in Switzerland, including natural catastrophes, water scarcity, biodiversity reduction, and heavy changes to agriculture. With stronger warming in Switzerland, many houses in Swiss cities will no longer be inhabitable without transformation, as—for example, temperatures in some cities could reach up to 45–50°C well before 2100.

Thanks, in part, to the catalytic role of the youth movement, there are still reasons to hope for a mitigation of the worst case.

- In many recent elections, climate and energy have become important for voters. This is the case, for example, for Switzerland, and has also influenced the new "European Green Deal".
- More and more cities and countries are announcing their intention to transition to a carbon neutral society by 2050 (or before), including Switzerland.
- The price and performance of PV systems, wind farms, batteries, or even hydrogen cars continue to improve. This is particularly true of photovoltaics, cheaper than a year ago, and beating by far any other electricity source, including new fossil fuel and nuclear power plants in terms of the direct cost of electricity.

To seriously address global warming, PV should become a, if not the, major contributor to electricity and energy production (including for transport, for power-to-gas transformation, and for heating).^[2] This in turn will require increasing the manufacturing of PV panels from today's around 120 GW per year to above 1 TW per year, indicating that a massive worldwide upscaling of solar energy should hence take place—by a factor at least 10—in the next decade.

What does this mean practically? Each country will have to adopt its own scenario. Switzerland (40,000 km²; 8.5 million people) is a good example. A recent study^[3] shows that the current energy system, which is based on 75 percent of energy coming from fossil fuels, could be almost entirely decarbonized by installing 50 GW of PV panels (which would cover about 320 km²). This is less than the potential electricity available from suitable roofs and facades, which is more than 67 TWh corresponding to a ~65 GW peak power potential of Swiss buildings.^[4] This massive penetration of PV should be accompanied by a full shift to electro-mobility, and to the heating of better-insulated houses,

mostly with heat pumps. Hydropower is essential to the system and electric cars would provide part of the required system flexibility. In this scenario, PV would be curtailed strongly at certain moments of the year, whereas a winter energy gap would remain. To fill it, power-to-gas (hydrogen) could be used, or imports of clean electricity, or in the last resort gas power plants, leaving—in this case—16 percent of residual CO₂ emissions, which should be sequestered or fully compensated for. Note that more and more experts tend to agree on the technical feasibility of such approaches, but much less on the way to reach the goal. A quick calculation shows, however, that in terms of imports this approach has everything to recommend it. Importing 50 GW of PV panels would cost CHF 15 billion and provide as much energy as 30 years of fossil fuel imports, whereas two years of fossil fuel import costs around CHF 15 billion.^[5]

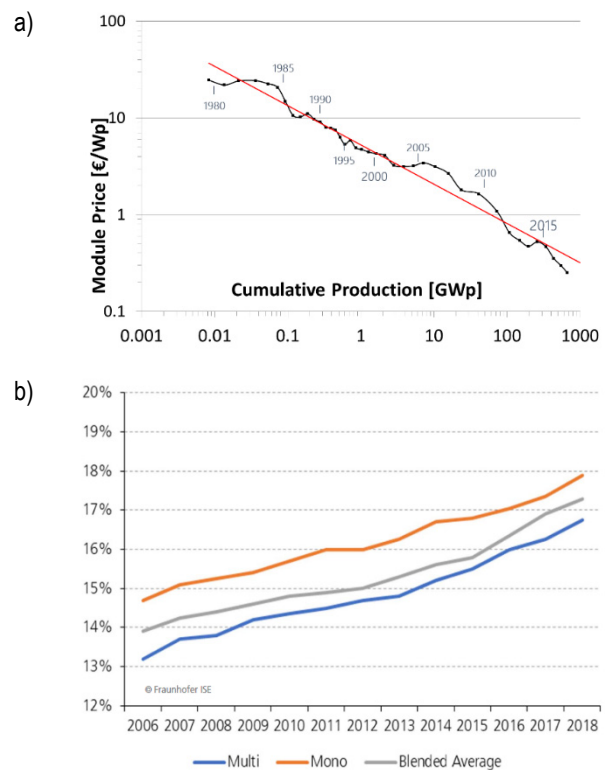


Figure 1: a) The learning curve for PV module manufacturing, showing a historical trend of 20–24% reduction in module cost with each doubling of cumulative production (some argue 24% has been occurring since 2015). b) Average module efficiencies for mono- and multicrystalline PV modules over time. (Source: Fraunhofer ISE: Photovoltaics Report, updated: March 2019).

With respect to photovoltaics, a further driving force will be given by the reduction of the levelized cost of electricity, which can be achieved most easily by module efficiency increases, and then by module cost reduction (see Figure 1b for the trend) and by increasing the modules' and components' lifetimes. Module efficiency is the key leverage, because it allows a direct reduction per watt peak of all area-related costs. Average mono c-Si module efficiency (around 18.5% in 2019) has continuously risen by around 0.35 percent per year in the last ten years (Figure 1b). Hence, to find a place in the market in 2025 at the multi-GW level a technology must typically be able to deliver more than 21 percent modules at (well) below 20 cts/W manufacturing cost.

Essentially, the further decrease in solar electricity costs will give even more financial means with which to manage solar electricity, favoring its penetration. This is even more true for Switzerland, where space constraints should also favor high-efficiency technologies for a large fraction of the installations.

Improvements in PV technology continue to open up other amazing opportunities and niche markets. These include the field of “active” building, where PV plays an architectural role (Figure 2), solar mobility, and energy scavenging for the IoT. Combined with, for example, intelligent energy management, there will be soon no reason why most surfaces should not become sources of electricity. All these topics also contribute to sensitizing people to the opportunities offered by photovoltaics. Together with the massive penetration of PV, a massive change in the way we manage and control energy flow/distribution will take place, in the surveillance and monitoring of assets. In parallel, the efficiency of all systems will need to be improved, including at the household/building or district level.

General objectives of the program

With its dense network of established companies, its start-ups, its network of universities and higher education institutions that receive public funding, and its popular vote supporting a new energy strategy, Switzerland has excellent cards at hand, as it can develop, test, and implement some of the solutions worked out in the energy field and in energy systems at a pre-market entry level. It is especially well positioned, with several high-tech companies, and many companies active in the modules field making/designing building integrated photovoltaics (BIPV), as well as with a grid and building infrastructure that allows for the testing of many advanced systems, controls, and digital solutions.

Noticeably though, Made in China 2025 and some of the trade practices of Asian countries continue to put many leading European equipment builders in a challenging position in the pure PV field. Still, Swiss equipment/solutions and know-how currently continue to play an important role. In addition, European companies continue to invest (e.g., Enel/3Sun and Ecosolifier, all investing in heterojunction technology), as do Russian companies (producing at the >300 MW heterojunction level based on Swiss technology) but at a lower volume level. There are now several initiatives at the European level to restart multi-GW production lines, considering the close to 100 GW annual requirement figure at the 2030 horizon. Noteworthy worldwide interest in silicon heterojunction is now on the map, including with a 600 MW plant ramping up at REC Singapore with Swiss/German technology. A similar trend is also developing with solar technologies based on other types of passivating contacts, which can allow an extension of the learning curve of standard PERC modules.

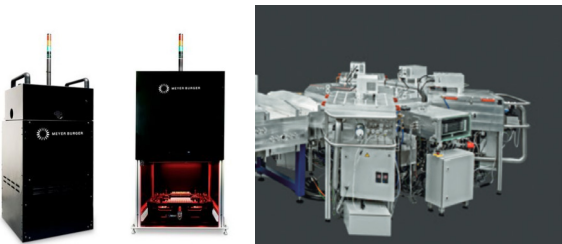
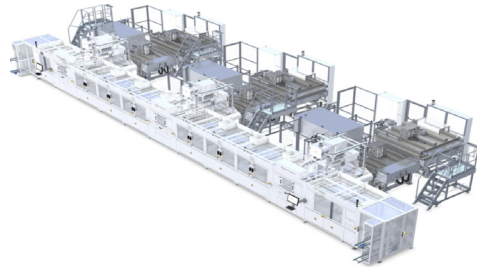


Figure 2: Some examples of products or processes where CSEM is involved with industrial equipments makers: PECVD mass production tool (top); metrology tool for solar cells (bottom left); and tool for piloting of PECVD and PV layers (bottom right).

In this context, the PV&E program at CSEM is to continue developing innovative process technologies, device concepts, and new high-tech solutions to better serve the Swiss and global renewable energy industry. More generally, the PV&E program targets the following objectives:

- To provide cutting-edge innovation in the field of photovoltaic devices, realizing the best devices with a high potential for industrialization, from advanced crystalline silicon to multi-junction solar cells.
- To design and develop highly reliable modules, for the power market, for the transportation sector, or with the highest potential for adoption by the public in the built environment.
- To support the development of next-generation equipment and metrology systems, all along the value chain of photovoltaics, creating a sustainable cleantech value for existing and future CSEM customers.
- To provide new solutions for specialized devices, coatings, or materials with higher added value, and for PV components with enhanced functionalities.
- To bring solutions to the energy/electricity management field as we transition toward a society essentially powered by renewables, in which energy efficiency and management will be realized through intelligent hardware and algorithms.

These solutions are brought to the market either by supporting companies or through the creation of start-ups. To meet these challenging objectives and to support the transition to an energy system in which solar will play an essential role, CSEM and its PV&E team collaborate particularly closely with the EPFL PV-Lab, with Swiss universities and ETH entities (EMPA, EPFL), as well as with universities of applied sciences—in particular SUPSI (accreditation, power plants) and BFH (the BFH-CSEM energy storage center). CSEM also collaborates with multiple international organizations or agencies, for example in the framework of European or bilateral projects.

The PV and Energy Management program in detail

In 2019, CSEM was able to further develop its activities related to the program PV&Energy. At the end of 2019, around 65 people (FTE) are involved in the program—an increase on the previous year. The program collaborates with, and works on mandates from, close to 40 companies along the energy value chain.

The program is summarized in Figure 3, along with its subdivisions by topic. The bottom part of the figure illustrates the technology infrastructure platforms available. These correspond to hardware facilities platforms, which are complemented by additional software/hardware in laboratories (e.g., simulation platforms for electrical grids and for plasma modelling, micro-grid hardware, IT infrastructure for AI, big data treatment...).

A particular emphasis is placed on maintaining advanced sets of infrastructure. In 2019, new tools have been installed for laser patterning of layers (sub-picosecond lasers), for glass electroerosion patterning, for soldering of solar cells, for deposition of conductive and semiconcotor layers, for inspection of circuits and solar cells, for evaporation of perovskite solar absorbers, for climate testing of battery cells.... These are in addition to the existing large infrastructure park at CSEM as well as to some of the equipement installed at EPFL in Neuchâtel.

Activities and topics	Emerging PV and thin-film devices	PV cells and modules	Energy systems
	<ul style="list-style-type: none"> Perovskite PV Thin-film devices Coatings 	<ul style="list-style-type: none"> Advanced c-Si solar cells Metalization and interconnections Polymers and reliability BIPV and mobile harvester 	<ul style="list-style-type: none"> Battery management Data-driven control Digital insights
Technology infrastructure platforms	Thin-film coatings and laserining	Cell pilot lines	Modules R&D lines
Metrology and characterization			
Data management			

Figure 3: Schematics of the activities in the PV-center and Energy management program. Top part: activities. Bottom part: technology infrastructure platforms.

A short overview of the program's various activities is provided below.

The activity *Emerging PV and Thin-Film Devices* deals with three different topics—

Perovskite PV: development of thin-film perovskites devices in view of their integration into industrial tandem solar cells combined with silicon (medium term) or with low bandgap perovskite, targeting efficiency of over 30 percent.

Thin-film devices: design and manufacture of small PV devices and sensors for the Internet of Things, with a focus on the use of thin-film silicon and on setting up all necessary integration steps (SMD-ready components).

In **coatings**, layers and concepts are developed for various applications, including i) passivating contacts for c-Si solar cells, ii) layers for packaging, or iii) power electronic devices.

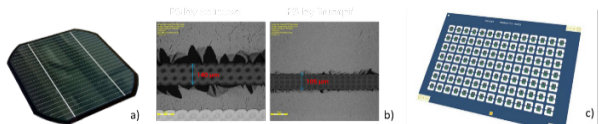


Figure 4: Examples of the activity Emerging PV and Thin-Film Devices. a) Screen-printed Pk/Si cells with 24.3% efficiency on full 4 inch wafer. b) Improvement of laser scribing processes to pattern thin-film PK solar modules. c) SMD (surface mount device) of small thin-film silicon solar cells.

The *PV Cells and Modules* activity deals with the following topics—

Advanced c-Si solar cells: technologies for c-Si high cell efficiency (>24–25%) and maximum module outdoor performance (kWh/kW) at controlled cost and CAPEX.

Metallization: cell interconnection materials and schemes with increased reliability and reduced PV electricity costs (e.g., improved multi-wire technology, a simplified contacting solution for back-contact cells).

In **Customized packaging**, compounding and extrusion of specialty polymers and thick coating techniques are developed for various applications that allow, for example, reduced degradation, or lighter PV, or simplified coloration techniques for PV elements.

Finally, the **Dedicated PV elements** topic includes the realization and prototyping of modules for building integration, mobility, space application, and c-Si based energy harvesting solutions.

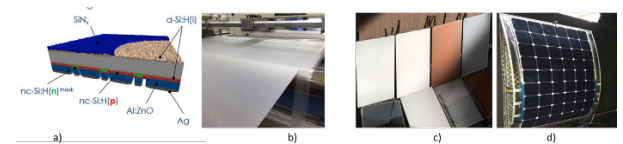


Figure 4: Examples of the activity PV Cells and Modules: a) >25% back-contacted solar cells in only 8 process steps realized by CSEM. b) Extrusion of special low-temperature encapsulation foil. c) Use of various colorization techniques for building-integrated modules (BIPV). d) New generation solar modules for high-altitude space application with reduced air drag and increased reliability, including special extruded foils for heavy thermal cycling.

In the *Energy Systems* activity the main topics are as follows—

Digital insights: new tools based on AI and big data to generate actionable information throughout the energy value chain, in particular for the operation and maintenance of production assets (wind turbines, PV systems) and distribution assets, and for market operations with distributed generation (high-resolution forecasting of PV production).

Data-driven control is used, for instance, to make buildings and grids more energy efficient and more flexible.

In the **Battery management** topic, based on measurements and advanced modeling, we focus on optimizing the way batteries are designed, monitored, and operated in renewable energy systems.

Typical results include robust, data-driven PV generation forecasting algorithms, neural networks as alternatives for the model-predictive control of buildings' energy management, peak shaving and self-consumption increase with a patent-pending microgrid control, and advanced battery testing to improve the

estimation of battery degradation taking multiple parameters into account.

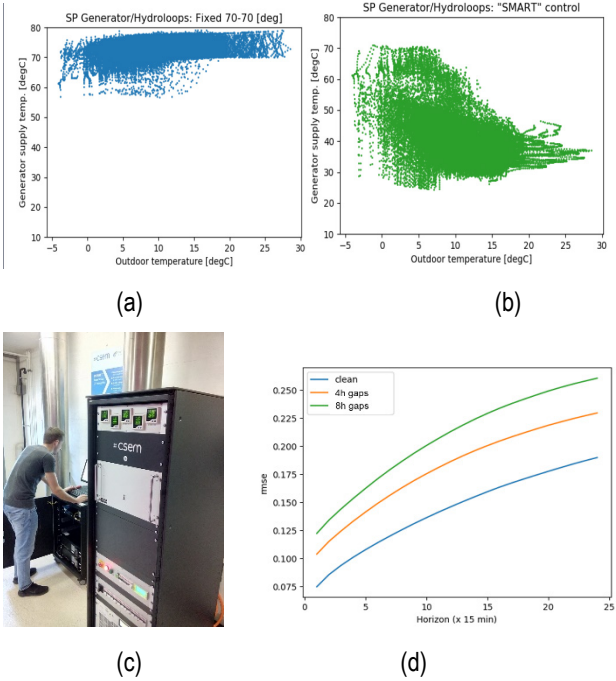


Figure 5: Examples of the activity Energy systems: (a) and (b) new smart control for heating valve regulation coupled to heat pumps allowing up to 40% energy reduction thanks to lower heating temperatures. (c) Hardware for the DC-smart project, where patent-pending control architecture enables ramp-rate control, increase in self-consumption of locally produced PV electricity, and peak shaving (d) Performance of CSEM's data-driven PV forecasting algorithms between 0 and 6h, showing robustness against faulty or missing data.

[1] <https://climeri-france.fr/>.

[2] Baseload electricity and hydrogen supply based on hybrid PV-wind power plants, Fasihi, Mahdi, Breyer, Christian, Journal of Cleaner Production, 243 (2020) 118466.

[3] Nordman, R., Sonne für den Klimaschutz – Ein Solarplan für die Schweiz, Zytglogge Verlag, 2019.

[4] www.admin.ch/gov/fr/accueil/documentation/communiques.msg-id-74641.html

[5] A more detailed calculation is available on request from the program's manager, including other components or even residual natural gas imports.

Progress towards High-efficiency Perovskite/Silicon Tandem Devices

A. Walter, S. J. Moon, B. Kamino, A. Paracchino, J. Diaz Leon, S. Nicolay

In the framework of the European Horizon 2020 project CHEOPS (low Cost and Highly Efficient phOtoVoltaic Perovskite Solar cells) and the Swiss SNF BRIDGE Program, CSEM has been working towards the realization of high-efficiency perovskite/silicon tandem cells, with a focus on the use of inorganic hole and electron collection layers. With devices exceeding 25%, and most processes compatible with production technologies, CSEM places itself at the forefront of research in that promising and highly competitive development area.

On top of the promise of high efficiency (as high as 23.7% for single junction devices^[1]) at reduced costs, perovskite-based devices have gained a lot of traction to be used in a multi-junction configuration. There, the high-bandgap perovskite (PK) absorber is stacked on top of a lower bandgap absorber (e.g., c-Si, CIGS or a low bandgap PK). By minimizing photo-generated carrier thermalization losses, multi-junction devices allow to overcome the theoretical Auger efficiency limit of single junction Si-based devices. This is of particular interest in an industrial landscape where c-Si PV manufacturers are beginning to look towards future technologies to continue to push their efficiencies even higher and to further lower system costs. CHEOPS and the BRIDGE Power project aims at tackling the difficult task of developing 2-terminal PK/Si tandem cells approaching the symbolic limit of 30% efficiency.

To that end, CSEM developed the different building blocks required for efficient tandem devices. In a first part, CSEM was charged with optimizing the single junction PK solar cells, as well as upscaling its deposition and processing to large area minimodules with record efficiencies^[2]. This included the development of charge transport layers (CTLs) by industry relevant techniques. Specifically, CSEM designed NiOx layers by low-temperature sputtering deposition as a hole transport material, as well as low-temperature ALD SnO₂ as an electron transport layer. The latter can be deposited without damaging the underlying sensitive PK and makes it possible to sputter the front TCO without suffering from sputter damage. Moreover, this achieved the desired goal of having fully inorganic CTLs, which is a condition for an improved thermal and air stability of the device.

Implementing these developments on a silicon heterojunction bottom cell with a polished front led to a best result of 24% using a standard ITO front contact. In addition, CSEM developed a more transparent conductive contact by low-power sputtering. This let more light pass into the bottom cell, allowing for higher current. Moreover, the low-power sputtering limits the sputter damage, leading to higher Voc. All in all, an efficiency of 25.4% (Figure 1) was achieved, surpassing the highest published PK/Si tandem efficiency to date. It is noteworthy that said published efficiency is also the result of a collaboration between EPFL-

PVlab and CSEM that led to the highest published and certified efficiency (25.2%) using a textured Si subcell for improved optical properties^[3].

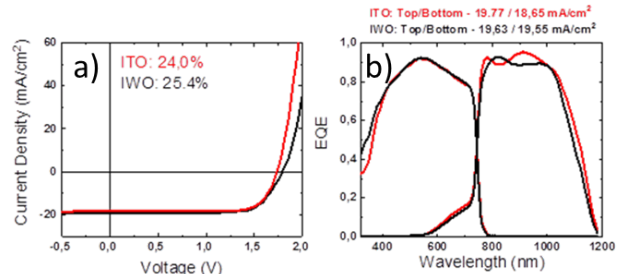


Figure 1: a) IV curve of hero cells comparing the difference between standard ITO and an optimized transparent electrode on small area cells (1.43 cm²) b) Comparison of EQE of devices upon improving the top TCO transparency. Note that this is the highest reported photocurrent values for flat perovskite-silicon tandems.

Building on the know-how in terms of both high-efficiency tandem design and upscaling, CSEM was then able to produce record efficiency large area (57.4 cm²) tandem of 24.3% (Figure 2). Such demonstrator cell features industrial front metallization schemes. This was made possible thanks to CSEM's expertise in low-temperature silver paste screen printing.

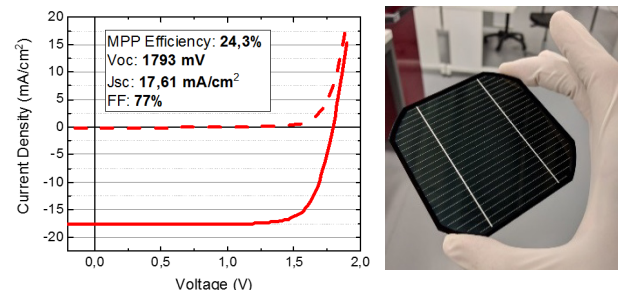


Figure 2: (left) IV curve of large area demonstrator tandem with screen-printed metallization at an aperture area of 57.4; (right) Photograph of large area demonstrator cell.

These recent developments position CSEM as a frontrunner in the PK/Si tandem research community, attracting the attention of traditional PV manufacturers.

[1] NREL, "NREL Efficiency Chart," 14 December 2018. [Online]. Available: <https://www.nrel.gov/pv/assets/pdfs/pv-efficiency-chart.20181214.pdf>. [Accessed 17 December 2018].

[2] A. Walter, S.-J. Moon, B. A. Kamino, L. Lofgren, D. Sacchetto, F. Matteocci, B. Taheri, J. Bailat, A. Di Carlo, C. Ballif, S. Nicolay, "Closing the cell-to-module efficiency gap: A fully laser scribed perovskite minimodule with 16% steady-state aperture area

efficiency", IEEE Journal of Photovoltaics, vol. 8, no. 1, pp. 151-155, Jan. 2018.

[3] B. A. Kamino, B. Paviet-Salomon, S.-J. Moon, N. Badel, J. Levrat, G. Christmann, A. Walter, A. Faes, L. Ding, J. J. Diaz Leon, A. Paracchino, M. Despesisse, C. Ballif, S. Nicolay, "Low Temperature Screen-Print Metallization for the Scale Up of 2-Terminal Perovskite-Silicon Tandems ", submitted, 2018.

High Performance Back-contacted Silicon Heterojunction Solar Cells

B. Paviet-Salomon, L.-L. Senaud, A. Descoeuilles, G. Christmann, K. Zagorova, N. Badel, G. Nogay, J. Geissbühler, A. Faes, J. Champliaud, J. Zhao, C. Allebé, P. Wyss, S. Nicolay, C. Ballif, M. Despeisse

CSEM is developing the next generation of back-contacted silicon heterojunction solar cells, aiming at demonstrating top-level conversion efficiencies with a cost-effective process flow based on CSEM "Tunnel-IBC" approach.

Crystalline silicon solar cells implementing passivating contacts based on hydrogenated amorphous silicon and transparent conductive oxide layers feature the key advantage of increased operating voltages, as demonstrated in CSEM silicon heterojunction solar cell (SHJ) platform. In addition, maximum optical performance can be achieved using an all back-contacted solar cell architecture, providing no metallization shadowing at the cell sunny-side. The back-contacted silicon heterojunction (BC-SHJ) architecture therefore represents one of the silicon solar cell approaches with the highest efficiency potential, combining optimum electrical and optical performances. This was demonstrated by Kaneka, Japan, with the world-record conversion efficiency of 26.7% for a silicon solar cell using such a BC-SHJ architecture. However, the successful industrial spread of BC-SHJ devices is impeded by their complex and delicate process flow, usually involving several costly photolithography steps, to realize the patterned rear contacts. In the frame of the European project "NextBase", CSEM, in close collaboration with EPFL and Meyer Burger Research, has been developing the next generation of BC-SHJ devices, targeting high conversion efficiency along with a cost-effective process flow.

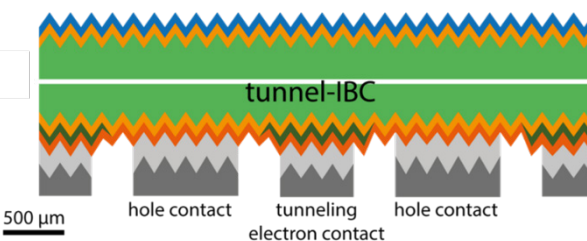


Figure 1: Schematic cross-section of the tunnel-IBC concept developed at CSEM.

CSEM developed and patented a novel BC-SHJ architecture, named "tunnel-IBC", featuring an interband silicon tunnel junction at the electron-collecting regions. In contrast to conventional BC-SHJ devices, where both the electron- and the hole-collecting fingers have to be patterned and aligned, in the tunnel-IBC concept only the electron collector is patterned. An overlaying full-area hole collector is then deposited. As a consequence, a tunnel junction is formed at the electron-collecting regions. Therefore, to work efficiently, the tunnel-IBC device requires an efficient carrier transport through the tunnel junction, and a low lateral conductance within the hole collector in order to avoid shunts between the electron- and hole-collecting regions. The key enablers of the tunnel-IBC technology are nanocrystalline silicon layers featuring anisotropic crystalline growth, hence simultaneously fulfilling the two above-mentioned contrasting requirements. Our innovative tunnel-IBC architecture dramatically simplifies the process flow of BC-SHJ devices as it eliminates the hole collector patterning as well as its alignment

to the electron collector. This novel design is thus a major step towards cost-effective processing of BC-SHJ devices.

As a major achievement, CSEM fabricated in 2019 a first record lab-scale tunnel-IBC solar cell (25 cm^2) reaching an efficiency of 25%, certified at Fraunhofer ISE Callab. Recently, CSEM further improved its materials and processes to reach a 25.4% efficient tunnel-IBC device (internal measurement calibrated using the certified record cell). The current-voltage curve of these record devices are plotted in Figure 2. Numerical simulations show that efficiency above 26% are reachable with the tunnel-IBC concept. These results demonstrate the high-efficiency potential of the tunnel-IBC technology developed at CSEM.

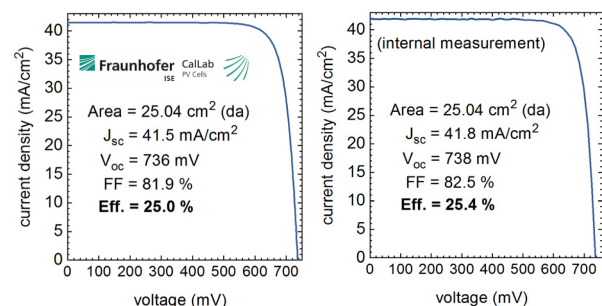


Figure 2: Current-voltage curves of the certified 25% (left) and newly manufactured 25.4%-efficient (right) record BC-HJT device developed by CSEM.

Remarkably, the manufacturing cost structure of the tunnel-IBC device proposed by CSEM was analyzed by the Nextbase EU project partners (CEA). By implementing individual tunnel-IBC devices at 25% efficiency, the CoO of the tunnel-IBC technology was estimated at 0.26 €/Wpeak at medium size production volume, with potential to go lower for multi-gigawatts factory. This convincingly demonstrates that back-contacted devices must not be considered as too expensive per se, and that the tunnel-IBC concept is an interesting option to provide high-efficiency modules at competitive CoO.

This work was funded by the European Union's Horizon2020 Programme for research, technological development and demonstration under Grant Agreement no 727523.

Technology Platform for High-efficiency Silicon Heterojunction Solar Cells and Modules

M. Despeisse, A. Descoedres, J. Zhao, L.-L. Senaud, G. Christmann, B. Paviet-Salomon, J. Geissbühler, A. Faes, A. Lachowicz, C. Allebé, N. Badel, G. Nogay, J. Champliaud, P. Wyss, J. Levrat, D. Petri, G. Cattaneo, H. Li, J. Escarre, K. Zagorova, S. Nicolay, C. Ballif

CSEM has set up a versatile platform for the fabrication and the characterization of silicon heterojunction solar cells and modules. Innovative and industry-relevant solutions are developed, aiming for high conversion efficiencies at competitive manufacturing costs. The topics covered at CSEM include wafer bulk improvements, wafer texturing and cleaning, depositions of ultra-thin passivating and contacting layers, depositions of low-cost and/or high-mobility transparent conductive oxides, advanced cell metallization and interconnection processes, various characterization techniques, encapsulant assessment and formulation, as well as module design and optimization for maximum performance and reliability.

Silicon heterojunction (SHJ) solar cells present the decisive advantages to combine a high efficiency (potential for modules with >22% conversion efficiency) with limited number of production steps (pre-requisite for keeping reduced fabrication costs). The technology further exhibits a low temperature coefficient (<-0.3%/°C) as well as a high bifaciality (>90%), triggering high energy yield for bifacial SHJ modules in the field. Thanks to its symmetric structure and to the high level of passivation, the SHJ bifacial cell architecture is also ideally suited for thin wafers integration.

A strong emphasis is set in CSEM on the development of a complete, performant and flexible platform covering all aspects of production and characterization of SHJ solar cells and modules, from as-cut wafers to optimized modules, including several testing structures to assess particular materials and processes impact on performance and reliability. A focus is set at the interface between cell and module, for which a cross-disciplinary R&D team has been established in 2019. This cell to module technological platform allows CSEM to conduct advanced R&D projects to develop new processes, materials, production and metrology equipment, as well as advanced concepts for improved performance, reliability and/or reduced production costs; and also to provide services and small batch production for its customers.



Figure 1: Illustration of test structures used to first achieve 24.2% certified efficiency on 4 cm² solar cells early 2019 using all CSEM processes, transferred to industrial silicon wafers.

SHJ solar cells implement carrier-selective contacts with high surface passivation formed on crystalline silicon wafer with the deposition of hydrogenated amorphous silicon (a-Si:H) and transparent conductive oxide (TCO) layers. These hetero-contacts are demonstrations of so-called passivating contacts, enabling for its key advantage: increased operating voltages. Following proper silicon wafer specifications combined with a-Si:H and TCO process developments, CSEM could demonstrate in 2019 >750 mV of implied VOC on both commercial n-type and p-type Cz wafers, demonstrating the key asset of the SHJ technology. CSEM developed a complete set of

testing structures at cell and module levels, enabling to perform detailed performance losses analysis, accounting for edge effects, passivation, series resistance breakdown, optical analysis, cell to module losses following varying metallization and interconnection schemes, and isolation of key contributions to losses. This enabled for continuous improvement of CSEM baseline SHJ solar cells, enabling to achieve in 2019 up to 24.4% efficiency for a 220 cm² cell on a n-type Cz wafer, and up to 23.6% efficiency for a 220 cm² cell on a p-type Cz wafer, using a busbarless printed metallization grid.

Table 1: Summary of high-efficiency SHJ solar cells developed on CSEM flexible R&D platform.

Metallization	Grid	Cell area	Voc	Jsc	FF	Eff.
Cu plating	4 BBs	Full 6"	742	39.4	81.7	23.9
Cu plating	4 BBs	221 cm ²	741	39.6	83.2	24.3
Ag printed	BB-less	Full 6"	740	39.5	82.1	24.0
Ag printed	BB-less	221 cm ²	738	39.9	83.0	24.4

CSEM developed to maturity a copper plating process enabling to achieve high performance and high reliability. This enables to achieve 24.3% efficiency on a CSEM SHJ solar cell with a 4 busbars metallization design. An efficiency certified at 24.73% could be achieved using CSEM plated grid on industrial partner cell precursor, for a 4 busbars cell, while reliability could be demonstrated with modules passing 3 times IEC test standards.

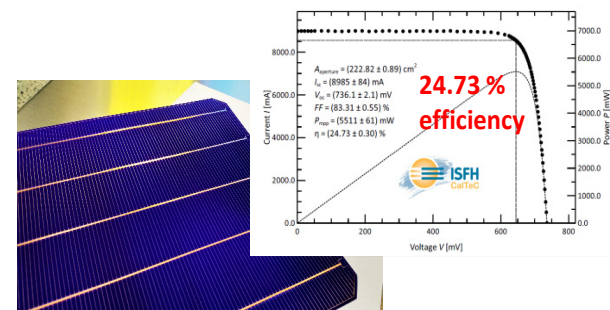


Figure 2: 24.73% certified efficiency demonstrated for a 4 busbars SHJ solar cell using CSEM plated metallization grid.

The solar cells achievements in 2019 are further detailed in [1].

CSEM established materials and processes for optimum integration of SHJ solar cells, providing its own encapsulant formulation, as well as key know-how for multi-wire as well as soldered interconnection approaches.

[1] A. Descoedres, et al., The versatility of passivating carrier-selective silicon thin films for diverse high-efficiency screen-printed heterojunction-based solar cells, PiP, (2020).

Energy Management with Smart Thermostatic Valves

D. Grivon, Y. Stauffer, A. Hutter

The information from smart thermostatic valves is exploited to optimize the operation of the central heating system. In this contribution, we describe the evaluation procedure that allows us to determine the efficiency increase for such approaches and present associated energy savings results. The analysis shows that significant savings can be achieved for different heating technologies, especially when using heat pumps.

In recent years, many control strategies for reducing building and district energy consumption have been demonstrated. Most of them use predictive algorithms, i.e., almost optimal control strategies. However, even if these strategies are promising, they are seldom deployed in practice because of the modelling burden. On the other hand, classic control strategies can be improved by adding simple expert rules which increase their reliability and effectiveness. However, such approaches require constant human interaction and are therefore rarely economic.

In this contribution, we present a data-driven, model-free approach that tries to achieve optimal solutions in an automated and economic manner. The idea is to use smart thermostatic valves as sensing elements in order to obtain a better information of the heat requirement distribution in the building according to the local thermal user settings, e.g., room temperature set points. This information is then used to adapt and optimize operation of the central heating system, e.g., by changing set points or heating curve parameters.

To evaluate such approaches a co-simulation software platform was developed, where the thermal building simulation platform DIMOSIM (www.cstb.fr) interacts with the python-based optimization algorithms. The entire process is driven by the optimization algorithm, which instantiates the simulation process via the generation of suitable DIMOSIM project files. The process communication is then achieved via a socket framework, where DIMOSIM is acting as server. During the simulation process, the measurement signals are passed to the optimization algorithm at regular intervals. The algorithm then determines optimum set points, which are fed back to the building simulator.

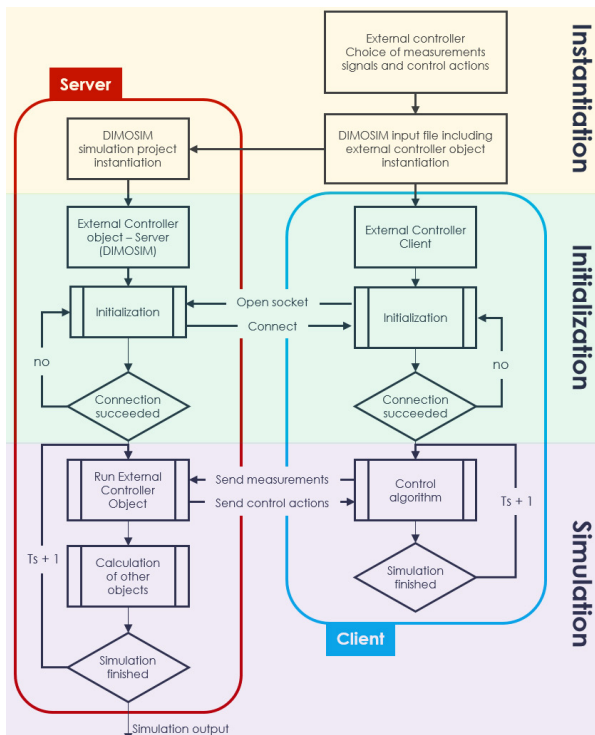


Figure 1: Interaction of building simulator and optimization algorithm.

Within the THERMOSS project, this approach was evaluated for a test site in the UK. The test site is a multi-apartment building with 43 dwellings and a total of over 150 radiators. The building currently uses an obsolete gas boiler technology and the upgrade towards either a modern gas boiler or emerging gas absorption heat pumps (GAHP) was investigated. For this purpose, the entire building was modelled in DIMOSIM and an evaluation for the 2015/2016 winter season with a total duration of nine months was carried out.

First, the consistency of the building modelling was validated by comparing the actual heating consumption of 192 MWh to the simulated consumption. For the typical set point settings provided by the building users an error of +7% was determined, which indicates a sufficiently good calibration of the thermal building model.

Second, the improvements coming from new heating equipment were evaluated. With a modern gas condensing boiler the total consumption can be reduced to 126 MWh whereas a GAHP results in 96 MWh. This corresponds to reductions of 34% and 50%, respectively.

Third, the potential savings from the data-driven automated optimization using data from smart thermostatic valves was evaluated. For the gas condensing boiler, the total consumption was reduced to 116 MWh, which corresponds to savings of 8%. For the GAHP savings of 24% were obtained (73 MWh). They originate from a consistent and continuous reduction of the flow temperature with respect to standard heating curve approaches used nowadays. For the gas condensing boiler this effect results in an increase of the average seasonal generation efficiency from 87% to 92% whereas for the GAHP the seasonal coefficient of performance (COP) is increased from 118% to 149%.

The evaluation demonstrates the significant improvements that are possible via the proposed data-driven optimization approach.

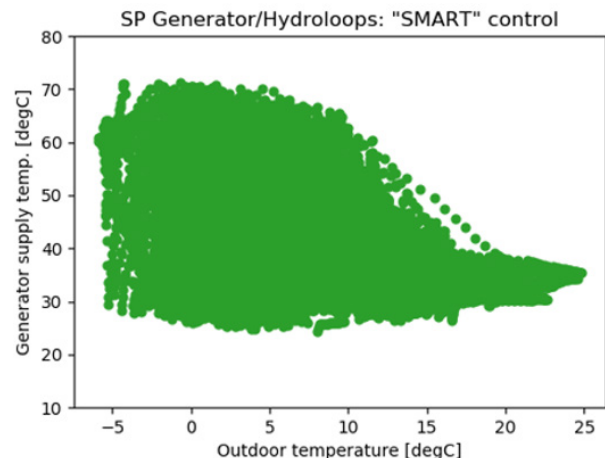


Figure 2: Flow temperature distribution of central heating unit.

The THERMOSS project has received funding within the Horizon 2020 framework program under grant agreement 723562.

Demonstration of Multi-service DC Microgrid in an Industrial Environment

N. Koch, P.-J. Alet

This report presents a lean control architecture for microgrids, with an implementation in direct current (DC) microgrids. The purpose of this architecture is to combine local objectives with system-level objectives. This patent-pending solution has been implemented and experimentally validated thanks to the commissioning of a building-scale demonstrator at Neuchâtel's wastewater treatment plant (WTP).

With the cost of photovoltaic power generation below socket parity in many places, end-users have a clear financial interest in self-consuming the power they produce. On the other hand, recognition that infrastructure costs are mainly driven by peak power, rather than energy, is leading to an increasing fraction of retail electricity prices being based on peak power. This evolution presents a challenge for end users with highly variable power profiles. Microgrids, especially with battery storage, are a promising way to manage the complexity of power networks with an increasing number of distributed, variable renewable energy sources (VRES). Through the DCSMART project, CSEM has developed a control architecture for microgrids to benefit both end users and system operations. The design has been experimentally validated by the commissioning of a demonstrator in an industrial environment.

System architecture

The architecture of the DCSMART microgrid is shown on Figure 1. It is composed of a bidirectional grid-tied inverter, DC-supplied loads, a photovoltaic installation and an energy storage system. The DC architecture eliminates conversion steps and the synchronization and balancing requirements associated with AC.

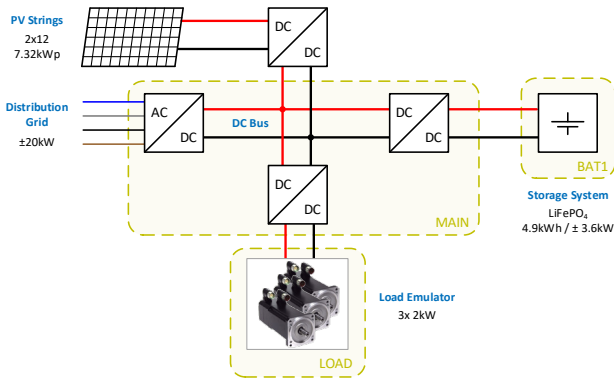


Figure 1: General topology of the microgrid.

Control strategy

The purpose of the developed strategy is to control the charging/discharging of the storage system in order to achieve local and system-level objectives:

- self-consumption to reduce energy cost for prosumers
- peak shaving on the grid power to reduce capacity charges for prosumers and peak load for DSOs
- ramp-rate control on the grid power to reduce rapid power and voltage fluctuations for DSOs.

Demonstrator

In order experimentally to validate the developed solution, CSEM has realized a building-scale DC microgrid whose key components are shown on Figure 2. This demonstrator has been commissioned at Neuchâtel's WTP. Electrosuisse inspected it and validated its safety features.

For a period of six months, the system has been intensively tested and monitored. This demonstration phase allowed to validate the correct behavior of the multi-service control strategy as well as the stable and safe operation of the hardware platform. Figure 3 illustrates the peak-shaving service performed by the battery in the event of a unit step in load consumption.

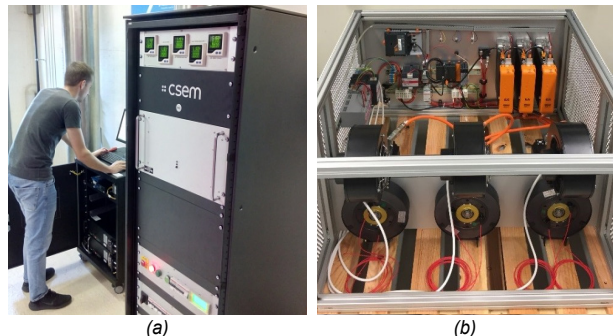


Figure 2: Main and battery cabinet (a) and load emulator (b).

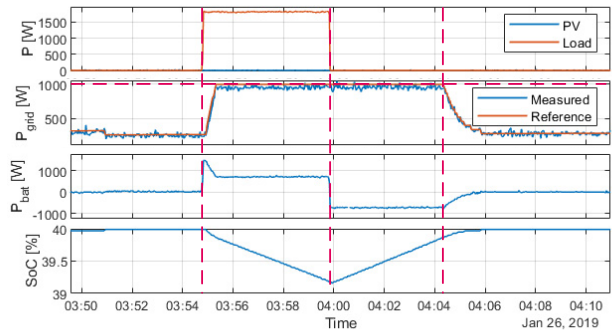


Figure 3: Load, PV, grid and battery power profiles and evolution of battery state of charge during a peak-shaving event.

Economic assessment

The economic value of the multi-service approach has also been validated. In a domestic application, the developed strategy reduces operating costs by 6% to 48% (depending on electricity rates) compared to a standard strategy with an equivalent storage capacity. For an industrial application, this reduction varies from 1.5% to 13%.

Outlook

The expertise acquired and the lessons learnt with this demonstration are already used for ongoing projects. Three improved units are currently being developed under the running European (H2020) project HYBUILD. They are compliant with the IEC 60204 standard and will be dispatched across Europe in three operational buildings for combination with heat pumps. Finally an additional unit will be deployed in an office environment at EMPA's NEST in Dübendorf.

The DCSMART project received funding with the joint initiative ERA-Net Smart Grids Plus, with support from the European Union's Horizon 2020 research and innovation programme under grant agreement No 646039 and support from Viteos.

Evaluation of Battery Technologies for Solar-powered Aviation

P. Iurilli, C. Brivio, Y. Stauffer, A. Hutter

Within the SPET^[1] project, CSEM is qualifying components for solar-powered mobility applications. The showcase will be the Solarstratos mission: achieving the first entirely manned PV-powered flight to the stratosphere at 25'000 m. The focus in the first year of the project was on testing battery chemistries to evaluate their performance and compatibility with this mission. High-energy density Li-ion cells have been tested (NMC811 and NCA) as today's market reference (generation 3a) together with emerging technologies (lithium-sulphur and lithium-silicon) as promising solutions for the future (generation 3b-4).

The cell performance evaluation has been carried out at CSEM premises by exploiting the newly commissioned battery testing equipment (24 channel 5 V/15 A cell tester, 1100 L, -40°C/+180°C climatic chamber). The investigation has followed three main steps.

Test in standard conditions

The first set of tests ran in the nominal conditions set by the cell manufacturers to position the different chemistries with respect to gravimetric and volumetric energy densities (Figure 1).

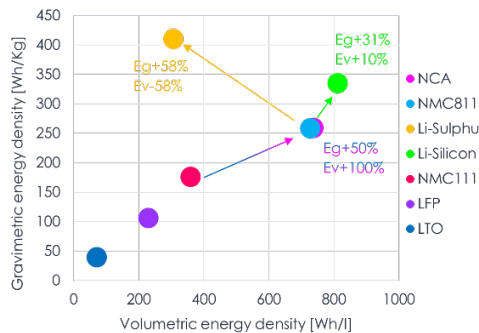


Figure 1: Chemistries' positioning as regards energy densities.

Li-sulphur (a non Li-ion chemistry) is confirmed to be a promising technology characterized by outstanding gravimetric energy density. Li-silicon shows consistent improvements in both gravimetric and volumetric energy densities when compared with today's Li-ion benchmark technologies: NCA and NMC 811.

Test in extended conditions

To make the results more directly comparable, all cells were then tested for energy capacity in a wider range of currents (from 0.1 C to 2 C) and ambient temperatures (from -20°C to 40°C). Results are shown on Figure 2:

- NCA and NMC 811 are quite resilient to external conditions. Current and temperature variations influence the gravimetric energy density by no more than 15% and 25%, respectively. When also considering they carry the lowest price, these chemistries are then the first choice for applications requiring high gravimetric energy density.
- Li-silicon is also quite resilient to external conditions. Variations are higher than for NCA and NMC 811 (25% and 35% for current and temperature, respectively). Since its price premium is only 50% in high-volume purchase, this technology is an interesting challenger for high-energy-density applications.
- Li-sulphur is instead quite sensitive to external conditions: increasing the current to 1 C or decreasing the temperature to 0°C means to lose 65% or 80% of the energy density,

respectively. Since these batteries are 80 times more expensive than NCA or NMC, we believe this technology still needs improvements to be the game changer in high-energy-density applications.

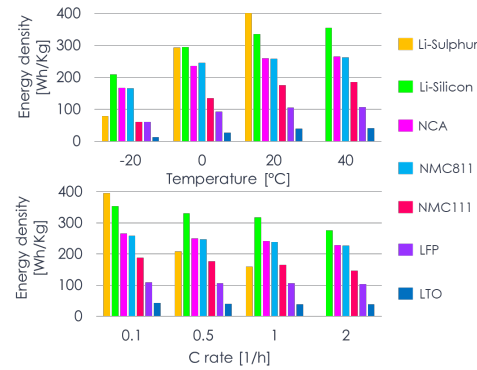


Figure 2: Dependence of energy density of various chemistries on current and temperature.

Application-oriented tests

Finally, we applied a Ragone testing protocol to better map the different technologies when used for solar-powered aviation. As shown in Figure 3, the energy capacities are expressed as a function of power capacities. The intersection of these curves with the characteristic area of the application shows the energy and power performance we should expect. This shows that Li-sulphur or Li-silicon could save respectively 34% or 27% of the battery cell weight on the plane.

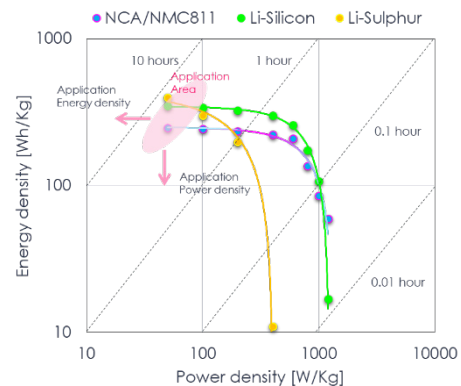


Figure 3: Ragone chart of tested technologies vs. application.

After a decision-making phase, the next step of the project will focus on modelling the chosen technology. It will use and further develop CSEM's battery modelling capabilities with an aim to deploy it into state-of-the-art BMS systems.

The SPET project has received funding from the Swiss Federal Office of Energy under contract SI/501727-01.

[1] High-performance versatile components for electrification of future solar-powered power trains (SPET project).

SYSTEMS

Jens Krauss

The **Systems** research program is application driven and our vision is to promote micro-technological innovations and new product concepts along the three application domains of (1) *Scientific Instrumentation*, (2) *Automation*, and (3) *Medical Device Technology*. Our *Scientific Instrumentation* research activities aim at meeting coming demands in the fields of astrophysics, space exploration, space-based systems, and watchmaking, as well as meteorology and industrial instrumentation. The research topics are structured into macro-MEMS technologies, opto-mechatronic instruments, time and frequency, and the recent focus topics of design methods for (metallic) additive manufacturing and laser sources and stabilized lasers. Within the *Automation* research activity we develop technologies for enhanced manufacturing and process flexibility, making high-quality, small-to-medium-volume products possible, and the three technological platforms—machine learning, advanced robotic systems, and integrated measurement technologies—support the objective of maintaining production sites in Switzerland. The *Medical Device Technology* research activity ranges from innovative sensing technologies for monitoring human vital signs to bio-signal processing and active medical device technologies. During the last reporting period emphasis was given to strengthening our ISO13485 process within our collaboration with the university hospitals of Switzerland.

Long-term objectives

Scientific Instrumentation: Switzerland is a key player in space instrumentation and large science missions. CSEM supports the Swiss space industry and the research activities within the scientific instrumentation domain aim to meet coming demands in the fields of space exploration, watchmaking, meteorology, and industrial and medical instrumentation. Rapid progress in material sciences and microtechnologies has led to rising ambitions in (scientific) instrumentation and a quest for ever-smaller and smarter multi-technology systems. In the near future, sensors, actuators, and mechanism will be integrated at the process level taking advantage of (metallic) additive manufacturing technologies to enable a new approach to complex instrument design. We design and implement complex, high-precision mechanisms for industrial applications and large science missions and strive for innovations in the domain of Si-based hybrid and compliant micro-mechanisms, laser sources and systems, and miniature atomic clocks. Our competencies in multi-physics simulations are key to our expertise in the design of such complex, miniature, and fully integrated systems, and thanks to our multidisciplinary expertise CSEM has become a European leader in the field of miniaturized flash imaging LiDAR. Finally, *Scientific Instrumentation* benefits from the latest advances in additive manufacturing, photonics, and quantum sensing technologies and CSEM coordinates a major European Quantum Technology Flagship Programme.

Automation: Maintaining industrial manufacturing activity is essential for the future prosperity of the Swiss economy. For a high-labor-cost country such as Switzerland this can only be achieved by innovative products in combination with smart production processes. Industry 4.0 addresses this optimization of

industrial processes and impacts the whole value chain from production, handling, and quality control to logistics. In the frame of the *Automation* research activity we develop Industry 4.0 solutions relying on data acquisition, smart algorithms, (deep learning) and adaptive concepts in order to deliver smart and highly adaptive processes, machines, and equipment. We automate and interconnect complex manufacturing tasks, applying intelligent control and sensor fusion techniques, and implement customized, integrated sensing lab automation solutions. We aim to further extend our Industry 4.0 application software framework in order to easily deploy innovative solutions to different manufacturing and quality processes: with the benefits of self-aware, smart components (SW and HW) and supportive robots (so-called work companions), an optimum balance between flexibility and throughput is sought.

Medical Device Technology: The Western world is facing huge challenges in its need to limit the increasing costs of its healthcare system. Chronic diseases significantly contribute to the health costs of an aging population. Medical wearables—as a source of valuable data measured in a real environment levered by digitalization, big data, and artificial intelligence—are one answer to this specific societal challenge. Wearables will also play a central role in the optimization of medication as well as in the development and monitoring of drugs. Having started working with wearable technologies 20 years ago, CSEM has accumulated an important patent portfolio and considerable know-how regarding both hardware (including ASICs) and software (including algorithms). Today, our medical device technology portfolio includes low-power optical sensors such as oBPM™ (cuffless blood pressure), oAFD™ (detection of atrial fibrillation), and reflective SpO₂ (arterial oxygen saturation), as well as miniaturized sensors for biopotential and bio-impedance sensing and embedded processing. CSEM's proprietary multiparameter cooperative sensor technology enables the design of smart medical textiles with embedded button-sensors so small that the overall wearable appears seamlessly flexible, stretchable, and breathable. Last but not least, CSEM is ISO13485-certified and works closely with the Swiss university hospitals (*i.e.*, CHUV, Inselspital, USZ, HUG, and UniBasel) in order to maximize its added value to medical customers, hence positioning itself closer to the targeted use case and the final product development phases.

Highlights

With its multidisciplinary teams across CSEM's operational divisions, the Systems research program continues to be the key driver of CSEM's mission to transfer its (micro-) technologies to (Swiss) industry. In the following, last year's scientific and technological highlights are summarized.

Scientific Instrumentation: Within our *Scientific Instrumentation* research activities we can report the successful flight model delivery of (i) the compliant high-precision mechanisms for the Meteosat Third Generation satellite (MTG) and (ii) the Re-Focus Mechanism (RFM) of the close-up imager for the Exomars mission. In addition to these successful close-outs we can highlight the end of the RemoveDebris space mission during which our LiDAR system, the so-called Vision Based Navigation

sensor (VBN), enabled the successful testing of three different space debris capturing techniques in orbit. In the MacroMEMS domain we further enlarged our portfolio of silicon-based oscillator concepts with two new patented watch escapements that have been designed, manufactured, and integrated into a watch. Moreover, we supported the Swiss watch manufacturer Armin Strom with its double resonance escapement by optimizing the coupling spring with a MEMS approach. In the frame of the European Quantum Technology Flagship initiative CSEM has been awarded the coordination of the research project macQsimal, which was launched at the end of 2018. MacQsimal aims to design, implement, and characterize new quantum sensor concepts such as a magnetometer, gyroscopes, and GHz/THz field sensors, while CSEM will focus its efforts on its long-standing track record in Miniature Atomic Clocks (MACs). During the reporting period, CSEM proceeded to reinforce its position in the photonics domain and was awarded a prestigious ERC grant with the aim of demonstrating novel microphotonic laser frequency combs to support the revolutionary advances in astronomical precision spectroscopy required to enable detection and characterization of habitable Earth-like planets.

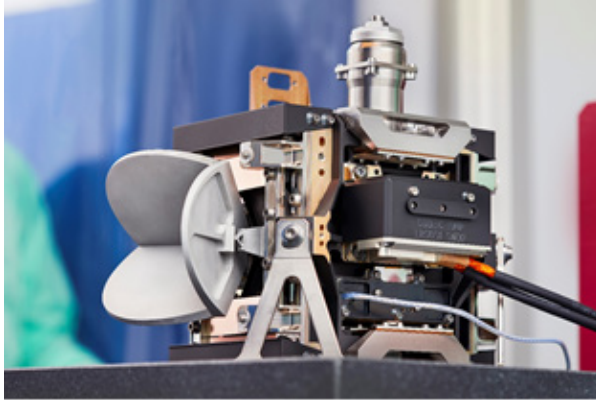


Figure 1: Delivered MTG-CCM flight model mechanism, mounted on the EUMETSAT's MTG satellite for climate and weather forecasts.

Automation: The development and deployment of innovative Industry 4.0 solutions across different industrial areas is at the heart of our *Automation* research activities. Within the industrial automation, manufacturing, and watch industries we rely on our high-level framework VISARD—Vision Automation Robotics Designer—which offers a strategic software platform for a fast and efficient implementation of hardware-independent automation system deployment. The platform has great potential, especially for complex vision tasks such as pattern recognition, aesthetic quality control, anomaly detection, and classification, and where we enhance the automation process with an integrated, robust decision-making tool. The deployment of these machine and deep-learning toolboxes was extended to space applications as well as datasets from the agriculture domain, where the digitalization process will increase considerably efficiency in fields and barns as well as their production output. Last but not least, the cooperation with our colleagues from the *Bio-Surface Engineering* research activity is of strategic importance for the life science sector and where we work on innovative lab automation tools to handle and monitor liquids in a precise and repetitive manner.



Figure 2: Predictive maintenance lab apparatus, with robot, cameras, and many industrial components. Training and testing new algorithms based on deep learning.

Medical Device Technology: Within the research activities of *Medical Device Technology* we continue along our roadmap toward medical certified portable vital sign monitors. Whereas our work on human activity profiling focuses on the valorization of our existing algorithm library within the consumer health domain, (medical) research on our comprehensive PPG technology platform continues to gain visibility and rewards thanks to the market traction of a cuffless, continuous blood pressure monitoring use case, our so-called oBPM™ (optical Blood Pressure Monitor) technology. Our cooperation with our start-up partners aktiia and Biospectral targets the product launch of a medical certified cuffless blood pressure monitor during the first half of 2020, which will rely on the successful completion of ongoing clinical studies.



Figure 3: Start-up Biospectral commercializing CSEM's optical blood pressure monitoring technology with a smartphone camera.

Huge research efforts have also been deployed with regard to our cooperative sensor technology platform to further miniaturize the cost-efficient and low-power smart and dry electrode concept. We entered into several cooperation agreements for different medical use cases relying on the concept of our cooperative sensor technology platform. Moreover, we can report first scientific results within our corporate Data Program initiative, where we focus our research on e-Health applications with an emphasis on the privacy and security of medical data.

Highly Sensitive Miniature Sensors thanks to Quantum Effects in Atomic Vapors

J. Haesler, S. Karlen, L. Balet, D. Grassani, D. Boiko, T. Overstolz, G. Bergonzi, B. Gallinet, F. Droz, S. Lecomte

The understanding and applying of physical laws in the microscopic realm, which resulted in ground-breaking inventions such as the transistor and the laser, was coined the first quantum revolution. Today, the ability to manipulate quantum effects in customized systems and materials is enabling the second quantum revolution. As a project under the Quantum Technologies (QT) Flagship of the European Commission, macQsimal is at the forefront of European efforts to push the boundaries for this new technology. The project, coordinated by CSEM, will help pave the way for transformative advancements in the domain of quantum sensing and metrology. In this area of research, macQsimal is working with atomic sensors as a new and improved interface between the physical and the digital world for enhanced applications in various fields such as navigation and medical imaging.

In macQsimal^[1] CSEM designs, develops, miniaturizes and integrates advanced quantum-enabled sensors with outstanding sensitivity, to measure physical observables in five key areas: magnetic fields, time, rotation, electro-magnetic radiation and gas concentration. The common core technology platform for these diverse sensors is formed by atomic vapor cells realized as integrated micro-electro-mechanical systems (MEMS) fabricated at the wafer level.

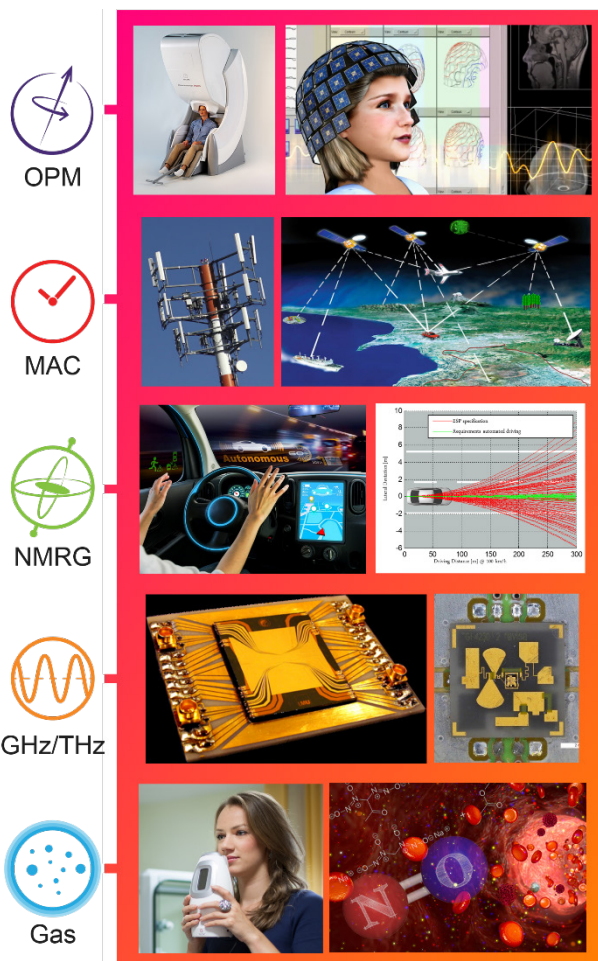


Figure 1: Miniature quantum sensor prototypes will be developed for five key applications: OPM, MAC, NMRG, GHz/THz and gas sensors.

Coordinated by CSEM, the project consortium includes leading research groups and companies who have been pioneering many of the recent advances in the field of atomic sensing and has been assembled to cover the entire knowledge chain from basic science to industrial deployment. The main objective of

macQsimal is to develop five different types of miniaturized quantum sensor prototypes (Figure 1): optically pumped magnetometers (OPM) for brain activity imaging, atomic clocks (MAC) for networks synchronization, nuclear magnetic resonance gyroscopes (NMRG) for autonomous cars, atomic GHz/THz sensors and imagers, and lastly, Rydberg-based gas sensors. It is the ultimate goal of macQsimal to develop scientific breakthroughs for atomic quantum metrology and sensing which will establish European leadership in the industry and drive excellence in quantum technologies.

macQsimal will contribute to the strategic objectives of the Quantum Technologies Flagship in the sub-domain of Sensing and Metrology. The choice of atomic vapor cells makes coherent quantum processes available to applications: advanced cell-based sensors optimally exploit single-particle coherence, with the potential to harness also multi-particle quantum coherence for even greater sensitivity. Fabricating such MEMS atomic vapor cells (Figure 2) at the wafer level^[2] will allow for high-volume, high-reliability and low-cost deployment of miniaturized and integrated sensors, critical to wide-spread adoption.



Figure 2: MEMS atomic vapor cell fabrication at the wafer level in CSEM's clean room facilities.

Through its balanced basic and applied research concept, macQsimal will address the fundamental questions of quantum-enhancement techniques such as squeezing, entanglement and quantum non-demolition measures to form a basis for scientific breakthroughs for future applications.

macQsimal has received funding from the European Union's Horizon 2020 research and innovation programme under grant agreement No. 20393.

[1] www.macQsimal.eu

[2] CSEM patent n°US8906470 (B2).

Validation of ÉChelle-based Quantum-classical Discriminator of Light

V. Mitev, L. Balet, N. Torcheboeuf, D. L. Boiko

The SUPERTWIN research project explores how de Broglie wavelength of a multi-partite quantum state of photons can be used to build super-resolution instruments, e.g., optical microscopes. Essential was to validate that de Broglie wavelength is not destroyed by the imperfections of optical systems.

In the framework of the European FET-OPEN SUPERTWIN project, 3 industrial, 3 academic and 3 Research Technology Organizations (RTOs) joined forces to achieve nanometer resolution in optical microscopy, a potential breakthrough enabled by quantum properties of entangled photons.

Imaging with non-classical photons allows one to bypass the Rayleigh resolution limit and classical shot-noise level [1,2]. Such schemes will operate with large photon number, produced by sources, where the entangled and classical states have the same wavelength. In this case, the discrimination of the classical and quantum states by wavelength selection with optical filters is not possible. It was already demonstrated, that the diffraction of bi-photons at reflection or transmission gratings manifests a pattern equivalent to that of classical photons with half of their wavelength [3,4]. These demonstrations point to the use of quantum diffraction in discriminating quantum and classical states, having the same (or close) wavelength. The motivation in this work is to validate the approach of quantum-classical photons discrimination (QCD).

The source of bi-photons at 810 nm is the spontaneous parametric down-conversion (SPDC) in a periodically poled potassium titanyl phosphate (PPKTP) crystal (Figure 1), pumped by diode laser operating at 405 nm.

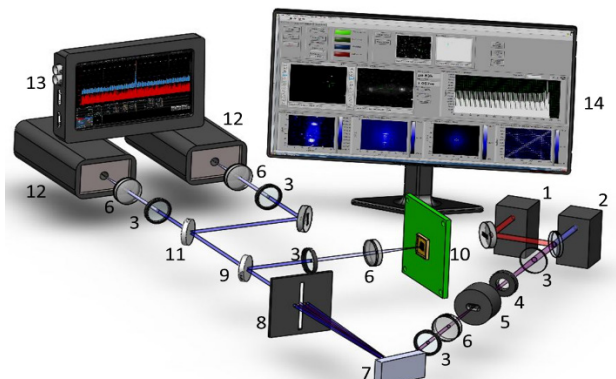


Figure 1: Breadboard: (1) Laser 795 nm; (2) Laser 405 nm; (3) Lenses; (4) Half-wave plate; (5) PPKTP crystal; (6) Filters; (7) Échelle grating; (8) Adjustable slit; (9) Flip-flop mirror; (10) 32x32 SPAD-array; (11) Beamsplitter; (12) Single SPAD detectors; (13) Oscilloscope; (14) PC.

A vertical cavity surface emitting laser (VCSEL) at 795 nm with beam propagating in the same direction as the SPDC, is added as a reference source of classical photons with wavelength close

to 810 nm. The combined beam, i.e., the SPDC and VCSEL, and residual pump, is directed to and diffracted by an échelle grating at high orders (31.6 gr/mm). The intensity signal detection $G^{(1)}$ and the evaluation of the Glauber correlation pattern $G^{(2)}$ are carried on a novelty SPAD array, developed purposely for imaging with entangled photons [5].

In this setup, all diffraction orders of bi-photons at 810 nm coincide with all diffraction orders of the classical pump beam at 405 nm, while the orders of the classical 810 nm photons (also VCSEL wavelength 795 nm, Figure 2a) coincide only with the even orders of classical photons at 405 nm. Placing a slit at an odd 405 nm order and a combination of filters transmitting 795/810 nm and blocking 405 nm we may select predominantly bi-photon states at 810 nm as this diffraction angle is prohibited for classical photons at 810 nm (Figure 2c). Bottom row in Figure 2 illustrates this effect on $G^{(2)}$. Panel (d) presents the spatial correlation pattern of classical 795 nm VCSEL beam. Panel (e) presents the features in (d) with added anti-diagonal (bi-photon) pattern from SPDC bi-photons. The diagonal feature is caused by crosstalk and accidental coincidences produce horizontal and vertical lines. For panel (f), additionally to the configuration in panel (e), a slit is placed after the grating to select only one order of SPDC. Note the clear bi-photon correlation pattern as anti-diagonal and the complete blocking of classical light at the same wavelength.

The partners contributing to the project results are Fondazione Bruno Kessler, University of Bern, Institute of Physics, National Academy of Sciences of Belarus. This work was partly funded by the H2020 program and we thank them for their support.

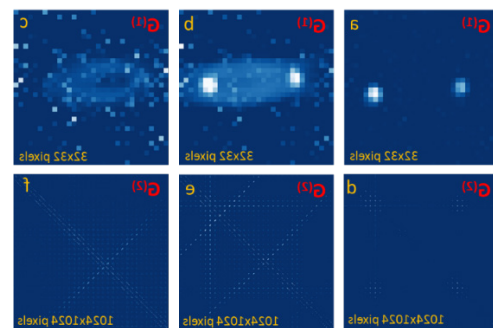


Figure 2: Intensity $G^{(1)}$ (top row) and correlations $G^{(2)}$ (bottom row): pure coherent 795 nm laser [a & d], mixed 795 laser and 810 nm bi-photon states at QCD input [b & e] and output [c & f] with filtered 810 nm bi-photon state.

- [1] Y. Kawabe, H. Fujiiwara, R. Okamoto, K. Sasaki, S. Takeuchi, "Quantum interference fringes beating the diffraction limit", Opt. Express, 15, 14244-14250 (2007).
- [2] T. Ono, R. Okamoto, S. Takeuchi, "An entanglement-enhanced microscope", Nat. Comm., 4, 2426 (2013).
- [3] M. Ostermeyer, D. Puhlmann, D. Korn, "Quantum diffraction of biphotons at a blased grating", J. Opt. Soc. Am. B, 26, 23472356, (2009).

- [4] R. Shimizu, K. Edamatsu, T. Itoh, "Quantum diffraction and interference of spatially correlated photon pairs generated by spontaneous parametric down-conversion", Phys. Review, A67, 041805-1/4, (2003).
- [5] L. Gasparini, B. Bessire, M. Unternährer, A. Stefanov, D. Boiko, M. Perrenzoni, D. Stoppa, "Novel CMOS sensor for improved quantum imaging", 11 April 2017, SPIE Newsroom. DOI: 10.1117/2.1201701.006847, (2017).

Laser Head Demonstrator for the Gravitational Wave Observatory in Space

S. Lecomte, L. Karlen, S. Kundermann, E. Portuondo-Campa, E. Obrzud, J. Bennès, F. Droz, E. Onillon

The recent detection of gravitational waves with ground-based interferometers opened a new eye on the Universe. The Laser Interferometer Space Antenna (LISA) mission candidate of the European Space Agency (ESA) has the ambitious goal to put such a gravitational wave observatory in space in 2034. Contracted by ESA, CSEM developed a breadboard of the laser system and the necessary metrological tools. CSEM has demonstrated that its laser breadboard essentially fulfills the demanding mission requirements.

The recent detection of gravitational waves^[1] has opened a totally new window on the Universe. This groundbreaking discovery followed by new observations leads to better understanding of the machinery of gravity at cosmic scale. Together with earlier electromagnetic field detectors they now bring the era of multi-messenger astronomy^[2] which is expected to lead to future major discoveries. Ground-based gravitational wave detectors rely on optical interferometry and the low frequency of the detection band is limited by the seismic noise. A space borne instrument with low frequency detection band spanning [30 μ Hz; 1 Hz] will complement the ground-based instruments coverage. The LISA mission, led by the European Space Agency (ESA), exactly aims at implementing such an observatory in space. Recently the LISA pathfinder mission validating key technologies for LISA implementation was successfully completed^[3]. In order to meet a launch date around 2034, the required technology has to be swiftly developed.

A key payload item of the LISA mission is the laser system. Indeed, the mission science capabilities are intimately linked to the laser system performance. Key specifications of the continuous-wave laser system include (i) 2 W of average output power in a diffraction limited beam, (ii) carrier wavelength of 1064 nm, (iii) polarization extinction ratio larger than 20 dB, (iv) low amplitude noise over a large frequency band covering [30 μ Hz; 5 GHz] and, (v) good frequency stability and spectral purity over [30 μ Hz; 1 MHz].

The CSEM laser breadboard is based on a master oscillator power amplifier (MOPA) architecture (Figure 1). The oscillator is a custom laser from OEwaves (US) and the amplifiers are made of efficient and robust Yb-doped fiber technology. Crucially, these technologies are well-suited to be space qualified. The system can emit close to 3 W of average output power in a diffraction-limited beam and with over 20 dB polarization extinction ratio.

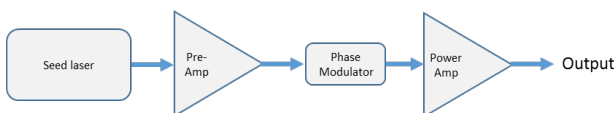


Figure 1: Laser system architecture.

Demanding frequency and amplitude metrology is requested to cover the over 12 orders of magnitude in frequency band. In Figure 2, the results of these measurements, in line with the required specifications, are shown^[4].

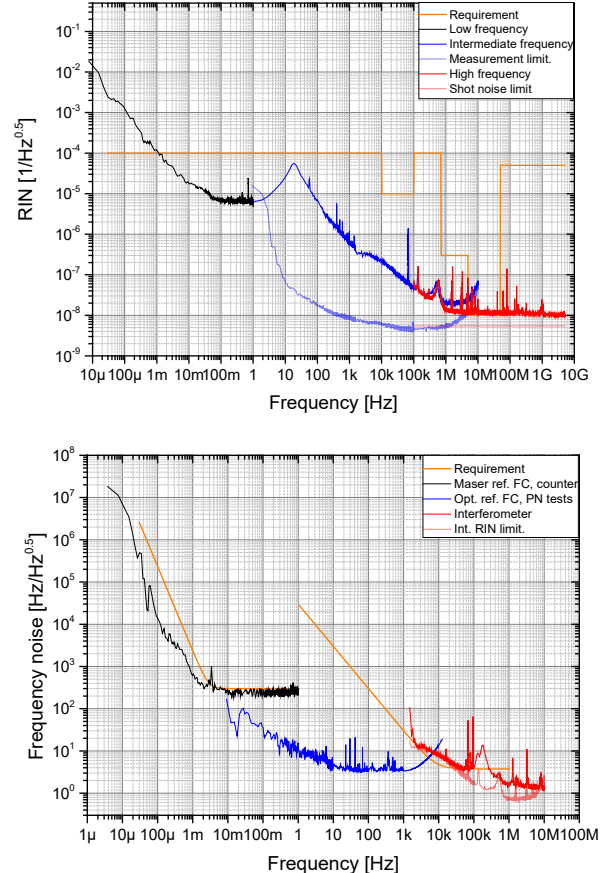


Figure 2: Top Relative intensity noise (RIN) and bottom frequency noise of the CSEM laser breadboard. The orange lines represent the required specifications.

In conclusion CSEM demonstrated a space-compatible laser head with performances meeting the LISA mission specifications. The full metrology apparatus was also developed and served to characterize the laser system. Further CSEM involvement in the LISA mission is expected.

The authors would like to thank Dr. B. Shortt, Dr. L. Mondin and Dr. P. McNamara from ESA for helpful guidance throughout the project. Furthermore, they are grateful to A. Matsko and the whole development team from OEwaves Inc. for the fruitful collaboration. The financial support from ESA (ESA contract 4000119714/17/NL/BW) is kindly acknowledged.

[1] B. P. Abbott, et al. (LIGO Scientific Collaboration and Virgo Collaboration), "Observation of Gravitational Waves from a Binary Black Hole Merger", Phys. Rev. Lett. 116, 061102 (2016).

[2] B.P. Abbott, et al., "Multi-messenger Observations of a Binary Neutron Star Merger", The Astrophysical Journal Letters 848:L12 (2017).

[3] M. Armano, et al., "Beyond the Required LISA Free-Fall Performance: New LISA Pathfinder Results down to 20 μ Hz", Phys. Rev. Lett. 120, 061101 (2018).

[4] L. Karlen, et al., "Laser System for the LISA mission", European Frequency and Time Forum (EFTF) and International Frequency Control Symposium (IFCS), Orlando (USA) April 2019.

Flash Imaging LiDAR for Space Debris Removal Demonstration Mission

A. Pollini, C. Pache, F. Droz

The project RemoveDebris disrupted the development time frame and risks mitigation for space missions to design and test devices. Within a time period of 4 years we moved from a paper concept to a TRL-8 hardware with a mission budget divided by a factor of 10. CSEM contribution, the vision-based sensor (VBN) was successfully operated in orbit and provided many color and 3D images of targets ejected on purpose by the main satellite.

The RemoveDebris mission is an initiative of the European Commission. This space mission has been the world's first Active Debris Removal (ADR) in orbit demonstration of some enabling technologies, including net and harpoon capture. It involved also the evaluation of CSEM's Vision-Based Navigation sensor (VBN) integrating a flash LiDAR and a color camera, the front-end of the guidance, navigation and control (GNC) of the ADR chain. Ultimately, the mission was terminated with the deployment of a dragsail to de-orbit the 100 kg main satellite. For the purposes of the mission, 2U CubeSats were ejected and then used as debris targets instead of real space debris.



Figure 1: CSEM's VBN sensor. (top right) color camera optics. (bottom center) laser illumination head and above LiDAR receiver optics.

CSEM has a long-term strategy to develop flash LiDARs. For the spatial domain, we achieved a Technological Readiness Level (TRL) of 4 at system level and we started in 2019 an ESA project targeting TRL-5/6 for one sub-system. Additional projects will be necessary to reach TRL-8 or 9, which are the levels where a technology can be considered for a full-scale space mission. Going through the TRLs stepwise with several projects is the traditional ESA development path for space.

RemoveDebris was special in the sense that it disrupted the traditional space approach. Unconventionally, within the same project we started at TRL-2 (paper concept) and ended at TRL-8 with an in-orbit demonstration. In itself, this is quite an achievement with the risks mitigation strategy and the pace of development, fabrication, test and integration involved. The development risk and budget mitigation started right at the beginning of the project with the choice of the components. None of the ones used is space qualified. The cost of such component simply does not match the available budget. Instead, we used commercial off-the-self components that we assessed according to space specifications for a one-year mission in Low Earth Orbit (LEO). The number of sensor versions were limited to one. Hence, the same hardware was used for sub-systems functional and environmental tests. Once the complete sensor assembled, it was qualified and assessed as a full system. After delivery to the satellite provider, the VBN was integrated and further tested on the platform according to functional and environmental requirements. This was made possible only with a careful design involving numerous engineering expertise areas including mechanical, optical, electronics and software.

The number and value of RemoveDebris outcomes are not easily measurable. The space debris environmental concern is appealing to the Medias, hence the project benefits from a large coverage by all kinds of media, including TV channels, radios, newspapers, etc. The website of the project got millions of hits. Technical and operational aspects are more measurable as CSEM possesses now a set of color and 3D images taken in orbit in real space operational conditions.

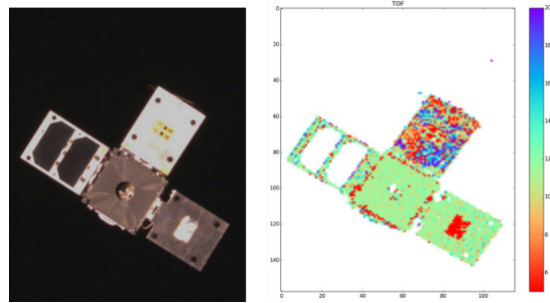


Figure 2: Example of pictures taken with the color camera (left) and the LiDAR at almost the same time (4s offset) of the 2U CubeSat with deployed panels 272 s and 268 s after ejection by the main satellite. The images are cropped and stretched as the field-of-view of the camera is twice the one of the LiDAR. The LiDAR image colors represents the measured time-of-flight (TOF) by each pixel.

In orbit experiments time windows were chosen to favor a strong illumination of the target by the Sun that was on the back of the main satellite compared with the CubeSat ejection direction. Bright areas can be seen in the color camera image (left and top panels, and center area of bottom right panel). The effect of the strong sunlight is visible in the LiDAR image where the same areas appear either with only red or mixed colors spots. They show the detector saturation. The panels hit with less sunlight (center and bottom right ones) appear with mostly green spots in the LiDAR image. The sensor settings defining the image dynamic range (aperture, integration time) were defined on Earth several days before the experiment.

The un-saturated areas provide measurements allowing to get correct TOF and distances. From these measurements several secondary figures can be calculated such as: 3D target image, relative attitude, velocity and rotation of the target, etc. These figures are mandatory to catch a debris in a controlled manner.

In relation with the long term LiDAR development strategy, the RemoveDebris experience is unevaluable as it shows what it takes in a real situation with strong Sun and Earth background perturbations to get proper visual measurements that can be considered with confidence to control the approach of space debris by waste collection crafts or more generally for in space Rendez-Vous between two objects.

This development was performed under the EU FP7-SPACE-2013-1, grant No. 607099 and we thank the Commission and the Swiss Secretariat for Education, Research and Innovation (SERI) for their support.

Close-up Imager for EXOMARS Mission: from Design to Flight Model

G. Perruchoud, A. Verhaeghe, P. Schwab, M. Gumi

Over the years CSEM has developed a particular expertise for high-precision opto-mechatronics systems used for space missions. The present report describes the flight model delivery of the Close-Up Imager (CLUPI) focus mechanism for the EXOMARS mission.

In the frame of the ESA EXOMARS mission, CSEM was in charge of developing three models of focus mechanism for the CLUPI instrument, including the Flight Model (FM). The CLUPI imager is mounted onto the drill of the EXOMARS Rover and will take high resolution images of the samples collected by the mission and of the rover surrounding. The CLUPI imager development is under the responsibility of Thales Alenia Space, Switzerland whereas the instrument Principal Investigator (PI) activity is performed by Space Exploration Institute (Neuchâtel). The CLUPI focus mechanism is based on CSEM's long-term flextec technology track record.

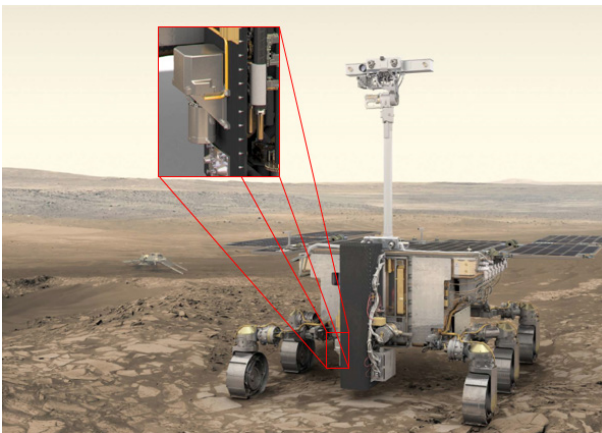


Figure 1: EXOMARS rover on which the CLUPI mechanism will be mounted (zoomed-in).

The CLUPI Focus Mechanism (CFM) allows the frictionless adjustment of the focal distance of the imager from 100 mm to infinite. It is resilient to the harsh mechanical loads of the rocket launch (high random vibration loads up to 29 Grms) and the extremely cold environment on Mars with non-operational temperatures down to -130°C. The key challenges were the low mass requirement (under 200 grams), together with the development of a new launch lock device.

The CFM is presented in Figure 2, where the key constitutive elements are depicted.

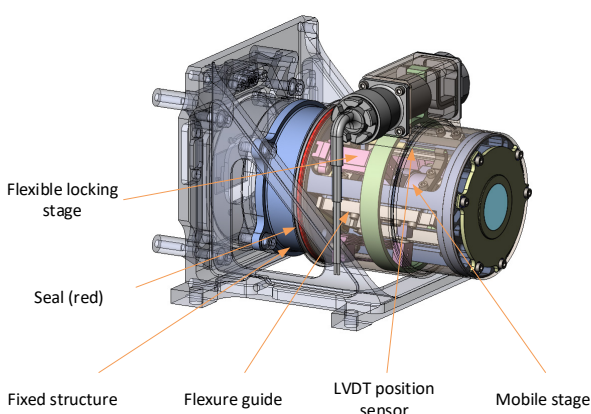


Figure 2: CFM (CLUPI Focus Mechanism) building blocks.

During the EQM and FM models design, manufacturing, assembly and testing, various challenges and issues were tackled and resolved, and which are presented hereafter.

1) The design was performed to meet the mission's needs. This led to a mechanism with the following performances:

- very low mass < 0.2 kg
- position accuracy of 5 µm
- lateral deviation of 50 µm
- minimum number of cycles ≥ 10'000

The compliant structure design was improved to survive high vibration and shock loads. Despite the very efficient launch lock mechanism, resilience to vibration and shock loads remained a critical aspect of the development. The intermediate stages of the compliant structure are only carried by flexible blades. Therefore, the compliant structure internal modes needed to be adjusted to remove any damaging effects. Additionally, the flexible blades buckling limit was improved to survive the high loads observed under shock.

2) The development of the mechanism included a great number of test and investigation in order to guarantee the mechanism performance for the mission. Early testing was performed to reduce development risks. Despite all these tests, some issues arose during the FM validation for which CSEM had to react promptly to find a solution within the very tight mission schedule. The most critical one was the unreliable behavior observed on the flight proven pin-puller. An update of the resetting procedure solved the issue.



Figure 3: CLUPI CFM detailed view of the flexures.

As a conclusion, the CFM design, manufacturing and testing were successfully performed within the schedule and mission constraints. The mechanism was integrated within the CLUPI instrument currently mounted on the EXOMARS rover to be launched in summer 2020. The first images of the Martian ground taken by CLUPI and its focus mechanism are expected to be acquired in spring 2021.

Large Angle Flexure Pivot Development for Future Science Payloads

P. Spanoudakis, L. Kiener, F. Cosandier, P. Schwab, L. Giriens, J. Kruis, D. Grivon

An innovative large angle flexure pivot was developed that is capable of performing an angular stroke of $\pm 90^\circ$ while maintaining a lateral shift error of less than $35 \mu\text{m}$. The findings of the resulting prototype shall be the base for future optical space components operating in a cryogenic environment.

An innovative design of a Large Angle Flexure Pivot (LAFFP) is described. Designed in the frame of an ESA activity, it combines the advantages of flexure mechanisms while surpassing one of their few flaws, small displacement strokes. The LAFFP design exceeds these angular limitations to reach a deflection of 180° ($\pm 90^\circ$). The center shifts laterally by less than $\pm 35 \mu\text{m}$ throughout the full rotation range. The LAFFP is meant to be mounted in pairs, coaxially and with the payload between them. The intended application of the LAFFP is to angularly guide an optical component in a space environment for future science missions operating in a cryogenic environment.

Pivot specifications

The high-level requirements for the pivot mounted in pairs with a mobile payload are:

- Angular range $\pm 90^\circ$ ($\pm 70^\circ$ infinite lifetime)
- Central shift $< \pm 35 \mu\text{m}$ (@ 70°)
- Angular stiffness 0.33 Nm/rad (@ 90°)
- Payload mass 1.8 kg
- Number of cycles $> 3 \text{ million}$
- Pivot mass 440 g , Marval X12 stainless steel
- Temperature range $-125^\circ \text{ to } +50^\circ\text{C}$
- Random vibration $12.2 \text{ grms (X, Y & Z)}$

Extensive FEM analysis was performed to validate the pivot design both at component level and as an assembly mounted on a test bench. Among the component tests performed, the pivot rotary stiffness was measured using a Kistler torque sensor and compared with the FEM values which showed a very good correlation (Figure 1).

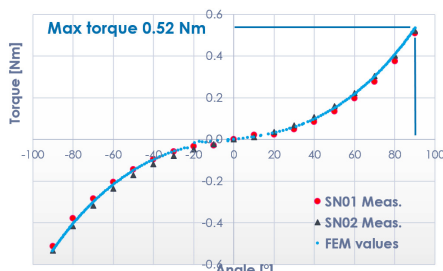


Figure 1: Pivot torque measurement curve.

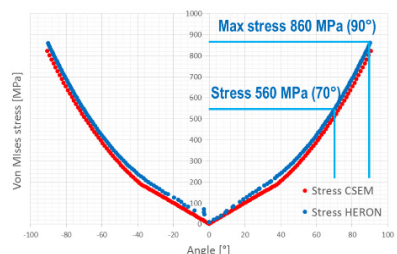


Figure 2: LAFFP blade stress as a function of rotation.



Figure 3: LAFFP Engineering Model.

A dedicated performance test bench (Figure 4) was developed and manufactured to test the pivot characteristics notably the lateral shift using Eddy current sensors. The test bench incorporates a representative dummy payload for mass and inertia, a custom rotary Voice-Coil Actuator (VCA) from Cedrat Technologies (FR) and a Renishaw Tonic angular encoder system for closed loop control. The test bench is operated using a MicroLabox controller from dSpace driving an amplifier on which a dedicated control algorithm was implemented.

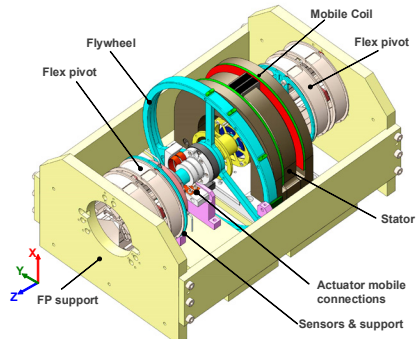


Figure 4: EM Test Bench.

Further FEM simulations were performed with the assembly which included a representative payload in an environment with random vibrations, shocks and thermal cycling. The vibration and shock test bench (Figure 5) incorporate a simplified launch locking device to offload the pivots from the payload.



Figure 5: Vibration test bench with LAFFP pivots assembled.

The pivots were successfully tested, and survived vibration loads for high level sine at 24 g and random vibration at 12 grms in all three directions. The performance tests have confirmed a lateral shift of less than $\pm 35 \mu\text{m}$ over an angular stroke of $\pm 70^\circ$.

Design Optimization for a Metal Additive Manufacturing Pilot Line

J. Kruis, H. Saudan, G. Perruchoud, O. Sereda, M. Dadras, E. Onillon

Metal additive manufacturing (AM) allows, by enabling use of advanced design, production of high added value components, at levels that cannot be reached with conventional manufacturing techniques. Still, the AM-based manufacturing sequence implies large amounts of critical steps – design for AM, AM fabrication, post processing, etc. – compared to conventional production sequences. Presently, the key competencies related to these steps are either not fully implemented at industrial level (process quality monitoring) or dispersed geographically with poor connection between different steps. Relying on two major AM technologies (LPBF: Laser Powder Bed Fusion and EBM: Electron Beam Melting), the H2020 research project MANUELA aims at deploying an open-access pilot line facility, covering the whole production sequence, to show full potential of metal AM for industrial AM production.

The H2020 research project MANUELA will deploy, with the collaboration of 20 EU partners, an open access pilot line addressing limitations of metal additive manufacturing (AM) process, namely limited speed, limited capability of right first-time production, limited number of qualified materials, limited of further data analytics. It is mainly composed of a hardware and dashboard layer as depicted in Figure 1.

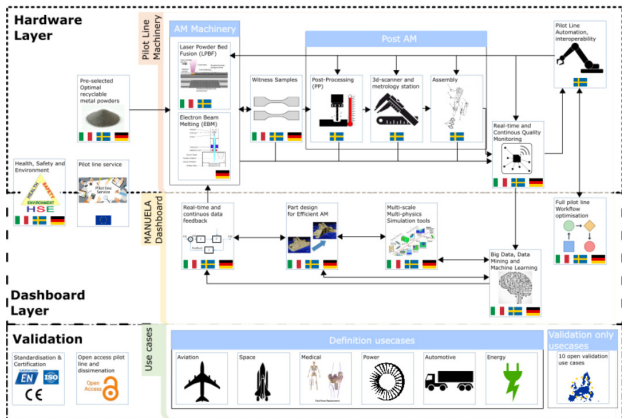


Figure 1: MANUELA pilot line deployment overview.

The pilot line hardware layer covers two main metal-AM technologies, Laser Powder Bed Fusion (LPBF) and Electron Beam Melting (EBM), as well as the post-treatment and which is essential to complete the whole part production sequence, including control and shipping. From a geographical point of view, the LPBF and EBM branches of the pilot line will not be located in the same place, LPBF being deployed in Sweden and Italy, and EBM in Germany. However, the parts production flow generated by each branch will essentially converge to a unique location when it comes to post AM treatments in Gothenburg, Sweden. Machines will be additionally equipped with the state-of-the-art monitoring systems.

The dashboard is comprehensive, with a graphical user interface enabling easy access to the pilot lines software capabilities. A machine learning approach, relying on collected big data and data mining will enable adaptive process parameters and suggests design corrections taking into account the entire pilot-line performance over its lifetime. In parallel, a set of multi scale and multi-physics simulation tools will enable the deployment of a pilot line digital twin. CSEM is playing a pivotal role within the MANUELA consortia re (i) the part design for efficient AM, (ii) the workflow optimization, and (iii) the quality control:

- The part design for efficient AM provides all relevant information enabling users to judge the feasibility and economic advantages of changing the manufacturing of a part or assembly of parts to an AM equivalent. The user just provides a CAD file of their part, answers a short questionnaire, adds assembly interfaces to their part and provides application specific constraints.

- The design tool interfaces with the simulation environment, the data as well as the data mining & machine learning and workflow optimization framework. It offers a manufacturability analysis, part specific process flow selection, suggested part optimisation (minimizing geometric distortions and weight, support structures where needed). It also provides the relevant process and part parameters with the design to the pilot line. As a consequence, less defects and distortions will propagate to the post-AM stage.

- In parallel, the line workflow will be continuously optimized.

The pilot line workflow optimization consists of three levels: part level, lot level, pilot line level. On the part level the inputs from the part design for efficient AM are used to select the optimal workflow for a specific part. On the lot level, the number of components per lot will be maximized by efficient stacking and combining of products with similar materials and workflows. On the pilot line level, usage will be parallelized to maximize workshop usage and reduce waiting times between parts.

The pilot line will be validated by the following 6 use cases from various industrial domains:

- Avionics use case (QIOPTIQ), design and pilot manufacturing of Helmet mounted displays (HMDs) components intended for aerospace applications.
- Space use case (RUAG), design and pilot manufacturing of novel slip rings allowing energy and signal transfers for rotating actuators.
- Medical use case (CBE), design and pilot manufacturing of custom-made cranial implants created by the usage of titanium alloy.
- Power use case (ENEL), design and pilot manufacturing of power plant machinery components subjected to high thermo-mechanical stresses.
- Automotive use case (OEB), design and pilot manufacturing of rocker for motorsport competition.
- Energy use case (SIEMENS), design and pilot manufacturing of gas turbine heat shields.

The project is financed partly by the European Commission under the H2020 program, grant number 880774, as well as the Swiss Secretariat for Education, Research and Innovation (SERI) and for which we would like to thank for their support.

Service-oriented Inference for Crop Classification using Satellite Images

P. Purwar, I. Kastanis, P. A. E. Schmid

The successful application of the crop classification method developed by CSEM in 2018 was followed by further verification to establish the robustness of the approach. Additional crop types were analyzed, and their results demonstrated high precision in classification. The maturity of the algorithm motivated the implementation of an online inference service integrated in the DataBio hub.

There are multiple aspects of a machine learning algorithm that need to be investigated and developed before it reaches a maturity that is attractive for the industry. For this purpose, the proposed approach^[1] was evaluated further with additional crops and a service-oriented architecture was implemented.

The initial study of 2018 focused on developing a crop classifier on wheat parcels using a temporal sequence of satellite images. The two-step approach for building a classifier is further evaluated with two additional crops, maize and legumes. According to agricultural taxonomy, each crop has different sub-varieties. The classifier trained using parcels of wheat sub-variety W_1 was also used to classify other sub-varieties of wheat. A similar approach is used to create and test classifiers for maize and legumes. The results are shown in Figure 1. The details of training and testing can be found in^[2].

Wheat			Maize		
Variety	Parcels	Accuracy	Variety	Parcels	Accuracy
W_1	1312	0.913	M_1	2003	0.859
W_2	882	0.959	M_2	1846	0.819
W_3	239	0.929	Legumes		
W_4	244	0.951	L_1	1437	0.855
W_5	380	0.918	L_2	160	0.250
W_6	335	0.863	L_3	126	0.222
W_7	451	0.911	L_4	163	0.515
W_8	146	0.877			

Figure 1: Classification accuracy for different crops and sub-varieties.

The classifiers trained using only one sub-variety, W_1 and M_1 , were able to classify other unseen sub-varieties of wheat and maize with accuracy greater than 81%. This establishes that the classifiers learn generic features for the crop and do not suffer from overfitting issues. Contrary to wheat and maize, the performance for unseen sub-varieties of legumes is much lower. This is most likely due to the natural variation of the legumes, which contains a plethora of plants such as lentils, beans, peas, etc.

All three binary classifiers are deployed as an online service based on RESTful APIs. The CSEM server receives the parcel information and infers classification results at a pixel level. The average time for a single request takes less than 1 second to compute the probabilities for each pixel in a parcel. The CSEM server is capable of handling multiple requests from multiple clients. The service is integrated in the DataBio platform^[3] with the GeoRocket^[4] data store. GeoRocket displays the crop type for each parcel as declared by farmers as seen in Figure 2. When a parcel is selected, it generates a request to the CSEM server for classification.

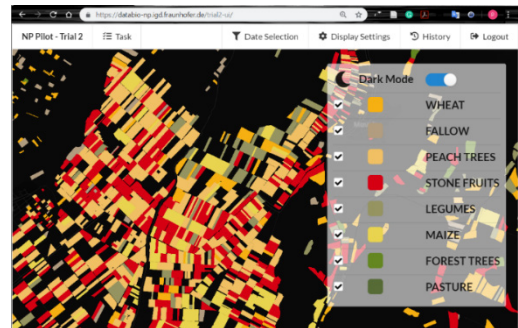


Figure 2: Screenshot of the online DataBio platform.

In Figure 3, a parcel, highlighted in green, has been selected. The declared crop (maize) is shown in top-left corner. Each classifier verifies and analyzes the corresponding satellite data and displays results as a heat map. The results below show that 98% of the pixels in the selected parcel are maize. In addition, the aggregated results are shown as a tick or a cross for each classifier.

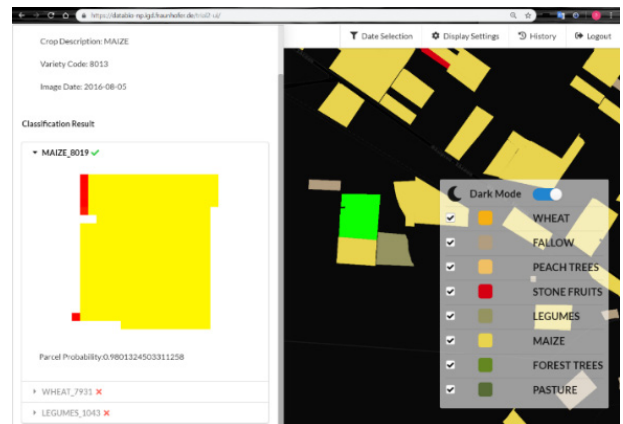


Figure 3: Screenshot of results obtained for selected parcel.

The proposed solution offers an efficient way for those looking to utilize Big Data in the agricultural domain for crop analysis. The two-step approach offers a structured and cost-efficient way of adding new types of crops. It is a cloud ready solution offering privacy through the use of JWT tokens, security, scalability, low latency and portability through Docker containerization.

This project has received funding from the European Union's Horizon 2020 research and innovation programme under grant agreement No 732064.

[1] P. Purwar, I. Kastanis, M. Hoechmer, P. A. Schmid, "Recurrent Neural Network (RNN) based temporal classification of land usage using satellite imagery", CSEM Scientific and Technical Report (2018) 69.

[2] P. Purwar, S. Rogotis, F. Chatzipapadopoulos, I. Kastanis, "A reliable approach for pixel-level classification of land usage from spatio-temporal images", 2019 6th Swiss Conference on Data Science (SDS), Bern, Switzerland, 2019, pp. 93-94.

[3] <https://www.databiohub.eu>

[4] <https://georocket.io/>

In-line Impedance Spectroscopy for Automated Bovine Milk Analysis

C. Beyer, M. Höchmer, T. Volden, J. Goldowsky, R. Limacher

Early screening of somatic cell count (SCC) in incoming raw milk samples loads, i.e. before pooling, is necessary for avoiding waste of large amounts of milk and would enable new services in herd management. In collaboration with an industrial and academic partner, CSEM developed a simple, portable and automated milk analysis tool that determines efficiently SCCs within less than three minutes. This project comprised the elaboration of high-level signal processing and auto-clustering algorithms based on various concepts of machine learning methods.

The quality of bovine raw milk depends, among other factors, on the concentration of somatic cells. A high somatic cell count (SCC > 100 cells / μ l) indicates a potential infection of the cow udder (mastitis) and decreases the quality of dairy products like cheese. Presently, analyses of the somatic cell load in raw milk are performed manually (by classical microscopy) at laboratories of large dairy facilities or fully automated at centralized analytical service laboratories. A microfluidic measurement system, based on impedance flow cytometry, provides a more cost efficient, label-free and real-time determination of SCC (Figure 1).

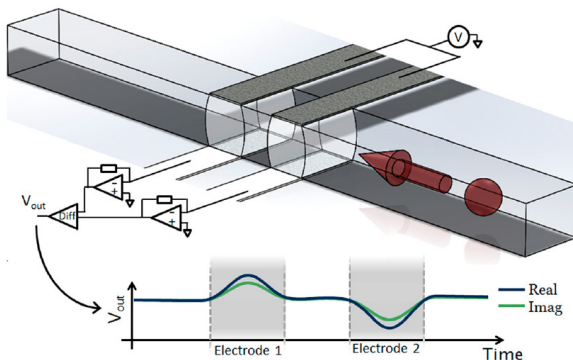


Figure 1: Measurement setup for impedance flow cytometry based on differential impedance spectroscopy – Figure from Spencer et al [1].

In the framework of an InnoSuisse project, CSEM developed in collaboration with a local SME and the University of Applied Sciences Lucerne a novel algorithm for determination of SCC in the range of 10 to 2000 cells per microliter. The project comprised three major steps: data collection, signal pre-processing and SCC determination (Figure 2).

Regarding the first step, a total of over 600 fresh milk samples of various origin including pooled milk from tanks and up to 350 individual cows from 5 different farms were processed over a time period of 18 months. The impedimetric time signal of each sample was recorded at least 4 times for at least 30s. Its somatic cell count was additionally determined by the independent SuisseLab institute.

Major challenge of the analysis is the missing bijective correlation between detected events and somatic cells. Only the somatic cell count, i.e., cell concentration, is known for each measurement sample, thus a correlation between roughly 25 million measurement points and one value has to be found.

An essential focus of the work was directed towards signal pre-processing with the aim to reduce the measured variance of samples with a similar number of somatic cells. Based on the raw time signal, automated algorithms for signal offset correction, event detection, i.e., potential somatic cells, and signal feature

extraction were developed and successfully implemented. Thus, reducing the input data for step 3 by a factor 1000 and more. Various measured parameters could be identified and extracted from the time signal allowing to reduce the overall assessed signal variance.

For the final SCC determination, two data analysis approaches have been investigated in parallel, based either on the time signal of detected events or on extracted signal features. Both approaches utilised and explored various concepts of machine learning, especially the deep learning ones. In the recent decade, deep learning concepts became dominant in the machine learning community for its strong feature of self-learning ability. The algorithm extracts multiple level representations of the data through its deep architecture and learns the underlying structures and sophisticated high-level features of the data. [2].

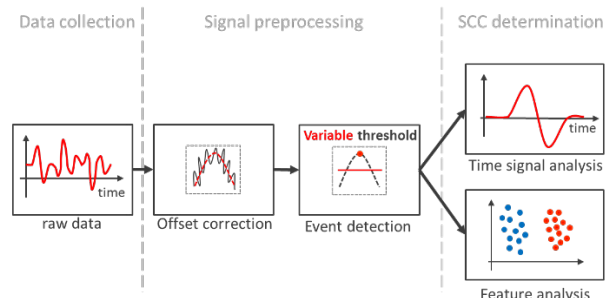


Figure 2: Implemented workflow of signal analysis path.

The first approach explored and optimized a recurrent neuronal network (LSTM) using clipped time signals of detected events from pre-processing. The algorithm estimates the probability for each event to be a somatic cell based on trainings of the assessed fresh milk samples. The second approach focused on cluster algorithms, like DBSCAN, and semi-supervised anomaly detection (AD) methods, such as Gauss-based, Isolation Forest and Robust Covariance, in combination with Support Vector Regression models. The first approach yields more promising results compared to the second, while both approaches provide comparable performance as human experts manually analyzing the measurements.

For final testing, both approaches have been integrated into a lean and cost-efficient embedded system (Raspberry Pi) together with a speed optimized pre-processing algorithm enabling a fully automated determination of SCC. This system is currently being evaluated. The idea is to combine it with the assessment of other milk quality parameters. Hence, the final device integrated as a mobile solution might avoid waste of large amounts of milk enabling novel services in herd management.

[1] Spencer, et. al. (2011) "Positional dependence of particles in microfluidic impedance cytometry." Lab on a Chip 11.7: 1234-1239.

[2] Bengio, et al. (2013) "Representation learning: A review and new perspectives." IEEE transactions on pattern analysis and machine intelligence 35.8 (2013): 1798-1828.

3D Lightfield Inspection System for Zero-defects Manufacturing

J. Pierer, M. Kirschmann, P. A. E. Schmid

State-of-the-art MEMS devices are found in many applications with various functionality. One thing all these MEMS devices have in common is their three-dimensional nature. There is a strong need for automated inspection tools that can inspect such 3D micro structures. CSEM is working within the European funded project CITCOM^[1] together with partners on a potential solution implementing a 3D Lightfield camera. The system is based on a commercial wafer prober and therefore simple to implement into existing manufacturing environments.

Quality control in manufacturing is a vast field and we cannot cover all of its aspects here but concentrate on microsystems and MEMS. Whereas the IC industry has developed many planar inspections tools, there is an urgent need for structural inspection of 3D microsystem as shown in Figure 1 and Figure 2. The first image shows a "flex-to-rigid" structure which was designed to assemble a complex electronics and MEMS transducer system into tips of smart catheters^[2], by folding the connected segments into the catheter tip. The second shows a dispensed dot of conductive adhesive used to bond an ASIC onto a PCB.

CSEM is working within the European project CITCOM to fill this gap in the manufacturing cycle by developing a fully automated 3D inspection system based upon two 3D light-field cameras, provided by the CITCOM partner company Raytrix^[3] (see Figure 3).

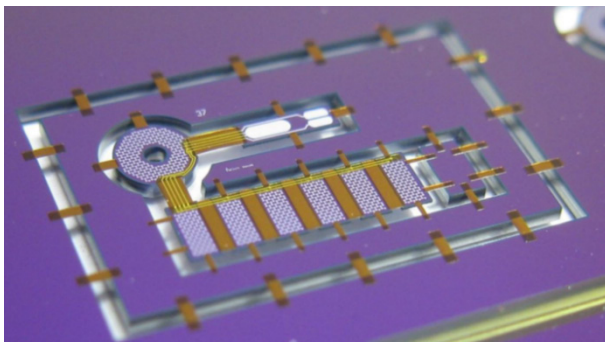


Figure 1: Flex-to-Rigid structures are fabricated wafer scale in a planar technology and are highly 3D structured (Image by courtesy of Philips Electronics Nederland B.V.).

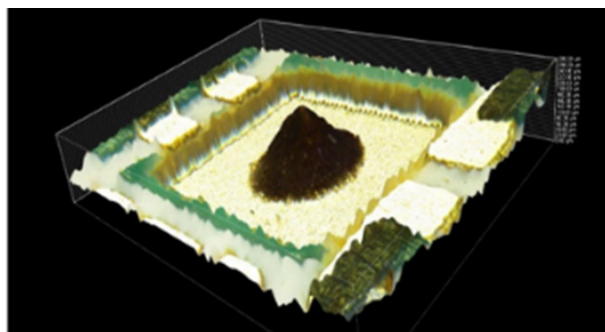


Figure 2: Image with correctly dispensed dot of silver epoxy adhesive for later ASIC placement (Image by courtesy of Microsemi Semiconductor Limited UK).

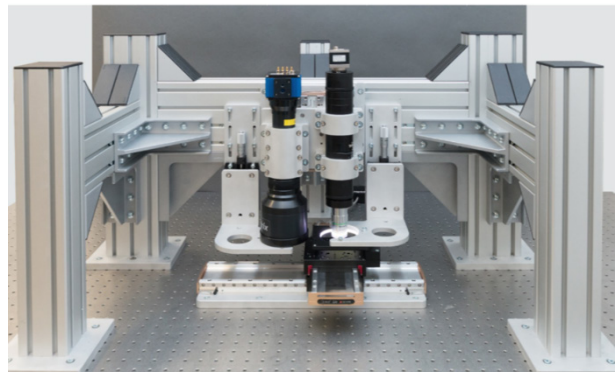


Figure 3: 3D Lightfield development setup.

The two cameras are combined to allow for fast low-resolution and slower high-resolution inspections (see Table 1). Two stacked linear stages enable the scanning of substrates up to 200 x 200 mm². This system represents an intermediate step towards a fully integrated wafer prober setup (in collaboration with CITCOM partner aixACCT)^[4]. All hardware components are driven by the modular software framework CSEM VISARD^[5].

Table 1: Main features of 3D optical inspection system.

	"R26 CITCOM" & Sill S5LPJ1268 3x	"R12 CITCOM" & Mitutoyo 20x
<i>working distance</i>	48 mm	20 mm
<i>field of view</i>	7.8 x 7.8 mm ²	0.65 x 0.44 mm ²
<i>lateral resolution</i>	3 um	0.7 um
<i>depth of field</i>	1.1 mm	60 um
<i>depth resolution</i>	2.5 um	0.4 um
<i>frame rate (max)</i>	81 fps	30 fps

The software will implement various access levels. A process engineer for example will be able to set up inspection processes and has access to data such as processed 3D images while an operator may only start a predefined process and receives abstracted detection results. Image processing for defect recognition will be based on convolutional neural networks, implemented in collaboration with partner BIC^[6] while metrology tasks could be based on traditional image processing algorithms. Data in- and output for, e.g., found defects will be based upon industry-standard wafer map files.

Finally, the entire system including metrology and defect recognition will run fully automated once the workflow has been properly implemented.

[1] www.citcom.eu; This project has received funding from the European Union's HORIZON 2020 research and innovation program under Grant Agreement no. 768883.

[2] <http://informed-project.eu/downloads/F2R.html>

[3] Raytrix GmbH, Schauenburgerstraße 116, D-24118 Kiel, Germany.

[4] aixACCT Systems GmbH, Talbotstr. 25, 52068 Aachen, Germany.

[5] M. Höchemer, I. Kastanis, P. A. Schmid, "VISARD - Vision Automation Robotics Designer", CSEM Scientific and Technical Report (2016) 95.

[6] Brunel Innovation Center, Granta Park, Great Abington, Cambridge, CB216AL, United Kingdom.

Process Design and Automation for Large Volume Hybrid Manufacturing Robot with High Accuracy and Quality

F. Crivelli, A. Steinecker, P. A. E. Schmid

A new machine combined with innovative manufacturing processes and technology bringing the advantages of 3D printing to large volume fabrication.

Industrial fabrication based on 3D printing or hybrid processes that combine additive (AM) and subtractive manufacturing (SM), is growing. Important sectors such as aerospace, energy industry, automotive, shipbuilding, oil & gas, etc demand large, high quality components. These branches could considerably benefit from AM and *hybrid manufacturing* (HM) technology; however, available machines are limited to small workspace and today there is no solutions for large parts. A large workspace ($>200 \text{ m}^3$) implies multiple challenges preventing a simple “scaling up” of existing technologies^[1]. The European Project KRAKEN^[2] addresses to this challenge with the objective of making 3D printing and rapid prototyping compatible with large volumes and finding an economically sustainable solution to guarantee high accuracy over large workspaces. The resulting machine is composed by a 6 degrees-of-freedom (DOF) manipulator (NJ130, Comau S.p.A., Torino, I) mounted on a 3-axes crane. The crane guarantees a large workspace (22x5.5x3.5 m), while the manipulator provides high agility. The end-effector was designed as a hybrid head including a permanently mounted spindle for SM completed by a retractable mechanism with automatic quick tool change, for easily switching from resin to metal AM.



Figure 1: Climb-up HM process, (left) Resin AM; (right) Milling.

Within the KRAKEN consortium several technology bricks were elaborated. A new machine-dispensable resin was developed. The 2-component polyurethane paste (ALCHEMIX PU3720A/B, Alchemie Ltd, Warwick, UK) cures rapidly and once cured it can be machined easily. A resin dispenser with deposition rate up to 120 kg/h was developed. Furthermore, *wire arc additive manufacturing* (WAAM) was included for aluminium 3D printing with deposition rate up to 1.5 l/h; and *arc spray metallisation* based on zinc alloys was developed to integrate metallic substructure and surfaces within resin parts. Traditional SM process has been adapted based on a *climb-up* methodology, specially designed for planar layer-by-layer and direct 3D freeform production (2 mm depth of cut and 6m/min speed for standard processes and up to 750 mm/min for high accuracy of $<0.1 \text{ mm}$ geometric error). Such hybrid process allows good finishing on difficult-to-reach areas as well as better controlling thermal stresses and deformations.

[1] F. Crivelli, et al., "An all-in-one robotic platform for hybrid manufacturing of large volume parts," In: Ratchev S. (eds) Precision Assembly in the Digital Age, IPAS 2018, 2019.

[2] <https://krakenproject.eu>

CSEM played a key role in developing the KRAKEN software suite, which provides user interaction combined with hardware integration, control tools and automation functionalities. This guarantees an efficient process flow from 3D models to manufactured parts. New computer aided manufacturing (CAM) tools including planar horizontal layer strategies and new direct 3D freeform approaches have been developed in an intuitive user interface dedicated to generation and simulation of HM tasks. High geometric accuracy over the large workspace, is guaranteed based on *laser tracking technology*^[3]. The laser tracker (AT960, Leica/Hexagon MI, Unterentfelden) provides real-time (1 kHz) measurement of absolute position and orientation of machine components and end-effector. The control software designed by CSEM integrates the laser tracker feedback in the robot motion control, to dynamically correct the deviations with respect to the reference trajectories. The metrology system is fully integrated within the KRAKEN software allowing automated calibration and continuous monitoring of the machine. Laser scanning technology combined with the laser tracking system provides in-process geometry validation of the parts^[3]. The KRAKEN machine was used to manufacture a mock-up of a Pininfarina (S.p.A., Turin, I) car design. The task was successfully completed based on climb-up approach, validating this novel HM process, as well as verifying the new CAM functionalities and the laser tracker-based robot controller. 5-DOF resin dispensing combined with arc spray metallisation has been validated by Acciona (S.A, Madrid, S) in the fabrication of hybrid lining panels for road tunnels, which embed electrical wiring for the emergency lighting. CRF (Torino, I) is testing the deposition of metals on composite materials to simplify assembly. Moreover, the KRAKEN machine was used to mill a wood mock-up of 90 m², installed in a museum in Qatar; to machine a big composite beam (Acciona); and polishing a windmill blade for a renewable energy company.



Figure 2: The KRAKEN robot machining the Pininfarina car mok-up.

This project received funding from the European Union's Horizon 2020 research and innovation programme (No 723759).

[3] F. Crivelli, V. Baumann, et al., "Large volume hybrid manufacturing based on absolute laser tracking technology ", In: Proc. of the 1st ICWNNDT, 2018, in press.

ModelStore—A Lightweight System for Storing Neural Network Models

I. Kastanis, M. Höchemer, E. Ntavelis, P. Purwar, P. A. E. Schmid

ModelStore is an easy to use framework for storing and managing neural network models. It offers extensibility, portability, traceability, and reproducibility. Minimal effort is required for storing a model making it an optimal solution for integration into existing machine learning based pipelines. It enables users to keep track of multiple models with practical overviews of the most important parameters, metrics, and results. It is a fundamental building block for any life-long learning application by managing model specific data upon which automatic decision support systems can be developed.

Training machine learning models is currently a laborious and manual task. The storage and management of the different instances of models is often left at the hands of the expert operator and typically lacks standardization and structure. While this works for brief periods of time, in the long run it becomes intractable to retrieve information about the model origins, its performance and training parameters. The often-used file and folder naming schemes fail to capture sufficient information about the model, are cumbersome to extend and do not provide informative overviews of the trained models.

ModelStore overcomes the aforementioned issues by standardizing the storage of models by managing not only the instances of the trained models but also their linked data.

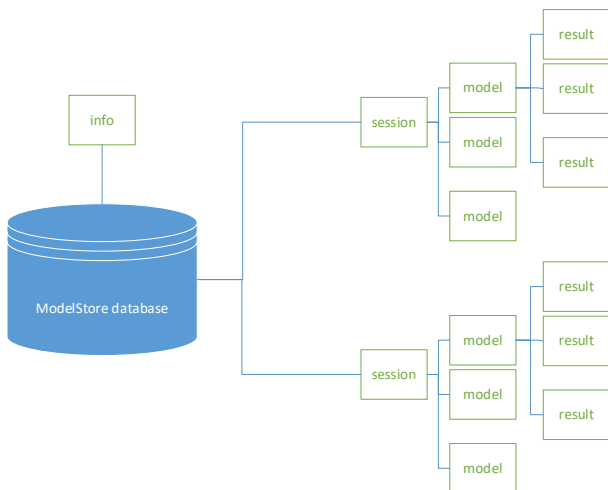


Figure 1: ModelStore database architecture.

The ModelStore consists of multiple layers. In the lowest level is a SQLite^[1] database with the architecture shown in Figure 1. On top of this a Python layer, encapsulating the most common machine learning frameworks (keras, tensorflow and Pytorch), offers functionality to push and pull models into the database with simple to use functions overcoming the need to write lengthy queries. Finally, a C# layer with graphical user interfaces can be used for deployment purposes.

The modular architecture allows users to easily extend the framework to fit their specific requirements. In practice SQLite

[1] <https://www.sqlite.org>

[2] <https://git-scm.com/>

queries are the common interface that allows implementation in any programming language. The SQLite database is self-contained and cross-platform. Porting means copying a single file. The framework generates a unique identifier for each model by hashing it. In this manner each model can be identified, and its origins traced, even in the case of stray models that are no longer inside the database. To be able to reproduce a model the source code that was used for training is referenced in ModelStore by integrating the version control software Git^[2]. The framework is capable of automatically inserting the latest commit ID in the database, which can then be used to retrieve the complete source code that was used for generating the model.

ModelStore has been integrated in CSEM's Visard^[3] platform that enables the design and execution of complete automation systems according to Industry 4.0 design principles. Small batch highly customized production lines can utilize Visard's advanced machine learning capabilities to efficiently introduce product variations and decrease integration time.

ModelStore is a framework designed for both development and deployment purposes. It is an invaluable tool during development, in particular for large teams of developers facilitating effortless knowledge exchange in the area of machine learning. Unused models can be stripped from a database for the purposes of deployment, while at the same retaining all the descriptive information required.

Life-long learning approaches present the true potential of machine learning. They enable dynamic solutions that can adapt to changing conditions. Such methods pave the road towards more advanced types of artificial intelligence. Currently such adaptive machine learning solutions that can incrementally learn on dynamic environments are rare, and mainly restricted in research environments. ModelStore offers a foundation for gathering models as well as related descriptive data in a systematic and efficient manner. Upon this foundation decision support systems can be built that determine the right time to train a new model and assess its performance in comparison with other instances of that model, while at same time being able to trace all of these steps.

[3] M. Höchemer, I. Kastanis, P. A. Schmid, "VISARD —Vision Automation Robotics Designer", CSEM Scientific and Technical Report (2016) 95.

Ultra-low-power Status Indication Device

T. Burch, C. Beyer, S. Bitterli, M. Fretz, J. Kaufmann, E. Schaller, R. Nussbaumer*, B. Zemp*

CSEM has developed an ultra-low power low-cost indication device to display the status of electrical fuses for mains powered devices. The indicator is based on polymer dispersed liquid crystals, excels state-of-the-art solutions based on LEDs and complies with the latest IEC norms regarding power consumption and safety. The development was conducted in cooperation with SCHURTER AG.

Fuses are among the first components in the history of electrical power engineering. Without fuses, the use of electricity as an energy source would be too risky. Because of their simple design and reliable function, electrical fuses have become the epitome of safety in electrical circuits.

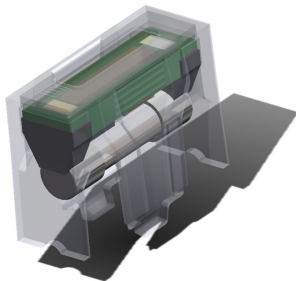


Figure 1: Graphical representation of a fuse holder with integrated status indicator based on PDLC film.

Most fuses in electrical building installations are equipped with a fuse state indicator to recognize broken fuses at first glance. However, in mains powered devices fuses are mostly mounted in fuse holders without indicator, mainly because there is no suitable and inexpensive solution around. Originally, fuse indicators for mains powered devices were based on miniature light bulbs which consume quite some energy, lack galvanic isolation and therefore, mostly due to non-compliance to latest IEC norms, disappeared from the market. Recent solutions use LEDs as an indicator. But these designs require dedicated electronics such as AC-DC power converters to drive the LEDs and therefore add complexity to the otherwise simple system.

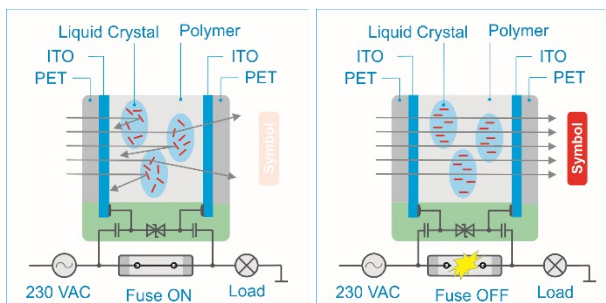


Figure 2: Schematics of operational principle for the novel ultra-low-power status device developed in cooperation with SCHURTER AG.

The novel indicator developed at CSEM (Figure 1) is based on polymer dispersed liquid crystals (PDLC). These materials consist of a polymer liquid crystal film sandwiched between two indium tin oxide (ITO) coated PET films.

In the off-state, the PDLC appears opaque because it strongly scatters light due to the refractive index mismatch between the misaligned LC droplets and the polymer, whereas in the on-state the PDLC becomes transparent because of the LC reorientation in the electric field. This effect is exploited to make a symbol

visible or invisible behind the PDLC element, depending on the state of the fuse (Figure 2). To control the state, the voltage built-up across the tripped fuse is directly applied to the PDLC element using a simple capacitive voltage divider. No complex electronics are required, and the power consumption is about 10 times lower than of indicators based on LEDs.



Figure 3: Small series production of fuse status indicators in the laboratory.

The development was conducted in two phases. First, the light transmissions of different PDLC samples were determined as a function of control voltage, frequency, and temperature. At the same time, the PDLC materials were subjected to environmental tests including temperature shock, humidity, and accelerated aging tests. The investigated materials differed noticeably in transmission and temperature behavior. In a second phase, manufacturing and packaging processes have been developed in order to produce indicators of different sizes and shapes and protect the films from environmental impacts. Processing the individual PDLC layers by means of specifically developed laser cutting techniques, as well as the reliable electrical contacting of the ITO layers presented a particular challenge. Both could be satisfactorily solved. Ultimately, a manufacturing and packaging solution could be found with high potential for industrialization (Figure 3).

Parallel to the PDLC packaging, the mechanical design of the entire fuse holder and the integration of the indicator was developed. Dedicated elastomeric connectors have been used to contact the PDLC film to the fuse. This design simplifies the entire mechanical structure and production assembly, since no metallic clamps or springs are required to be installed (Figure 1). The novel ultra-low-power status indication device offer compact design while reducing the production cost by 50% compared to state of the art devices.

The novel status display is now part of a technology platform, which in future can also be used in smaller fuse holder types or in different other products where indication of a binary status is of interest. A market launch in near future is envisioned.

* SCHURTER AG

Continuous Non-invasive Blood Pressure Monitoring during General Anesthesia Induction

M. Proen  a, Y. Ghamri*, G. Bonnier, F. Braun, P. Renevey, D. Ferrario, A. Lemkadem, C. Verjus, P. Schoettker*, M. Lemay

Automated brachial cuffs are used to monitor arterial pressure (AP) in most anesthetized patients. Commonly inflating at regular intervals of 3–5 minutes, these devices only provide an intermittent monitoring, and may miss rapid hypotensive or hypertensive events. We investigated the ability of our oBPM® algorithm in detecting such changes in AP in 40 patients undergoing general anesthesia from pulse oximeter photoplethysmographic signals. The results demonstrated good trending ability in detecting rapid changes for both systolic and mean AP. Implemented in clinical settings, this solution may help in decreasing the duration of intraoperative hypo-/hypertensive events, thereby improving clinical outcome.

Arterial pressure (AP) is routinely monitored by means of automated brachial cuffs in most anesthetized patients. These devices only provide intermittent measurements, typically at intervals of 3 to 5 minutes. Thus, rapid intraoperative hypotensive events – associated with postoperative complications^[1] – may go unnoticed. We investigated the ability of our oBPM® algorithm^[2] in detecting such rapid changes in AP by pulse wave analysis of photoplethysmographic (PPG) signals acquired at the fingertip.

In a clinical study^[3] (ClinicalTrials.gov ID: NCT02651558) in 40 patients scheduled for an elective surgery necessitating invasive AP monitoring, we evaluated the trending ability (ability to track AP changes) of our oBPM® algorithm applied to pulse oximeter PPG signals compared to the invasive method. Significant AP changes – commonly defined as changes of at least $\pm 20\%$ ^[4] – were automatically identified in the invasive data. In particular, changes occurring of various durations, from 30 seconds up to 5 minutes, by increments of 30 seconds, were identified. The trending ability was assessed through four-quadrant plots and polar plots, using the concordance rate (CR), the angular CR at $\pm 30^\circ$, and the angular bias as trending performance metrics.

Figure 1 shows the results for mean AP (MAP). The upper panel (four-quadrant plot) depicts excellent concordance (CR = 100 %). The lower panel (polar plot)^[5] confirms this concordance (angular CR at $\pm 30^\circ$ of 100 %), with an angular bias of -3° . By analogy with non-invasive cardiac output monitoring techniques^[5], good trending ability can be claimed with CR > 90–95 %, angular CR at $\pm 30^\circ$ > 90–95 %, and angular bias < $\pm 5^\circ$. The results shown in Figure 1 are for rapid changes occurring over a time span of 60 seconds. Similar performance was obtained for faster (30 seconds) and slower (90 seconds) changes, complying with the aforementioned criteria. With changes of 120 seconds and more – of lesser clinical importance as they are less likely to be missed by a cuff – the criteria were not met anymore. Nevertheless, the CR, the angular CR at $\pm 30^\circ$, and the angular bias remained respectively > 97 %, > 89 %, and < $\pm 8^\circ$ for changes of all durations, up to 5 minutes. Results for systolic AP showed comparable behavior, complying with the criteria for changes ≤ 90 seconds as well.

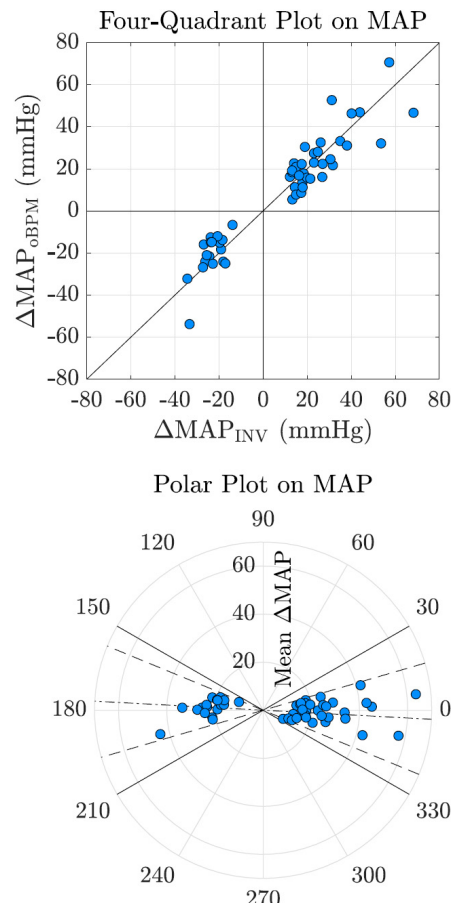


Figure 1: Four-quadrant plot and polar plot demonstrating the trending ability of the oBPM® algorithm for mean AP (MAP). The dash-dotted line in the polar plot depicts the angular bias, and the two dashed lines the 95 % confidence interval.

Rapid and possibly deleterious changes in AP may be missed by the current non-invasive monitoring solutions (brachial cuffs). Without requiring any additional equipment in the operating room – pulse oximeters being already part of standard equipment – our solution has shown to be able to detect rapid changes both in systolic and mean AP with good accuracy. Implemented clinically, this solution may be used for the "intelligent" triggering of cuff measurements, thus decreasing the duration of hypo- and hypertensive events, thereby improving clinical outcome.

* Department of Anesthesiology, Lausanne University Hospital and University of Lausanne, Switzerland

[1] M. Walsh, et al., "Relationship between intraoperative mean arterial pressure and clinical outcomes after noncardiac surgery: toward an empirical definition of hypotension", *Anesthesiology*, 119 (2013) 507.

[2] M. Proen  a, et al., "Method, apparatus and computer program for determining a blood pressure value", WO 2016138965 A1, 9th of September 2016.

[3] Y. Ghamri, et al., "Automated pulse oximeter waveform analysis to track changes in blood pressure during anesthesia induction", submitted manuscript, 2019.

[4] J.B. Bijk  , et al., "Incidence of intraoperative hypotension as a function of the chosen definition: literature definitions applied to a retrospective cohort using automated data collection", *Anesthesiology*, 107 (2007) 213.

[5] L.A. Critchley, X.X. Yang, A. Lee, "Assessment of trending ability of cardiac output monitors by polar plot methodology", *J. Cardiothorac. Vasc. Anesth.*, 25 (2011) 536.

Noninvasive Measurement of Pulmonary Artery Pressure via EIT

F. Braun, M. Proen  a, M. Sage*, J.-P. Praud*, M. Lemay, A. Adler**, E. Fortin-Pellerin*

There is a high clinical demand to measure pulmonary artery pressure (PAP). However, existing solutions are either highly invasive or only allow for intermittent measurements by a trained clinician. Research at CSEM during the last years has revealed a potential alternative to measure PAP by means of electrical impedance tomography (EIT). Being low-cost and safe, EIT allows for the fully noninvasive and continuous measurement of PAP. This was first evaluated in a study on healthy volunteers, confirming its potential. More recently, these findings were corroborated in a second study on neonatal lambs where EIT-derived measurements were compared to the invasive gold-standard PAP reference over a large range of pressure values. These promising results pave the way towards a novel way of PAP measurement in clinical settings.

While non-invasive measurements of systemic arterial pressure are routine, few techniques exist to measure pulmonary artery pressure (PAP). Even though PAP can be measured with ultrasound, it requires a high level of expertise, is not possible in all patients, and cannot provide continuous readings. A potential solution is electrical impedance tomography (EIT), a noninvasive medical imaging modality. With EIT and CSEM's original approach^[1], the pulsatile signal measured in the lungs can be used to estimate the pulmonary pulse arrival time (PAT) which is inversely related to PAP.

In a first study, this approach was tested on 27 healthy human volunteers in a controlled desaturation study. EIT-derived PAP showed good agreement with transthoracic echocardiographic (TTE) measurements^[2,3], as also shown in Figure 1.

In a second step, this approach was verified against the gold-standard PAP reference (right heart catheter) and with larger variations in PAP. To this end, an animal experiment was performed on 11 healthy neonatal lambs. Analysis on four animals led to a high overall correspondence between EIT and gold-standard PAP measures with an average correlation of $r = 0.81$ (range 0.76 – 0.87). Representative data for one animal is shown (Figure 2), showing good agreement between PAP measures, except in the last phase of the protocol, in which the epinephrine injection caused a decreased duration of the pre-ejection period, thereby affecting the EIT-derived PAT measurement. Data of three animals were rejected due to EIT

electrode errors or missing data. In four more animals there was no lung signals present in the EIT data, which is assumed to be due to circulatory shunts in young animals. This phenomenon has never been observed in EIT recordings on humans (neither healthy nor patients) and corroborates the assumption that it is due to the animal model and likely not a limitation of our approach.

Our results demonstrate the feasibility for non-invasive and continuous monitoring of PAP by means of EIT in an unsupervised manner. This opens new perspectives for the clinical management of pulmonary hypertensive patients.

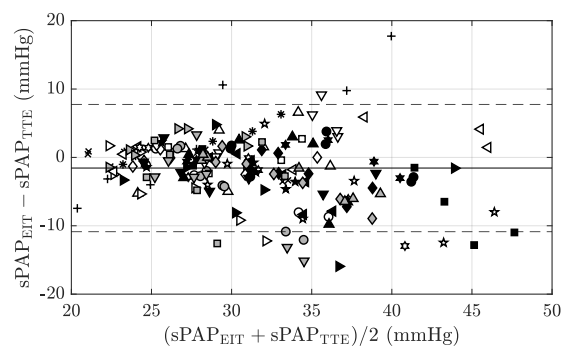


Figure 1: Bland-Altman plot comparing EIT-derived systolic PAP (sPAP) versus TTE-derived sPAP for 27 healthy human volunteers undergoing normobaric hypoxia exposure in a controlled desaturation study.

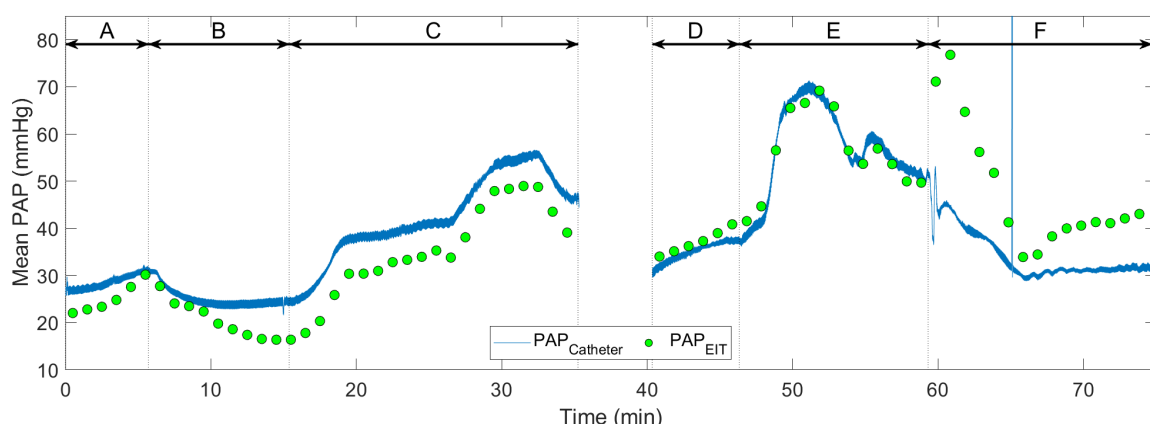


Figure 2: Invasive reference PAP_{Catheter} versus PAP_{EIT} for one representative animal. A: $\text{FiO}_2 = 21\%$, B: $\text{FiO}_2 = 100\%$, C: $\text{FiO}_2 = 12\text{--}14\%$, D: $\text{FiO}_2 = 21\%$, E: $\text{FiO}_2 = 12\text{--}14\% + \text{hypoventilation}$, F: $\text{FiO}_2 = 100\% + \text{epinephrine}$.

* Universit   de Sherbrooke, Sherbrooke, Canada
** Carleton University, Ottawa, Canada

^[1] J. Sol  , J. Brunner, "Method and Apparatus for Time-Based Analysis of Electrical Impedance Tomography Data", Patent: WO/2012/007425 (2012).

^[2] M. Proen  a, et al., "Non-invasive monitoring of pulmonary artery pressure from timing information by EIT", Physiological Measurement, vol. 37, no. 6, pp. 713–726 (2016).

^[3] M. Proen  a, et al., "Non-invasive pulmonary artery pressure monitoring by electrical impedance tomography: validation in a preclinical controlled desaturation study", in preparation, 2019.

Driven Shield for a Robust Heart Bio-potential Monitor for Stress and Wellbeing Applications

P. Heck, G. Banderet, M. Crettaz, E. Haenni, P. Liechti, J.-N. Pfeuti, M. Rapin, O. Chételat

Smartbeat is a wearable sensor recording heartrate variability, physical activity, sleep and stress in lifestyle assessments for better wellbeing. To identify and make stress-reducing behavioral changes actionable by the user, data needs to be accurate and available in real time for analysis and feedback. This project developed a technology which combines an innovative electronic circuit with superior EMI and ESD immunity, as well as a Bluetooth Smart connected device optimized for cloud-based computing of context detection and real-time actionable feedback.

Wearable ECG is subject to electromagnetic interference (EMI) and electrostatic discharge (ESD) which limit accuracy of beat-to-beat detection especially when superimposed to motion artefacts produced by intense activities, representing up to 5–7% of monitoring time. Analytics of heartrate variability offer rich and holistic assessment of the wellbeing of the user, therefore increasing the robustness of electronics to perturbations and therefore improving data quality. Furthermore, actionable feedback based on automatic context detection significantly improves the value of this analytics and leads to better user acceptance and market penetration. CSEM together with its finish partner Firstbeat, proposed the Smartbeat concept to address these two issues.

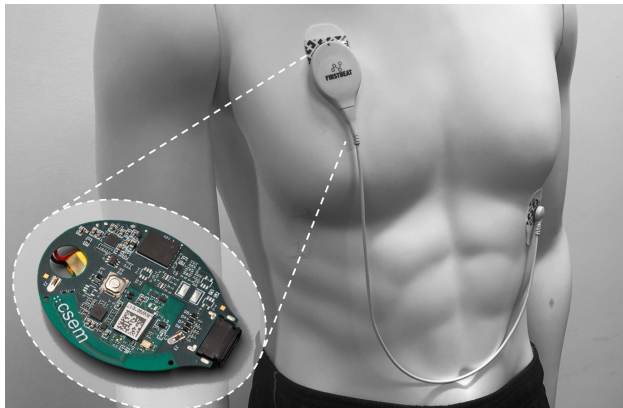


Figure 1: Smartbeat wearable heart rate monitor.

Figure 1 illustrates the miniaturized PCB implementing the driven shield and a Bluetooth Smart communication. The proposed electronic circuit uses two gel electrodes to measure ECG, and a third dry electrode to improve the robustness against EMI generated by various electronic devices or fluorescent lamps. Figure 2 illustrates the activation of the driven shield and consequent suppression of perturbations on the baseline signal.

Preliminary measurements show a significant reduction of EMI generated by various electronic devices or fluorescent lamps. Figure 2 illustrates the activation of the driven shield and consequent suppression of perturbations on the baseline signal.

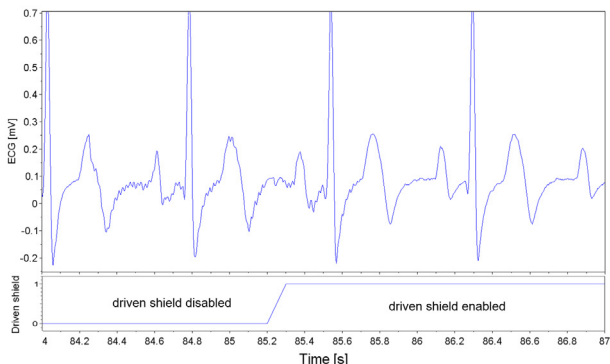


Figure 2: EMI resilience before and after activation of the driven shield.

Additional measurements show the strong attenuation of ESD events generated by synthetic garments. Figure 3 compares the behavior of a commercial device (in red) featuring several "additional" spikes similar to R-peaks, while the driven shield (in blue) absorbs most of ESD events and shows mainly regular R-peaks (green arrows).

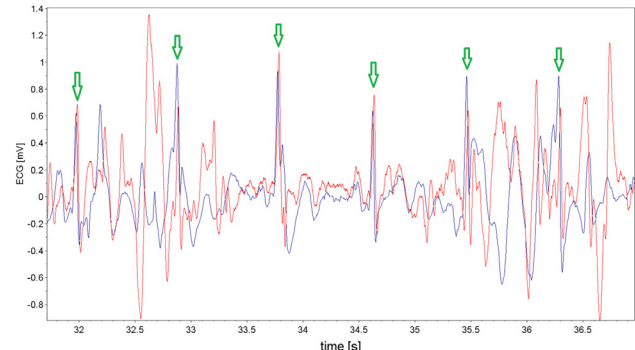


Figure 3: ESD resilience (driven shield in blue, commercial sensor in red).

Special attention has been paid to implement a seamless wireless connection to the cloud via a mobile device. Either live data can be streamed on-demand to a mobile device for instantaneous display, or recorded data can be seamlessly uploaded to the cloud by a background running task (via the mobile device). This synchronization process has been specifically optimized for frequent disconnections between the sensor and mobile device without compromising efficiency and focused to upload most recent data first.

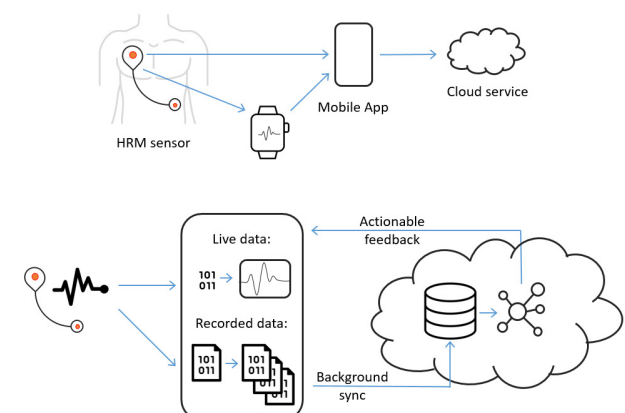


Figure 4: Connected device for actionable feedback.

The sensor developed at CSEM proposes a circuit with very high immunity to EMI and ESD events, and an almost real-time and seamless data upload to a cloud service, enabling a user actionable feedback while maintaining a monitoring autonomy of more than 1 week.

The project is supported by Innosuisse and EUREKA under the Eurostars-2 Program (E! 11944) and we thank them for their support.

MDFD—a Portable Medical Device for Measuring the Electromechanical Properties of Skeletal Muscles through Electrical Stimulation

J. Wacker, G. Yilmaz, E. Haenni, P. Liechti, M. Crettaz, S. Droz, M. Frosio, J. Jemec, S. Djordjevic, J. Žumer, S. Rozman, O. Chételat

Developed together with the Slovenian company TMG-BMC in the framework of a Eurostars project, MDFD allows assessing the health state of skeletal muscles by measuring their mechanical and electrical responses to an electrical stimulus. While CSEM designed and manufactured the electronical and mechanical hardware, as well as the embedded software of the device, the industrial partner developed algorithms for extracting relevant indicators from the measured data and performs trials on volunteers.

Musculoskeletal disorders affect more than 1.7 billion people worldwide. Existing diagnostic methods lack accessibility and are expensive and time-consuming. The MDFD project (medical device for measuring electro-mechanical properties of skeletal muscles) aims at developing a cost-effective, fast, portable, non-invasive, and selective tool for diagnosing pathologies. The device developed at CSEM has three modules: a stimulating module which injects precisely controlled electrical impulses into a selected muscle; a stylus probe which measures the mechanical displacement of the muscle (tensiomyography, TMG); and an electromyography (EMG) module which records the electrical response of the muscle after the electrical stimulation. The simultaneous recording of TMG and EMG allows quantifying training- and illness-induced changes of muscle fibers and their ability to contract.

The MDFD device shown in Figure 1 consists of a hand-held device and a table-top device. The hand-held device contains a trigger for starting the stimulation and a stylus probe for measuring the displacement of the muscle. The main parts of the electronics are located in the table-top device. They include the EMG module, batteries which make the device portable, and a Bluetooth module for communication with a smartphone and/or tablet. The inset in Figure 1 shows the setup of a recording with the MDFD device.

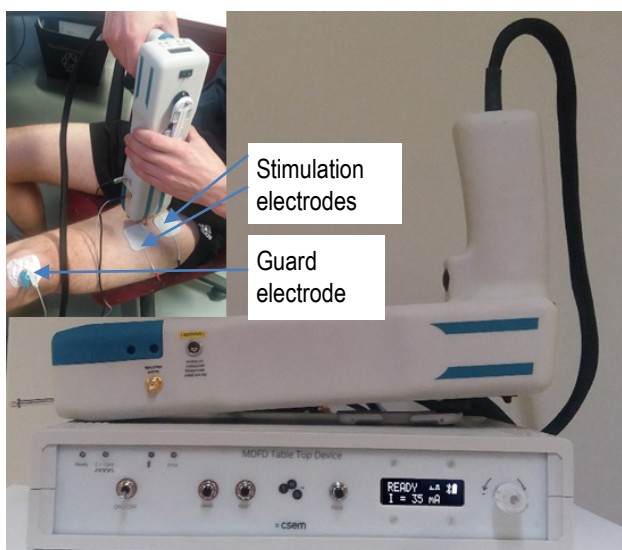


Figure 1: MDFD demonstrator, comprising (1) a hand-held device and (2) a table-top device. Inset: Use of the MDFD device on the vastus medialis muscle. The EMG recording electrodes are integrated in the hand-held device.

[1] "Medical electrical equipment – Part 1: General requirements for basic safety and essential performance", International Standard IEC 60601-1.

An important aspect of the development was the electrical safety of the device, since it is meant to inject electrical stimuli into the body. Therefore, the development was guided by the quality management system of our Medical Device Technology research activity (ISO 13485-certified), in particular the parts related to risk analysis and control, and by applicable standards^[1,2].

Figure 2 shows EMG and TMG curves from a surface transcutaneous femoral nerve stimulation in the inguinal region with a 90 mA x 1 ms impulse. The MDFD allows assessing simultaneously the mechanical and electrical activity of a muscle. In this regard, one of the most unique and important parameters is the ratio between the EMG and TMG amplitudes. This parameter is called the muscle performance index and is considered an objective parameter of the status of a muscle. The following additional figures—indicative for the health status of a muscle—are also derived from the EMG and TMG curves: contraction velocity, level of sustained contraction, relaxation velocity, muscle fibers composition, and maximum muscle force and endurance parameter. The industrial partner now studies if these data allow quantifying the recruited motor units and their ability to contract. Detailed results are expected at the end of 2019. In a future integration, the electronics will be further miniaturized and completely integrated in the hand-held device.

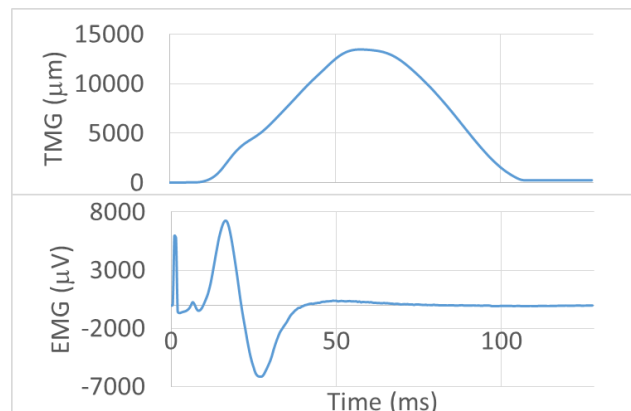


Figure 2: TMG and EMG signals recorded from transcutaneous nerve stimulations of the inguinal region with a 90 mA x 1 ms impulse.

This project has received funding from InnoSuisse through the Eurostars research and innovation program (project number: E!11095). This support is gratefully acknowledged.

[2] "Medical electrical equipment – Part 2-40: Particular requirements for the safety of electromyographs and evoked response equipment", International Standard IEC 60601-2-40.

Body Fluid Transfer

M. Crettaz, T. Maulaz, J.-P. Porchet, P. Pilloud, R. Rusconi, G. Dudnik, M. Lemay, M. Correvon

According to the World Health Organization, lymphedema affects over 250 million people worldwide. Despite this fact, the research evaluating the lymphatic system and the effectiveness of treatment has been scarce. The unfortunate result is that far too many patients are left undiagnosed and untreated and therefore have pain and suffer unnecessarily. The symptoms of lymphedema can be managed, however, with manual or mechanical lymphatic drainage. Lymphatica, a Swiss start-up, is developing the first implantable device for body fluid transfer based on a peristaltic pump magnetically coupled with a wearable controller device developed by CSEM.

CSEM developed the external devices of the Lympho Pilot in compliance with the Medical Device Regulation (MDR217/745) and according its ISO13485-certified quality system. Since the Implantable Peristaltic Pump is a Medical Device class III, the Wearable Controller Device, which influences the behavior of the Implantable Peristaltic Pump, has the same class. A Docking Station, classified as an accessory medical device class I, completes the system.

The main challenges to cope with are: (i) the magnetic coupling requirements in terms of alignment; (ii) the torque transmission; (iii) the attraction / repulsion force between the magnet in the Implantable Peristaltic Pump; the magnet in the Wearable Controller Device; (iv) the autonomy of the Wearable Controller Device versus size and weight; (v) the detection of the rotation of the rotor of the Implantable Peristaltic Pump (occlusion detection) and; (vi) the relative position of the two magnets allowing an easy placement by the patient.

Although the efficiency of the peristaltic pump is lower than 1%, the operating point of the actuator driving the magnet of the Wearable Controller Device has a direct impact on the efficiency of the overall system and therefore on the power consumption. Based on an off-the-shelf DC micromotor, the kinematic chain has to be optimized based on: (i) the medical requirements of the daily volume of fluid to be transferred, which is dependent on patient and therapy; (ii) the user requirements related to the autonomy, which must be 16 hours in the worst use case and; (iii) the technological requirements enforcing a torque of 5 mN on the rotor of the pump.

The torque to be provided to the Implantable Peristaltic Pump is modulated by the irregular friction of the rollers on the tube. This variation creates a phase shift between the two magnetic axes and then creates a modulation of the attraction / repulsion force. This dependency must be reduced as much as possible to ensure the comfort of the patient and to mitigate the risk of a potential irritation of the tissues.

The exploded view of the actuator presented in Figure 1 highlights the full kinematic chain embedded in the Wearable Controller Device. All the parts must be non-magnetic.

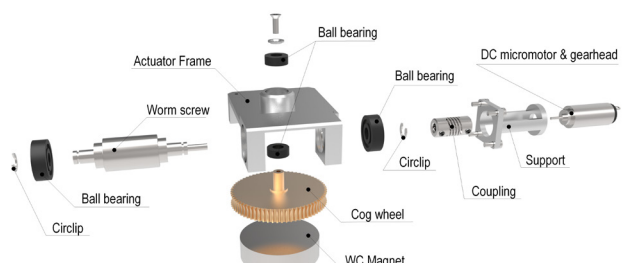


Figure 1: Magnet actuator driving of the Wearable Controller Device.

The actuator acoustic noise is one of the main constraints. Although the Wearable Controller Device is compliant with the noise requirements, after testing, one of the main source of noise resulted to be the planetary gear placed on the DC micromotor shaft. This issue has been overcome by the replacement of the aluminum coupling with a plastic tube damping the mechanical vibrations. The final design of the Wearable Controller Device is detailed in Figure 2. The battery (660 mAh) is compliant with the safety requirements for portable sealed secondary lithium cells. By design, the device cannot be used during the battery recharge, avoiding this way the risks of electrical shock for the patient.



Figure 2: Exploded view of the Wearable Controller Device.

Each patient has two Wearable Controller Devices to ensure pump operation for 24/7. The Docking Station and an AC/DC Adapter compliant with the user safety and electromagnetic compatibility complete the system. Figure 3 shows the external parts of the LymphoPilot ready for clinical investigation.



Figure 3: Device developed by CSEM.

The main improvement for the final product will be the suppression of the planetary gear and the modification of the actuator with the aim of keeping the same efficiency (autonomy) with a drastic reduction of noise (objective -6 dB).

This project was funded by the Swiss Commission for Technology and Innovation, project No. 27751.1 PFLS-LS and we thank them for their support.

Obstacle Detection for Visually Impaired and Blind

G. Dudnik, M. Correvon, A. Pollini, C. Pache, T. Maulaz, M. Crettaz, M. Frosio

For most visually impaired and blind people (VIB), the main barrier to improve their quality of life is the inability to navigate across a large variety of environments with a considerable quantity of obstacles. INSPEX^[1] is an H2020 EU project that develops a portable multi-sensor system for obstacle detection, integrating a combination of distance measurement sensors such as ultrasonic, LiDAR, and RF UWB radars, intended to be used in multiple industries including high-end autonomous cars, smart-canies for VIB, safer human navigation in reduced visibility conditions, and drone navigation.

The first prototype of the smart-cane has been developed as a Medical Device Class I. The system adds a miniaturized Mobile Detection Device (MDD) to a typical white cane for VIB people. An augmented reality audio interface in extra-auricular earphones and the head attitude, tracked with an Attitude and Heading Reference System (AHRS) in a headset, provide 3D spatial sound feedback of an obstacle's real direction and range. Context aware messages guide the user within a wider smart environment such as smart traffic lights, navigation beacons and ID tags (Figure 1). The smartphone is the gateway between the smart-cane and the headset, enabling also the localization by means of mapping apps (embedded GPS or other means).

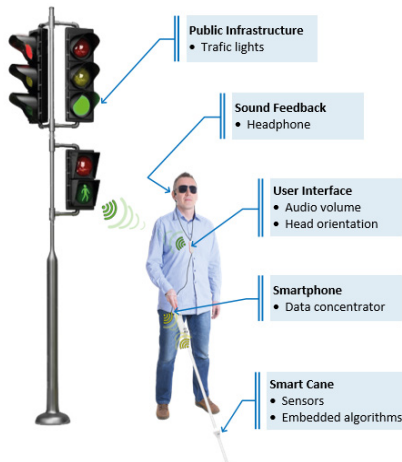


Figure 1: Full navigation system for the VIB.

The project follows the V-model design approach, and the documentation for a Medical Device Class I follows the prototype development. Figure 2 shows the concept of the final smart-cane.

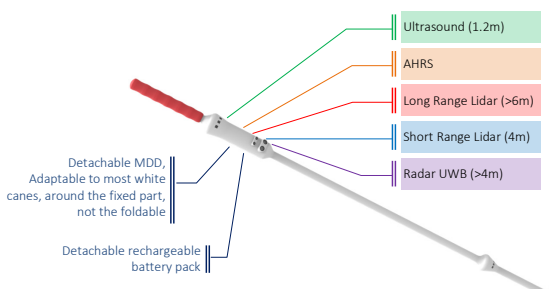


Figure 2: Projection of the final prototype to be implemented.

The detachable MDD is designed to be easily attached around the fixed part of the most used types of white cane. The MDD embeds four distance measurement sensors of different technologies, which cover different ranges and environmental conditions (short- and long-range LiDAR, ultrasound sensor and

UWB radar). The MDD also embeds a detachable rechargeable battery and a simple user interface. Figure 3 shows the processing from sensor acquisition to 3D data generation to be further converted into audio messages.

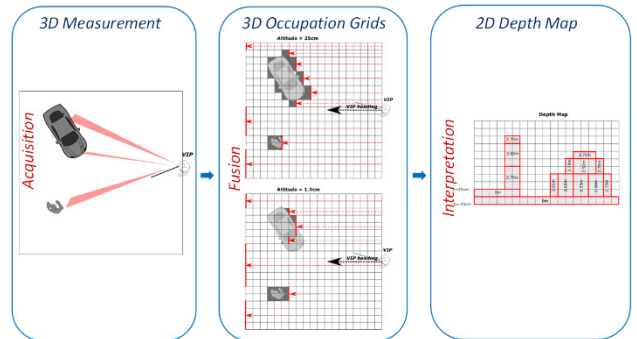


Figure 3: From sensor acquisition to 3D data generation.

To illustrate the system capabilities, Figure 4 shows the test setup representation for a detection test with the first prototype. The cane is placed on a swiping module and a pole is positioned from 4 m to 0.5 m by steps of 50 cm. For each pole position, sensor data is acquired over a full rotation of the platform. The distance information of the cane is shown in the bottom-right of Figure 4 where the obstacle is clearly visible on the profile.

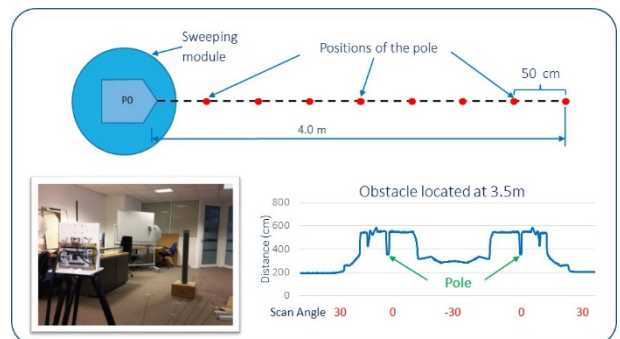


Figure 4: Test setup and results.

The first test results for obstacle detection in the shape of a smart cane are very promising: small objects such as poles are visible and feedback can be given to the VIB. A second demonstrator is being integrated for final system verification tests.

The project partners are: Commissariat à l'énergie atomique et aux énergies alternatives (FR), University of Manchester (UK), Cork Institute of Technology (IE), STMicroelectronics SRL (IT), University College Cork (IE), Université de Namur (BE), GoSense (FR) and SENSL Technologies Limited (IR). The project has been funded by the H2020 research program as well as the Swiss Secretariat for Education, Research and Innovation (SERI) and for which we would like to thank them for their support.

[1] INSPEX project official website (<http://www.inspex-ssi.eu/>)

Efficient Privacy-preserving Neural Network Inference for Heart Arrhythmia Detection

P. Chervet, A.-M. Olteanu, J. R. Troncoso-Pastoriza*, D. Froelicher**, J. Van Zaen, R. Delgado-Gonzalo, J.-P. Hubaux**

The raise of AI and machine learning as a service (MLaaS) poses a risk to the privacy of those using it. In today's data-driven application landscape, it is common that a party needs to process sensitive (personal) data using third party resources (such as computation, storage, or communication infrastructure), which constitutes a risk with respect to the privacy of such data. CSEM is working on performing neural network (NN) inference without revealing user input data to other parties involved and while hiding the model parameters from the user. Relying on homomorphic encryption and secure two-party computation, we present here a service as a client-server application for privacy preserving NN inference.

With the increasingly extensive use of machine learning in domains like facial recognition, credit card risk assessment, or medical diagnosis, the privacy threat for the people being analyzed or monitored is growing. Our work aims at preventing such threats by protecting the users' privacy, while still allowing useful analyses to be done.

We consider the case of a neural network (NN) used to detect heart arrhythmia from electrocardiogram (ECG) data. Considering the sensitivity of such data, our goal is to perform this task without revealing user input data to other parties involved and while hiding the model parameters from the user. Thus, we aim to protect the privacy of the users of the service and, at the same time, partially the confidentiality of the NN model (parameters are only visible to whoever runs the model). We use homomorphic encryption (HE) and secure two-party computation techniques, and implement the service as a client-server application for privacy-preserving NN inference.

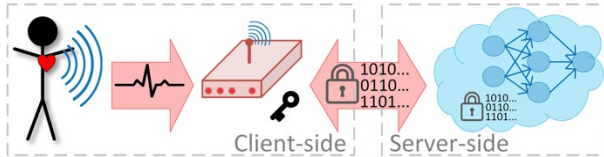


Figure 1: Health monitoring ecosystem composed of a client side, which is under the control of the user, and a server side which offers cloud computing capabilities (e.g., Amazon Web Services, Google Cloud, Microsoft Azure).

In our use case, the system is composed by the triplet Sensor-Gateway-Cloud, where the sensor collects the ECG data and sends it to the gateway. On the gateway, the client side of the application encrypts the data and, together with the server-side application on a cloud, runs the privacy-preserving NN.

As the basis of our work, we used a convolutional NN named DeepCardio^[1] developed at CSEM. It takes single-lead ECG segments of 30 seconds duration, cut into 25 equally sized windows, and classifies them to detect and classify arrhythmias. The NN mainly consists of 6 convolutional layers with non-linear activation functions (ReLU and max pooling). At each layer, the number of channels is doubled, and the signal length is halved.

- Laboratory for Communications and Applications 1 (LCA1), Ecole polytechnique fédérale de Lausanne (EPFL), Switzerland
- Laboratory for Data Security (LDS), Ecole polytechnique fédérale de Lausanne (EPFL), Switzerland

To implement a privacy-preserving version, we extended the approach described in GAZELLE^[2] for the linear parts (convolution) we use HE and for the non-linear parts (activation functions) secure two-party computation, specifically garbled circuits (GC).

To evaluate our approach, we run the client side on a laptop and the server side on a powerful workstation. Figure 2 shows the average execution time per layer for one window. The time spent for the HE operations is dominated by actual computation time. The exponential growth is due to the doubling of the channels. The time spent for GC operations is dominated by data transmission time, similar for all layers because the number of GC evaluations stays constant.

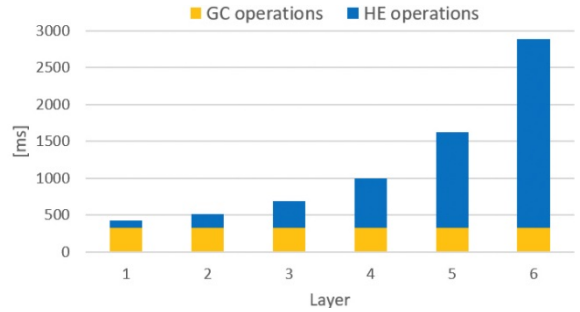


Figure 2: Execution time and distribution (between GC and HE operations) per layer for one window, averaged over 25 windows (one classification).

The results show an achieved latency of ~7 seconds for one window, resulting in ~175 seconds for one classification. However, we were able to identify the important bottlenecks and we propose approaches to improve it. The heavy computations performed using HE are mainly done on the server side; further parallelization of the server code is thus a good starting point. By optimizing the GC implementation and its parameters, an important gain in transmission time should be possible as well.

Our work shows that performing NN inference in a privacy-preserving way is possible and that there is promising potential to improve its current performance, thus, limiting the leakage of private data to computing centers and cloud service providers.

[1] J. Van Zaen, et al., "Classification of cardiac arrhythmias from single lead ECG with a convolutional recurrent neural network", BIOSTEC 2019.

[2] C. Juvekar, et al., "Gazelle: A low latency framework for secure neural network inference," USENIX Security 2018.

DeepCardio—Cardiac Arrhythmia Detection with a Neural Network

J. Van Zaen, O. Chételat, M. Lemay, E. M. Calvo, R. Delgado-Gonzalo

Monitoring cardiac arrhythmias over long periods of time is a resource-intensive task as a specialist needs to review ECG signals. Methods for automatic detection can help to reduce the time needed to review the data by selecting interesting segments. However, these methods need to be accurate to avoid erroneous detections. We trained a neural network model to detect arrhythmias from a single-lead ECG signal and applied it to data collected with a smart vest previously developed at CSEM. The results are promising for screening cardiac arrhythmias in large populations.

Heart arrhythmias are caused by irregular electrical conduction in cardiac tissue. Atrial fibrillation (AF), which affects 1–2% of the population^[1], is the most common one. Furthermore, its prevalence increases with age, from < 0.5% at 40–50 years to 5–15% at 80 years. While not directly life-threatening, it can lead to serious complications^[2]. Typical symptoms include heart palpitations, shortness of breath, and fainting. However, about one third of the cases are asymptomatic which prevents early diagnosis. This, in turn, precludes early therapies which might protect the patient from the consequences of AF but also from its progression. Indeed, AF causes electrical and structural remodeling of the atria which facilitates its further development.

The gold standard for diagnosing AF and other heart arrhythmias is the 12-lead electrocardiogram (ECG). A trained electrophysiologist can select the most appropriate treatment after reviewing ECG signals and the patient history. This is, however, a time-consuming task, especially for long recordings. To alleviate this task, several approaches have been proposed to detect arrhythmias from ECG signals. Even without perfect detection accuracy, these approaches are useful as they facilitate reviewing ECG by selecting relevant signal excerpts. Recently, neural networks (NNs) have shown impressive performance in various classification and regression tasks. In particular, several architectures have been proposed to detect and classify heart arrhythmias from ECG signals^[3].

Based on the promising results obtained with NNs, we developed an architecture to tackle the issue of early detection of cardiac arrhythmias. Our architecture takes as input a sequence of sliding windows extracted from a single-lead ECG signal. It combines convolutional layers to extract high-level features from the windows, a recurrent layer to take into account sequences with different lengths, and a softmax layer to output class probabilities. The network includes seven convolutional layers and each layer is composed of a 1D convolution, a ReLU activation, and a max pooling operation. The recurrent layer is a long short-term memory (LSTM) layer that aggregates the features extracted by the convolutional layer over sliding windows.

We trained this network on the dataset used for the challenge of Computing in Cardiology 2017^[4]. This dataset includes 8528 single-lead ECG records with durations ranging from 9 to 60 seconds. Each record is labeled with one of the following four classes: normal rhythm, AF, other rhythm, and noise. We divided

the dataset into two subsets stratified by label: a training set with 7000 records and a test set with 1528 records. To limit overfitting, we applied dropout to the LSTM layer and used data augmentation strategies. The accuracy of the trained NN was 92.64% on the training set and 87.50% on the test set. In addition, it achieved a score of 0.8495 on the test set when evaluated with the metric used to rank participants of the challenge (the mean of the F1 scores for normal rhythm, AF, and other rhythm). This is comparable to the scores obtained by the winning entries.

After training and validating the NN, we applied it to ECG data collected with the Sense smart vest developed at CSEM to classify cardiac rhythms. This smart vest uses two dry stainless steel bi-electrodes to record a single-lead ECG signal. An example of arrhythmia detection is shown in Figure 1. In this example, the NN correctly identified premature ventricular contractions. These results suggest that combining a NN model with a smart vest could be helpful for long-term monitoring of heart arrhythmias in large populations.

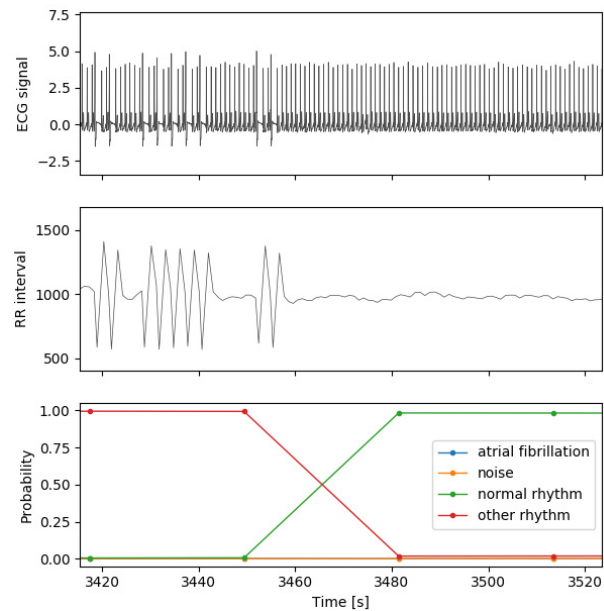


Figure 1: Cardiac rhythm classification from an ECG signal recorded with the smart vest. The ECG signal (top) includes premature ventricular contractions which are visible in the RR intervals (middle). The NN correctly identifies this segment of the signal as reflected by the class probabilities (bottom).

[1] Camm, et al., "Guidelines for the management of atrial fibrillation: the Task Force for the Management of Atrial Fibrillation of the ESC." European Heart Journal 31.19 (2010): 2369-2429.

[2] January, et al., "2014 AHA/ACC/HRS guideline for the management of patients with atrial fibrillation: a report of the ACC/AHA Task Force on Practice Guidelines and the HRS." Journal of the American College of Cardiology 64.21 (2014): e1-e76.

[3] Rajpurkar, et al., "Cardiologist-level arrhythmia detection with convolutional neural networks." arXiv preprint arXiv:1707.01836 (2017).

[4] Clifford, et al., "AF Classification from a short single lead ECG recording: the PhysioNet/Computing in Cardiology Challenge 2017." Computing in Cardiology. IEEE, 2017.

oAFD®—Optical Atrial Fibrillation Detector

E. Genzoni, F. Braun, J. Van Zaen, M. Lemay, J.-M. Vesin •, E. Puvot **

Atrial Fibrillation (AF) is predicted to affect 17.9 million of people by 2060 in Europe. Its early detection is essential as AF is associated with high comorbidities and an increased mortality. Because of their limited recording duration existing solutions – such as ambulatory electrocardiogram (ECG) – do not allow to detect AF in its early stage in large populations. Moreover, 21-50% of patients suffering from AF are asymptomatic, which makes event-triggered-measurement devices unable to detect this arrhythmia. Recent advances in photoplethysmography technology give promise to detect AF in large populations with conveniently small wearable devices at low cost.

While ECG is the gold-standard tool to monitor heart rate in clinical settings, existing tools for ambulatory monitoring are not optimal for an accurate screening of intermittent and asymptomatic AF in large population. Atrial fibrillation has a prevalence of 2.3-3.4% [1], increasing with age up to 10-17% for people 80-year-old and more [2], and is associated with an increased mortality rate. Therefore, an early detection of AF is needed to provide optimal treatment and prevent complications. Recent advances in photoplethysmography (PPG) technology are promising for screening the early paroxysmal stage of AF, as well as its asymptomatic expression. Indeed, PPG can easily be embedded in small and low-cost wearable devices such as smartwatches, which are especially adapted for screening AF in large and elderly populations.

An embedded algorithm was developed to distinguish AF from sinus rhythm (SR) (Figure 1). For this, a recurrent neural network composed of two layers – a gated recurrent unit and a sigmoid – was trained with inter-beat intervals. These inter-beat intervals (Figure 1, red line) were computed from ECG beat labels (obtained from the Long-Term AF Database from Physionet) to predict the nature of the heart rate (AF or SR).

In a recent study [3], this embedded neural network was tested to distinguish AF from SR and regular arrhythmias such as sinus bradycardia, sinus tachycardia and atrial tachycardia based on PPG-derived inter-beat intervals. 21 simultaneous PPG and ECG recordings were obtained during a clinical study conducted in the Service of Cardiology at the University Hospital of Lausanne. A beat detection algorithm was coupled with an artifact detector which identifies inter-beat intervals reflecting poor PPG signal quality. This identification was used to detect AF with two different approaches. In the first one, all data were treated for a continuous prediction while in the second approach, segments of the signal that were affected by motion artifacts or side factors were discarded prior to the RNN predictions.

When all data were given to the RNN, AF was detected with an accuracy of 93%, whereas the selection of good signal quality segments allowed to reach an accuracy of 99%. It is worth noting that the use of ECG data to train the neural network was an interesting approach, considering the large amount of data available.

These results are promising for the screening of AF in large populations. Relatively simple, the selected neural network can be easily embedded in small and light devices especially adapted

for detecting AF in elderly population mostly affected by this condition. Furthermore, the reported sensitivity and specificity compare favorably with the values obtained by recently FDA-approved FibriCheck and AliveCor products (specificity of 95% and 64% and sensitivity of 97% and 99%, respectively).

We would like to acknowledge our project partners for their collaboration: The University Hospital of Lausanne (CHUV) and the Federal Polytechnic School of Lausanne (EPFL).

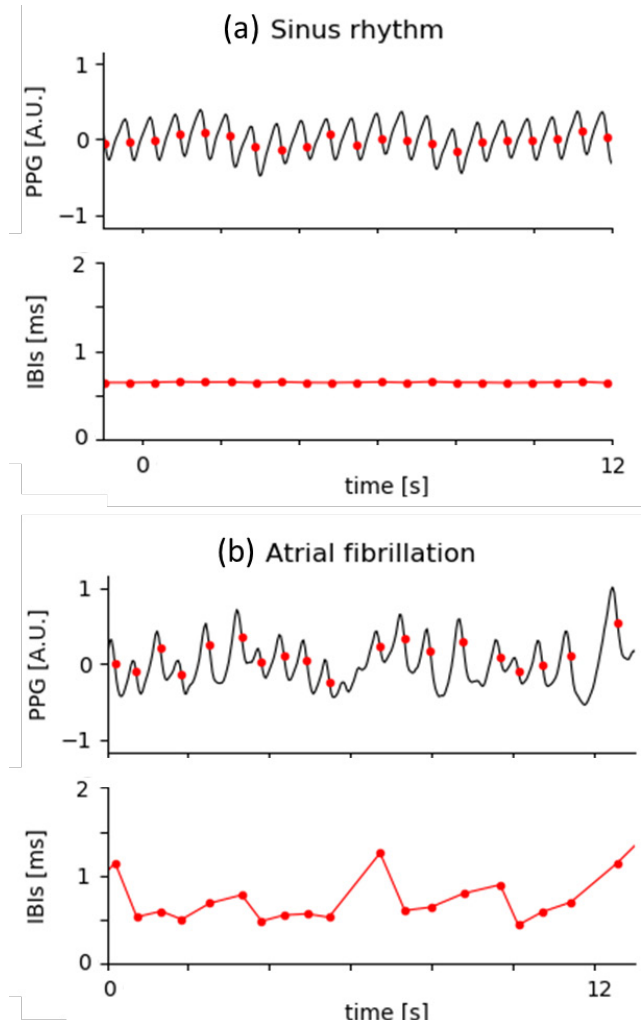


Figure 1: Two examples showing PPG signal (black line) and IBIs (red line) of (a) sinus rhythm and (b) atrial fibrillation. For (a) and (b) each detected heartbeat is noted with red dots.

• Federal Polytechnic School of Lausanne (EPFL)

** University Hospital of Lausanne (CHUV)

[1] J. Ball, M. J. Carrington, J. J. V. McMurray, S. Stewart, 'Atrial fibrillation: Profile and burden of an evolving epidemic in the 21st century', International Journal of Cardiology, 2013.

[2] M. Zoni-Berisso, F. Lercari, T. Carazza, S. Domenicucci, 'Epidemiology of atrial fibrillation: European perspective', Clinical Epidemiology, 2014.

[3] J. Van Zaen, E. Genzoni, F. Braun, P. Renevey, E. Puvot, J.-M. Vesin, M. Lemay, 'Atrial Fibrillation Detection from PPG Interbeat Intervals via a Recurrent Neural Network', CinC2019, 2019.

A Contact Microphone for Cardiac and Respiratory Sound Acquisition

G. Yilmaz, P. Starkov, M. Crettaz, L. Zhou, M. Frosio, O. Chételat

An electronic stethoscope comprising a contact microphone and USB connectivity has been developed with the goal of recording cardiac and respiratory sounds. While the presented device, MICC, can be used stand-alone, it has been designed with a vision to integrate it into CSEM's cooperative sensors measuring physiological signals of different origins. Such integration is envisaged to reinforce CSEM's technology offer in the medical devices and wearables domain. The device has been benchmarked with a widely accepted clinical electronic stethoscope for cardiac and respiratory sound acquisition.

Stethoscope auscultation is a prevalent clinical practice in diagnosing lung related diseases which make up 5 of the 30 most common causes of death^[1]. Despite its widespread use in clinic, digitalization and standardization of this method fall behind. However, an increasing incidence rate of respiratory diseases combined with the need and will to increase the efficiency in medical practice have begun to give a thrust to these belated developments, even with additional expectations such as multi-channel recordings and continuous monitoring, particularly at remote settings.

This article reports the design and development of a contact microphone that aims to address the needs mentioned above. The developed device, MICC, converts the acoustic signals originating from the thorax to electrical signals and transmit it to a computing and storage device via USB. The prominent features of the device are its simple connectivity and small form-factor which does not translate into a compromise in signal quality.

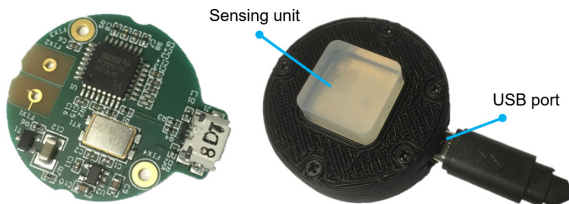


Figure 1: Electronic circuit board (left) of the system and assembled MICC device (right) with a USB cable connected.

Since a sensor satisfying all the requirements of the application is not readily available as an off-the-shelf component, we have developed it in-house. This approach is further motivated by the vision to integrate these sensors into the wearables where handling the motion-induced noise is crucial: Understanding the physics behind the operation of these transducers and mastering the technology to produce them, we believe, are the key tools to cope with the motion artefacts. The transducer, converting acoustic waves to electrical signals, is realized by means of a piezoelectric film (PVDF) which is curved along its machine direction and clamped from its ends^[2]. This structure enables control over the sensitivity and the flat-response bandwidth by changing the radius of curvature. While the heart sounds cover a frequency range from 20 Hz to 200 Hz and the lung sounds from 200 Hz to 800 Hz, certain anomalies can create sound signals up to 2 kHz. As the developed contact microphones are intended to be used to detect such adventitious sounds, the curvature of the film is designed such that the first resonance peak occurs at 7 kHz, thus providing at least 2x margin against the non-idealities during fabrication and unaccounted secondary effects.

The piezoelectric transducer, exhibiting a high source impedance, has been interfaced with an impedance converter which drives the data conversion module. The data conversion module (PCM2912A, Texas Instruments) has an integrated USB 2.0 compliant full-speed protocol controller; thus the device can be connected to any portable device acting as a host simply by a USB cable. In addition to data streaming, USB is used to power the device up. The contact microphone and the electronic circuit board have been assembled within a 3D-printed conductive plastic housing to ensure a signal acquisition free of the spurs at the line frequency. Figure 1 exhibits the electronic board and the assembled device to which a USB cable is attached.

Figure 2 compares the spectrums of the cardiac and respiratory sounds acquired by our device MICC and Littmann® 3200 from 3M. Both devices are placed next to each other and 20-second synchronous recordings are performed on the mitral area and right-middle lobe for cardiac and respiratory sound acquisition, respectively. The commercial stethoscope has been used in its "extended" mode, therefore the corresponding filter frequency response^[3] is applied on the signals acquired by MICC.

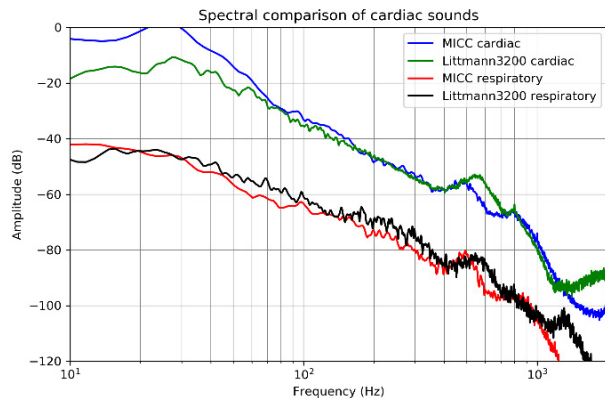


Figure 2: Spectral comparison of cardiac and respiratory sounds acquired by our device (MICC) and Littmann® 3200 stethoscope (amplitude of respiratory signals is decreased for visualization purposes).

In conclusion, we have developed an electronic stethoscope which is capable of acquiring cardiac and respiratory signals with a quality comparable to a clinically accepted electronic stethoscope. The modularity of the design and the form factor enable multi-channel recordings by placing several microphones on a vest. In the next phase, we plan to leverage the established competence of our cooperative sensor technology to integrate multiple units into a garment along with other physiological signal monitoring means such as ECG and electrical impedance tomography (EIT).

[1] Global Alliance against Chronic Respiratory Diseases
<https://www.who.int/gard>

[2] M. Toda, Contact-type vibration sensors using curved clamped PVDF film, IEEE Sensors Journal 6(5), 1170-1177 (2006).

[3] V. Oliynik, "On potential effectiveness of integration of 3M Littmann 3200 electronic stethoscopes into the third-party diagnostic systems with auscultation signal processing", IEEE 35th Int. Conf. on Electronics and Nanotechnology, Kiev (2015), pp. 417-421.

Customized 3D-printed Seat Cushion for Wheelchair Users

T. Parkel, I. Stergiou, S. Cattaneo, A. Gautschi •

Building and fitting customized wheelchair seat cushions for paralyzed people today is still a 100% analog hand craft process trying to find the best seating cushion solution and with it preventing pressure ulcers. CSEM knowledge on developing flexible 3D-printed parts and medical validation models has now been used to build a customized anatomically shaped seat cushion for wheelchair users, with open celled multi-softness zones, to provide an efficient pressure relief and improve air circulation at the body interface.

As paralyzed people are compelled to be seated in their wheelchair for many hours, an optimal seat interface is essential. By individually shaping seat cushions, wheelchair specialists try to build the best possible seat interface, to provide good comfort and avoid decubitus skin defects caused by pressure overload on prominent anatomical spots (ischial tuberosity/ sitting bone and coccyx). In addition, skin temperature and transpiration have a big impact on the healthy skin condition. Therefore, air circulation at the body interface, which is the key to control skin temperature and skin moisture, is an essential requirement, which however is not met by today's standard cushions.

Approach

A proof of concept model of a 3D printed open celled flexible seat cushion with multiple softness zones was created for the Swiss Paraplegic Centre in Nottwil based on their requirements.

As a starting point, a precise 3D scan of a conventional customized seat cushion made of Alveolux (low density polyethylene foam) covered by an elastic honeycomb structure was realized (Figure 1).

Softness information were gathered from the existing cushion and directly from the user, leading to the definition of four softness zones of varying dimensions and softness (Figure 2). As the entire seat cushion was printed with the same material (TPU thermoplastic polyurethane of shore hardness A85), to achieve the desired softness zones design variations of the inner structures and its dimensions where applied.

The surface of the entire seat cushion device holds hundreds of small holes letting air or water flowing through the open celled inner structure (Figure 3).

For stability reasons the seat cushion was reinforced, at the bottom, by a lightweight plywood base plate building an interface to the wheel chair.

Result

The benchmarking of the 3D-printed multi zone softness seat cushion gave very promising results, as all requirements could be achieved and the user test on daily comfort were very satisfying. According to the user, a big improvement was achieved by significantly reducing the isolation factor, by allowing air to circulate at the body interface. Even after an extensive full-day usage no skin irritation was observed. Finally, washing the seat cushion is now simple and the drying time of the seat cushion is shorter.

The benefit of digital workflow integration

Today fitting and shaping a customized seat cushion is still a 100% analog hand craft process. No data on the current design is available. It is not possible to make an exact copy of an existing

device due to the variation of carving the surface by hand. With a complete digital workflow each design and all its variations will be available as data sets. Rebuilding an exact device, applying changes based on existing data will help improve developing better seat cushions. When this is achieved any technician will be able to apply the required design changes to the latest data set, always having a history track, and not having to start from scratch as currently the case.



Figure 1: 3D printed seat cushion (red) and existing Alveolux seat cushion with a top layer of honeycomb structure.

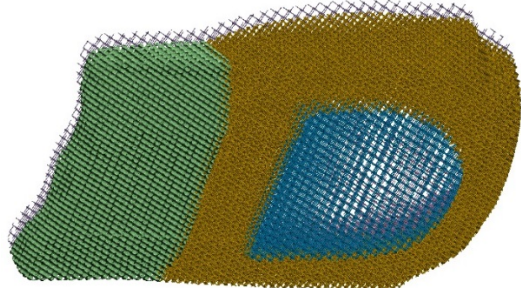


Figure 2: The four sections of different softness are marked with different colors.



Figure 3: 3D printed open-celled customized multi soft zone seat cushion.

Next steps

- Standardizing the soft zone structures for seat cushion building blocks.
- Development of entire digital process flow.
- Integration of sensors (pressure, temperature, humidity).

• Swiss Paraplegic Centre SPZ, Nottwil

ULTRA-LOW-POWER INTEGRATED SYSTEMS

Alain-Serge Porret

The Ultra-Low-Power (ULP) Integrated Systems program addresses the key challenges and technologies required to build very low power, (often) wirelessly interconnected, embedded smart systems or remote sensing nodes. The availability of such components is central to several global technological trends such as the Internet of Things (IoT) revolution, the advent of wearable technologies for wellness and medical applications (in line with the needs of an aging population), and the generalization of machine-to-machine (M2M) communications required by Industry 4.0.

The IoT is a dramatic extension and generalization of the “wireless sensor networks” approach that CSEM has been promoting since the late 90s. The ultimate goal is to enable the quantification of every piece of useful information captured by a great number of distributed, inexpensive, network-connected, sensor-enabled, computerized devices.

Today's IoT architecture generally mostly relies on fairly “dumb” remote nodes uploading raw data to a centralized processing unit or to the cloud. Distributed sensors (and portable terminals) collect as much data as possible from their environment and dump them in “data lakes” to feed “big data” algorithms. In the process, humongous quantities of raw and mostly useless information are generated, transmitted, stored, and processed, soon to reach yottabyte levels and wasting considerable resources and raising significant privacy-related concerns. This paradigm is also impractical for many industrial and medical applications with high-security or latency constraints.

However, a different model, where information processing occurs upstream, in the sensing node, and only significant events or statistics are communicated, is possible. It emerges more and more as a useful, and in many cases necessary, alternative (“smart edge”). This program focuses on the specialized low-power and/or resource-limited components required to enable

such solutions. It also addresses the needs of many sensors that cannot be physically wired, either because the device is attached to a moving part, is mobile or worn, is implanted, or is not located near a suitable power source, or simply because the wiring required to connect large numbers of remote nodes is costly or impractical. Consequently, such devices:

- Need either to be battery-operated (ideally button batteries lasting years) or to rely on harvested energy from their surroundings (toward “zero-battery” devices), leading to a typical power budget in the range of $10 \mu\text{W}$ (from sub μW to a few $100 \mu\text{W}$ range).
- Are required to exchange information wirelessly—since the device is untethered. Wireless transmission of information is energetically very costly, practically $>10 \text{nJ per bit sent}$ (with overheads), with well above 1nJ/bit seemingly being a hard limit for most applications today.
- Should be able to preprocess information locally. A mean data rate of only 10kbit/s (such as for base ECG) costs a minimum of $100 \mu\text{W}$ to transmit wirelessly, and, in practical implementation, likely significantly more. This is larger than the consumption of a commercial medical-grade ECG front end, and much more than the best published research numbers. There are therefore plenty of opportunities to reduce power consumption by using smart local processing to reduce the transmit data rate.

Battery-operated surveillance cameras and keyword spotters are illustrating even more clearly these limitations. For such devices, streaming video (respectively sound) continuously is not an option. Only pre-filtered information about detected incidents can be transmitted. This is, of course, only possible if the remote sensing node is equipped with hardware and software components that are sufficiently low-power, yet capable of

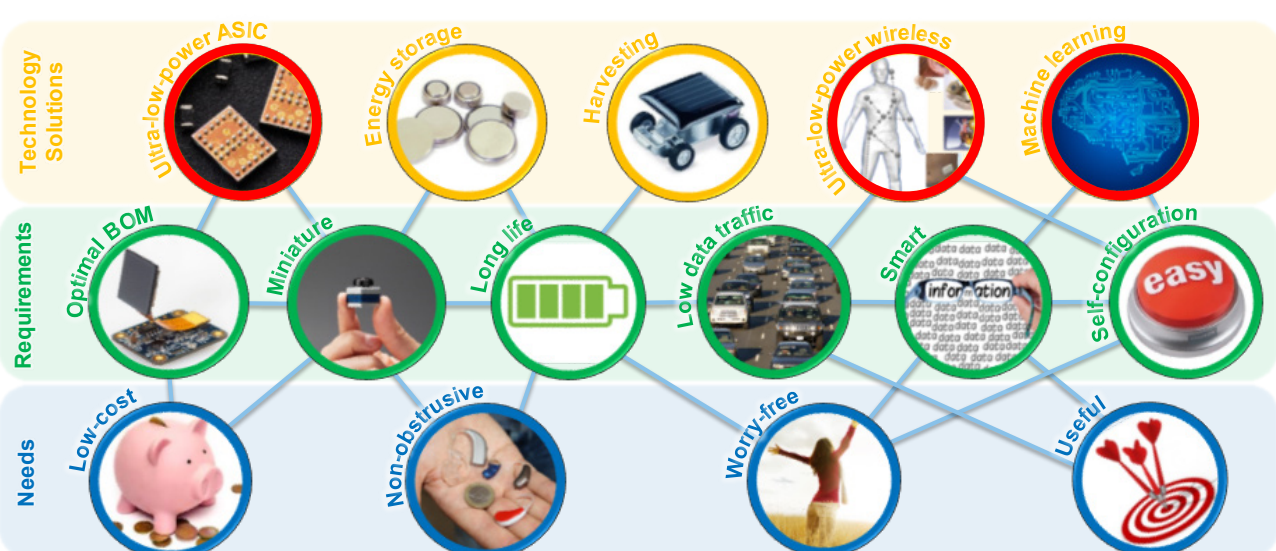


Figure 1: Needs, requirements, and solutions for modern IoT and wearable devices.
The circles highlighted in red are some of the key challenges covered by the program.

achieving either high levels of data compression or, alternatively, able to understand and classify—at least to a limited extent—the meaning of the collected data. In many practical cases, advanced signal processing techniques are required or even, increasingly, embedded machine learning and artificial intelligence algorithms. Such equipped devices rightly qualify as smart sensors.

Long-term objectives

This ambitious vision requires significant advances in several fields, ranging from system architectures to hardware devices and algorithms (see Figure 1). It covers energy storage (not studied here), energy harvesting sources (investigated in the Photovoltaics and Energy Management program), power management, wireless communications, sensor interfaces, advanced embedded data processing hardware, efficient machine learning algorithms, and resource-limited machine vision.

The markets covered by the program are very diverse, as the generic nature of Figure 1 suggests, and are growing in scope with the continuous development of the Internet of Things. Applications specifically covered by this research program include:

- Consumer electronics (Bluetooth Smart devices, GPS-enabled devices, home automation and security systems, and image processing for occupancy analysis);
- Industrial systems (high-performance sensor interfaces, sensor networks for harsh environments, and optical quality control);
- Metrology (integrated measurement microsystems or optical encoders for various purposes);
- Medical and wellness (implants, vital sign monitoring, and electronic prostheses);
- Automotive (smart sensors in harsh environments, tire monitoring, driver attention monitoring);
- Aeronautics (distributed sensors, touchless man-machine interfaces).

The ULP Integrated Systems program is subdivided into three research activities. The main areas of attention are indicated below for each.

Wireless Systems: (1) Reduction of the effective energy per bit required to send information through a realistic network, with stringent latency, security, robustness, or quality-of-service requirements. (2) Development of high-performance integrated transceivers. (3) Use of electromagnetic waves for ranging, localization, and remote sensing (for instance vital sign monitoring).

Vision Systems: (1) Development of very-low-power imagers. (2) Development of machine learning algorithms with a special emphasis on embedded systems. (3) Design of specialized compact smart cameras, inside and outside of the visible spectrum, including multi-/hyper-spectral capabilities. (4) 1D to 6D accurate position measurement through optical means.

System-on-Chip: (1) Mastering of extremely low power (ELP) subthreshold logic design techniques. (2) Design of ELP mixed-signal sensing interfaces, with an emphasis on vital sign

monitoring and timing devices. (3) Dedicated architectures suitable for ELP logic, including multi-core processors and dedicated accelerators, for example for artificial intelligence inference. (4) Design of the supporting power management circuits.

Highlights

The investments in these activities resulted in notable advances in 2019, as underlined by the papers following this introduction, a selection of which are briefly highlighted below.

In “MODAL: A multi-modal sensing platform for IoT applications”, a robust platform for people tracking and health state monitoring of the ill and elderly is described. This work is a collaboration with Idiap and is focused on merging the output of several sensor types (today, sound and vision, but other sensors are planned to be added) to provide accurate monitoring and alarm triggering.

Multispectral imaging is increasingly considered to extend the capabilities of machine vision for a wide variety of applications, one of which is described in “Handheld Multi-Spectral Imaging Device Designed to Aid Skin Cancer Detection”.

Application of deep-learning-based computer algorithms is often problematic due to their need for large annotated datasets. A novel algorithm architecture is proposed and applied to surface defect detection in “Deep Learning Architectures for Detecting Surface Defects using Multiple Illuminations”. It benefits from seeing the defect from different vantage points and can operate from a very limited annotated dataset.

Two efficient hardware machine-learning inference implementations are described in “FaceDET: A 1.4GOPS Face Detection System-on-chip based on Binary Decision Trees” and “Binary weight CNN hardware accelerator for ULP computer vision”. We also continue to explore and improve on traditional low-power embedded processors in “icyflex-V: a new ultra-low-power processor based on RISC-V architecture”.

Three papers present recent advances in our family of low-power transceiver IP: increased performances in “A frequency synthesizer for ultra-low phase noise multi-clock generation”, added features in “Bluetooth Direction Finding”, and higher frequency of operation in “60 GHz FMCW RADAR-on-Chip”.

Sensitive applications such as aeronautics require the development of dedicated, robust, and secure solutions, far from the requirements of consumer electronics. WAIC (Wireless Avionics Intra-Communications) is a new radio communication standard linking avionics components. CSEM has designed and implemented one of the first WAIC demonstrators, which will connect wireless sensors to a data concentrator.

Finally, privacy and security are increasingly major concerns for all IoT applications. In “End to end security and privacy in a heterogeneous multi-platform environment”, a risk and impact analysis is performed enabling the selection of targeted protection measures.

Anomaly and Event Detection in Data Streams in Practice – Gesture Recognition using WiFi

E. Daskalaki, J.-D. Decotignie, D. Piguet

An important aspect of data quality validation relies on and relates to the detection of anomalous data points or regions, which may represent faulty/"bad" data or events, within a set of normal/"good"/nominal data. Developing algorithmic techniques which permit the detection of events/anomalies within a nominal data stream is one of the cornerstones of data validation. This is here illustrated through gesture recognition using wireless channel state.

Data quality validation comprises numerous aspects, from detection of wrong values, duplicates and timelines issues, to the detection of complex multi-variable context-related problems. The latter is one of the most challenging aspects of data validation as it requires prior problem knowledge and advanced algorithmic strategies for the detection of faulty data. Such strategies mainly rely on the detection of statistical deviations within the data which indicate that parts of the data are governed by a different probability distribution. Although this block of the data may be considered to be faulty in some scenarios (e.g., if the underline sensor is malfunctioning), it can represent rare and/or interesting events in other cases (e.g., an important change on the system under measurement which may be, e.g., a failure). Consequently, an important aspect of data quality validation relates to the detection of anomalous data points or regions, which may represent faulty/"bad" data or events, within a set of normal/"good"/nominal data. To this end, the development of algorithmic techniques which permit the detection of events/anomalies within a nominal data stream is one of the cornerstones of data validation.

Gesture recognition using channel state information serves as an illustration of complex data validation. The demonstrator is based on exactly the principle of event detection within a nominal data stream. Although, in the setup, the empty channel is not intuitively regarded as "good" data and the gestures as "bad", the principles of addressing the problem remain the same.

The impulse response of the channel serves as source of information for the detection of gestures. The channel impulse response can be measured through the use of the channel state information (CSI), a metric which is now available with a few commercial WiFi cards. This metric provides data about the amplitude and phase of each of the OFDM subcarriers.

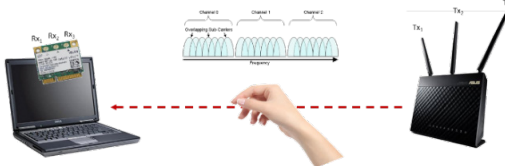


Figure 1: WiFi channel based gesture detection setup.

In the test setup, a WiFi channel is established between a laptop with Intel Link 5300 NIC and an Access Point (Asus AC1900), as shown in Figure 1. A dedicated software tool available from Intel, the "Linux 802.11n CSI Tool", is used to interface with the Network Card and read the CSI data. The Intel card is connected to 3 patch antennas in order to increase directivity and reduce the perturbations due to surrounding motion. The CSI is extracted from the ICMP echo reply packets for a selected OFDM channel of bandwidth of 20 MHz sampled over 30 equidistant subcarriers. The channel power and phase for each subcarrier

and six (3 Rx and 2 Tx) of the Rx-Tx antenna pairs are registered for every ping request. The packet rate was set to 10 Hz. To this end, 6x30 CSI time-series with sampling rate of 10 Hz are recorded.

The proposed algorithmic strategy follows the principle of the Auto-Encoder (AE). An AE can be used to detect events [1], defined as data regions which are produced along a different probability distribution than the rest of the data which are considered as "normal". In our case, we define as "normal" data, the CSI of the empty channel and as "events", the CSI during a gesture.

The standard AE encoder and decoder are implemented as LSTM networks with a hidden size of 128 and sequence length of 10 (past of 1 sec). The training and validation sets consist of only data from empty channel recordings, while the test set is comprised of data from both the empty and the "with-gesture" channel. The input to the encoder is the CSI amplitude per antenna pair and subcarrier (i.e., 6x30 features), and the mean spectrogram of this input. The data are first low-pass filtered with 1Hz cutoff frequency. The spectrogram is calculated for an FFT window of 50 samples (5 sec), thus with frequency resolution of 0.2 Hz. The spectrogram frequency bins are considered as additional features and are concatenated to the input.

Figure 2 shows 3 subcarriers for one Tx-Rx pair, where the gestures are marked by the red rectangles. Although we can see the channel change during the gestures, it is not evident how to distinguish this perturbation from the ones of the empty channel.

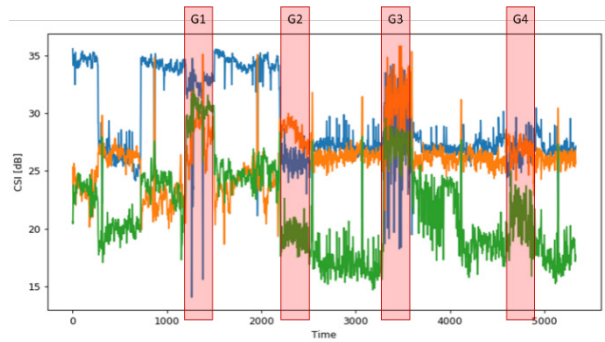


Figure 2: 3 subcarriers CSI during 4 gestures (3 possible gestures).

The mean reconstruction error could be used as way to identify gestures. However, the Mahalanobis distance and KL divergence yield a much better indication. The results demonstrate the importance of the selection of the appropriate distance metric for the accurate detection of the gestures. Most importantly, however, they demonstrate the feasibility of gesture detection even in a strongly perturbed WiFi channel. The results are promising and motivate further algorithmic investigation and improvement.

[1] P. Malhotra, et al., LSTM-based encoder-decoder for multi-sensor anomaly detection. arXiv preprint arXiv:1607.00148 (2016).

First Hardware Platform for Wireless Avionics Intra-communications (WAIC)

C. Hennemann, D. Piguet, P. Dallemagne

Today, wired sensors are used for monitoring the condition of aircraft engines, airframes, structures, gearboxes, etc. Wireless Sensor Networks promise unprecedented operational benefits, such as reduced airplane sensor wiring costs and weight. To this end, the aeronautic industry proposes the Wireless Avionics Intra-Communications (WAIC), a new radiocommunication standard between avionics components. CSEM designed and implemented one of the first WAIC band transceiver demonstrators, which will connect wireless sensors to a Wireless Data Concentrator.

An Airbus A380-800 contains around 100'000 wires for a total length of 470 km and a mass of 5700 kg. 30% of these electrical wires could be replaced by wireless communication, more given redundancy (as the wiring is usually doubled or even tripled), bringing advantages in terms of added diversity and lower weight.

The frequency band 4200 to 4400 MHz was recently allocated to the aeronautical WAIC standard. The technical conditions for the use of WAIC systems operating in the aeronautical mobile are described by the ITU [1] (ongoing process).

CSEM has been active in the domain of wireless aeronautic application for years and has delivered numerous demonstrators and prototypes of innovative wireless solutions for aircraft monitoring and control. Recently, CSEM developed and tested a first WAIC proof of concept platform, addressing a transceiver front-end system architecture operating in the target WAIC frequency band (4.2 to 4.4 GHz).

The up/down frequency conversion requires the distinction between the transmission (Tx) and the reception (Rx) channels in order to run the TDMA protocol. Only the 2.4 GHz transceiver (TRX) knows the operating mode (Tx, Rx, sleep, idle...) and can externally provide this information to correctly drive the frequency converter (Tx or Rx mode). Figure 1 depicts the architecture using two switches.

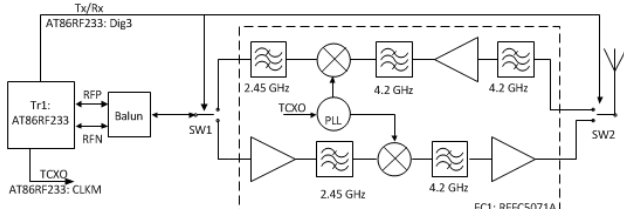


Figure 1: WAIC architecture using two switches.

Alternatively, we can use an RF circulator, which allows for separation of the TX and RX paths. With this architecture, there is no need for a control signal (TX / RX), as shown in Figure 2.

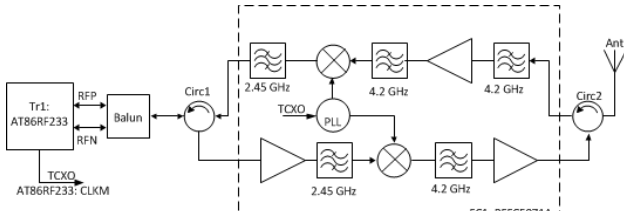


Figure 2: WAIC architecture using two circulators.

Figure 3 illustrates the implementation based on the latter architecture employing an RF circulator.

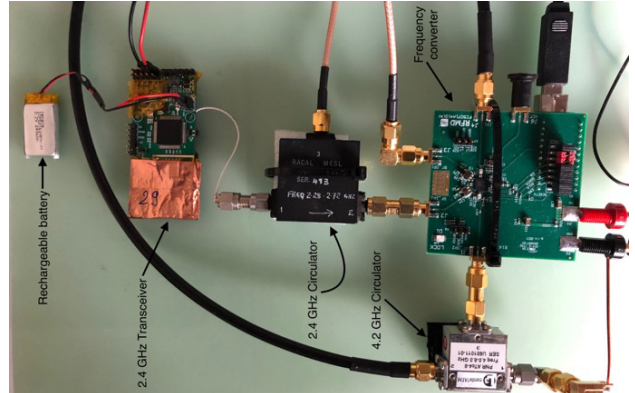


Figure 3: Implemented platform.

The Packet Success Rate (PSR) was measured with and without the up/down converter (4.4 and 2.4 GHz) to evaluate the frequency conversion implementation. The PSR is defined as the ratio of the number of correctly Rx packets divided by the number of Tx packets. The table below summarizes the results.

Frequency	Rx Packets	Tx Packets	PSR [%]
2.4 GHz	346'500	382'845	90.5%
4.4 GHz	385'842	406'493	94.9%

The 4.4 GHz system was found to perform better, despite the conversion electronics, as it avoided interference in the crowded 2.4 GHz ISM band due to, e.g., WiFi and Bluetooth, which creates collisions, degrading the performance of the TDMA system. The addition of a frequency converter does not modify or degrade the performance of the original 2.4 GHz TRX. Further tests will be performed in a representative environment and protocol research will focus on solving the radio altimeter coexistence issue.

Additional characterization will be performed in a real environment consisting of sensor nodes and one Wireless Data Concentrator (WDC) organized in star topology. Ultimately, the sensor node will be energy-autonomous and will measure physical quantities such as strain, acceleration or electrical current, which are transmitted in real-time to the WDC, via the TDMA protocol developed by CSEM for aerospace applications. This protocol requires a half-duplex TRX, among other requirements, which are met by the experimental WAIC platform. In addition, WAIC is partly shared with the radio altimeter band, which brings challenging coexistence issues that CSEM ambitions to solve in the near future.

This project has received funding from the European Union's Horizon 2020 research and innovation programme Clean Sky 2 under grant agreement No 785495.

[1] ITU-R M.2085 and ITU-R M.2319 recommendations (in progress).

Large-scale Demonstration of RF-based Localization of Persons in Cruise Ships

C. Kassapoglou Faist, P. Dallemande

An innovative person localization system for the safe evacuation of large numbers of people (over 500) from passenger ships has been demonstrated in real environment, with excellent results. It is designed to meet requirements for high reliability, robustness, scalability and user acceptance, while being low-cost and low maintenance. The system was handled by the crew during their drills over an extended period, confirming its operational benefits.

The cruise industry is booming. Along with the number of ships, the size of the vessels has also increased substantially, with recent cruise ships accommodating over 5000 passengers. Safety at sea has always been a major concern of the actors involved and unfortunate mishaps have shown that the ability to efficiently and rapidly localize persons in vessels during crisis situations is crucial. Nevertheless, until now, no real-time localization system has proven satisfactory, leaving a time-consuming systematic search as the only option.

The Lynceus^[1] system is the culmination of two EU projects that brought together developers, safety equipment manufacturers, commissioners, cruise ship operators, as well as maritime regulators, in order to realize a system that would "see behind obstacles", as the mythological character (Lynceus) could do. During an evacuation procedure, the system is able to track, localize and depict in real-time, all of the persons on-board who are wearing their Lynceus device. Lynceus uses low-cost, low-power, battery-powered radio-frequency (RF) devices embedded in wearable items (life jackets, bracelets or key cards), which communicate with fixed elements (gateways) interconnected to the ship's wired backbone network (Ethernet). Sensors integrated on the devices can also provide an indication of the person's current health status (heart-beat detection, movement). In addition to localization, the Lynceus system can count and identify the missing persons, as well as provide updates on incident escalation, interacting with the on-board fire system. Furthermore, the safety officers can follow the evacuation status on an interactive, highly customizable, graphic interface.

The Lynceus devices are shown in Figure 1. They are developed based on the ultra-low power (ULP), CSEM icyCOM and WiseNET wireless technologies, which operate at 868MHz and 916MHz, adapting to European and American continental waters. The Medium Access Control (MAC) protocol is a high-availability variant of the ULP WiseMAC protocol, designed to exploit the asymmetry in resources between the mobile and the fixed devices. Custom antennas have been designed for optimal radio connectivity. Localization is based on received signal strength, using a simple proximity algorithm, thus coping with strict scalability requirements, while maintaining accuracy at acceptable levels for this application.



Figure 1: Lynceus mobile devices used at the large-scale tests.

Large-scale testing took place on-board the Royal Caribbean cruise ship the Rhapsody of the Seas. The deployment consisted

of 724 gateways (see Figure 2) that covered a large part of the vessel, extending over 10 decks and including the engine room. Installation and test were performed while the ship was in full operation, which was quite challenging.



Figure 2: Lynceus gateways and their deployment shown on the GUI (partial view).

Not surprisingly, moving from the lab to a real-world, large-scale deployment revealed a number of operational issues. For example, longer transmission delays and absolute synchronicity of some events at node level affected device and network stability. Despite the complexities of deployment in an operational environment, these problems were solved and the solutions implemented thanks to the remote update function, resulting in a robust system and successful demonstration. All along, the firmware has also been greatly enhanced; in particular, the retransmission policy from the wired to the wireless medium, its wireless routing algorithms (used as a backup in case of local wired network disruptions) and remote firmware update.



Figure 3: Graphic User Interface at large-scale demonstration.

The crew used and evaluated the system in their weekly drills over a 6-month period, providing valuable feedback. Figure 3 illustrates the security officers' GUI during the final demonstration, which was attended by several guests from the maritime sector. Over that period, 539 keycards had been distributed (number determined by the drill), among which 523 were used at the drill and successfully localized. Localization accuracy is estimated to be between 5 to 10 meters, depending on area type (indoor open space, cabins, outdoors). User acceptance, as well as overall feedback from crew, cruise officials and guests has been extremely positive if not enthusiastic. An exploitation plan has been discussed among the partners and a new project is planned that will extend the concept to oil and gas platforms.

[1] <https://fr.euronews.com/2019/06/24/une-technologie-europeenne-accelere-le-sauvetage-en-croisiere>

End-to-end Security and Privacy in a Heterogeneous Multi-platform Environment

C. Kassapoglou Faist, D. Vizár, P. Dallemagne

The Internet of Things opens new perspectives for aging well, enabling remote health monitoring and assistance. However, interconnecting IoT devices and offering large-scale services over publicly available infrastructures poses serious security and privacy concerns. CSEM and its partners carried out security risk analyses and data protection Impact assessments enabling us to propose targeted protection measures.

Adjusting the living-room temperature from the workplace, or measuring a patient's medical condition remotely, have become common-place actions, thanks to the Internet of Things. By 2025, market analysts predict over 20 billion interconnected devices worldwide, enabling new services and enhancing the quality of life. But what guarantee do we have with respect to the authenticity and the integrity of the data that we receive? And how can we be sure that confidential information has not leaked or is not available to unauthorized parties? These and other security and privacy concerns have been raised and IoT solution providers have started addressing requirements identified by customers or regulatory bodies by, e.g., encrypting the data. However, efficient solutions require a global, end-to-end (E2E) perspective and must be tailored to the needs of the application.

CSEM and its partners are studying this problem in the context of the H2020 EU Large-scale Pilot project ACTIVAGE. The project enables IoT services for Active and Healthy Aging, supporting independent living of older adults in their living environments and responding to the needs of caregivers, service providers and public authorities. The project's main objective is to build a European IoT ecosystem across nine deployment sites in seven European countries. The idea is to reuse and scale up several existing IoT platforms (based on frameworks such as Fiware, Sofia, SensiNact, Universaal, openIOT), providing interfaces for interoperability.

Although inter-dependent, security and privacy were handled separately. Security deals with confidentiality, integrity and availability. Since security measures are costly and may also hinder performance, special care must be taken in their design. Adopting the reference architecture shown in Figure 1, the methodology described below was applied to the design.

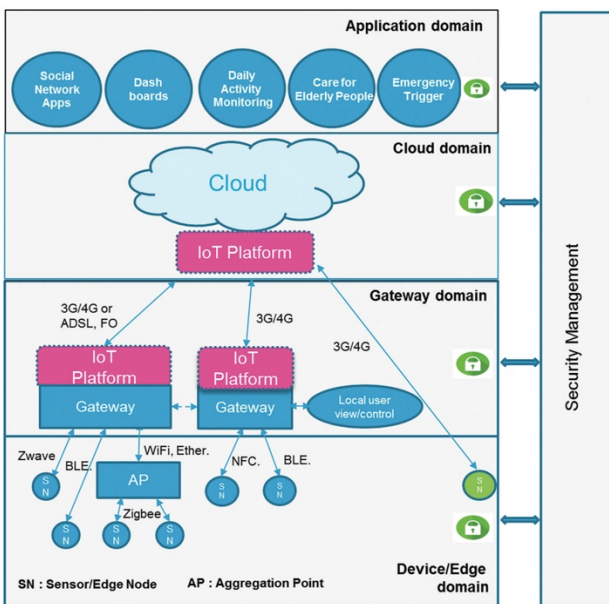


Figure 1: Reference architecture for security risk analysis.

First, a reference, E2E security risk analysis was performed. Using the Microsoft STRIDE method, we identified threats and

vulnerabilities for the system assets, within each domain and across the IoT domains (Device, Gateway, Cloud and Application). The threats were categorized, and their risk was quantified taking into account criteria such as probability of occurrence, damage extent, population affected etc. At the same time, security countermeasures were identified, to be proposed as the threat risk demands.

In a second step we assessed the current status of each deployment site through questionnaires that reflected the risks identified in the reference study. In this effort, publications and guidelines by the IoT Security Foundation and the Open Web Application Security Project were highly valuable. Based on the answers, security recommendations were made, tailored to each of the nine deployment sites in the project.

The third step dealt with the identification and high-level specification of the overall, cross-platform security services in an E2E perspective. As in the case of the oneM2M specification, the security services were defined to be Authentication and Authorization (which includes Access Control and Consent Handling), E2E Security Association, Sensitive Data Handling and Security Provisioning, along with underlying functions, such as Identity Management and a Public Key Infrastructure. In particular, in order to guarantee confidentiality across any data path, a scheme similar to Transport Layer Security was proposed for E2E encryption, to be integrated at application layer.

With the emergence of Big Data technologies, the European General Data Protection Regulation (GDPR) came into force; responding to the growing public demand for privacy. The GDPR defines who the data owner is and it requires, e.g., privacy by design and by default in a data system. Typical approaches to comply with the GDPR rely on existing frameworks and processes, such as the Data Protection Impact Assessment (DPIA), put in place by consultancy companies, national agencies (such as the French CNIL) and standardization bodies. A DPIA guides the designer through the following steps: description of the use and processing of all personal data in the system, assessment of the necessity of processing and the risks with respect to a person's rights, documentation of the measures taken (e.g., security mechanisms) and demonstration of compliance. DPIAs were carried in the project deployment sites.

Implementation of security and privacy in ACTIVAGE, which largely relies on existing, widely accepted tools and frameworks is under way. In addition, CSEM has defined a framework providing Consent Management and Personal data management services, to be enriched in the future with several tools for privacy-preserving data analytics, such as multi-party computation and homomorphic encryption. These tools will be supported by security and cryptography functions designed for low-end platforms (e.g., an environmental sensor or a wearable device) as well as for high-end ones (e.g., cloud), allowing the deployment of E2E private computations.

Integration of a Passive UHF RFID into a Metallic Package

A. Vorobyov, C. Hennemann

The demand for RFID's in the industrial environment is growing, especially for real-time tracking applications, in harsh conditions, with the aim of improved reading speed. RFID tag's operating in such harsh environments (e.g., metallic surface or even metallic box) require smart antenna design and integration. The integration of a passive UHF RFID into a metallic package is described in the report.

RFID is an identification technology with many potential applications in the domain of contactless object monitoring and tracking. The most common COTS RFID tags, like many barcodes, are self-adhesive labels. Unlike the barcode, where the information is stored in a graphic form, the data on a RFID label is recorded in a circuit, which is read by reader using magnetic or electromagnetic (EM) waves.

For data transmission, passive RFID tags use the energy of the reader EM field. The principle of an RFID communication system is presented in the following block diagram in Figure 1.

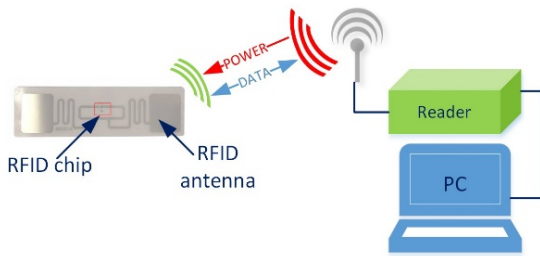


Figure 1: Basic RFID communication system blocks.

An RFID reader does not require direct visibility of the tag in order to read its data. In case of circular polarized reader antenna, the tag orientation also does not matter. Tags may be read through the packaging, which makes hidden placement possible. By comparison, a barcode reader requires direct visibility of the barcode for reading.

RFID systems can be distinguished by their operating frequency ranges (e.g., LF, HF, UHF and microwave). Our focus is on an UHF RFID solution operating at 868 MHz (Europe) and 915 MHz (USA). Passive RFID tags can be detected at a distance up to 10 meters, depending on the radiated power of the RFID reader and the architecture of the tag.

Real-time tracking of goods may be performed in the warehouse or upon delivery. This allows the reception and shipment processes to be accelerated, reliability and transparency of operations are increased, and the influence of the human factor is reduced. Beyond tracking of goods, RFID solutions can provide protection against theft of products or even implement counterfeiting solutions. They may be used as a smart device with sensor functionality, e.g., analog to digital conversion and timer. Some RFID tags even have a built-in microcontroller enabling a wide range of applications.

Today though, a very small number of available RFID tags can operate in harsh environments (e.g., metallic surfaces, metallic construction). These tags are bulky and have a predefined size. This makes it difficult or even impossible to use them in a confined space. One of the reasons for the predefined size is the antenna. The antenna is very important part of the RFID system. A non-optimized or detuned antenna can drastically degrade the system performance (*i.e.*, tag reading range).

The aims of this work are: 1) to integrate an UHF RFID tag into a metallic case without mechanical or structural modification of the

case, and 2) to verify the conditions and limitations of the approach, as well as, the other exploitable properties with respect to the targeted applications.

A cylindrical metallic container or box (50 mm in diameter x 60 mm height) is used for the demo. The top cover of the container is detachable. The EM Microelectronic EM 4325 FID chip is located inside the top cover of the metallic box as presented in Figure 2. Two wire antennas with optimized lengths are connected to the tag and to the top cover of the metallic box as presented in Figure 2.

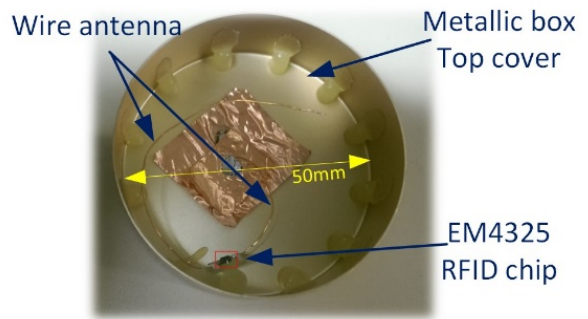


Figure 2: RFID tag and wire antennas location in the metallic box (top cover).

The proposed configuration allows the metallic box to be leveraged as part of the antenna. As a result, the reader with 200 mW output power can easily read the tag at a distance of about 60 cm (see Figure 3).

An additional metallic strip line, as presented on the photo (Figure 3) can further improve the communication range and add a security feature. The RFID tag will not work if the metallic strip is broken due to the box opening.

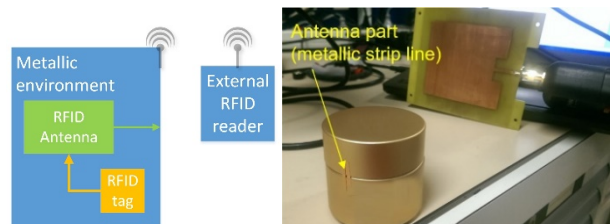


Figure 3: Block diagram of the RFID in the metallic box solution and implemented solution under laboratory test.

A passive UHF RFID was successfully integrated into a metallic package. The approach can be easily translated to much smaller metallic volumes, e.g., 2 to 5 times the current tested volume.

Dual-mode Bluetooth Silicon IP in 22 nm CMOS

N. Raemy

For years, CSEM's icyTRX BLE silicon IP has led the race towards the lowest power consumption, highest sensitivity, resilience to interferers, and maximum integration. It is available in several process flavors and foundries in the 65 and 55 nm technology nodes. IcyTRX-DM is the successor and brings performances improvement, reduced size and 50% power-savings (RX mode) for longer battery life. It is also fully backward-compatible with Bluetooth Classic, including the EDR mode, which makes it the ideal versatile candidate for applications requiring audio streaming.

Bluetooth Low Energy (BLE) has become omnipresent in our daily lives, enabling low-power connectivity with our smartphones, from simple temperature sensors to sophisticated smartwatches. Today even a rice steamer can log its cooking temperature profile to a smartphone through a BLE connection.

Before the introduction of BLE in 2010, in version 4.0 of the Bluetooth standard, Bluetooth (BT) Classic could be found in nearly all cellphones, starting with the Ericsson T39 in 2001, but was mostly used for audio streaming for hands-free headsets. With its drastically reduced power requirement, BLE was the trigger enabling a variety of new applications such as mice, keyboards and remote controls.

The Bluetooth SIG (Special Interest Group) finally added audio functionality to the BLE standard in January 2020 with the announcement of LE Audio, allowing portable audio devices to also benefit from the more efficient BLE. Nevertheless, to ensure backward compatibility audio streaming will require for the foreseeable future support of the power-hungry legacy Bluetooth classic mode (see Figure 1).

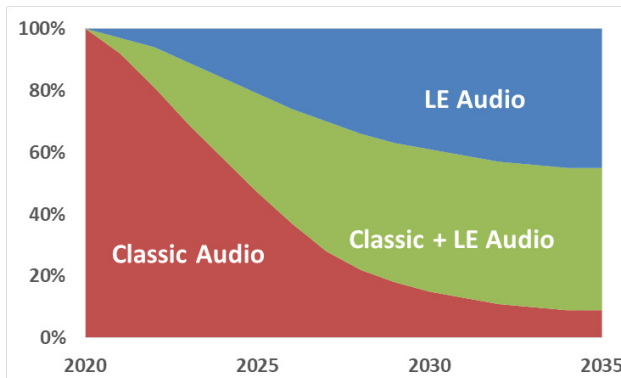


Figure 1: Expectation of Bluetooth Audio market.

In order therefore to address the immediate and growing need for low-power audio-enabled applications, and in particular the market of hearables, CSEM rearchitected and fully redesigned its existing IP, baptised icyTRX-DM, to simultaneously support dual-mode operation (classic and LE) audio streaming, while limiting the energy penalty associated with BT Classic. With less than half of the power consumption of the best BLE products, and up to 8x less than standard BT Classic products, icyTRX-DM offers a clear value proposition for portable audio products such as hearing aids and earbuds.

CSEM selected Global Foundries' 22 nm FD-SOI (Fully-Depleted Silicon-On-Insulator) as the first target for integration, benefitting from the outstanding performances at extremely low

power and ultra-low standby leakage. Other 22 nm CMOS options are planned to follow shortly.

The choice of such a high-performance target process allowed a design without compromise on the radio performances (budget link and interferers immunity among others). The increased complexity and more demanding modulation required by the Enhanced Data Rate (EDR) scheme in BT classic mode is offset by the capabilities of the lower-geometry node, which allow much more digital processing while minimizing both the silicon footprint and the power consumption. The architecture includes a newly designed flexible digital frequency synthesizer and modem. It supports a fallback BLE mode which provides all-round improved performances, including a higher power output capability, reduced spurious emissions and better blocking performances, for the best error-free audio streaming experience.

More than just a replacement, LE Audio promises attractive new features and new use cases, such as audio sharing, multi-stream, broadcasting and improved audio quality with the LC3 (Low Complexity Communication Codec). For instance, hearing-aid manufacturers had so far to support proprietary solutions like Apple's MFI [1], in order to stream efficiently a stereo audio signal from a smartphone. With LE Audio (Figure 2), True Wireless Stereo (TWS) audio streaming across all software platforms and smartphone manufacturers is finally possible, instead of using workaround with BT Classic.

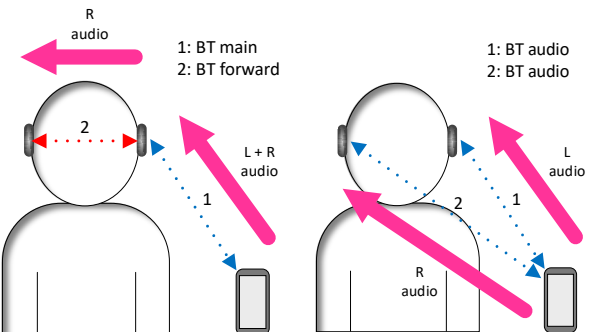


Figure 2: TWS Bluetooth Classic (left) vs TWS LE Audio (right).

IcyTRX-DM provides unparalleled benefits, including low-overhead backward compatibility and, in line with previous generations, best-in-class RF performances.

In addition to an overall improved robustness, it boasts a sensitivity @ 1 Mbs of -98 dBm (-95 dBm @ 2 Mbps) for half of the power consumption (3 mW) of previous solutions, and an output power scalable up to +10 dBm, all this with a low footprint of 0.65 mm² and no external component required besides the quartz reference.

[1] <https://developer.apple.com/programs/mfi/>

60 GHz FMCW RADAR-on-Chip

S. Cerida Rengifo, F. Chicco, E. Le Roux

System level study of a 60 GHz FMCW RADAR-on-Chip was carried out in order to evaluate the parameter trade-offs and define specifications for a short-range low-power application. A RADAR architecture is proposed for addressing the limitations regarding phase noise, flicker noise and DC offset.

Radio detection and ranging (RADAR) systems, which have been developed since the 1930s, have in recent years found their way into consumer electronics thanks to miniaturization. One example where RADARs can be found today is in the automotive industry as part of adaptive cruise control systems. However, there is still a gap in the market due to the lack of low-power, low-cost and fully integrated RADAR-on-Chip (RoC) solutions. This is a research opportunity, considering that there is still substantial room for improvement, in particular, targeting short-range applications, such as gesture recognition and vital signs monitoring. RADARs may be pulsed, continuous-wave (CW) or frequency-modulated continuous-wave (FMCW), the latter is best suited to fully integrated solutions. Pulsed-RADAR uses a transmitted pulse with a duration that is inversely proportional to the desired radial resolution (e.g., 0.15 ns for 22 mm): the average transmitted energy being strongly limited by the relatively low maximum voltage of CMOS technology. Pulsed-RADARs also require a power-hungry, fast ADC, which is often replaced in practice by sample-and-hold circuits for time sweeping of the sampling instant, which tends to lower the speed and overall power efficiency. CW RADARs are limited to Doppler (i.e., velocity) measurement as the ranging capability is missing and the absence of distance discrimination, except for very specific applications, significantly degrades the signal available for processing. The FMCW RADAR scheme provides the minimum peak-to-average transmitted power ratio, with a rather low-frequency baseband signal that is the sum of beat frequencies proportional to the distance to the reflectors (e.g., 6.7 kHz for 1 m with 1 GHz/ms sweeping slope).

The trend in RADARs is to operate at higher frequencies where larger bandwidths are available. This is advantageous because the radial resolution and accuracy are inversely proportional to occupied bandwidth. Higher frequency operation also corresponds to smaller antennas, as well as, better radial resolution per effective antenna surface area, for steerable or multiple-antenna systems. These are the main reasons for designing our RoC to operate in the millimeter wave (mmWave) frequency range: The license-free 57-64 GHz band is allocated to short range devices (SRD), offering a range resolution of 22 mm. The range accuracy is limited by the SNR due to noise in the receiver chain (e.g., thermal, flicker and phase noise).

Designing at mmWave frequencies imposes a challenge with respect to phase noise. However, the use of a RADAR with a single frequency synthesizer alleviates the problem. Contrary to communications, where one device transmits and the signal is received in another device, RADARs receive the same signal that they transmitted, after reflection off of the target. If the received signal is down converted using the same synthesizer which generated the transmitted signal, the phase noise is correlated.

The strength of the correlation depends on the range at which the target is located; the closer the target, the shorter the Time-of-Flight (TOF), the more correlated the signals. Experimental results were obtained using one and two PLLs [1,2]. A comparison of the phase noise at the down-converted Intermediate Frequency (IF) is shown in Figure 1. The measured IF phase noise for the two PLL setup is lower than the calculated value because they were not completely separated: they shared the frequency reference. The measured phase noise for the single PLL case is a good match with the calculated phase noise for high frequency offsets.

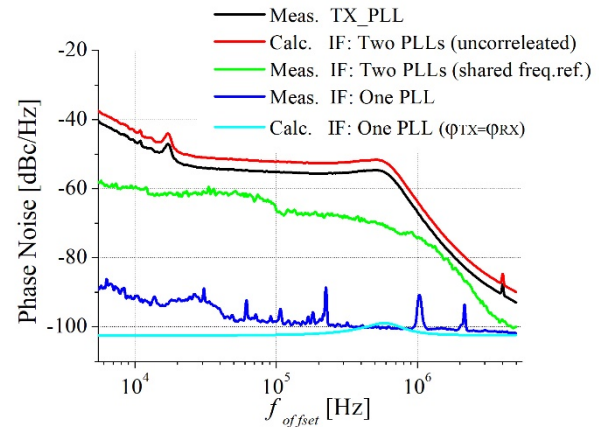


Figure 1: Calculated and measured values of the correlated phase noise.

The SNR attributable to thermal noise is dependent on the transmitted power, as well as, the noise figure (NF) of the receiver chain. Flicker noise optimization and DC offsets are especially important in short-range applications; since the TOF is short, the beat frequency, in practice, falls below 1/f corner frequency. This limitation is addressed by implementing phase modulation, such as BPSK, which translates the beat frequency higher. The RoC architecture and specifications are shown in Figure 2. The first integration in GF 22 nm FDSOI is been planned in Q4 2019.

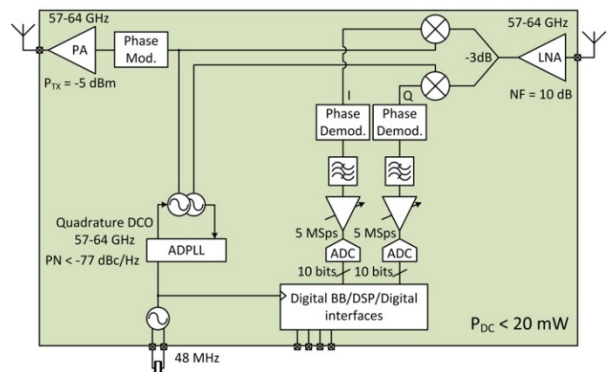


Figure 2: Block diagram of the RADAR architecture.

[1] M3TERA (EU project under GA No 644039) <https://m3tera.eu>

[2] E. Daskalaki, et al., "Measurement principles and hardware considerations for remote vital signs monitoring with a FMCW radar," IEEE Trans. Microw. Theory Tech. Submitted.

Bluetooth Direction Finding

N. Scolari, D. Nonaca

Localization is a hot topic and the recently released Bluetooth 5.1 specification adds a feature to improve it called "Direction Finding". It is based on the concept of Angle of Arrival and Angle of Departure (AoA/AoD) that provides information about the direction of the transmitted/received message. In the course of its continuous improvements, the icyTRx IP developed at CSEM has implemented this feature.

There are many techniques that can be used to localize a node inside a wireless network, such as the Time-of-Flight, phase calculation, etc. The Bluetooth SIG decided to use the AoA/AoD technique. In this case, the Transmitter node (Tx) or the receiver node (Rx), are intended to deploy an array of antennas. When the array is on the Tx side, we speak of the AoD, while if it is on the receiver, it is known as the AoA. During a transmission, the Tx or the Rx switches the antennas within a specific part of the packet. On the receiver side, the phase of the incoming RF signal changes between a chosen antenna and the phase difference is geometrically related to the angle formed by the RF signal propagation direction and pair(s) of antenna plane(s), as shown in Figure 1.

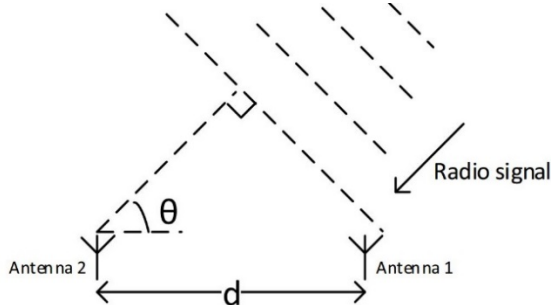


Figure 1: Angle of Arrival principle.

The Bluetooth specification does not define any particular configuration for the setup, number, or position of the antennas, in order to provide the flexibility and capabilities needed to configure the system for a wide range of use cases. In our implementation of the Direction Finding feature on icyTRx IP, we include as much as configurability as possible in order to enable the user to choose and program the antenna configuration. In particular, the number of antennas and the switching pattern are fully programmable (within the limits of the hardware implementation). Furthermore, the Bluetooth SIG does not specify any particular algorithm to perform the evaluation of the AoA or AoD. The task of finding the best solution is left to the customer. The digital baseband only needs to provide the signal samples from the receiver. The evaluation of the angle is then left to the network stack implementation.

The hardware changes to icyTRx consisted of modification of the packet handler in order to detect the optional phase sampling period, very precisely controlling the antenna switching pattern, and sampling the consequent data. Validation of the new hardware implementation was performed using an existing version of icyTRx as RF frontend, with the digital baseband implemented in a FPGA. The first measurements showed that calculation of the angle from the phase values obtained in the Rx is not straightforward: several issues due to phase ambiguity and multipath propagation need to be resolved in order to obtain a good estimate of the angle. Thus, in order to validate the principle of the AoA/AoD, a series of measurements have been performed in an anechoic chamber, in which a controlled rotating table is available, as shown in the Figure 2.

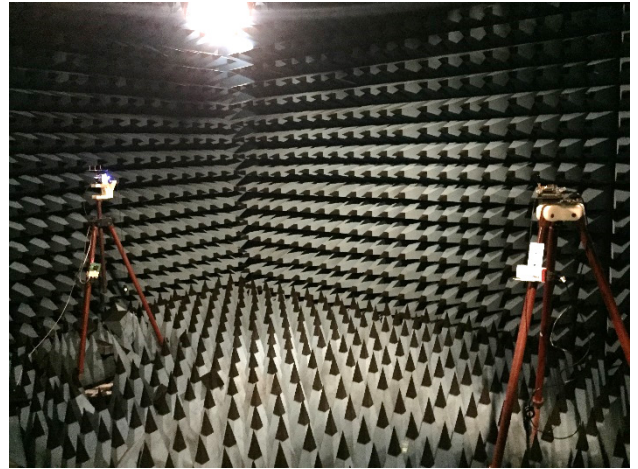


Figure 2: Measuring setup in the anechoic chamber.

For the initial tests, an array of 3 antennas was placed on an equilateral triangle separated by $\lambda/2$. The algorithm used to evaluate the angle was based on a brute force maximum likelihood principle. The results were nonetheless very encouraging, with a maximum error of 10° over the whole range of angles, as shown in Figure 3. It is interesting to note that some periodicity on the error measurements was found due to the antenna geometry, demonstrating that the angle calculation is not a trivial task.

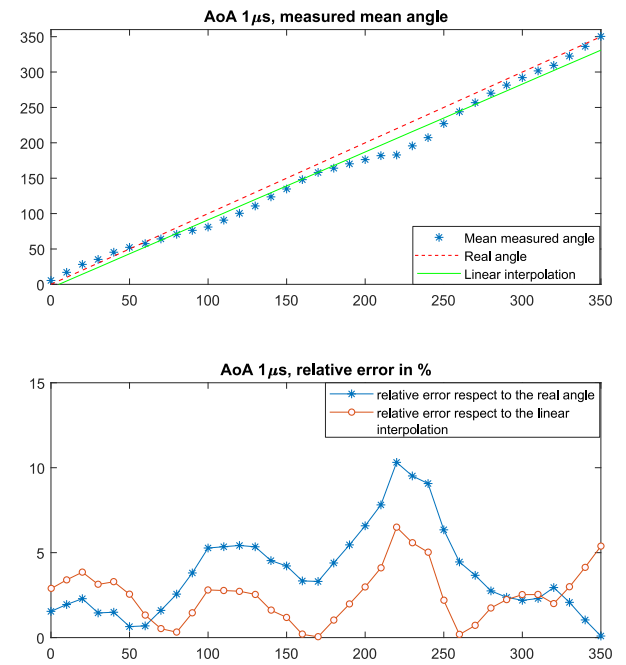


Figure 3: Measurement results for the AoA 1us.

The Direction-Finding feature of the Bluetooth Low Energy standard has been successfully implemented at a hardware level and a real silicon chip has been fabricated. The software aspects of the localization technique were found to be the most challenging; especially, due to the multipath propagation issue.

A Frequency Synthesizer for Ultra-low Phase Noise Multi-clock Generation

C. Salazar, P.-A. Beuchat, R. Godinho Caseiro, C. Monneron, F.-X. Pengg, E. Pérez Serna, P. Persechini, N. Raemy, D. Ruffieux, N. Scolari, D. Sigg, S. Stanarevic, A. Vouilloz

The project Pheros focuses on the development of an integrated 2.7 GHz ultra-low phase-noise Phase-Locked Loop (PLL) frequency synthesizer with an up to 2.7 GHz programmable multi-clock generator for low-jitter and high-speed time-based applications.

The continuous Complementary Metal-Oxide-Semiconductor (CMOS) technology scaling has allowed for the development of high-speed communication modules such as Analog-to-Digital Converters (ADC). With the operating frequency of such devices nowadays reaching up to the gigahertz range, clock jitter has become the dominant source of sampling noise, increasingly driving sampling noise optimization.

Pheros has focused on the design of an ultra-low phase noise Radio Frequency (RF) Phase-Locked Loop (PLL). Illustrated in Figure 1 is the simplified block diagram of the proposed analog PLL. It uses a 54MHz crystal oscillator (XO) reference, an integer-N loop frequency divider, a Phase-Frequency Detector (PFD), a Charge Pump (CP), a loop filter and a Voltage-Controlled Oscillator (VCO) operating in the range of 2.41 to 2.72 GHz. The core of the circuit, including the digital circuitry, is supplied from a 1.1 V source, while the XO is powered at 2.5 V. The proposed circuit uses a versatile programmable frequency divider in order to extend the user application domain. It provides divide-by-2 and divide-by-5 clocks with tunable duty cycle and phase shift. The VCO and the XO clocks are also accessible. Alternatively, an optional external clock allows the circuit to be driven by an external source, which may be required in multi-chip synchronized systems, where a single master chip can be used to drive the others, or where it may be convenient to reduce the component count by sharing a common XO.

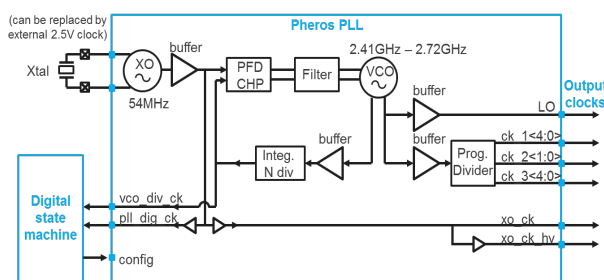


Figure 1: Block diagram of the proposed ultra-low phase-noise PLL.

As in any other conventional analog PLL's, the noise contributions of the crystal reference, the frequency divider, the PFD and the CP are filtered by a low-pass transfer function as seen from the output clocks; whereas, the VCO phase noise is high-pass filtered. As a result, the in-band phase noise is dominated by the reference clock, and the high-frequency phase noise by the VCO. Optimization of the XO and VCO phase noise is challenging. It is mainly composed by a flicker noise

[1] Sharma, et al., "A Dividerless Reference-Sampling RF PLL with - 53.5dB Jitter FOM and <-67dBc Reference Spurs", ISSCC (2018).

component generated by the up conversion of the 1/f noise of the active devices around the carrier and a thermal noise component induced by the losses on the oscillator's tank. Hence, the flicker noise contribution was reduced by increasing the active transistor area, while the thermal noise component was minimized by regulating the oscillation to maximize the amplitude within the safe operating area of the devices.

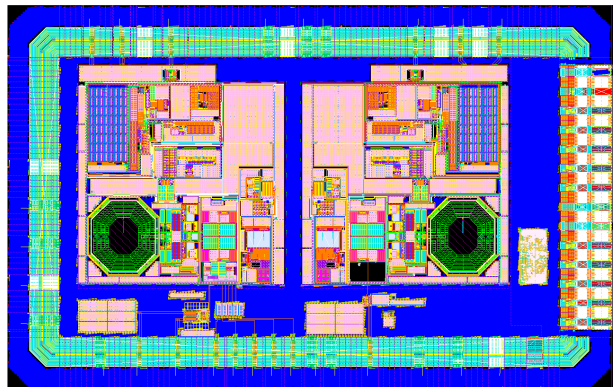


Figure 2: Layout view of the test circuit.

Figure 2 presents the layout view of the test circuit. The 1.26 mm x 2 mm circuit was integrated in a low power RF 40 nm TSMC technology. The circuit implements two symmetrical cores for test purposes with a core active area of 675 μm x 720 μm . The core PLL consumes 11 mA from a 1.1 V supply, while the XO current consumption is 0.45 mA from a 2.5 V supply. The results of measurements show a 100x XO phase noise improvement (20 dB) with respect to our previous in-house low power PLL reference and an 8x enhancement (9 dB) relative to the VCO. With -132 and -152 dBc/Hz at 1 kHz and 1 MHz offsets respectively, the 54 MHz XTAL oscillator has a Figure-Of-Merit (FOM) of -226 and -186, respectively.

Compared to the previous SOTA, very few circuits integrate the reference clock with the PLL [1,2]. Instead, they rely on external sources to achieve very good phase noise and jitter performance, hindering fair comparisons by obscuring the additional costs, integration complexity and power consumption of such solutions. Notably, 2019 reference [3], from the most reportable conference, presents only similar performance to Pheros, thereby demonstrating the excellent cutting-edge performance of the high-frequency time-reference, allowing us to further extend the operating frequency and resolution of the ADC's.

[2] X. Yang, et al. "-246dB Jitter-FoM 2.4GHz Calibration-Free Ring-Oscillator PLL Achieving 9% Jitter Variation over PVT", ISSCC (2019).

[3] Song, et al. "A Fractional-N Synthesizer with 110fsrms Jitter and a reference Quadrupler for Wideband 802.11ax", ISSCC (2019).

Talbot Effect Increases spaceCoder Resolution by more than One Order of Magnitude

E. Grenet

An innovative configuration of the spaceCoder allows a dramatic increase in the performances of the spaceCoder technology by using the diffraction pattern generated by the periodic grating. Opening new horizons for the spaceCoder technology.

The spaceCoder^[1] technology, invented and developed at CSEM, is an absolute measurement system based on shadow imaging. It consists in the detection of the position of a light source in its field of view with high precision and accuracy. The regular pattern of a reticle fixed on an imager is shadowed on its pixel array and processed with a Fourier-like algorithm, providing the position of the light source.

The aim here is to enhance the spaceCoder sensitivity by increasing the lever-arm effect of the technology (Figure 1). This means increasing the distance between the imager and the shadow mask (regular grating), but this effect degrades the signal due to interferences (diffraction). The use of a regular pattern enables us to turn this drawback into an advantage by working with the Talbot effect.

The Talbot effect is a diffraction effect: when a plane wave is incident upon a periodic diffraction grating, the image of the grating is repeated at regular distances away from the grating plane. The regular distance is called the Talbot length (Z_T), and the repeated images are called Talbot images. At regular fractions of the Talbot length, sub-images can also be observed: for example, at three quarters of the Talbot length, the self-image is halved in size, and appears with half the period of the grating, this creates a Talbot carpet pattern, see Figure 1. The Talbot length Z_T depends on the light wavelength λ and the grating period a : $Z_T = 2 a^2 / \lambda$.

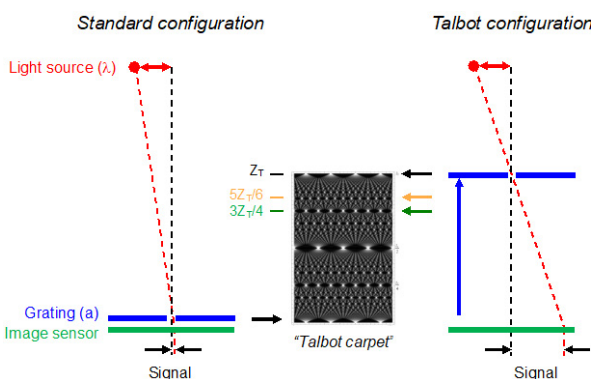


Figure 1: Lever-arm effect illustration between spaceCoder standard and Talbot configurations, Sub-periodicity effect illustration for particular Talbot distance fractions (orange and green positions).

As an example, a standard spaceCoder configuration consists of a regular pattern (period $a=100 \mu\text{m}$) fixed at 1 mm of the sensor active area, illuminated by a near-infrared source ($\lambda=850 \text{ nm}$). Placing the pattern at the Talbot distance ($Z_T=23.5 \text{ mm}$) allows the imaging of a pattern shadow without any diffraction effect (Figure 2). At 1 m distance, a $100 \mu\text{m}$ lateral displacement of the light source induces a displacement of the shadow signal of 100 nm in the standard configuration and $2.4 \mu\text{m}$ in the Talbot configuration, increasing the detection resolution by a factor of 24. Moreover, placing the pattern at twice the Talbot

distance ($2Z_T$) provides an increase by a factor close to 50 whilst maintaining a good image quality. This lever-arm effect has been measured for various multiples of the half-Talbot distance, the enhanced measurements matching with the theory.

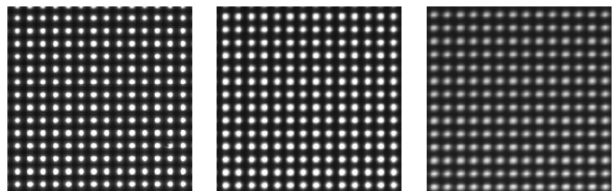


Figure 2: Image of a $100 \mu\text{m}$ regular grating in spaceCoder standard configuration (left) and in Talbot configurations, placed à Z_T (middle) and $2Z_T$ distances (right).

The measurement resolution can also be enhanced by an additional multiplicative sub-periodicity effect: In the spaceCoder technology, the signal precision is relative to the observed period. Placing the regular grating at a given Talbot distance fraction, where sub-periods are observed, provides an enhancement of the precision by the period multiplicative factor. For example, the precision enhancement is doubled at $3Z_T/4$ distance and tripled at $5Z_T/6$ distance (Figure 1, resp. green and orange arrows).

Both of these enhancements (lever-arm and sub-periodicity) can be combined, and their effects are multiplicative, allowing in such conditions to increase the spaceCoder resolution by more than two orders of magnitude, leading to the detection of displacements of the light source that are not perceptible with the standard configuration. The spaceCoder Talbot configuration has been successfully tested on large incident angles ($>60^\circ$) with different combinations of pattern period (a), illumination wavelength (λ) and Talbot distance (Z_T) fractions and multiples.

Finally, this new Talbot configuration allows the use of very small grating periods to achieve even higher precision. Using such small periods was previously not possible with the standard configuration due to the substantial noise from diffraction. This is now resolved by placing the regular grating at a specific Talbot distance as this provides a clean Talbot image without interferences.

An absolute code can be designed in the regular pattern (for example with missing holes) to implement high-resolution absolute encoders based on Talbot effect. Such absolute code implementations have already been successfully tested.

This new patented Talbot configuration gives great perspectives for the spaceCoder technology. Practically, this solution appears applicable in many situations, providing higher precision, higher resolution and potentially higher accuracy. Next developments in spaceCoder industrial projects may include this new approach to achieve performances previously not possible.

^[1] E. Grenet, et al., "spaceCoder: a nanometric 3D position sensing device", CSEM Scientific and Technical Report (2011) 89.

MODAL—a Multi-modal Sensing Platform for IoT Applications

N. Cantale, P. Nussbaum, P. Molticek

Robust sensors for people tracking and health state monitoring are needed to allow the ill and elderly to maintain their independence and to relieve the burden on the healthcare system. This work, in a collaboration with Idiap, is focused on merging the output of several sensor types to provide accurate monitoring and alarm raising in the context of eldercare.

CSEM has a track record of developments in building occupancy detection and monitoring using embedded vision. CSEM and Idiap's recent collaborations with industry has revealed an interest and potential of autonomous smart sound devices. Applications exist in security, surveillance and eldercare. Given the aging population, the segment of elder care and more specifically key technologies that can detect and manage critical situations (falls, distress, ...) is expected to grow.

Visual detection and localization of people in buildings finds limitations in many ambiguous situations where the absence of motion or presence of artefacts are reducing the accuracy and robustness of detection. Furthermore, the information necessary to evaluate the seriousness of a situation (people care) is often absent from the images alone. The goal of the present project is to bring complementary information from the analysis of ambient sound and combine it with the visual analysis. Going multi-modal improves substantially the robustness of the system and provides the necessary features (speech analysis, sound localisation, and automatic speaker and speech recognition) to address several market segments.

The combination of the visual and sound information is done on an embedded platform based either on the Nvidia TX2 or Nano IoT solutions. The platform can host up to 3 MIPI cameras or several USB cameras. The audio comes from a 6 channels microphone array from MiniDSP and the communication is done through Ethernet or a Wifi access point. The platform is designed to easily host additional sensors in the future, in order to improve their input for better accuracy or functionality (e.g., RF sensing).

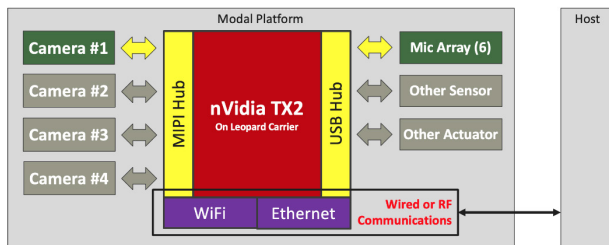


Figure 1: The Modal platform.



Figure 2: The housing for the Modal platform.

The platform is mounted inside a 100 x 100 x 70 mm housing, containing the Nvidia module, the carrier board, the camera, the microphone array, a USB hub, a Wifi antenna. There is extra-space for optional modules like a LoRa modem.

Two machine learning algorithms run side-by-side on the platform. The first one does the people detection, based on a network previously developed by E. Türetken [1]. The system achieves a detection precision of 95% and a recall of 94% on the test dataset. It can distinguish people with a spatial resolution of less than half a meter on the floor, sufficient for most applications. The trained model has 37 thousand weights, which takes less than 200 KB memory to store, and can run real-time with limited computational resources.

The information from the visual monitoring is sent to the second algorithm, which analyses the audio inputs and does the following tasks:

- Audio activity detection detects the presence of active speakers and discriminates from other sound sources;
- Speaker identification: identifies the speaker from a list of registered users;
- Keyword spotting: detects commands from a list of keywords;
- Source localization: performs the 3D location estimation of the speaker using beamforming.

The output is then an audio command from an identified speaker, with its location, which can be sent to a server or another device.

Future works include further miniaturization of the platform and improved algorithms natively implementing tracking capabilities.



Figure 3: Illustration of the audio and video fusion. Image from the MODAL platform. The people are detected (in green), the speaking (blue speaker icon) and non-speaking (blue wave icon) sound sources are separated, the speakers are identified, and the keywords are spotted (bullets on the right).

[1] E. Türetken, L. A. Dunbar, "Efficient Deep Learning Algorithm for Person Detection from Ceiling-mount Cameras", CSEM Scientific and Technical Report (2018) 99.

Handheld Multispectral Imaging Device Designed to Aid Skin Cancer Detection

S. Blanc, P. Pad, L. A. Dunbar

Dermoscopy is an instrument-aided procedure used for the examination of skin lesions with the help of a dermatoscope with relatively wide field-of-view and high resolution. Digital dermoscopy also includes image processing techniques where a specialized digital camera allows a digital record and analysis of the structures. The most commonly use of digital dermoscopy is for early stage melanoma detection. In this project, we develop a prototype of a new generation digital dermoscopy device which is based on multispectral imaging technology.

CSEM multispectral imaging strategy is to provide application-specific solutions from both a hardware and software perspective. This strategy contrasts with general purpose hyperspectral imaging. The advantage of dedicated solutions is that they are optimized in many aspects such as data rate, physical size, accuracy and cost. To this end, CSEM provides multispectral imaging systems with diverse technologies such as spectral filtering on the image sensor or using multispectral illumination.

The SpectroX system combines multispectral imaging and deep learning in order to provide instant predictions about the risks of the underlying skin conditions. During a pre-study phase, the suitable specifications for the dermoscopy application, such as the central wavelength and bandwidth of the spectral bands, spatial resolution, field of view, cube acquisition rate and so on have been obtained (Table 1).

Table 1: Specifications of the multispectral imaging device.

Characteristic	Value
Number of spectral bands	14
Wavelength range (nm)	400 – 970
Spatial resolution (pixel)	1096 x 1096
Field of view (mm)	20 x 20
RGB display frame rate (1/s)	16
Total cube acquisition duration (s)	2.0
Camera interface	USB 3.0

Based on these investigations, a multispectral imaging device has been designed and implemented using the multispectral illumination strategy. The device is constructed using off-the-shelf components in order to optimize the cost and delivery time and then packaged using 3D printing technology (Figure 1).



Figure 1: Two views of the SpectroX device designed and produced by CSEM.

Once the camera is on, a color image of the target is displayed in the software. After pointing at the region of interest, by pressing the button on the device, a multispectral image of this region will be saved on the computer. The design is centered around ease-of-use for medical doctors and also potentially for general public in the future. It has a single USB 3.0 connection for both power delivery and data transfer and a single button to trigger the acquisition. Some sample slices of an acquired multispectral hypercube are shown in Figure 2.

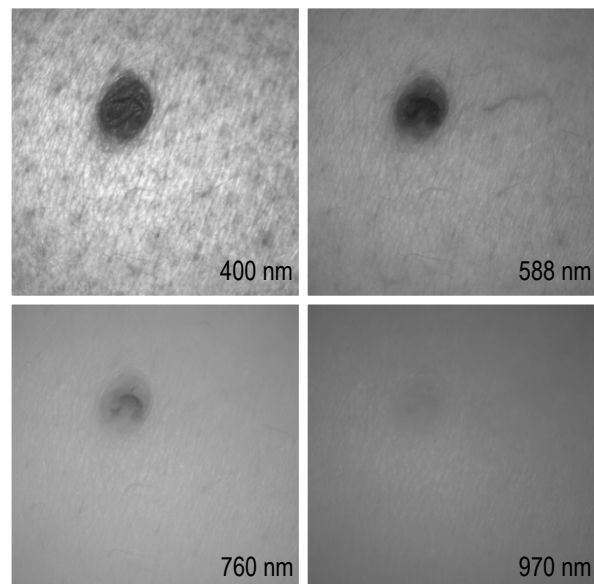


Figure 2: Samples of taken images at 400 nm, 588 nm, 760 nm and 970 nm, respectively from top-left to bottom-right.

In combination with deep learning algorithms, this system is expected to be able to detect melanoma and other skin cancer conditions (like basal cell carcinoma) much earlier than existing dermoscopy systems. Such early stage diagnosis increases the success rate of the treatment, reduce the medical and insurance costs, providing a benefit for the society as a whole (it is known that skin cancer can be an aggressive metastatic form of cancer).

Thanks to these innovative features, SpectroX system expected to be able to penetrate the market since (i) it will be more effective and accurate than current systems, (ii) it minimizes the need for repeated examinations, saving time and costs and (iii) it can be scaled as a screening device by non-experts for the massive examination of a larger portion of the population. By enabling digital dermoscopy for consumer applications out of the close-boundaries of skin healthcare professionals, a new market will be created [1].

[1] S. Blanc, P. Pad, L. A. Dunbar, "A fast, simple to use and inexpensive multispectral camera to detect skin conditions", submitted to conference on Photonic Instrumentation Engineering VII, part of SPIE OPTO (2020).

Deep Learning Architectures for Detecting Surface Defects using Multiple illuminations

D. Honzákto, E. Türetken, S. Bigdeli, M. Kozinski[•], P. Fua[•], L. A. Dunbar

Application of deep-learning-based computer algorithms for surface defect detection is often problematic due to their need for large annotated datasets. Here we tackle this problem using a novel algorithm architecture that benefits from seeing the defect from different vantage points, i.e., multiple illuminations. Using self-supervised techniques, we capture defining, illumination-invariant, features of the surface which are later used for defect detection with a very limited annotated dataset.

Defect detection has long been of key importance to a wide range of industrial applications. Many of these applications are complex, require high-speed and yet must be cost-effective. Automated visual quality checks at frequent intervals have emerged as an efficient alternative to traditional inspection by (human) experts. In recent years, as with many other image analysis tasks, machine learning (ML) has become a standard tool used for defect detection.

The visibility of a defect depends on many factors such as illumination, reflection properties of the material, the relative orientation of the camera, etc. Nevertheless, to spot most of the defects, it is often sufficient to observe the surface using a light dome, where the camera is located on the top and the illumination angle can be controlled. Figure 1 shows an image of a watch part with many scratches captured using such a setup.

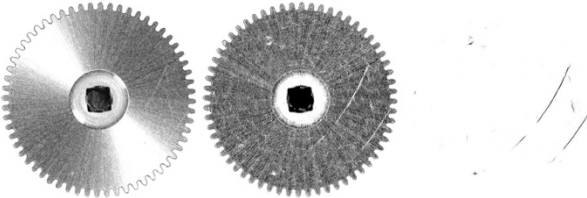


Figure 1: Defect detection of a watch part. (left) One of the many input images, (middle) Extracted features; (right) Defect predictions.

The manufacturer is usually interested in a binary decision about the defectiveness of a part. Nevertheless, due to the scarcity of the defects and resulting small number of samples that can be used to train and test ML algorithms, annotations have to be more precise – ideally, pixel-level-precise. Although the precise localization of defects dramatically reduces the problem of overfitting, the state-of-the-art deep learning architectures, such as the U-Net^[1], still struggle to generalize well on relevant test sets. This can be attributed to the *curse of dimensionality* as each sample consists of multiple high-resolution images.

A well-known technique to tackle the *curse of dimensionality* is to first extract defining features from the sample and then use the ML algorithm on these features. For most image analysis tasks, the feature extraction part is performed by networks pretrained on large databases of natural images. Unfortunately, images of surfaces vary substantially in these databases and as such a more sophisticated solution is needed.

Here we propose a self-supervised feature extractor based on auto-encoder (AE) architecture. AE consists of two networks – Encoder, which extracts the features, and Decoder, which uses the features to estimate the original input. Although simple AE already exhibits minor improvements, further improvement by exploiting certain prior knowledge stemming from the controlled

environment of a light dome may be possible. Such knowledge consists of the fact, that the image can be decomposed into object and light features where only the object features are useful for the defect detection.

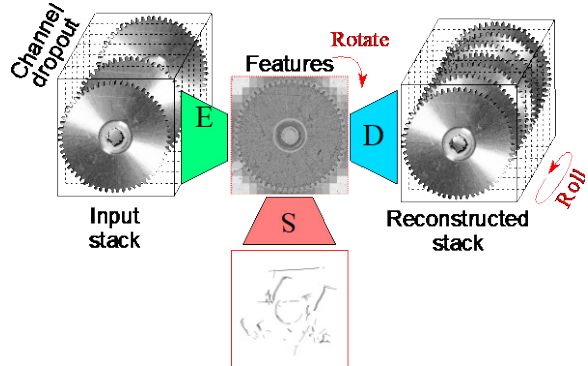


Figure 2: Rotate & Roll Channel Auto-Encoder architecture: Encoder (E) extracts the features, Decoder (D) estimates the original images, and Detector (S) segments the defects.

Such behavior can be imposed by Rotate & Roll Channel Auto-Encoder (RRCAE), which is visualized in Figure 2. It randomly rotates the features (before the decoding) as well as the desired image estimate. The desired output is also reordered (rolled) such that it seems to be illuminated from the same angle as if no rotation occurred. The random rotations are therefore limited to the angles of the possible illuminations. Such training process forces the features to contain object information only, while the light information gets implicitly encoded in the weights of the encoder and decoder network.

The core parts of the channel RRCAE – the Encoder, Decoder, and Detector are U-Nets, differing only in certain parameters, such as the number of output channels, up-sampling function, or the number of root features. To increase the generalization, during the training time, half of the input images are randomly dropped out (i.e., multiplied by zero).

The proposed architecture was empirically tested on a dataset of 40 cogged wheels of size 512 x 512 px captured in a light dome under 12 different illuminations. Results of cross-validation on 20 defective samples shows that the defect detection performance of the model significantly improved compared to the standard U-Net solution. The mean AUROC score increased from 0.94 to 0.97 while the standard deviation dropped from 0.05 to 0.03.

As well as improving the defect detection with a reduced number of samples compared to the standard technique, as shown in Figure 1, this method provides a clear visualization of the intermediate features of the sample in a single image.

[•] CVLAB, EPFL, Lausanne

[1] O. Ronneberger, P. Fischer, T. Brox, “U-net: Convolutional networks for biomedical image segmentation”, MICCAI (2015).

icyflex-V—a New Ultra-low-power Processor based on RISC-V Architecture

J.-L. Nagel, C. Arm, R. Cattenoz, H.-R. Graf, V. Moser

The icyflex-V processor is a new ultra-low-power core based on the RISC-V 32-bit ISA, a long-awaited addition to the CSEM icyflex processor family, compatible with off-the-shelf open-source and/or proprietary programming tools. This new development represents a cost effective yet performing alternative to proprietary cores for next-generation ultra-low-power system-on-chip developments. The core was optimized for performance, code density and power consumption and delivers up to 3.2 CoreMark/MHz while consuming as low as 14 μ A/MHz in TSMC 55 nm low-power process.

RISC-V is an open-source initiative developed by the eponym foundation^[1], whose main goal consists in defining and standardizing a state-of-the-art open-source instruction set architecture (ISA). The base ISA exists in 32-bit and wider flavors, and can receive several extensions (multiplication/division, compressed instructions, multi-precision floating point, vector instructions, etc.). While several hardware implementations and tools are freely available as open-source initiatives, commercially available solutions are also common.

RISC-V is perceived as a game-changing initiative. While the market was long split between ARM for mobile applications and Intel for computer or server applications, RISC-V cores may well become in the coming years the unifying framework spanning both worlds, thanks to its standardization and open access. The extensibility of the ISA indeed allows designing both ultra-low-power embedded cores and multi-gigahertz supercomputer cores. While RISC-V is today a reference platform in the academic world, key industrial players such as NVIDIA or Western Digital already joined the party, with real products soon to appear on the market.

As a member of the RISC-V foundation, CSEM is following the standardization of the RISC-V ISA and its ecosystem, implementing new features as they become standard and when these bring value to its customers. For instance, CSEM is currently actively following the debug and tracing workgroup activities.

CSEM has a long track record in ultra-low-power processors, dating back to 4 bit watch processors and to the 8-bit CoolRisc success story. More recently the 32-bit icyflex2/4 cores were successfully embedded in several customer products.

The icyflex-V is a classical 4-stage pipeline (fetch, decode, execute and write-back, Figure 1), implementing the RV32IMC ISA, i.e., a 32-bit integer core supporting the compressed instructions and multiplications. Data forwarding is implemented to avoid pipeline stalls on both ALU outputs and load-store (LSU) outputs caused by read-after-write dependencies. The main target of the core is to be embedded efficiently with a small footprint in ultra-low-power system-on-chip. The main criteria are thus an excellent code density (thanks to compressed instruction) and a limited gate-count achieving good performances. Several options were further taken to reduce the gate-count: the M extension of the ISA is implemented without hardware support for division, which would imply a significant number of gates for a feature not largely used in embedded applications. Similarly, floating-point is left as software emulation to reduce gate-count. In order to achieve state-of-the-art performance though, the 4 stage pipeline was preferred over a 2 stage pipeline that would assuredly be more compact but which would have degraded

performances drastically. Similarly, the instruction prefetch buffer implements a simple yet effective branch prediction mechanism that improves the core efficiency at a reasonable gate-count cost.

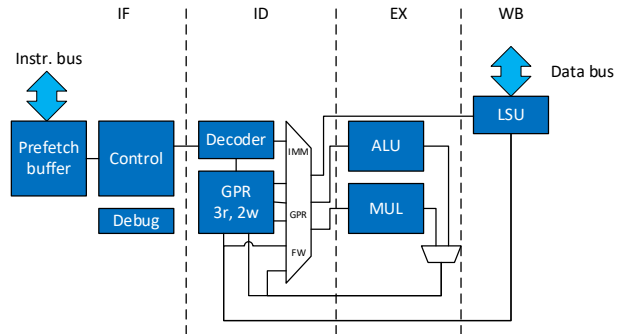


Figure 1: icyflex-V pipeline (IF: fetch stage; ID: decode stage; EX: execution stage; WB: write-back stage).

With these choices, the core achieves a remarkable 3.2 CoreMark/MHz with maximum compiler optimizations, or a 2.8 CoreMark/MHz in balanced performance/code density mode, when using the open-source GCC compiler. The core also reaches a 1.36 DMIPS/MHz. Vendor specific compilers (e.g., IAR) can also be used with the icyflex-V.

Currently, the icyflex-V does not implement non-standard extensions, aiming at keeping a de-facto compatibility with off-the-shelf tools. Specific non-standard extensions might however be added in the future and be used as "intrinsic" assembly instructions to accelerate application specific systems. This could be done seamlessly, without requiring to customize standard compilers.

A debug interface based on the official specification allows to interface the system to on-chip debug tools through a 4-wire JTAG interface. Triggers can optionally be implemented to allow placing breakpoints in flash memories, or to perform data watchpoints. Both open-source software (OpenOCD, GDB, MCU Eclipse) and proprietary tools are supported (Segger Jlink/Embedded Studio, Lauterbach Trace32, IAR Embedded Workbench) by this standard debug interface.

The icyflex-V comes with several peripherals (bus controllers, serial and communication interfaces) that allow customizing systems based on customer requirements. The subsystem can be easily extended with external IP using standard peripheral busses such as APB.

The core is silicon-proven, and an evaluation FPGA-based platform is available. The core is currently being integrated in first customer products and evaluation of its performance in subthreshold libraries is ongoing, paving the way to new ultra-low-power records.

[1] <http://www.riscv.org>

Binary Weight CNN Hardware Accelerator for ULP Computer Vision

P. Jokic, S. Emery

Convolutional neural networks are the state-of-the-art algorithms for object detection and classification in many computer vision applications. The high accuracy comes at the price of deeper architectures, resulting in large networks and high associated computational requirements. This limits their deployment on wearables, IoT devices and other power-restricted platforms. Recent advances in quantized neural networks have achieved comparable performance at a significantly lower memory footprint and reduced computational complexity. We present a low power convolutional neural network hardware accelerator featuring efficient exploitation of binary weights and elaborate on the benefits of quantized weight networks.

The key components of today's state of the art object detectors are convolutional neural networks (CNN). Applications range from high-speed obstacle detection in autonomous driving to low-power face detection in smart wearables. While cars are already designed to supply large amounts of power to electronic subsystems, mobile devices are limited by their small batteries, requiring every single sub-system to consume as little power as possible. To enable meaningful computer vision applications on such low power devices, efficient CNN processing is needed. This work presents a binary weight CNN hardware accelerator that efficiently computes binary weight neural networks, which minimize the memory footprint and enable low-power processing of embedded computer vision applications.

Computing a CNN is a highly data intensive task, dominated by millions of multiply-accumulate (MAC) operations, which are needed to convolve input activations with kernels consisting of learned weights. This process is repeated for each network layer, using the outputs of the previous layer as inputs for the following one. Recent improvements in the performance of neural networks were largely a consequence of the transition to deeper networks, leading to a data bottleneck which manifests itself in a large memory footprint, overloaded memory interfaces and a high-power consumption. Reducing the vast amount of data to be processed and simplifying the involved computations therefore became a hot topic in the field of embedded machine learning. One proposed approach is data quantization, aiming for smaller data entries due to compressed data and reduced precision computational elements. Different levels of quantization applied on activations and/or weights have been proposed. Even fully binary networks^[1] (BNN), with activations and weights being quantized to 1 bit (representing -1 or 1) have been shown to be viable options, though at the cost of a reduced accuracy.

This work is using binary weight CNNs, which are a trade-off between accurate full-precision CNNs and BNNs, featuring binary weights but standard-precision activations. From a computational point of view, binary weights are very practical for the convolution operation: the summed multiplications of input activations and weights (+/- 1) are simplified to additions. This helps saving power as multipliers can consume more than 50x more power and 25x more area than adders of the same precision^[2]. Compared to a non-quantized 16-bit CNN, binary weights can reduce the memory of the weight parameters by 16x, reducing memory leakage and power for accessing data. This is especially beneficial for deep networks, where the memory size for storing weights can be comparable to the activation memory

size. We evaluated the memory savings on a real-world 9-layer CNN for face-detection that was ran on our accelerator: the overall memory footprint was reduced by almost 35% when changing from 16 bit to the implemented binary weights.

The implemented CNN accelerator is a standalone system that can directly interface a connected memory, allowing to take over the complete CNN processing from a microcontroller. It consists of 5 main blocks, as shown in Figure 1:

- Control: reads layer settings from memory, configures other blocks, requests addresses of activations and parameters.
- Address generator: computes memory addresses of data.
- Memory interface: buffers requests and interfaces memory.
- Data pre-processing: extracts and sorts data from memory words, buffers operands to keep all parallel MAC units active and writes results back into memory words.
- MAC processing: multiple parallel units performing the MAC operation with binary weights, pooling and output activation.

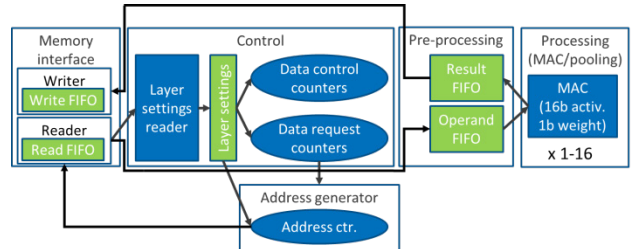


Figure 1: CNN accelerator block diagram.

The number of parallel MAC processing units can be chosen using a generic design parameter, achieving a peak performance of 360 MOPS with a single memory interface and two MAC units. An implementation supporting higher memory bandwidths using multiple memory ports is under development. All network architecture settings, such as layer width or channel depth, can be changed at runtime by configuring the layer settings region in the memory. This allows the accelerator to process any kind of CNN that fits in the memory, enabling different applications to be processed with the same chip. Other fields of use include signal processing, image classification or compression. With an area of 128 kGE (gate equivalents, for a version with 2 parallel MAC units), the accelerator is light-weight and can be easily used to offload data-intensive CNN computations from a microcontroller. The estimated power consumption in a 22 nm FDX process is 2 mW at 180 MHz.

[1] M. Courbariaux, et al., "BinaryConnect: Training Deep Neural Networks with Binary Weights During Propagation," NIPS (2015).

[2] M. Horowitz, "Computing's energy problem (and what we can do about it)," ISSCC (2014).

FaceDET—a 1.4 GOPS Face Detection System-on-chip based on Binary Decision Trees

E. Azarkhish, E. Türetken, P. Nussbaum, S. Emery

FaceDET is a high performance low-power system-on-chip (SoC) designed to perform face detection in edge-applications with power requirements of a few milliwatts. The design follows a modular approach with a general-purpose RISC-V based processor (main controller), a memory-mapped Binary Decision Tree (BDT) accelerator (BDTAcc), and the associated memory subsystem and peripherals. Synthesis results prove feasibility with system frequency reaching around 180 MHz, providing nominal system performance up to 1.4 GOPS^[1] and a memory bandwidth above 20 GB/s. The place-and-route of the complete system-on-chip is being done in the Globalfoundries 22 nm FDX technology.

Figure 1 illustrates an overview of the FaceDET SoC. It reuses icyflex-V, a 32-b RISC-V based micro-processor designed and maintained by CSEM, as its main controller. This is to enhance programmability and ensure compatibility with the software stacks developed inside CSEM and by the rest of the RISC-V community. 16 KB of ROM and 64 KB of private memory (L0) are dedicated to the main-controller, accessible by icyflex-V and its peripherals.

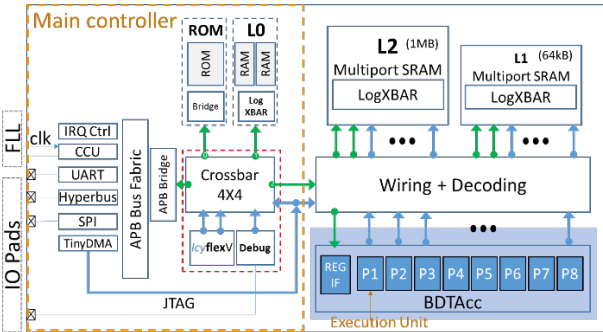


Figure 1: An overview of the FaceDET SoC.

The icyflex-V core handles communication with the peripherals, including CSEM's low-power VGA imager^[2] attached to the Hyperbus, an external flash attached to standard SPI, an FLL for clock generation, and a UART for user interaction. The main controller has a visibility of the whole memory space including all memory levels, peripherals, and the accelerator's registers. The Central Configuration Unit (CCU) is responsible for configuring pads, peripherals and memories, as well as, power management.

An optimized fetch-and-deposit DMA (TinyDMA), with a very small footprint and power consumption, is responsible for transfers between memory and the peripherals. The Hyperbus IP enables high-speed communication (>100 MBps) with the imager.

The key differentiating point about the architecture of FaceDET is a highly parallel memory organization with a unified address space thanks to an especially designed logarithmic crossbar interconnect (LogXBAR), providing all-to-all connectivity with 2-by-2 arbitration trees. Word-level interleaving is adopted to remove the burden of bank-conflicts from the programmers, and banking factor has been increased to 4, to naturally reduce bank conflicts to below 5%. This is in opposition to standard bank-interleaving schemes, in which the programmer must explicitly allocate memory banks to accelerator units and mind the bank conflicts. The L1 (64 KB) and L2 (1 MB) memories, both organized in 16 banks, operate at the same system frequency, except that access to L1 is less costly in terms of energy

compared to L2. Efficient use of the L1 memory by the software helps bring down the overall energy consumption.

BDTAcc implements an optimized version of the AdaBoost algorithm using 8 parallel execution units (ExU). Each ExU contains a hardware state-machine, capable of traversing binary decision tree nodes in the memory and making decisions independently. AdaBoost is an easily parallelizable algorithm breaking the image into several overlapping bounding-boxes of different sizes and orientations and calculating the likelihood of detecting faces in them with two levels of tree based classifiers, as illustrated in Figure 2. A large batch of bounding boxes can be dispatched to each ExU to parallelize and accelerate execution.

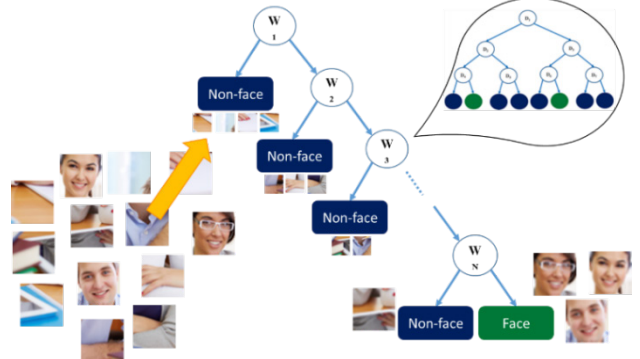


Figure 2: An illustration of the AdaBoost face-detection algorithm.

Each ExU implements two variations of AdaBoost: FAST with a larger memory footprint but fewer memory accesses per operations, and COMPACT with smaller footprint and more accesses resulting in higher consumption and execution time. The user program can define a threshold to switch from the FAST to the COMPACT method to dynamically benefit from both of them.

The 22 nm FDX technology from GlobalFoundries has been selected as one of the most advanced nodes for the IoT and low-power applications. We use body-biasing to dynamically adjust face-detection performance in a trade-off with power consumption.

Synthesis results show that more than 90% of the area is devoted to the L1 and L2 memories and their interconnections. BDTAcc uses less than 2%, and the rest of the area is used by the main controller. A new revision is under preparation with a convolutional neural network (CNN) accelerator beside the BDTAcc, allowing for hierarchical detection/classification with the two approaches to find the right balance between accuracy and energy consumption.

^[1] Comparison of two integers is considered an operation.

^[2] P.-F. Rüedi, et al., “An Ultra-low-power High Dynamic Range Image Sensor”, CSEM Scientific and Technical Report (2018) 101.

A Miniaturized Motor Control Unit for Space Exploration Missions

H.-R. Graf, G. Gruener, T. Burch

The ESA project Miniaturized Motion Controller Customization for Exploration (MCC-X) aims to develop and validate a general and standardized motor controller to form a complete integrated node in a distributed motion control system. The product to be developed in the project is a miniaturized motion control device designed to withstand the environmental requirements of several different space applications, including the Martian environment and geostationary orbits.

The Miniaturized Motion Controller Customization for Exploration (MCC-X) is designed to be a closed-loop motor control unit with a simple interface. The latter consists of only connectors for power and standardized communication buses, towards the user platform in order to enable distributed motor control. The unit is very compact ($<120 \text{ cm}^3$) and must withstand the extreme environment of space exploration missions. The targeted non-operational temperature range is -130°C to $+100^\circ\text{C}$. In order to cope with such harsh requirements, it is realized using hybrid mounting technology, where several modules are assembled on a carrier which is placed in a single enclosure (Figure 1).

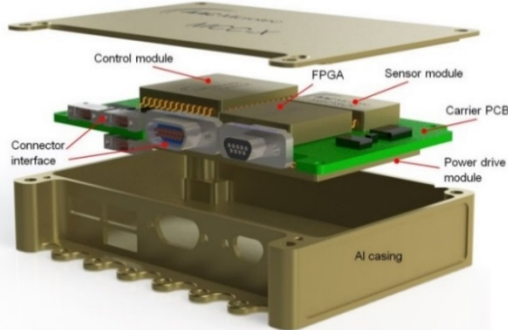


Figure 1: Conceptual view of the MCC-X assembly.

Each MCC-X unit is a stand-alone component that includes modules for power drive, control and sensing. It allows the autonomous operation of a brushless motor (or up to two brushed motors) in torque, position or velocity mode. A radiation tolerant FLASH-based field-programmable gate array (FPGA) performs closed-loop motor control as well as the communication over CAN bus (or optionally SpaceWire) with a host unit. The unit also has an internal heater. The MCC-X design is modular in terms of the available subsystems: power electronics for driving the motors, on-board logic for implementing the control algorithms, telemetry functionality and sensor data acquisition. The reconfigurable FPGA allows customization of the design according to the needs of various applications.

The ESA project MCC-X is a follow-up to an earlier MCC activity with the goal of advanced miniaturization and higher computation power. Both CSEM and Maxon Motor are again part of the consortium. CSEM is in charge of the development of the FPGA firmware and host-based graphical user interface (GUI). Maxon Motor contributes to the definition of requirements, review of the electrical design and is responsible for functional and environmental testing.

All communication protocol and motor control logic is implemented directly in FPGA firmware. No soft processor is used. This reduces the hardware components and fault-sources significantly, as no external memories are needed. Advanced techniques like triple modular redundancy (TMR) can be used for further radiation-hardening of the FPGA design.

For closed-loop motor control, the FPGA implements cascaded proportional-integral-derivative (PID) controllers, filters and interpolators (Figure 2). To save resources, all these operations are implemented in time-multiplex with a single multiply-and-accumulate (MAC) instance.

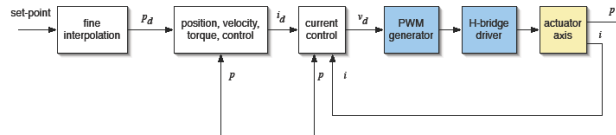


Figure 2: Closed-loop motor control block diagram.

An application-specific digital-signal-processing (DSP) engine in the FPGA implements a 32-bit fractional data path, by using a single 16×16 bit signed/unsigned HW multiplier, a 32-bit barrel shifter and a 64-bit accumulator. At every clock cycle, the intermediate result of the multiplier is fed to the accumulator, correctly shifted and sign/zero extended. The 32-bit read-out of the accumulator is saturated and can get clipped to lower and upper boundaries.

In the FPGA design, a programmable sequencer controls the DSP engine. The assembler for the sequencer and DSP engine, but also the many GUIs for different motor configurations and motor control applications were developed in Python (Figure 3).

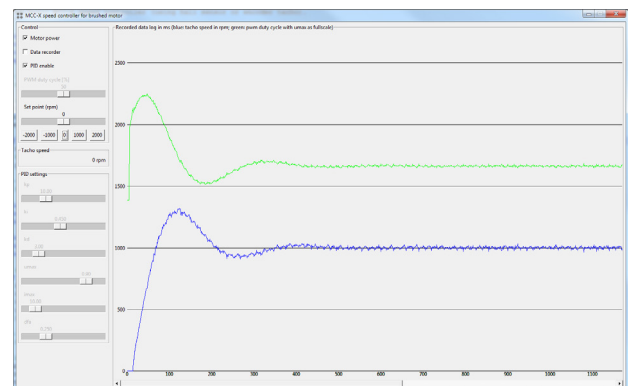


Figure 3: Example Python GUI for motor speed PID control.

The motor H-bridges are controlled from the FPGA using pulse-width modulated (PWM) outputs. For closed-loop control, various digital and analog inputs (ADCs, Hall-effect sensors, digital encoders etc.) get processed in the FPGA. To calculate motor speed from measured pulse lengths, the DSP engine got extended to support radix-2 divisions.

Overall, this results in a very compact closed-loop motor control implementation, outperforming the requirements with a substantial margin.

The project is currently in the design stage. A second generation of prototypes has been manufactured and is used for validation of both hardware and firmware performances.

A 20-b Resolution Dual Quartz-based Oscillator Gas-density Readout Circuit

D. Ruffieux, E. Azarkhish, D. Huber •, J. Kilchoer, M. Kunz •, C. Monneron, N. Raemy, C. Schmid •, N. Scolari, D. Severac, A. Vouilloz

This Innosuisse-funded project targeted the development of a high-resolution gas-density measurement circuit based on a custom integrated circuit driving two off-the-shelf 32 kHz watch-type tuning fork crystals (XTAL), one of which being exposed to SF₆ at pressure levels up to 10 bars.

Sulfur hexafluoride (SF₆), a gas about five times denser than air, is used at a pressure of 10 bars in high voltage, gas-insulated circuit breakers (switchgear). Owing to its high dielectric strength, it avoids fire onset by quenching the electrical arc arising when such mechanical switches open, e.g., after a short is detected further down the power line. Failure to detect a leak in such an equipment could lead to dramatic consequence exemplified through one of the huge summer 2018 Californian fire, most likely attributed to a defective electrical power plant equipment. Trafag AG, a world leader provider of pressure and density sensors for harsh environment, and CSEM have teamed up to develop a novel resonant gas-density readout circuit. The sensor is able to operate adaptively and with high resolution over equivalent air pressures ranging from 0 to 50 bars with the goal to serve other rapidly growing energy market segments such as SF₆-based switchgears for medium voltage photovoltaic power plants. On the medium term, the novel sensor, when combined to precise temperature and pressure measurements, will help replace SF₆, a greenhouse gas by an environmentally friendly bi-component gas mixture whose two partial pressures could also be monitored accurately.

The sensor is based on 32 kHz watch-type tuning fork crystals (XTAL) whose frequency exhibits a linear dependency with respect to the gas density ρ , the resonator being slowed down by the mass adsorbed on its surface. One easily shows, using the perfect gas law ($P \cdot V = n \cdot R \cdot T$), that the ratio of pressure P over temperature T is proportional to $\rho = m / V$ with a multiplying factor given by R / M , $M = m / n$ being the gas mass / mole and R the perfect gas universal constant. Figure 1 shows measurements of the phase of the XTAL impedance at varying SF₆ pressures resulting in a relative shift of its two resonance frequencies ($\varphi=0$) by -1 ppm / mbar. The plot gives several read-out circuit design challenge insights that will be discussed below.

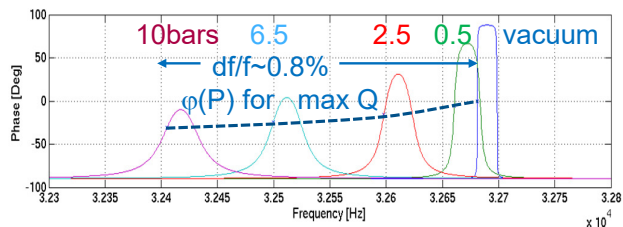


Figure 1: Measured phase of a 32 kHz XTAL at various SF₆ pressures.

A phase discrimination circuit may elegantly be implemented using a XTAL oscillator (XO) which must meet unity gain (magnitude and phase) condition at steady-state. Consequently, the phase shift introduced by the circuit should be balanced by that of the resonator. From Figure 1, one sees that under vacuum condition, the resonator phase change is so abrupt and spanning 180° that the circuit barely influences the XO frequency. Typical watch oscillators exhibit a capacitive phase shift ($\varphi < 0$) forcing the resonator in its inductive region ($\varphi > 0$). However, such a topology would fail as ρ gets higher due to increased damping since the

Q-factor is reduced 100-fold at 10 bars as shown by the corresponding phase change slope and excursion reductions. For optimum frequency stability, the circuit phase should match that of the resonator at its steepest phase change point (see dashed dot line in Figure 1). To meet the above goals, one may use instead a trans-impedance amplifier (TIA) topology that flips the sign of the resonator phase shift. The latter may be compensated in the TIA using a parallel RC feedback matching the resonator loss and dielectric capacitance to reach unity gain at its series resonance, maximizing Q, as shown in Figure 2 which illustrates the readout circuit concepts and XOs topologies. The actual TIA implements several additional features to ensure a reliable start-up, adjust its phase shift and prevent parasitic oscillations as well as overdriving the XTAL. The TIA operates adaptively, without trim, over the complete pressure range.

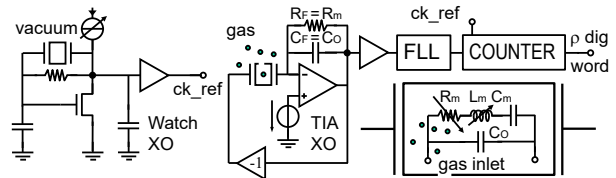


Figure 2: Simplified block diagram of the gas density read-out circuit.

Frequency to digital conversion is achieved using a double oscillator configuration. The first one defines the gate time ($\tau = M / f_1$) consisting of M periods during which the number of periods of the second one are counted delivering a digital word N , that is proportional to the two clocks frequency ratio ($N = M \cdot f_2 / f_1$). Two XTALs originating from the same manufacturing batch are used to yield an absolute differential measurement compensating the temperature effect to the first order (up to 200 ppm). One is exposed to the gas by punching a pinhole through its metal case while the reference XTAL is left in vacuum. With ideally matched XTALs, in the absence of gas, N / M is always 1, whatever the temperature. As surrounding molecules load the second XTAL, affecting f_2 , the count value decreases proportionally. To shorten the read-out time and enhance the sensing resolution, a frequency lock loop (FLL) is implemented to lock a ~100 MHz RC oscillator on f_2 , multiplying the number of counted edges N by the respective FLL multiplying ratio. At a 1 s gate time, assuming a total jitter of 10 ns ($\Delta f / f = 1E-8$), 1% frequency deviation at 10 bars SF₆, the sensor limit of detection is a density change corresponding to an equivalent pressure loss of 1 Pa yielding a resolution of 20 bits.

A one-time programmable non-volatile memory (NVM) allows storing dedicated configuration and calibration parameters on-chip to compensate for offset and gain errors. Several digital interfaces have been implemented so that the circuit can be operated with a simple companion chip to form a 4 to 20 mA analog sensor transmitter or with a microcontroller for more advanced products. The circuit is currently being characterized.

• Trafag AG, Bubikon, Switzerland

Improving 55 nm Technology System-on-chip Functionality through In-house focused Ion Beam Corrections

K. Vaideeswaran, L. Zahnd, M. Pons, S. Emery, D. Manic

Debugging of disruptive elements in chip design is a regular process in order to obtain a fully functional chip. During the debugging of the chips designed by CSEM for prosthetic hand control in the DeTOP project, it was necessary to disconnect certain capacitive elements to remove problems associated with overconsumption of power without harming the system. To this end, Focused Ion Beam (FIB) was employed by using a focused Ga-ion beam, metallic connects at a precise depth were milled locally resulting in the disconnection of the disruptive capacitive elements. As a result, the corrected chip design was fully functional and was integrated into an ASIC for the demonstration of the prosthetic hand.

In the framework of the DeTOP project [1] we designed a 55 nm technology system on chip (see Figure 1) which addresses the recovery of hand function after amputation. The system on chip includes an electromyography (EMG) analog front end with an integrated 32b RISC core for prosthetic control [2]. However, we found an overconsumption issue, creating a noisy supply that was limiting its functionality. Currents in the order of 100 mA were drawn which were one order of magnitude bigger than expected. Design debug led to the identification of the misconnection in the supply network of the analog front-end block. It was required to disconnect already integrated capacitive elements without harming the functionality of the rest of the chip.

In order to achieve this, CSEM in-house Dual Beam FIB Thermo Fischer SCIOS 2 was used. A highly focused Ga-ion beam is used to remove material, resulting in extremely localized 'milling'. From the chip design, the metallic connects supplying power to the defective elements were identified, and areas were localized that would allow for the FIB milling to reach these layers without affecting any other elements. The FIB was operated with a 30 kV acceleration and beam currents of 3nA-5nA were used. By controlling the time for each milling operation, the depth of the milling process was controlled (which was critical for the 55 nm technology of the chip). Following each cut, the cross section was observed using a Scanning Electron Microscope (SEM) to verify the layers disconnected by the milling process (see Figure 2). For each chip, 14 cuts were undertaken. 6 chips were corrected.

After FIB correction, supply current was then measured again on the 6 chips and no overconsumption remained for 5 of them, allowing for fully functional design. The 6th chip was damaged during FIB, reaching 83.3% yield, which is high for this 55 nm technology considering the number of cuts performed.

Thanks to the FIB correction we were then able to control a prosthetic hand using EMG signals sensed on our arm [3] (see Figure 3). EMG signals are first used to train the prosthetic hand applying a pattern recognition algorithm. Once training is complete, the EMG signals that are sensed by CSEM ASIC control directly the prosthetic hand movements (the hand movements are reproduced by the prosthetic hand).

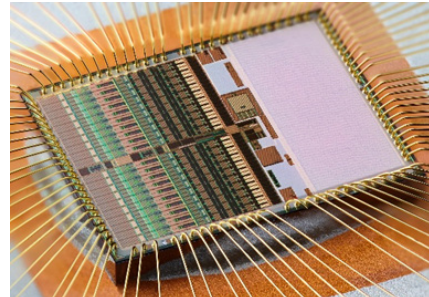


Figure 1: DeTOP system on chip micro-photograph ($3 \times 3.7 \text{ mm}^2$).

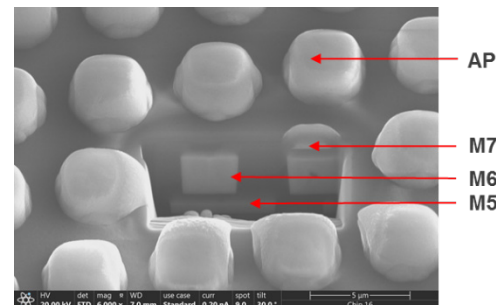


Figure 2: Cross section from FIB showing precise milling up to metal M5 layer while only touching inactive M6 and M7 layers.



Figure 3: Prosthetic hand control using DeTOP system on chip (CSEM ASIC).

[1] DeTOP project: European Commission under the Horizon 2020 Framework Programme for Research and Innovation (LEIT ICT 24 2015, GA #687905). <http://www.detop-project.eu/>

[2] M. Pons, et al., "A 20 Channel EMG SoC with an Integrated 32b RISC Core for Real-Time Wireless Prosthetic Control," IEEE

European Solid State Circuits Conference (ESSCIRC), Krakow, Poland (Sept. 2019).

[3] Video "DeTOP – CSEM: Miniaturised low-power ExG sensing front end ASIC for prosthetic applications", <https://youtu.be/7PtQfvcDbCY>

ANNEXES

Publications

- [1] T. Aderneuer, O. Stefani, O. Fernandez, C. Cajochen, R. Ferrini, "Circadian tuning with metameric white light: Visual and non-visual aspects", Preprints, September 2019, 2019090227.
- [2] A. B. Aebersold, L. Fanni, A. Hessler-Wyser, S. Nicolay, C. Ballif, C. Hebert, *et al.*, "Quantifying competitive grain overgrowth in polycrystalline ZnO thin films", *Acta Materialia*, vol. 173, pp. 74-86, July 2019.
- [3] E. Annigoni, A. Virtuani, J. Levrat, A. Faes, F. Sculati-Meillaud, M. Despeisse, *et al.*, "Quantifying and modeling the impact of interconnection failures on the electrical performance of crystalline silicon photovoltaic modules", *Progress in Photovoltaics*, vol. 27 (5), pp. 424-432, May 2019.
- [4] J. Anso, T. W. Balmer, Y. Jegge, H. Kalvoy, B. J. Bell, C. Dur, *et al.*, "Electrical Impedance to Assess Facial Nerve Proximity During Robotic Cochlear Implantation", *IEEE Transactions on Biomedical Engineering*, vol. 66 (1), pp. 237-245, January 2019.
- [5] M. Asgari, F. Lucci, J. Bialek, B. Dunan, G. Andreatta, R. Smajda, *et al.*, "Development of a realistic human respiratory tract cast representing physiological thermal conditions", *Aerosol Science and Technology*, vol. 53 (8), pp. 860-870, August 2019.
- [6] L. M. Babrak, J. Menetski, M. Rebhan, G. Nisato, M. Zinggeler, N. Brasier, K. Baerenfaller, T. Brenzikofler, L. Baltzer, C. Vogler, L. Gschwind, C. Schneider, F. Streiff, P. M. A. Groenen, E. Miho, "Traditional and Digital Biomarkers: Two Worlds Apart?", *Digital Biomarkers*, August 2019, 3, pp. 92-102.
- [7] R. Banach, J. Razavi, S. Lesecq, O. Debicki, N. Mareau, J. Foucault, *et al.*, (2019), Formal Methods in Systems Integration: Deployment of Formal Techniques in INSPEX. E. Bonjour, D. Krob, L. Palladino; F. Stephan(eds) Complex Systems Design & Management. CSD&M 2018. Springer, Cham.
- [8] V. Brasch, E. Obrzud, S. Lecomte, T. Herr, "Nonlinear filtering of an optical pulse train using dissipative Kerr solitons", *Optica*, vol. 6 (11), pp. 1386-1393, November 2019.
- [9] F. Braun, M. Proenca, A. Wendler, J. Sola, M. Lemay, J. P. Thiran, *et al.*, "Noninvasive measurement of stroke volume changes in critically ill patients by means of electrical impedance tomography", *Journal of Clinical Monitoring and Computing*, p. 9.
- [10] C. Brivio, V. Musolino, M. Merlo, C. Ballif, "A Physically-Based Electrical Model for Lithium-Ion Cells", *IEEE Transactions on Energy Conversion*, vol. 34 (2), pp. 594-603, June 2019.
- [11] E. Chinello, M. A. Modestino, J. W. Schuttauf, L. Coulot, M. Ackermann, F. Gerlich, *et al.*, "A comparative performance analysis of stand-alone, off-grid solar-powered sodium hypochlorite generators", *Rsc Advances*, vol. 9 (25), pp. 14432-14442, 2019.
- [12] F. C. Dezza, V. Musolino, L. Piegari, R. Rizzo, "Hybrid battery-supercapacitor system for full electric forklifts", *Iet Electrical Systems in Transportation*, vol. 9 (1), pp. 16-23, March 2019.
- [13] A. Faes, D. Petri, J. Champliaud, J. Geissbühler, N. Badel, J. Levrat, B. Roustom, A. Hessler-Wyser, N. Wyrsch, C. Ballif, G.-O. Getaz, G. McKarris, M. Despeisse, "Field test and electrode optimization of electrodynamic cleaning systems for solar panels" (2019) *Progress in Photovoltaics: Research and Applications*, 27 (11), pp. 1020-1033.
- [14] S. Fallet, M. Lemay, P. Renevey, C. Leupi, E. Pruvot, and J. M. Vesin, "Can one detect atrial fibrillation using a wrist-type photoplethysmographic device?", *Medical & Biological Engineering & Computing*, vol. 57 (2), pp. 477-487, February 2019.
- [15] O. Fernandez, F. Zanella, T. Aderneuer, R. Ferrini, "Design and Tolerancing of Freeform Microlens Arrays for Solid-State Lighting", *LED professional review*, September 2019, pp. 58-62.
- [16] O. Fernandez, T. Aderneuer, R. Ferrini, "Semi-Empirical Characterization of Freeform Microlens Arrays", *LED professional review*, March 2019, (72), pp. 42-48.
- [17] J. Foucault, S. Lesecq, G. Dudnik, M. Correvon, R. O'Keeffe, V. Di Palma, *et al.*, "INSPEX: Optimize Range Sensors for Environment Perception as a Portable System", *Sensors*, vol. 19 (19), p. 18, Octobre 2019.

- [18] I. Frerichs, B. Vogt, J. Wacker, R. Paradiso, F. Braun, M. Rapin, L. Caldani, O. Chételat, N. Weiler, "Multimodal remote chest monitoring system with wearable sensors – a validation study in healthy subjects", *Physiological Measurement*, December 2019.
- [19] F. Fu, S. Pisoni, Q. Jeangros, J. Sastre-Pellicer, M. Kawecki, A. Paracchino, *et al.*, "I₂ vapor-induced degradation of formamidinium lead iodide based perovskite solar cells under heat-light soaking conditions", *Energy & Environmental Science*, vol. 12 (10), pp. 3074-3088, October 2019.
- [20] F. Grass, B. Pache, F. Butti, J. Sola, D. Hahnloser, N. Demartines, *et al.*, "Stringent fluid management might help to prevent postoperative ileus after loop ileostomy closure", *Langenbecks Archives of Surgery*, vol. 404 (1), pp. 39-43, February 2019.
- [21] B. Grychtol, J. P. Schramel, F. Braun, T. Riedel, U. Auer, M. Mosing, C. Braun, A. D. Waldmann, S. H. Böhm, A. Adler, "Thoracic EIT in 3D: experiences and recommendations", *Physiological Measurement*, August 2019, 40 (7), pp. 074006.
- [22] A. Ingenito, G. Nogay, J. Stuckelberger, P. Wyss, L. Gnocchi, C. Allebé, J. Horzel, M. Despeisse, F.-J. Haug, P. Löper, C. Ballif, "Phosphorous-Doped Silicon Carbide as Front-Side Full-Area Passivating Contact for Double-Side Contacted c-Si Solar Cells," in *IEEE Journal of Photovoltaics*, 9 (2019) pp. 346-354, March 2019.
- [23] P. Iurilli, C. Brivio, M. Merlo, "SoC management strategies in Battery Energy Storage System providing Primary Control Reserve", *Sustainable Energy, Grids and Networks*, September 2019, 19, pp. 11.
- [24] D. A. Jacobs, M. Langenhorst, F. Sahli, B. S. Richards, T. P. White, C. Ballif, *et al.*, "Light Management: A Key Concept in High-Efficiency Perovskite/Silicon Tandem Photovoltaics", *Journal of Physical Chemistry Letters*, vol. 10 (11), pp. 3159-3170, June 2019.
- [25] D. Kallweit, R. Ferrini, "Flex LED Based Smart Light System for Healing of Chronic Wounds", *LED professional review*, January 2019, (71), pp. 48-71.
- [26] B. A. Kamino, A. M. Szawiola, T. Plint, T. P. Bender, "Formation and application of electrochemically active cross-linked triarylamine-siloxane films using the Piers-Rubinsztajn reaction", *Canadian Journal of Chemistry*, vol. 97 (5), pp. 378-386, May 2019.
- [27] B. A. Kamino, B. Paviet-Salomon, S. J. Moon, N. Badel, J. Levrat, G. Christmann, *et al.*, "Low-Temperature Screen-Printed Metallization for the Scale-Up of Two-Terminal Perovskite-Silicon Tandems", *Acs Applied Energy Materials*, vol. 2 (5), pp. 3815-3821, May 2019.
- [28] M. M. Kivambe, J. Haschke, J. Horzel, B. Aissa, A. A. Abdallah, A. Belaidi, *et al.*, "Record-Efficiency n-Type and High-Efficiency p-Type Monolike Silicon Heterojunction Solar Cells with a High-Temperature Gettering Process", *Acs Applied Energy Materials*, vol. 2 (7), pp. 4900-4906, July 2019.
- [29] V. Kopta, C. C. Enz, "A 4-GHz Low-Power, Multi-User Approximate Zero-IF FM-UWB Transceiver for IoT", *IEEE Journal of Solid-State Circuits*, vol. 54 (9), pp. 2462-2474, September 2019.
- [30] M. Krakowski, P. Resneau, M. Garcia, E. Vinet, Y. Robert, O. Parillaud, B. Gérard, S. Kundermann, N. Torcheboef, D. L. Boiko, "Stabilized High Pulse Energy Passively Mode-Locked Monolithic and External Cavity Tapered Lasers for Space Applications", *IEEE Journal of Selected Topics in Quantum Electronics*, July 2019, 25 (6), pp. 1100615.
- [31] D. Lachenal, P. Papet, B. Legradic, R. Kramer, T. Kossler, L. Andreetta, *et al.*, "Optimization of tunnel junction IBC solar cells based on a series resistance model", *Solar Energy Materials and Solar Cells*, vol. 200, p. 8, September 2019.
- [32] G. H. Lee, X. Bulliard, S. Yun, D. S. Leem, K. B. Park, K. H. Lee, *et al.*, "Green-light-selective organic photodiodes for full-color imaging", *Optics Express*, vol. 27 (18), pp. 25410-25419, September 2019.
- [33] M. Lehmann, N. Valle, J. Horzel, A. Pshenova, P. Wyss, M. Dobeli, *et al.*, "Analysis of hydrogen distribution and migration in fired passivating contacts (FPC)", *Solar Energy Materials and Solar Cells*, vol. 200, p. 7, September 2019.
- [34] A. C. Martins, V. Chapuis, A. Virtuani, C. Ballif, "Robust Glass-Free Lightweight Photovoltaic Modules With Improved Resistance to Mechanical Loads and Impact", *IEEE Journal of Photovoltaics*, vol. 9 (1), pp. 245-251, January 2019.
- [35] J. P. Niemela, B. Macco, L. Barraud, A. Descoedres, N. Badel, M. Despeisse, *et al.*, "Rear-emitter silicon heterojunction solar cells with atomic layer deposited ZnO:Al serving as an alternative transparent conducting oxide to In₂O₃:Sn", *Solar Energy Materials and Solar Cells*, vol. 200, p. 5, September 2019.
- [36] G. Nogay, F. Sahli, J. Werner, R. Monnard, M. Boccard, M. Despeisse, *et al.*, "25.1%-Efficient Monolithic Perovskite/Silicon Tandem Solar Cell Based on a p-type Monocrystalline Textured Silicon Wafer and High-Temperature Passivating Contacts", *ACS Energy Letters*, vol. 4 (4), pp. 844-845, April 2019.

- [37] E. Obrzud, V. Brasch, T. Voumard, A. Stroganov, M. Geiselmann, F. Wildi, *et al.*, "Visible blue-to-red 10 GHz frequency comb via on-chip triple-sum-frequency generation", *Optics Letters*, vol. 44 (21), pp. 5290-5293, November 2019.
- [38] B. Pache, M. Hubner, J. Sola, D. Hahnloser, N. Demartines, F. Grass, "Receiver operating characteristic analysis to determine optimal fluid management during open colorectal surgery", *Colorectal Disease*, vol. 21 (2), pp. 234-240, February 2019.
- [39] S. Perrin, H. Y. Li, K. Badu, T. Comparon, G. Quaranta, N. Messaddeq, *et al.*, "Transmission Microsphere-Assisted Dark-Field Microscopy", *Physica Status Solidi-Rapid Research Letters*, vol. 13 (2), p. 4, February 2019.
- [40] K. Petropoulos, S. F. Bodini, L. Fabiani, L. Micheli, A. Porchetta, S. Piermarini, G. Volpe, F. M. Pasquazzi, L. Sanfilippo, P. Moscetta, S. Chiavarini, G. Palleschi, "Re-modeling ELISA kits embedded in an automated system suitable for online detection of algal toxins in seawater", *Sensors and Actuators B: Chemical*, March 2019, 283, pp. 865-872.
- [41] M. E. Pfeifer, D. Ulrich, "Report of the 2nd Swiss Symposium in Point-of-Care Diagnostics Chur, October 18, 2018", *Chimia*, vol. 73 (1-2), pp. 101-105, February 2019.
- [42] M. Proen  a, P. Renevey, F. Braun, G. Bonnier, R. Delgado-Gonzalo, A. Lemkadem, C. Verjus, D. Ferrario, M. Lemay (2019), "Pulse Wave Analysis Techniques", J. Sol  , R. Delgado-Gonzalo (Eds.), The Handbook of Cuffless Blood Pressure Monitoring, (pp. 107-137), Springer.
- [43] N. Razek, J. Neves, H. von Kanel, P. Le Corre, P. F. Ruedi, R. Quaglia, *et al.*, "Low temperature covalent wafer bonding for X-ray imaging detectors", *Japanese Journal of Applied Physics*, Volume 59, Number SB.
- [44] R. Razera, D. Jacobs, F. Fu, P. Fiala, M. Dussouillez, F. Sahli, T. Chien-Jen Yang, L. Ding, A. Walter, A. F. Feil, H. Ivanov Boudinov, S. Nicolay, C. Ballif, Q. Jeangros, "Instability of p-i-n perovskite solar cells under reverse bias", *J. Mater. Chem. A*, 2019, 10.1039/C9TA12032G.
- [45] C. Sanchez, L. Bloch, J. Holweger, C. Ballif, N. Wyrtsch, "Optimised Heat Pump Management for Increasing Photovoltaic Penetration into the Electricity Grid", *Energies*, vol. 12 (8), p. 22, April 2019.
- [46] P. A. E. Schmid, "Machines with Brain – Predictive Maintenance with Deep Neural Networks", *CIO Applications Europe*, July 2019, 03, 2019, pp. 29-30.
- [47] L.-L. Senaud, G. Christmann, A. Descoeuilles, J. Geissbuhler, L. Barraud, N. Badel, C. Allebe, S. Nicolay, M. Despeisse, B. Paviet-Salomon, C. Ballif, "Aluminium-Doped Zinc Oxide Rear Reflectors for High-Efficiency Silicon Heterojunction Solar Cells"(2019) *IEEE Journal of Photovoltaics*, 9 (5), art. no. 8788567, pp. 1217-1224.
- [48] J. Sol  , R. Delgado-Gonzalo (2019), *The Handbook of Cuffless Blood Pressure Monitoring: A Practical Guide for Clinicians, Researchers, and Engineers*, (Eds.), Springer, Cham, 3030247007.
- [49] F. Sorba, A. Poulin, R. Ischer, H. Shea, C. Martin-Olmos, "Integrated elastomer-based device for measuring the mechanics of adherent cell monolayers", *Lab on a Chip*, vol. 19 (12), pp. 2138-2146, June 2019.
- [50] A. Vizbaras, I. Simonyte, S. Droz, N. Torcheboeuf, A. Miasojedovas, A. Trinkunas, *et al.*, "GaSb Swept-Wavelength Lasers for Biomedical Sensing Applications", *IEEE Journal of Selected Topics in Quantum Electronics*, vol. 25 (6), p. 12, Nov-Dec 2019.
- [51] J. Werner, F. Sahli, F. Fu, J. J. Diaz Leon, A. Walter, B. A. Kamino, B. Niesen, S. Nicolay, Q. Jeangros, C. Ballif: "Perovskite/Perovskite/Silicon Monolithic Triple-Junction Solar Cells with a Fully Textured Design" *ACS Energy Lett.* 2018, 3, 9, 2052-2058.
- [52] T. Wildi, V. Brasch, J. Q. Liu, T. J. Kippenberg, T. Herr, "Thermally stable access to microresonator solitons via slow pump modulation", *Optics Letters*, vol. 44 (18), pp. 4447-4450, September 2019.
- [53] S. Yakunin, B. M. Benin, Y. Shynkarenko, O. Nazarenko, M. I. Bodnarchuk, D. N. Dirin, *et al.*, "High-resolution remote thermometry and thermography using luminescent low-dimensional tin-halide perovskites", *Nature Materials*, vol. 18 (8), pp. 846-852, August 2019.
- [54] J. H. Yum, S. J. Moon, L. Yao, M. Caretti, S. Nicolay, D. H. Kim, *et al.*, "Robust Electron Transport Layers via In Situ Cross-Linking of Perylene Diimide and Fullerene for Perovskite Solar Cells", *Acs Applied Energy Materials*, vol. 2 (9), pp. 6616-6623, September 2019.

Proceedings

- [1] P.-J. Alet, G. Adinolfi, G. Barchi, R. Bründlinger, G. Graditi, N. Henze, M. Jung, A. Stavrou, G. Yang, "The inverter: à multi-purpose control element", 36th European Photovoltaic Solar Energy Conference and Exhibition, Marseille (FR), September 2019.
- [2] M. Anderson, R. Bouchand, E. Obrzud, J. Q. Liu, S. Karlen, S. Lecomte, *et al.*, "Broadband Efficient Soliton Microcombs in Pulse-Driven Photonic Microresonators", IEEE Conference on Lasers and Electro-Optics (CLEO), May 2019.
- [3] G. Andreatta, A. Grivel, O. Chandran, C. Alleb  , A. Lachowicz, M. Despeisse, S. Lani, N. Hendricks, R. Pugin, "Innovative chemical nanolayers for substrate metallization", EMRS European Materials Research Society 2019 Spring meeting, Nice (FR), May 2019.
- [4] S. A. Bigdelli, S. Susstrunk, "Deep Semantic Segmentation using NIR as extra physical information", The 26th IEEE International Conference on Image Processing - IEEE ICIP, Taipei (CN), September 2019.
- [5] N. Blondiaux, "Nanosphere lithography: a flexible surface structuring process for MEMS and 3D parts", euspen SIG Meeting, Berlin (DE), November 2019.
- [6] D. L. Boiko, S. Kundermann, N. Torcheboeuf, M. Krakowski, P. Resneau, M. Garcia, E. Vinet, Y. Robert, C. Theveneau, M. Lecomte, O. Parillaud, B. Gerard, "Stabilized Mode-Locked Tapered Monolithic Laser Diode with 200pJ Pulse Energy for Space Metrology Applications", 2019 Joint Conference of the IEEE International Frequency Control Symposium & European Frequency and Time Forum (IFCS-EFTF), Orlando (US), April 2019.
- [7] G. Borque Gallego, L. Rossini, T. Achtnich, C. Zwyssig, D. Martins Araujo, Y. Perriard, "Force and Torque Model of Ironless Passive Magnetic Bearing Structures", IEEE International Electric Machines and Drives Conference - IEMDC 2019, San Diego (US), May 2019, pp. 507-514.
- [8] V. Brasch, E. Obrzud, S. Lecomte, T. Herr, "Noise Filtering in Synchronously-driven Kerr Frequency Combs", 2019 Conference on Lasers and Electro-Optics (CLEO), May 2019.
- [9] F. Braun, M. Proen  , M. Lemay, A. Adler, "Distribution of Pulmonary Pulse Arrival in the Healthy Human Lung", 20th International Conference on Biomedical Applications of Electrical Impedance Tomography - EIT2019, London (UK), July 2019.
- [10] F. Braun, M. Proen  , M. Sage, J.-P. Praud, M. Lemay, A. Adler, E. Fortin-Pellerin, "EIT measurement of pulmonary artery pressure in neonatal lambs", 20th International Conference on Biomedical Applications of Electrical Impedance Tomography - EIT2019, London (UK), July 2019.
- [11] F. Braun, M. Proen  , M. Sage, J.-P. Praud, M. Lemay, A. Adler, E. Fortin-Pellerin, "Noninvasive measurement of pulmonary artery pressure in neonatal lambs via electrical impedance tomography", 2019 Annual Meeting of the Swiss Society of Biomedical Engineering - SSBE2019, Geneva (CH), August 2019.
- [12] F. Braun, P. Renevey, J. Van Zaen, A. Lemkaddem, E. T  retken, A. Dunbar, R. Delgado-Gonzalo, M. Lemay, K. De Jaegere, C. Horvath, C. Roth W  lti, A.-K. Brill, S. R. Ott, "Sleep Staging Using Deep Neural Networks", International Conference on Advanced Sleep Modulation Technologies - ASMT, Ascona (CH), October 2019.
- [13] X. Bulliard, A. Grivel, G. Weder, R. Ischer, G. Voirin, R. Smajda, R. Pugin, "Mesoporous hierarchical layer as a versatile coating for optical sensing", SAOG 2019 (Surface Science and Thin Films Community of Switzerland), Fribourg (CH), January 2019.
- [14] X. Bulliard, R. Pugin, A. Grivel, R. Steiger, "Increase in QD film luminescence efficiency by FRET transfer from J-aggregates", 19th International Meeting on Information Display - IMID 2019, Gyeongju (KR), August 2019.
- [15] L. Burr, D. Schmid, H. Chai-Gao, S. Generelli, S. Cattaneo, "Hydrophobicity of nanomaterials measurements for risk assessment", EuroNanoForum 2019, Bucharest (RO), June 2019.
- [16] L. Canals Casals, C. Corchero, J. Ortiz, J. Salom, D. Cardoner, L. Igualada, R. E. Carrillo, Y. Stauffer, "How Building and District Algorithms Enhance Renewable Energy Integration in Energy Markets", IEEE International Conference on the European Energy Market (EEM), September 2019.
- [17] O. Chandran, V. Pejchal, S. Lani, M. Auchlin, M. Dadras, O. Sereda, "Optimization of 17-4 PH SLM process parameters toward mesoscale parts", Alloys for Additive Manufacturing Symposium 2019, Gothenburg (SE), September 2019.
- [18] P. Chervet, A.-M. Olteanu, J. Ram  n Troncoso-Pastoriza, D. Froelicher, J. Van Zaen, R. Delgado-Gonzalo, J.-P. Hubaux, "Efficient privacy-preserving neural network inference for heart arrhythmia detection", 2019 Annual Meeting of the Swiss Society of Biomedical Engineering (SSBE), Geneva (CH), August 2019.

- [19] F. Cosandier, P. Schwab, L. Kiener, J. Kruis, L. Giriens, P. Spanoudakis, "Large angle flexure pivot development for high accuracy positioning of optical payloads", euspen's 19th International Conference & Exhibition, Bilbao (ES), June 2019.
- [20] F. Cosandier, "Six design principles for SLM-based compliant mechanisms", EUSPEN SIG AM, Nantes (FR), September 2019.
- [21] A. Costa, P. De Cinque, M. Elagiry, F. Passerini, A. Bassani, J. Febres, S. Lopez, R. Sterling, M. Keane, R. Carrillo, Y. Stauffer, M. Rama, K. Krzysztof, G. N. Lanz, J. A. Urquijo, "INDIGO Project: A Simulation Based Approach To Support District Cooling Design And Operation", Building Simulation 2019, Rome (IT), September 2019.
- [22] M. Dadras, S. Unterhofer, V. Pejchal, C. Biselli, O. Sereda, "High strength supersaturated alloy fabrication by Selective Laser Melting", European Congress and Exhibition on advanced materials and processes - EUROMAT 2019, Stockholm (SE), September 2019.
- [23] L. Driencourt, D. Kazazis, Y. Ekinci, F. Federspiel, R. Frantz, R. Ferrini, B. Gallinet, "Electrically tunable multicolored filter based on plasmonic nanoscale phase retarder and liquid crystals", META 2019, July 2019.
- [24] L. Driencourt, D. Kazazis, Y. Ekinci, F. Federspiel, R. Frantz, R. Ferrini, B. Gallinet, "Tunable filter using birefringent plasmonic structures and liquid crystals", SPIE digital optical technologies, June 2019.
- [25] G. Dudnik, O. Debicki, S. Lesecq, R. Delgado-Gonzalo, "Obstacle detection for the visually impaired and blind with a multisensor smartcane", 2019 Annual Meeting of the Swiss Society of Biomedical Engineering (SSBE), Geneva (CH), August 2019.
- [26] O. Fernandez, T. Aderneuer, R. Ferrini, "Freeform Optics for Precise Non-uniform Illumination Patterns", LED professional Symposium +Expo 2019, Bregenz (AU), September 2019, pp. 328-338.
- [27] A. Gajic, J. Radovanovic, N. Vukovic, V. Milanovic, D. L. Boiko, "Broadband Multimode Emission of Quantum Cascade Lasers in Strong Magnetic Fields", VII International School and Conference on Photonics (Photonica 2019), Belgrade (RS), August 2019.
- [28] A. H. Ghadimi, "Opto-mechanical sensors based on high Q mechanical resonators for precision sensing and their applications in seismic field ", Frontiers of Nano-science 2019, Palm Springs (US), February 2019.
- [29] N. Glaser, J. Disser, F. Zanella, N. Marjanović, C. Hennemann, S. Generelli, D. Migliorelli, J. Moll, T. Erb, R. Greutmann, "Hybrid Sensing Platform and Sensing Applications: Respiration Pressure Monitoring and Sweat Ions Monitoring", LOPEC 2020, Munich (DE), March 2019.
- [30] J. Gouman, P. Renevey, S. Dasen, S. Chin, T. Herr, G. Buchs, F. Lütfolf, S. Lecomte, G. Vergara, H. Martin, P. M. Moselund, F. J. M. Harren, L. Balet, "Compact, UAV compatible 2D Spectrometer for multi-species atmospheric gas analysis", CLEO EUROPE 2019, Munich (DE), June 2019.
- [31] D. Grivon, P. Riederer, Y. Stauffer, A. Hutter, "Smart Control Strategy For The Reduction Of Energy Consumption Of Central Heating Systems In Large Buildings", Building Simulation 2019, Rome (IT), September 2019.
- [32] E. Györvary, S. Paoletti, V. Revol, G. Weder, "Organ-on-Chip Microengineering", European OOC conference, Graz (AT), July 2019.
- [33] N. Hendricks, S. Lani, R. Pugin, "Aerosol Jet Printing of Functional Materials for Sensing Capabilities", Swiss ePrint 2019 The Swiss Conference on Printed Electronics and Functional Materials, Fribourg (CH), September 2019.
- [34] S. Heub, R. Smajda, G. Voirin, G. Weder, "Enabling cost-effective glass microfluidics for life sciences: the example of a complete sequencing device fabricated at wafer scale", Miniaturized Systems for Chemistry and Life Sciences (Microtas 2019), Basel (CH), October 2019.
- [35] A. Hoogerwerf, G. Spinola Durante, R. Jose-James, M. Despont, "Silicon carbide pressure sensors for harsh environments", IEEE 20th International Conference on Solid-State Sensors, Actuators and Microsystems & Eurosensors XXXIII (Transducers & Eurosensors XXXIII), Berlin (DE), June 2019.
- [36] D. Inaudi, R. Blin, B. Timotijevic, D. Z. Bayat, Y. Pétremand, M. Luetzelschwab, N. Niketic, "Integrated Optics Inclinometers for SHM", International Conference on Smart Monitoring, Assessment and Rehabilitation of Civil Structures (SMAR 2019), Potsdam (DE), August 2019.
- [37] S. Jafari, D. Migliorelli, S. Generelli, S. J. Sturla, "Toward the smartphone-based electrochemical detection of aflatoxins in food samples ", 9th International Symposium on recent advances in food analysis, Prague (CZ), November 2019.
- [38] A. James, M. Boegli, A. Bollinger, P.-J. Alet, M. Wiget, "Speed optimization of simulation models for rapid performance evaluation of heating and energy management systems", Building Simulation 2019, Rome (IT), September 2019.

- [39] Y. Jegge, A. Adler, M. Apelt, G. Yilmaz, D. Ferrario, K. Seidel, J. Ansó, "Tissue classification during surgical drilling using impedance spectroscopy", 20th International Conference on Biomedical Applications of Electrical Impedance Tomography, London (UK), July 2019.
- [40] S. Karlen, T. Overstolz, J. Gobet, J. Haesler, F. Droz, S. Lecomte, *et al.*, "Alkali metal condensation zones in MEMS alkali vapor cells and characterization in CPT clock", IEEE Conference on Lasers and Electro-Optics (CLEO), July 2019.
- [41] L. Kiener, H. Saudan, F. Cosandier, G. Perruchoud, P. Spanoudakis, "Innovative concept for additive manufacturing of compliant mechanisms", TCT Formnext, Frankfurt (DE), 19-11-2019.
- [42] L. Kiener, H. Saudan, G. Perruchoud, V. Pejchal, "Development of a Compliant Mechanism Based on Additive Manufacturing", 1st ESA Advanced Manufacturing workshop 2019, Noordwijk (NL), March 2019.
- [43] B. Kirwan, M. Wies, R. Charles, C.-A. Dormoy, T. Letouze, A. Lemkaddem, N. Maille, J. Nixon, D. Ruscio, C. Schmidt-Moll, "Charting the Edges of Human Performance", EASN, Athens (GR), September 2019.
- [44] L. Komini, J. Kruis, G. Perruchoud, F. Cosandier, L. Kiener, H. Saudan, "Toward Compliant and Structural Optimization of a Compliant Rotational Reducer Mechanism", SIM-AM 2019, Pavia (IT), August 2019, pp. 237-245.
- [45] A. S. Kowligy, H. Timmers, A. J. Lind, S. Karlen, F. Cruz, P. G. Schunemann, *et al.*, "Near-single-cycle long-wave infrared pulses for coherent linear and nonlinear optics", IEEE Conference on Lasers and Electro-Optics (CLEO), May 2019.
- [46] R. Krähenbühl, A. Luu-Dinh, R. Ferrini, "Wafer-scale Folded Micro-optical Interconnects", 45th European Conference on Optical Communication (ECOC19), Dublin (IE), September 2019.
- [47] S. Lani, Y. Pétremand, O. Dubochet, M. Dadras, F. Barrot, E. Dominé, M. Despont, "Tic-Tac" made in Silicon, Congrès International de Chronométrie, CIC 2019, Montreux (CH), September 2019, pp. 17-23.
- [48] S. Lani, "3D printing with embedded functionalities", Swiss ePrint, Fribourg (CH), September 2019.
- [49] S. Lani, "Additive Manufacturing: how to embed functionalities", Additive International, Nottingham (GB), July 2019.
- [50] S. Lani, O. Chandran, M. Auchlin, I. Marozau, B. Dunan, "3D Printing on MEMS: Integration of 3D shock stopper on a micro mirror", IEEE 20th International Conference on Solid-State Sensors, Actuators and Microsystems & Eurosensors XXXIII (Transducers & Eurosensors XXXIII), Berlin (DE), June 2019.
- [51] D. Migliorelli, J. L. D. Nelis, S. Jafari, J. Lou-Franco, S. Generelli, P. Salvador, P. Marco, C. Cao, C.T. Elliott, K. Campbell, "Characterization of the electrochemical properties of Carbon Black modified Screen Printed Electrodes and their application for food contaminant screening", 11th Euro Biosensors & Bioelectronics Congress, Rome (IT), October 2019.
- [52] V. Mitev, "Elastic backscatter lidar in PBL study", 20th International Conference and School on Quantum Electronics: Laser Physics and Applications. vol. 11047, T. Dreischuh and L. Avramov (eds.), ed Bellingham: SPIE-Int Soc Optical Engineering, 2019.
- [53] V. Mitev, L. Balet, N. Torcheboeuf, L. Gasparini, M. Perenzoni, B. Bessire, *et al.*, "Validation of echelle-based quantum-classical discriminator with novelty SPAD array sensor", Proc. Optical, Opto-Atomic, and Entanglement-Enhanced Precision Metrology. vol. 10934, S. M. Shahriar and J. Scheuer, Eds., ed Bellingham: SPIE-Int Soc Optical Engineering, 2019.
- [54] C. T. Muller, M. Pons, D. Ruffieux, J. L. Nagel, S. Emery, A. Burg, *et al.*, "Minimum Energy Point in Constant Frequency Designs under Adaptive Supply Voltage and Body Bias Adjustment in 55 nm DDC", Proc. Conference on PhD Research in Microelectronics and Electronics (PRIME), July 2019.
- [55] J. L. D. Nelis, D. Migliorelli, S. Jafari, J. Lou-Franco, S. Generelli, P. Salvador, P. Marco, C. Cao, C.T. Elliott, K. Campbell, "Carbon black modified screen printed electrodes and magnetic beads for point of site detection of domoic acid in shellfish", 9th International Symposium on recent advances in food analysis, Prague (CZ), November 2019.
- [56] E. Obrzud, V. Brasch, S. Lecomte, F. Wildi, F. Bouchy, F. Pepe, *et al.*, "All-fiber Electro-optic Frequency Comb for Near-Infrared Astronomical Spectrograph Calibration", Proc. Conference on Lasers and Electro-Optics (CLEO), July 2019.
- [57] V. Pejchal, M. Dadras, O. Sereda, "High Al content Ti6Al4V alloy fabrication by SLM for mechanical properties improvement, Selective laser melting of ceramic particle reinforced metal matrix composites", EUROMAT 2019 - European congress and exhibition on advanced materials and processes, Stockholm (SE), September 2019.

- [58] V. Pejchal, V. Hoqui, O. Sereda, M. Dadras, "3D microscopy for exploring 3D printing", Interdisciplinary Symposium on 3D microscopy, Engelberg (CH), October 2019.
- [59] D. Piguet, U. Riesen, "LORNO – An Industrial Grade Wireless Sensor Network for Leakage Detection and Localization in Water Distribution Networks", 28th European Conference on Networks and Communications - EuCNC, Valencia (ES), June 2019, pp. Poster session 1.
- [60] M. Pons, C. Müller, D. Ruffieux, J. L. Nagel, S. Emery, "A 0.5 V 2.5 μ W/MHz Microcontroller with Analog-Assisted Adaptive Body Bias PVT Compensation with 3.13nW/kB SRAM Retention in 55nm Deeply-Depleted Channel CMOS", IEEE Custom Integrated Circuits Conference (CICC), Austin (US), April 2019.
- [61] M. Pons Sole, K. Badami, J. Deng, T. Mavrogordatos, E. Azarkhish, L. Zahnd, C. Cosentino, M. Augustyniak, Y. Zha, A. Bischof, L. Bergamini; P. Dallemande, S. Emery, "A 20 Channel EMG SoC with an Integrated 32b RISC Core for Real-Time Wireless Prosthetic Control", IEEE ESSCIRC 2019 - IEEE 45th European Solid State Circuits Conference (ESSCIRC), September 2019.
- [62] M. Proen  a, Y. Ghamri, F. Braun, G. Bonnier, G. Hofmann, P. Renevey, J. Sol  , A. Axis, P. Schoettker, M. Lemay, "Non-invasive blood pressure monitoring during anesthesia induction", SSBE Annual Meeting, Geneva (CH), August 2019, pp. 9.
- [63] R. Pugin, T. Overstolz, N. Blondiaux, "Nanosphere lithography: an alternative process for the low-cost surface structuring of 3D part", AET Symposium on SMART and ACSM Manufacturing (AETS2019), Dublin (IE), August 2019.
- [64] P. Purwar, I. Kastanis, S. Rogotis, F. Chatzipapadopoulos, P. A. E. Schmid, "A Recurrent Neural Network (RNN) based approach for reliable classification of land usage from satellite imagery", Living Planet Symposium, Milan (IT), May 2019.
- [65] P. Purwar, S. Rogotis, F. Chatzipapadopoulos, I. Kastanis, "A reliable approach for pixel-level classification of land usage from spatio-temporal images", 6th Swiss Conference on Data Science, Bern (CH), June 2019, pp. 93-94.
- [66] P. Renevey, F. Braun, J. Van Zaen, A. Lemkaddem, M. Lemay, K. De Jaegere, C. Horvath, C. Roth W  lti, A.-K. Brill, S. R. Ott, "Optical monitoring of breathing disorders and sleep phases at the wrist", International Conference on Advanced Sleep Modulation Technologies - ASMT 2019, Ascona (CH), October 2019.
- [67] H. Saudan, L. Kiener, S. Liberatoscioli, F. Cochet, M. Henry, "Redesign, manufacturing and validation testing of a space-compatible slipring rotor based on additive manufacturing", ESMATS, Munich (DE), September 2019.
- [68] E. Schaller, T. Burch, "Performance Measurement at Rotor Blades ", The First Swiss Wind Energy R&D Forum, Rapperswil (CH), May 2019.
- [69] J. Schleuniger, M. Zinggeler, S. Fricke, M. Waser, U. Pieles, "Eisenoxid-Partikel in Nanodispersionen zur Speicherung elektrischer Energie", SNI Nano-Tech Ap  ro, Baden-D  ttwil (CH), October 2019.
- [70] D. Schmid, L. Burr, P. Cristofolini, F. Kurth, G. Oravez, S. Ismaeel, S. Cattaneo, "Sample preparation for solubility of nanomaterials risk assessment", EuroNanoForum 2019, Bucharest (RO), June 2019.
- [71] C. Segarra, E. Muntan  , M. Lemay, V. Schiavoni, R. Delgado-Gonzalo, "Secure Stream Processing for Medical Data", The 41st Annual International Conference of the IEEE Engineering in Medicine and Biology Society (EMBC2019), Berlin (DE), July 2019.
- [72] C. Segarra, M. Lemay, R. Delgado-Gonzalo, V. Schiavoni, "Using Trusted Execution Environments for Secure Stream Processing of Medical Data", 19th International Conference on Distributed Applications and Interoperable Systems (DAIS2019), Copenhagen (DK), June 2019.
- [73] O. Sereda, "Surface tribology improvement of Brass by Multicharge Ion Implantation", European Congress and Exhibition on advanced materials and processes - EUROMAT 2019, Stockholm (SE), September 2019.
- [74] P. Spanoudakis, L. Kiener, F. Cosandier, P. Schwab, L. Giriens, J. Kruis, D. Grivon, "Large angle flexure pivot development for future science payloads for space applications", 9th EASN International Conference on Innovation in Aviation & Space, Athens (Gr), September 2019.
- [75] P. Spanoudakis, L. Kiener, F. Cosandier, P. Schwab, L. Giriens, J. Kruis, D. Grivon, "Large angle flexure pivot development for future science payloads", 18th ESMATS European Space Mechanisms and Tribology Symposium 2019, Munich (DE), September 2019.
- [76] P. Spanoudakis, P. Schwab, L. Kiener, G. Perruchoud, H. Saudan, M. Gumy, Y.-J. Regamey, "Corner Cube Mechanism (CCM) for MTG IRS: qualification and acceptance test campaign results and lessons learned", 18th ESMATS European Space Mechanisms and Tribology Symposium 2019, Munich (DE), September 2019.

- [77] R. Sterling, J. Febres, A. Costa, A. Mohammadi, R. E. Carrillo, B. Schubnel, Y. Stauffer, P. De Cinque, M. M. Keane, "A virtual test-bed for building Model Predictive Control developments", 13th International Modelica Conference, Regensburg (DE), March 2019.
- [78] J. Szabados, V. Brasch, S. J. Herr, E. Obrzud, Y. C. Jia, S. Lecomte, *et al.*, "High-repetition-rate frequency comb up- and down-conversion in synchronously driven ((2))(chi) microresonators", Proc. Laser Resonators, Microresonators, and Beam Control Xxi. vol. 10904, A. V. Kudryashov, A. H. Paxton, and V. S. Ilchenko, Eds., ed Bellingham: SPIE-Int Soc Optical Engineering, 2019.
- [79] B. Timotijevic, A. Dunbar, A. Hoogerwerf, N. Niketic, M. Despont, R. Stanley, "MEMS Fabry-Perot Filters in the Infrared", Photonics West 19, San Francisco (US), February 2019.
- [80] A. Tsagkaris, D. Migliorelli, D. Filippini, J. Pulkrabova, J. Hajsova, "Wax printing application on a hybrid paper-3D printed lab-on-a-chip injector with smartphone-based colorimetric read-out", 9th International Symposium on RECENT ADVANCES IN FOOD ANALYSIS, Prague (CZ), November 2019.
- [81] E. Türetken, J. Van Zaen, R. Delgado-Gonzalo, "Embedded Deep Learning for Sleep Staging", 6th Swiss Conference on Data Science - SDS, Bern (CH), June 2019.
- [82] G. D. Tzeremes, D. Jones, M. Hernandez, T. Sousa, A. Pollini, C. Pache, J. Haesler, I. Carnelli, "Altimetry, Imaging and Landing Location Selection Lidars for ESA Space Applications", 2019 IEEE International Geoscience and Remote Sensing Symposium (IGARSS), July 2019.
- [83] K. Vaideeswaran, J. Gobet, P. Margraf, O. Sereda, "Hybrid Surfaces for Improved Component Lifetime", ECOTRIB 2019 - European Conference on Tribology, Vienna (AT), June 2019.
- [84] J. Van Zaen, E. Genzoni, F. Braun, P. Renevey, E. Pruvot, J.-M. Vesin, M. Lemay, "Atrial Fibrillation Detection from PPG Interbeat Intervals via a Recurrent Neural Network", Computing in Cardiology, Singapore (SG), 8-11 09 2019.
- [85] J. Van Zaen, O. Chételat, M. Lemay, E. M. Calvo, R. Delgado-Gonzalo, "Classification of Cardiac Arrhythmias from Single Lead ECG with a Convolutional Recurrent Neural Network", 12th International Joint Conference on Biomedical Engineering Systems and Technologies (BIOSTEC2019), Prague (CZ), February 2019.
- [86] A. Vizbaras, I. Šimonytė, A. Trinkūnas, A. Miasojedovas, T. Bučiūnas, A. De Groote, M. Greibus, G. Naujokaitė, V. Andrusis, D. Martens, S. Droz, N. Torcheboeuf, D. Boiko, Ž. Dambrauskas, A. Gulbinas, K. Vizbaras, "GaSb-based Swept-Wavelength Lasers for Spectroscopic Sensing Applications in the 1.7-2.5 micron Spectral Range ", IEEE Conference on Lasers and Electro-Optics Europe & European Quantum Electronics Conference (CLEO/Europe-EQEC), June 2019.
- [87] A. Vorobyov, C. Hennemann, P. Dallemande, "Solar Cell Antenna for IoT and Wearable Applications", IEEE 13th European Conference on Antennas and Propagation (EuCAP), March 2019.
- [88] A. Vorobyov, P. Dallemande, "Efficient, Compact 868MHz Antenna for Retrofit of Electronic Appliance", IEEE 13th European Conference on Antennas and Propagation (EuCAP), March 2019.
- [89] N. Vukovic, J. Radovanovic, V. Milanovic, D. Boiko, "Exploring possibilities of regular self-pulsing in monolithic and external cavity mid-IR QCLs", VII International School and Conference on Photonics (Photonica 2019), Belgrade (RS), August 2019.
- [90] W. L. Weng, R. Bouchand, E. Lucas, E. Obrzud, T. Herr, T. J. Kippenberg, *et al.*, "Heteronuclear Soliton Molecules in Optical Microresonators", IEEE Conference on Lasers and Electro-Optics (CLEO), May 2019.
- [91] G. Yilmaz, P. Starkov, M. Crettaz, J. Wacker, O. Chételat, "A low-cost USB-compatible electronic stethoscope unit for multi-channel lung sound acquisition", 15th Mediterranean Conference on Medical and Biological Engineering and Computing, Coimbra (PT), September 2019.
- [92] F. Zamkotsian, Y. Petremand, P. Lanzoni, S. Lani, R. Barette, B. Timotijevic, *et al.*, "Large 1D and 2D micro-mirror arrays for Universe and Earth Observation", Proc. Moems and Miniaturized Systems XVIII. vol. 10931, W. Piyawattanametha, Y. H. Park, and H. Zappe, Eds., ed Bellingham: SPIE-Int Soc Optical Engineering, 2019.
- [93] I. Zhurinsky, M. Schnieper, R. Ferrini, S. Fricke, "Interference lithography for nanostructure fabrication ", Proc. SPIE, April 2019, 11030, pp. 110300U-1-11.

Conferences and Workshops

- C. Ballif, "Advanced Concepts and Materials for Photovoltaics Modules: from Mass Production to Specialised PV Applications ", TUV workshop on module reliability, Köln (DE), February 2019.
- C. Ballif, "Developments in PV production technology", VDMA Annual Meeting, Neuchâtel (CH), October 2019.
- C. Ballif, "Die Photovoltaik als tragende Säule der Energie Zukunft - global, in der Schweiz und im Aargau", Aargauer Tech Day, Aarau (CH), October 2019.
- C. Ballif, "In the air, on sea and on land: when will everything become solar?", Seminar, University of Ljubljana (SI), June 2019.
- C. Ballif, "Perovskite-silicon multi-junction solar cells: progresses, opportunities and future market challenge", 2nth international conference on Perovskite solar cells and optoelectronic, PSCO, Lausanne (CH), September 2019.
- C. Ballif, "Photovoltaic research and implementation Switzerland", 3rd Swiss-China workshop organised by SFOE, Neuchâtel (CH), December 2019.
- C. Ballif, "Photovoltaics: is there still a need for R&D and what should come next?", EU-EITPV Conference, Bruxelles (BE), Mai 2019.
- C. Ballif, "Photovoltaik, von der Nischenanwendung bis zum Terawattstrommanagement: technologische (R)Evolution und Perspektiven", Schweizer Stromkongress, Bern (CH), 2019.
- C. Ballif, "Photovoltaik: technologische (R)Evolution und Perspektiven", Swiss Tunnelling Society Annual Meeting, Neuchâtel (CH), April 2019.
- C. Ballif, "Photovoltaïque : (R)évolutions et perspectives", Assemblée Générale du Groupe e, Bulle (CH), June 2019.
- C. Ballif, "Photovoltaïque : (R)évolutions et perspectives, Assemblée Générale Minergie", Neuchâtel (CH), June 2019.
- C. Ballif, "Photovoltaïque : Quelle part dans la transition énergétique ?", Université Populaire, Neuchâtel (CH), Septembre 2019.
- C. Ballif, "Photovoltaïque: (r) évolution", Fédération romande des consommateurs, Neuchâtel (CH), Mars 2019.
- C. Ballif, "Photovoltaïque: (r)evolutions et solutions pour la Suisse", Groupement de montage du Valais Romand, Grimentz (CH), Octobre 2019.
- C. Ballif, "Photovoltaïque: les révolutions technologiques et leur impact pour les bâtiments en Suisse", Forum organisé par la BCGE, Genève (CH), September 2019.
- C. Ballif, "Recent improvements in research and industrialization of front and back-contacted solar cells and modules using low-temperature passivating contacts", International Photovoltaic Science and Engineering Conference, Xi'an (CN), November 2019.
- C. Ballif, "Révolutions technologiques et impact pour la Suisse", séminaire commission CEAT conseil National, EPFL, Lausanne (CH), June 2019.
- C. Ballif, "Technologie, Digitalisierung, Dezentralisierung: Die grossen Trends für die nächsten 10 Jahre", Schweizer Photovoltaik Konferenz, Bern (CH), March 2019.
- C. Ballif, Closing session, 2nd International workshop on Silicon Heterojunction solar cells, Chengdu (CN), November 2019.
- S. A. Bigdeli, S. Susstrunk, "Image Denoising via MAP estimation using Deep Neural Networks", International Biomedical and Astronomical Signal Processing - BASP, Villars (CH), 10 February 2019.
- C. Brivio, P. Iurilli, A. Hutter, "The High Energy Density Challenge in Solar-Powered Aviation: The Case of Solarstrato", The Battery Show, Stuttgart (DE), 7 May 2019.
- F. Cosandier, "Large angle flexure pivot development for high accuracy positioning of optical payloads", COMSOL Day at CSEM, Neuchâtel (CH), November 2019.
- M. Fretz, "CITCOM - General Slides", EFFRA – European Factories of the Future Research Association, Brussels (BE), 22 May 2019.
- S. Fricke, "Functional Printing for Life Sciences", Symposium on 3D Printing for Life Sciences, Muttenz (CH), 02 July 2019
- M. Höchemer, J. Casutt, "Track Inspection Powered by Deep Learning", Track Maintenance & Data Utilisation 2019, London (GB), 26 June 2019.
- M. Höchemer, M. Zurkirchen, "Railway Inspection mit Deep Learning", CSEM microDay 2019, Luzern (CH), 14 May 2019.
- A. Hutter, "Battery Modeling with Application to High Energy Density Systems", Mont Soleil PhD Summer School, Biel (CH), 16 August 2019.
- A. Hutter, "Flexible Gebäude", BE!conference, Rotkreuz (CH), 2 Octobre 2019.
- A. Hutter, M. Kauert, "Individuelle Heizkostenerfassung 2.0", CSEM microDay 2019, Luzern (CH), 14 May 2019.
- A. Hutter, "SOH-Prognosen für SL-Zellen durch Messung und Modellierung", Second-Life Tagung, Zürich (CH), 09 December 2019.
- A. Hutter, "Stockage de l'énergie photovoltaïque, où en sommes-nous ?", Swiss Solar Connect event, Neuchâtel (CH), 26 November 2019.
- S. Karlen, J. Haesler, L. Balet, T. Overstolz, G. Bergonzi, J. Gobet, F. Droz, S. Lecomte, "MEMS alkali vapor celltechnologies for atomic sensors", European Quantum Technology Conference, Grenoble (FR), 18-22 February 2019.

- M. Kirschmann, "High-Speed 3D Inspektion mit Lichtfeldtechnologie und Deep Learning", ETH Zürich Kolloquium zum Thema 'Einsatz optischer Systeme in Kombination mit intelligenten Auswerteverfahren', Zürich (CH), 27 October 2019.
- M. Krieger, "Krisol AG, Global Leader in Ultra Light Weight PV Power Generation for Deep Space Missions", NSS New Space Show Monte Carlo, Monaco (MC), 17 October 2019.
- M. Krieger, "Light Field Imaging Technology, Advanced High-speed 3D Imaging for industrial applications", W3 Optics Messe Dornbirn, Dornbirn (A), 19 September 2019.
- M. Krieger, "CSEM - Innovationsschmiede für Smart Connected Mobility", Swissmem Workgroup Automotive Event "Umwälzung in der Automobilindustrie, Zukunftssicherung durch Innovation", Riverside Hotel, Spinnerei Glattfelden (CH), 9 May 2019.
- R. Matsubara, J.-D. Decotignie, K. Oshima, "Improvement of Downlink Reliability in RPL and Performance Evaluation", Ambient intelligence and Sensor Networks, Kyuukamura Ibusuki (JP), 28-29 January 2019.
- V. Mitev, L. Balet, N. Torcheboeuf, D. L. Boiko, "Validation of échelle-based quantum-classical discriminator with novelty SPAD array sensor", SQUAD 2019 - Advanced School on Quantum Detectors, Trento (IT), September 2019.
- V. Mitev, L. Balet, N. Torcheboeuf, L. Gasparini, M. Perenzoni, B. Bessire, A. Stefanov, A. Mikhalychev, D. Mogilevtsev, D. Boiko, "Validation of échelle-based quantum-classical discriminator with novelty SPAD array sensor", 26th Central European Workshop on Quantum Optics (CEWQO), Paderborn (DE), 3 June 2019.
- E. Ntavelis, I. Kastanis, P. A. E. Schmid, "Generative Adversarial Networks: When fake never looked so real", 6th Swiss Conference on Data Science (SDS2019), Bern (CH), 14 June 2019.
- J. Pierer, "Real-time 3D MEMS inspection using light field camera", Micronarc Alpine Meeting 2019, Villars-sur-Ollon (CH), 10-12 February 2019.
- B. Platerrier, "Machine Learning au service de la qualité", BaselArea.swiss - Expert Workshop - Machine Learning, Courroux (CH), 15 November 2019.
- P. Purwar, I. Kastanis, P. A. E. Schmid, "Robust crop classification using satellite images based on deep learning", Joint Meeting, ML Clinics and Spatial data group, Zürich (CH), 13 September 2019.
- V. Revol, "Digitale Transformation im Labor im Dienst der Benutzerfreundlichkeit", F&E-Konferenz zu Industrie 4.0, Rapperswil (CH), 24 January 2019.
- V. Revol, "Digitalized laboratory space: support systems to reduce human errors", ILT Symposium on Lab Automation, Rapperswil (CH), 14 March 2019.
- V. Revol, "Personalized medicine – from patient stratification to patient-grown organoids", Smart Health 2019, Zürich (CH), 25 June 2019.
- V. Revol, "Personalized tumour models - from diagnosis to therapy planning", Cancer Care 2019 - New Horizons for better Cancer Care, Bern (CH), 20 September 2019.
- M. Russi, "Praktisches Beispiel Predictive Maintenance", AUROVIS TechMeet – Predictive Maintenance, Alpnach (CH), 21 November 2019.
- P. A. E. Schmid, "3D Light-field Technology in Combination with Deep-Learning for Industry", Inno Talk - Industrial 3D Vision Technologies, Nidau (CH), 07 March 2019.
- P. A. E. Schmid, "3D Vision Technologien", AUROVIS TechDay, Alpnach (CH), 28 March 2019.
- P. A. E. Schmid, A. Meyer, "Automatisierte Pumpenmontage mit Neuronalen Netzen", CSEM microDay 2019, Luzern (CH), 14 May 2019.
- P. A. E. Schmid, "AI for Industrial Processes", Deep Tech Digitalization, Zürich (CH), 10 September 2019.
- P. A. E. Schmid, "Deep Learning für Predictive Maintenance", ETH - Fertigungstechnischen Kolloquium, Zürich (CH), 16 October 2019.
- P. A. E. Schmid, "Deep Learning für Predictive Maintenance", F&E-Konferenz zu Industrie 4.0, Rapperswil (CH), 24 January 2019.
- P. A. E. Schmid, "Deep Learning, Anwendungen in der Industrie", AUROVIS TechMeet - Deep Learning, Alpnach (CH), 18 October 2019.
- P. A. E. Schmid, "Deep Learning, Neural Networks into Production", Swissphotonics - Image Processing, Chur (CH), 28 May 2019.
- P. A. E. Schmid, "Deep Learning: Revolution im Alltag", SATW TecNight, Heerbrugg (CH), 26 March 2019.
- P. A. E. Schmid, E. Barret, "Condition-based maintenance with Deep Learning", CSEM Business Day - Deep Tech in the digital space, Basel (CH), 12 November 2019.
- P. A. E. Schmid, I. Senner, "Visuelle Exploration und KI-gestützte Analyse großer Datenmengen - DATABIO", Intergeo, Stuttgart (DE), 18 October 2019.
- P. A. E. Schmid, "KRAKEN - Grösste Hybrid-3D-Druckmaschine der Welt", Swiss Mechatronics Day 2019, Zürich (CH), 26 June 2019.
- P. A. E. Schmid, M. Zurkirchen, "Track inspection powered by Deep Learning", Mass Transport Conference, Tokyo (JP), 29 November 2019.
- P. A. E. Schmid, "Predictive maintenance mit deep learning für die Industrie", csemviva! - Smart factory: Digitalisierung in der Praxis, Trimmis (CH), 16 May 2019.
- P. A. E. Schmid, "Predictive Maintenance mit Deep Learning", RhyTalk - Wissen über Mittag, Teufen (CH), 27 June 2019.
- P. A. E. Schmid, "Predictive Maintenance vom Labor auf die Maschine", AUROVIS TechMeet – Predictive Maintenance, Alpnach (CH), 21 November 2019.

P. A. E. Schmid, "Predictive Maintenance with Deep Learning for Industry", Swiss-Swedish Innovation Initiative AI/BIG DATA/VR/AR, Baden (CH), 26 September. 2019.

P. A. E. Schmid, "Predictive Maintenance with Deep Learning", Deloitte, Tokyo (JP), 29 November 2019.

P. A. E. Schmid, "SmartProfile – Deep Learning for the Powder Coating Industry", 6th Swiss Conference on Data Science, Bern (CH), 14 June 2019.

G. Spinola Durante, R. Jose James, M. Fretz,
K. Krasnopsolski, S. Mohrdiek, "Miniature hermetic optical-transparent packages for harsh environments", APAC - ESA Workshop on Advances in Packaging and Components, Noordwijk (NL), 14-15 March 2019.

G. Spinola Durante, "Thermal Management Simulations for optimized Optoelectronic Packaging", COMSOL Day Zürich 2019, Zürich (CH), 14 May 2019.

G. Spinola Durante, "Thermal Management Solutions for Optoelectronics Packages", Thermal Management Workshop - Swissphotonics, Neuchâtel (CH), 3 April 2019.

A. Steinecker, "3D Inspektion in Echtzeit mit Lichtfeldtechnologie", F&E-Konferenz zu Industrie 4.0, Rapperswil (CH), 24 January 2019.

A. Steinecker, "Active Implants - Technology and Examples", tfz Medical Cluster Insights, Steinhausen (CH), 10 December 2019.

A. Steinecker, "Digitalization of traditional working places – Cooperating with AI and robots", IVAM High-Tech Summit, Dortmund (DE), 04 April 2019.

A. Steinecker, E. Schaller, "Strategisches Innovationsmanagement", Modul des Executive MBA Studiengangs der HSLU, Alpnach (CH), 15 March 2019.

A. Steinecker, V. Revol, S. Graf, "Integrated sample preparation and bio-sensing technologies for liquid biopsy", microTEC Südwest Clusterkonferenz, Freiburg (DE), 20-21 March 2019.

F. Zanella, G. Basset, C. Schneider, A. Luu-Dinh, I. Marozau, S. Fricke, A. Madrigal, D. Van Aken, M. Zahir, "Microlenses Deposition for backside-illuminated Imagers", ESA Space Engineering and Technology Final Presentation Days (SET-FPDS), ESA-ESTEC, Noordwijk (NL), 04 July 2019.

F. Zanella, G. Basset, C. Schneider, A. Luu-Dinh, I. Marozau, S. Fricke, A. Madrigal, D. Van Aken, M. Zahir, "Results of microlens testing on back-illuminated image sensors for space", Space & Scientific CMOS Image Sensors, Toulouse (FR), 26-27 November 2019.

Research Programs

ECSEL	APPLAUSE – Advanced packaging for photonics, optics and electronics for low cost manufacturing in Europe
Eurostars	3DBrainScreen – An in vitro 3D brain-on-a-chip model for advanced drug discovery and neurotoxicological assays
Eurostars	AIRSWIM – Airborne Instrument for Reliable Shallow Water Imaging
Eurostars	DEBORAH – Optimization of design and control of district level thermal energy systems
Eurostars	DIAMANT – Direct Sensor Integration by Additive Manufacturing Technology
Eurostars	ENLIGHTENMENT – Enabling Next-generation Lighting Manufacture in Europe
Eurostars	EXRIL – Frequency stabilized laser with compact low-cost fiber ferrule based optical reference
Eurostars	FEMTOXIDE – High power femtosecond laser system based on ytterbium doped sesquioxide crystals
Eurostars	LEVES – Mid-infrared system utilizing LEVEL-crossing chirp-Spectroscopy in Quantum Cascade Lasers
Eurostars	MDFD – Medical device for measuring electro-mechanical properties of skeletal muscles
Eurostars	MINIHR – A wrist worn wearable device for women for stress detection and management
Eurostars	POLYOMINO – All-in-one platform for the design and the production of customized free-form OPV modules
Eurostars	POLYOMINO – PREVenting Anastomotic LEakage by developing an Anastomotic Perfusion Measurement Device (APM)
Eurostars	SMARTBEAT – ECG system for HRV lifestyle assessment

Forschung Aargau	LIGHTING-ROOF – Flöchige Leuchten
Interreg	BATHY 3D – Autonomous boat equipped with a LiDAR for precision 3D bathymetry
Interreg	HARISSA – Fabrication de pièces plastiques 3D microstructurées par injection plastiques : applications dentaires, médicales et horlogères
Interreg	INNOSMAD – Maggiore collaborazione trasfrontaliera tra imprese e altri attori dello sviluppo
Interreg	PRODIMED – Développement d'un procédé de revêtement de protection intégrale des dispositifs médicaux
Interreg	SBRA – Smart bra for diagnosing breast cancer
ITER	ITERBOLO – Bolometers prototyping for ITER
NCCR PlanetS	SKY-RULER – EOM-based comb for spectrograph calibration: TRL increase and tests
SATW	MICROTRAVEL – Microstrukturierung of material for photonics
SNI – Nanoargovia	DISP-BAT – Development of flow dispersion batteries
SNI – Nanoargovia	PLASMORETARDER – Plasmonic nanoscale retarder controlled with liquid crystals
SNI – Nanoargovia	PLASPEC – PhD on Plasmonic enhanced photoelectro chemistry
SNI – Nanoargovia	UltraNanoGRACO – Customized, nanostructured grating compressors for high repetition rate ultrafast lasers
SNSF	ACTIVE INTERFACES – Holistic strategy to simplify standards, assessments and certifications for building integrated photovoltaics
SNSF	AMELIZ – Advanced MEtallIzation Strategies for Heterojunction Solar Cells
SNSF	ASTROTWIN – Dual-comb system for FP calibration used in exoplanet search
SNSF	CELLSTRATES – Smart engineered substrates for high throughput mechanobiology
SNSF	MUSCLELAB – Silicon elastomer structures to measure mechanical properties of muscle models
SNSF	PERSI – Advanced functional Perovskites for tandem solar cells
SNSF	SALTO – Nitrides Semiconductors deposited at low temperatures for photovoltaic
SNSF / BRIDGE Discovery	FEMTOCHIP IP – Research on pulsed lasers for ultraefficient microresonator frequency combs.
SNSF / BRIDGE Discovery	POWER PI – Development of next generation solar cells and modules based on perovskite /silicon tandem architecture and perovskite/CIGS structure.
SNSF / BRIDGE Discovery	SMARTROBOT – Towards intelligent sensor-enhanced robotic neurosurgery
SNSF / BRIDGE Discovery	VIPS – Ultra-low power Visual Perception System
SNSF / Program NRP 70	PV2050 – Novel generation perovskite devices
SNSF / Program NRP 70	PV2050 – Photovoltaics into the built environment: from semi-transparent PV glazing to high efficiency roof integrated solutions
Swiss Federal Office of Energy (SFOE)	CLEAN-PV – Electrodynamic Cleaning for Solar PV Systems
Swiss Federal Office of Energy (SFOE)	DCSMART – Distribution en courant continu dans les réseaux intelligents
Swiss Federal Office of Energy (SFOE)	IEA-TASK13 – Performance, Operation & Reliability of Photovoltaic Systems

Swiss Federal Office of Energy (SFOE)	PAPERWALL – Test and demonstration of new solution for colored PV modules
Swiss Federal Office of Energy (SFOE)	PROSUMER-LAB – Einfluss neuartiger Strategien und Komponenten des Energiemanagements von netzintegrierten, intelligenten Gebäuden auf die Stabilität und Qualität des Haus- und Verteilnetzes
Swiss Federal Office of Energy (SFOE)	SKYCAM – Lokale Vorhersage der Sonneneinstrahlung
Swiss Federal Office of Energy (SFOE)	SODA – Solar data analytics for production forecasting and anomaly detection
Swiss Federal Office of Energy (SFOE)	SPET – Flexible Hochleistungskomponenten für die Elektrifizierung von zukünftigen aeronautischen Antriebssystemen basierend auf photoelektrischer Energieerzeugung
Swiss Food Research	LEAFYE STUDY – Automatic Pest Detection& Classification

Innosuisse – Swiss Innovation Agency

18101.1 PFNM-NM	3D NANOMET	Surface micro-nanostructuring of metallic surfaces for improved tribological performances
31952.1 INNO_ENG	AAOMVD	Vacuum Alumina Sealing
26245.1 PFLS-LS	AGAT	Automated Goldmann Applanation Tonometer
27751.1 PFLS.S	ALYVE	Artificial Lymphaedema Vessel
25701.1 PFNM-NM	AMTI	Additive Manufacturing of Ti based alloy for aerospace application
35490.1 IP-ENG	ASYPICK	Fast and robust binpicking for small parts
25714.1 PFNM-NM	AUTOMIA	Automated bovine milk analysis by push-button identification and characterisation of somatic cells
34738.1 IP-EE	BATMAN	smart BATtery MANagement for enhanced balancing and diagnostic of battery cells
28008.1 PFNM-NM	BESTIMATOR	Data-driven inline estimators of the state of charge and state of health of batteries
29605.1 IP-EE	BESTRADE	Battery energy storage for optimal renewable power trading
30120.1 IP-ENG	BIOASSAY	Wellplate bioassays based on highly sensitive resonant gratings
18623.1 PFNM-NM	BIOWAVE	Realisation of the BIOWAVE pre-product, a BIometric Watch Activated by Veins
27656.1 PFNM-NM	B-SOFT	Beam-Shaping Optical Film Technology for LED-based downlights
27049.1 PFES-ES	CBM	Deep learning for Condition Based Monitoring on railway vehicles
26704.2 PFLS-LS	CERAMIC-TOOTH	Development of a manufacturing solution and surface topography for dental ceramic implant applications, using a novel two-piece implant design
17863.2 PFLS-LS	COCO	Sustainable intensification of agricultural cropping systems supported by smart swiss ICT-AGRI solutions
27655.1 PFNM-NM	COMBI-NED	High field of view diffractive optical combiner for near-eye displays
33792.1 INNO-EE	COMOPA	Use of a multi-physics app to optimize air flow configurations for max efficiency of air water heat pumps
28345.1 PFNM-NM	CONTACTS	Next generation industrial passivating contacts for high efficiency silicon solar cells manufacturing.

18888.1 PFES-ES	CUBIC 2	The world's lowest-power platform to wirelessly exchange information peer-to-peer
16692.2 PFIW-IW	CUMAPRO	Massenproduktion von kundenspezifischen PV-Modulen für die Gebäudeintegration, Customised Mass Production
38614.1 IP-EE	DAGR	Disruptive innovation in solar energy technologies for building(human) integrated photovoltaic
33587.1 IP-ICT	DANUBE	High-performance integrated circuits for precise UWB localization
35855.1 IP-LS	DENOVOCAST	Automated skin tissue formation device
25600.1 PFNM-NM	DENSXO	Gas density sensors based on adaptive oscillators
38522.1 IP-LS	DIGITAL-SALIVA	Digital saliva health monitoring device for dental disease prevention with printed biosensors
32348.1 IP-EE	DIPPS	Development of integrated production processes for perovskite/silicon high efficiency photovoltaic
25726.2 PFNM-NM	DORES	Mirrored force resonance with double balance wheel for watches
38639.1 INNO-ICT	DRONEPLATFORM	Platform D-LOG ONE – DPENDENT – drone independent system
36538.1 IP-LS	DURALOCK	Non-autologous dura substitute with self-sticking properties, a feasibility study
36826.1 INNO-EE	DUSTBUSTER	Dust buster
25790.1 PFIW-IW	EMAILLE	Oberflächeninspektion für grossflächige Emaillekörper
25365.1 PFNM-NM	EMIRS 2	Development of new infrared light sources for gas detection application.
38946.1 INNO-ENG	E-PRO ROLLATOR	Vorstudie e-Rollator
34950J IP-ENG	ERGO	Ultra-low power image sensor for IoT applications
31942.1 INNO-ENG	ERGOTRACKING	Outil digital pour évaluation ergonomique de places de travail industrielles
30156.1 IP-ICT	FINGER-SENSE	Tactile fingertips for service robots
31563.1 INNO-ENG	FIREHUM	Physiologische Parameter, Sensoren und deren Integration in Schutzkleidung zur frühzeitigen Erkennung von Überhitzungsanzeichen bei Feuerwehrleuten
28478.1 PFIW-IW	FLASH	Advanced cell tester
35444.1 INNO-ENG	FLUT	Non-resonant ring-down of a flexural ultrasonic transducer
33436.1 IP-ENG	FREELMA	Freeform lens and microlens arrays for high-quality lighting systems
31439.1 IP-ENG	FT-MEMS	High accuracy fiber-optic MEMS temperature sensor
28236.1PFNM-NM	GLAM	Glass micro-fluidics
25799.2 PFIW-IW	GMD	Predictive maintenance for mill drive power train systems
32074.1 IP-ENG	GOBEYOND	GoBeyond: Commercialisation of a breakthrough optical solution in fluorescence imaging for medical diagnostic
25839.2 PFLS-LS	GRAINVIEW	Flow speed measurement and morphological analysis of food grains
31841.1 IP-ENG	HEART	High precision additively manufactured Ti-based active medical device component

29971.1 IP-EE	HELIOS	High efficiency direct and diffused light optimum photovoltaic system
27655.1 PFNM-NM	HI-NIL	Waveguide-based combiners for augmented reality processed by high refractive index nanoimprint lithography
28715.1 IP-LS	HOPE	Hypertension detection through Optical blood pressure monitoring in Pregnancy by an Electronic wearable (HOPE)
35562.1 IP-LS	INFINIPRINT	Multi-material microfluidic printhead for “on-the-fly” formulation for advanced bioprinting
27291.2 PFLS-LS	IN-SITU	Intelligent process control for 3D-bioprinting technology
27100.1 PFLS-LS	INTUBSENS	Development of a pressure sensor for medical applications
33074.1 IP-LS	iTooth	An intelligent in-mouth monitoring system for the optimization of dental care
32970.1 IP-ENG	LEADME	Drug screening technology platform based on micro-LED and high resolution MEA
35819.1 IP-ENG	LIFI-NED	Light-field near-eye display
37361.1	LIGHT-ROOF	Lighting device integrated in glass roof
35299.1 IP-ENG	LIGHTSAFE	Lightguiding Security Features
35163.1 IP-ICT	LubriSafe	Axino.IoT.LubriSafe – an online quality and safety control system for metal working industry
34476.1 INNO-LS	LYMPHIT	The first lymphatic activity tracker
27435.1 PFNM-NM	MAGNETO	Inspection platform for magnetically oriented optical features
18959.1 PFIW-IW	MAXIMAL	Modular radial and axial active magnetic bearing for maxon motors
30037.1 IP-EE	MEGAWHITE	New-generation diffuser for industrial production of white PV technology
27513.1 PFNM-NM	MEMCELL	MEMS cells for miniature atomic clocks
26565.2 PFIW-IW	MODECORES	Speed-optimised simulation models for instant consulting on heating systems and energy management systems
27901.1 PFLS-LS	MUSCLEANALYSER	Electrical stimulation & optical force measurement apparatus for 3Dprinted muscle tissues in multiwell plate
18760.1 PFNM-NM	NEURUG	Multi-well biosensor for drug screening applications
32688.1 IP-ICT	OPTIBP	SmartphonE blood Pressure App
37517.1 IP-LS	ORGACHIP	Combined parasite and host models for high-throughput drug pharmacokinetics in animal health
34473.1 IP-ENG	PANORAMA	Powder-based Novel Raw Materials
39699.1 INNO-ENG	PARQUETROBOT STUDY	Preliminary study on Parkett-Schleifroboter
25485.1 PFNM-NM	PERMUT	Investigation of feasibility of MEMS based ultrasonic air transducers for industrial applications
34956.1 IP-ENG	PHOMIPRO V2	Smartphone readable digital scrambled pixelated microstructures for part identification and brand protection
25701.1 PFNM-NM	PI3	Additive Manufacturing of Ti based alloy for aerospace application
28063.1 PFNM-NM	PRECISENSE	Development of a generic, high-performance, low-cost, absolute position sensor prototype

25422.2 PFIW-IW	PUMPOMAT	Robotergesteuerter Präzisionsmontagearbeitsplatz
26116.1 PFES-ES	RAILCHECK	RailCheck with Fingerprinting
33797.1 INNO-ENG	ROPESENS	Feasibility on the Kombination einer visuellen und magnetinduktiven Seilprüfeinrichtung zur Verbesserung der Fehleridentifikation
36894.1 INNO-ICT	SIDIS	SIDIS
18462.1 PFNM-NM	SILICON EYE	Design of a vision for positioning systems
16584.1 PFEN-IW	SILVERLINE 2	Next generation production processes and quality controls for watch batteries
34509.1 INNO-LS	SKINFACTORY PREP	Preliminary study for denovoSkin automation
35418.1 IP-ENG	SLAM4-0	Smart Laser Manufacturing for precision industry 4.0
36619.1 INNO-ENG	SMART WHEELCHAIR	Smart Wheelchair Wheel
30759.1 IP-EE	SMART-LIGHT	Safe and Smart Control of Blind and Lighting
31392.1 IP-EE	SMART-MAT	Advanced Materials and design for cost-effective, high-performance and high-reliability SmartWire Connection Technology
30363.1 INNO-ICT	SMARTPROFILE	Mobile Applikation zur Erkennung von komplexen Aluminiumprofilen in der Produktion
33395.1 IP-EE	SMINTEBI-MVP	Smart individual tenant billing minimal viable product
37762.1 INNO-ENG	SPV	Preliminary study on smart pinch valve
26845.1 PFNM-NM	SPYDERMAN	Indoor 2D and 3D device positioning system
16694.2 PFIW-IW	STABILITY	Dynamische Lageregelung für Hydraulikmodule demonstriert an einem Stelzentraktor im Rebberg
34545.1 IP-ENG	STERLING	Improve the production processes of RF components by developing new silver-plating methods
35471.1 INNO-ENG	TOUCHAUTOCHECK	Feasibility on bonding technologies for contactless die attach process
18539.1 PFLS-LS	TRACTEUR	Development of an automated seed drill for the site-specific reseeding of grassland
31512.1 IP-EE	Uppero	Development of deposition processes for future large-scale production of perovskite based photovoltaic devices
33466.1 IP-ENG	VERSACE	Versatile Electrical Regulation for Spark Assisted Chemical Engraving
18394.1 PFLS-LS	ZEPTOTRACK	Real-time surgical instruments positioning with reference integrated in surgical lamp

European Commission Projects

H2020 – NMBP 2016	ACENANO	Analytical and Characterisation Excellence in nanomaterial risk assessment: A tiered approach
H2020 – IOT 2016	ACTIVAGE	ACTivating InnoVative IoT smart living environments for AGEing well
H2020 – LCE 2016	AMPERE	Automated photovoltaic cell and Module industrial Production to regain and secure European Renewable Energy market
H2020 – Clean Sky	AMPWISE	Autonomous Wireless Current Sensor for Aircraft Power Lines
H2020 – ECSEL 2018-1-IA	APPLAUSE	APPLAUSE – Advanced packaging for photonics, optics and electronics for low cost manufacturing in Europe

H2020 – Clean Sky 2	AUDACITY	Compact powerful and reliable piezoelectric actuator for landing gear systems
H2020 – LC-SC3-RES-6 2018	BE-SMART	Innovative Building Envelope for Sustainable, Modular, Aesthetic, Reliable and efficient construction
H2020 – ICT 2016	BIOCDX	A miniature Bio-photonics Companion Diagnostics platform for reliable cancer diagnosis and treatment monitoring
FP7 – ICT	BIOFOS COMPLEMENT	Microring resonator-based biophotonic platform for food analysis
H2020-FETOPEN	CFLOW	Coherent ultraFast Long Wave infrared communications
H2020 – LCE 2015	CHEOPS	Production technology to achieve low Cost and Highly Efficient photovoltaic Perovskite Solar cells
H2020 – IND CE	CITCOM	Complimentary Inspection Technique based on Computer Tomography and Plenoptic Camera for MEMS Components
H2020 – ICT 2016	DATABIO	Data-Driven Bioeconomy
H2020 – ICT 2015	DETOP	Dexterous Transradial Osseointegrated Prosthesis with neural control and sensory feedback
H2020 – LCE 2016	DISC	Double-side contacted cells with innovative carrier-selective contacts
FP7 – SEC 2009	E-SPONDER COMPLEMENT	A holistic approach towards the development of the first responder of the future
H2020 – ICT 2016	FED4SAE	Federated CPS Digital Innovation Hubs for the Smart Anything Everywhere Initiative
H2020 – IOT-2016	FITPIG	HR monitoring of pigs at the ear
H2020 – ICT 2016	FLAIR	Flying ultra-broadband single-shot infrared sensor
H2020 – MSCA-ITN 2016	FoodSmartPhone	Smartphone analyzers for on-site testing of food quality and safety
H2020 – MG 2014	FUTURESKY	Smart, Green and Integrated Transport
H2020 – SPACE 2018	HEATPACK	New generation of High thermal efficiency components packages for space
FP7 – ENERGY	HERCULES COMPLEMENT	High efficiency rear contact solar cells and ultra-powerful modules
H2020 – LC-SC3-RES-15 2019	HIGHLITE	High-performance low-cost modules with excellent environmental profiles for a competitive EU PV manufacturing industry
H2020 – LC-SC3-RES-15 2019	HIPERION	Hybrid photovoltaics for efficiency record using integrated optical technology
H2020 – Clean Sky	HIPNOSIS	Hardware Implementation of Pilot-Non-intrusive Cognitive States Identification System
H2020 – EEB 2017	HYBUILD	Innovative compact hybrid electrical/thermal storage systems for low energy buildings
H2020 – EE 2015	INDIGO 2	New generation of intelligent and efficient district cooling systems
H2020 – ICT 2016	INSPEX	Integrated smart spatial exploration system
H2020 – FOF 2016	KRAKEN	Hybrid automated machine integrating concurrent manufacturing processes, increasing the production volume of functional on-demand using high multi-material deposition rates
FP7 – ICT	LASSIE-FP7 COMPLEMENT	Large area solid state intelligent efficient luminaires

H2020 – MG 2014	LYNCEUS2MARKET	Safer and more efficient waterborne operations through new technologies and smarter traffic management
H2020 – ICT 2014	M3TERA	Micromachined terahertz systems –a new heterogeneous integration platform enabling the commercialization of the THz frequency spectrum
H2020-FETFLAG-2018-2020	MACQSIMAL	Miniature hot Atomic vapor Cells based Quantum devices for Sensing and Metrology AppLicationS
H2020-NMBP-FOF-2018	MANUELA	Additive Manufacturing Using Metal Pilot Line
H2020 – NMBP 2017	MANU-SQUARE	MANUfacturing ecoSystem of QUAlified Resources Exchange
H2020 – ICT 2015	MIRPHAB	MidInfraRed Photonics devices fABrication for chemical sensing and spectroscopic applications
H2020 – ICT 2017	MOLOKO	Multiplex photonic sensor for plasmonic-based detection of contaminants in milk
H2020 – LCE 2016	NEXTBASE	Next-generation interdigitated back-contacted silicon heterojunction solar cells and modules by design and process innovations
H2020 – SFS 2018	NutriShield	Fact-based personalized nutrition for the young
H2020 – NMBP-FOF 2018	OLEDSOLAR	Innovative manufacturing processes and in-line monitoring techniques for the OLED and thin film and organic photovoltaic industries (CIGS and OPV)
FP7 – ICT	PEGASO COMPLEMENT	Personalised guidance services for optimising lifestyle management in teen-agers through awareness, motivation and engagement
H2020 – Clean Sky	PEGGASUS	Pilot Eye Gaze and Gesture tracking for Avionics Systems using Unobtrusive Solutions
H2020 – LCE 2016	PENTAGON	Unlocking European grid local flexibility trough augmented energy conversion capabilities at district-level
H2020 – LCE 2017	PERTPV	Perovskite Thin-film Photovoltaics (PERTPV)
H2020 – FETFLAG 2018	PHOG	Sub-Poissonian Photon Gun by Coherent Diffusive Photonics
H2020 – SPACE 2018	PULSAR	Space Robotics
FP7 – KBBE	RADAR COMPLEMENT	Rationally Designed Aquatic Receptors integrated in label-free biosensor platforms for remote surveillance of toxins and pollutants
H2020 – ICT 2014	RAWFIE	Road-, Air- and Water-based Future Internet Experimentation
H2020 – MSCA-RISE	RDC2MT	Research, demonstration and commercialization of DC microgrid technologies
H2020 – LC-SC3-RES-4 2018	RE-COGNITION	Renewable cogeneration and storage technologies integration for energy autonomous buildings
FP7 – SPACE	REMOVE-DEBRIS	A low-cost active debris removal demonstration mission
H2020 – SEC 2016/7	ROBORIDER	Autonomous swarm of heterogeneous Robots for BORDER surveillance
H2020 – LCE	SABINA	Smart bi-directional multi energy gateway
H2020 – ICT 2018-2	SARMENTI	Smart multisensor embedded and secure system for soil nutrient and gaseous emission monitoring
H2020 – SPACE 2018	SELECTOR	Surface mount technology (SMT) compatible ELECTroMechanical relay for cOMPact redundancy Ring

FP7 – ICT	SEMIAH COMPLEMENT	Scalable multi-criteria energy management infrastructure for aggregation of households
FP7 – NMP	SMARTNANO COMPLEMENT	Sensitive measurement, detection, and identification of engineered nanoparticles in complex matrices
FP7 – ENVIRONMENT	STRATOCLIM	Stratospheric and upper tropospheric processes for better climate predictions
FP7 – ICT	SUNFLOWER COMPLEMENT	Sustainable novel flexible organic watts efficiently reliable
H2020 – FETOPEN 2014-2015	SUPERTWIN 3	All Solid-State Super-Twinning Photon Microscope
H2020 – ATTRACT	SWAP	Smart Wall Pipes and ducts
H2020 – EE 2016/7	TABEDE	TowArds Building rEady for Demand rEsponse
H2020 – EEB 2016	THERMOSS	Building and district thermal retrofit and management solutions
FP7 – NMP	TRIBUTE COMPLEMENT	Take the energy bill back to the promised building performance
H2020 – ICT 2018-2	WELMO	Wearable Electronics for Effective Lung Monitoring

European Space Agency and Swiss Space Office Projects

ESA Projects

AGAL	To improve lifetime of the atomic clocks used in Galileo satellites
CCM-MTG	Development and manufacture of corner cube mechanisms for MTG satellite
CLUPI	CLUPI instrument for Exomars
COMAM	Development of a compliant mechanism based on additive manufacturing
COOLER	Compact Opening Louver
CS4SPACE	Compressive sensing
DANOE	High-dynamic absolute nanometric optical encoder technology assessment for space phase II
DELIAN	Dextrous lightweight arm for exploration
ELAINE	Electronic fetal monitoring system
EUSO-B2	Extreme Universe Space Observatory – Phase B2
FIFREDO	Fibered frequency doubler at 1560 nm
GERANIUM	Generative Artificial Intelligence for High Performing Inversion Models
HIGHTS	Highly thermally conductive silver sintered die mounting
HOPP	Photodiode development
HOPWELL	Space validation of glass lid soldering techniques to hermetically seal small size optoelectronic parts
IMPROVE	Microvibration simulation and analysis tools
ISABELA	Development of a fine steering mirror breadboard
ISOL	Development of a high performance Microvibration isolation system
ITI-WHEEL	How to adapt Celerons wheel towards agility?
LAFP	Develop a large angle flex pivot for space applications
MACAREW	Magnetic Characterization of Reaction Wheels
MATMAT CCM	Matrix material for programmable flexure mechanism
MBRW	Magnetic Bearing based Reaction Wheel
MCC-X	Miniaturised Motion Controller Customisation for Exploration

MEMS GC-MS	MEMS-based gas chromatograph and mass spectrometer
MILA4GROUND	Proof of concept for MILA ground applications
MILEB	Miniaturized imaging LIDAR systems for the landing of spacecraft's
ML-BI-CIS	Microlenses Deposition for Backside Illuminated Imagers
MLSCL	Sub-picosecond model-locked semiconductor laser for space missions
MONALISA PHASE 1	Laser for LISA mission
MTS	Miniature Timing Source (mTS): miniature atomic clock, MEMS vapor cells, ASIC specifications
NIRS	NIR immersed grating in transmission for high resolution spectroscopy
NPI-BEARING	Miniature Magnetic Bearings for Space Actuators
OBSIDIAN	SYSID toolbox
OEO	Ultra-low phase noise reference oscillator
OSRC	Digital stabilisation electronics for lasers
REAC	Reliability evaluation of MEMS by accumulative tests for space application
SMARTIES	Design, procurement and qualification testing of a Slip Ring Assembly rotor based on Additive Manufacturing
STAR	Lidar for Wavefront distortion
STIFS	Definition for optical atomic clock
TOPCAM-CCM	Topologically optimised compliant mechanisms based on additive manufacturing
TRIPP	Verification of straylight rejection of optical science payloads using a pulsed laser source
WALLIE	Development new TOF detector. Follow-up MILA

Swiss Space Office Projects

MEGA	Micro-fabricated Electron Gun for Atomic clocks
PRINTHEATERS	Fully printed heaters on CFRP structures for space applications
SPACEWAVE	Ultra-low phase noise microwave generation with modelocked laser and high-power handling photodiodes

Industrial Property

Patent portfolio

In 2019, 19 invention reports were submitted internally for examination which have led to 18 patent applications filed in 2019 (15 regular applications and 3 provisional applications). The patent portfolio has been further enhanced by the extension of different countries of 33 patent files based on prior patent applications.

Collaboration with Research Institutes and Universities

University	Institute	Professor	Field of collaboration
AO Research Institute Davos	Musculoskeletal Regeneration	M. Alini	Intervertebral disc biomechanics
Aristotelio Panepistimio Thessalonikis	Medical School	N. Maglaveras	Clinical assessment of WELMO devices in the context of COPD
CEA	INES	D. Munoz	Silicon Heterojunction, Metallization
Christian-Albrechts-Universität zu Kiel	Department of Anaesthesiology and Intensive Care Medicine	I. Frerichs	Clinical assessment of WELMO devices in the context of COPD
Chur University of Applied Sciences (HTW)	Departement Angewandte Zukunftstechnologien, Institut für Photonics und ICT IPI	U. Hauser-Ehninger	Solid state lighting

University	Institute	Professor	Field of collaboration
EMPA	Laboratory for Thin Films and Photovoltaics	F. Fan	Perovskite based tandem cells
EMPA	Swiss federal laboratories for materials science and technology	P. Hoffmann	Solid state lighting
EPF Lausanne	LIPID	M. Andersen	Human Centric Lighting
EPF Lausanne	PVLAB	C. Ballif	High performance solar cells and high reliability PV modules
EPF Lausanne	Laboratory of Construction Materials (LMC)	P. Bowen	Cement Hydration
EPF Lausanne	Microengineering	D. Briand, V. Subramanian	Printed Electronics
EPF Lausanne	Laboratory of Microsystems (LMIS1)	J. Brugger	
EPF Lausanne	Advanced Quantum Architecture Laboratory	E. Charbon	Micro-optics
EPF Lausanne	Collège de Management de la Techologie	G. de Rassenfosse	Efficient Data Base Collection
EPF Lausanne	Bioengineering	B. Deplancke	ChIP-Sequencing
EPF Lausanne	ICLAB Integrated Circuits Laboratory	C. C. Enz	60GHz radar, Approximate arithmetic, ULP Radio and protocol for WiseSkin
EPF Lausanne	Computer Vision Laboratory	P. Fua	Reduced labelling Machine learning
EPF Lausanne	Laboratory of advanced semiconductors for photonics and electronics	N. Grandjean	Solid state lighting
EPF Lausanne	EPFL-ECAL Lab	N. Henchoz	Digital experience - Meditation study in collaboration with Ming Shan (Bullet's Taoist center)
EPF Lausanne	Laboratory for Communications and Applications (LCA)	J.-P. Hubaux	Development of oblivious neural networks for making predictions on encrypted medical data
EPF Lausanne	LAP Processor Architecture Laboratory	P. lenne	Embedded systems
EPF Lausanne	Laboratory of Photonics and Quantum Measurements	T. J. Kippenberg	Bridge
EPF Lausanne	Automatic Control Laboratory 3	C. Jones	Automatic building model identification and optimized control
EPF Lausanne	Microengineering	O. J. F. Martin	Resonant waveguide gratings
EPF Lausanne	TCL Telecommunications Circuits Laboratory	A. P. Burg	Good enough circuits, Ultra-low power and sub-threshold design, bias control, library characterization
EPF Lausanne	LESO	J.-L. Scartezzini	Human Centric Lighting
EPF Lausanne	LTS2 Signal processing laboratory 2	P. Vandergheynst	Newborn vital signs monitoring based on multiple vision sensors

University	Institute	Professor	Field of collaboration
EPF Lausanne	SCI STI JMV Group	J.-M. Vesin	Newborn vital signs monitoring based on multiple vision sensors
ETH Zürich	Integrated Systems Laboratory	L. Benini	Sub-Near-Threshold Multicore, Neural Network
ETH Zürich	deMello Group	A. De Mello	Microfluidics
ETH Zürich	Health Sciences and Technology	S. Ferguson	Intervertebral disc biomechanics
ETH Zürich	D-BSSE	A. Hierlemann	Electrochemical sensor functionalization
ETH Zürich	Data Analytics Lab	T. Hofmann	Machine Learning
ETH Zürich	D-HEST	S. J. Sturla	Food analysis
ETH Zürich	Institute for Particle Physics and Astrophysics	A. Rubbia	X-ray read-out circuit characterization
ETH Zürich	Computer Vision Laboratory	L. van Gool	Machine Learning
Idiap Research Institute	Speech and Audio Processing	P. Motlicek	Modal a people monitoring system using multiple sensing modes (video, audio, ...)
Imperial College of London	Faculty of Engineering, Department of Electrical and Electronic Engineering	E. M. Yeatman	Energy harvesting for wireless sensor networks in aerospace applications; smart materials
INAIL (National Workers' Compensation) Prosthetic Center, Bologna, Italy	Aids Area and Research and Training Area	R. Sacchetti	Clinical implantation and assessment
IPC - Centre Technique Industriel de la Plasturgie et des Composites	Innovation Plasturgy Composites	L. Tenchine, S. Dessors	Injection Molding
Istituto Ortopedico Rizzoli (IOR)	2nd Orthopaedic and Traumatology Clinic	S. Zaffagnini	Clinical implantation and assessment
Katholieke Universiteit, Belgium	Computer Security and Industrial Cryptography group	A. Purnal	Cryptography & Security
Lausanne University Hospital (CHUV)	Department of Anesthesia	P. Schoettker	Automated Pulse Oximeter Waveform Analysis to Track Changes in Blood Pressure during Anesthesia Induction
Lucerne School of Engineering and Architecture (HSLU)	CC Electronics	E. Niederberger	Solid state lighting
Lund University	Department of Biomedical Engineering	C. Antfolk	Prosthetics, decoding of user intent, control, clinical assessment
ONERA-France	Modane-Avrieux Center	M. Lyonnet, Y. Michou	Pressure Sensitive Painting
ONERA-France	Meudon Center	M.-C. Mérianne	Pressure Sensitive Painting

University	Institute	Professor	Field of collaboration
Paul Scherrer Institute (PSI)	Laboratory for Micro- and Nanotechnology	Y. Ekinci	Plasmonic retarders for imaging
Politecnico di Milano	Department of Aerospace Science and Technology	A. Airoldi	Simulation 3D printing
Scuola Superiore Sant'Anna, Pisa, Italy	The BioRobotics Institute	C. Cipriani	Artificial wrist, mechatronic couplers, artificial sensors for hand/wrist prosthesis, control algorithms, user assessment tools
Technical University of Denmark	Department of Applied Mathematics and Computer Science	E. Andreeva	Cryptography & Security
Technical University of Kaiserslautern	Chair of real-time systems	G. Fohler	Real-time networking
Uni. Basel	Chemistry	E. Constable, C. Housecroft	Photochemistry
Universidade de Coimbra	Department of Informatics Engineering	J. Henriques	WELMO algorithms
Università Campus Bio-Medico, Roma, Italy	Department of Orthopaedics and Trauma Surgery	V. Denaro	Clinical implantation and assessment
Université de Bourgogne	Laboratoire d'Electronique, Informatique et Image, Le2i	J. Dubois	Remote vital signal monitoring
Université de Caen	Department of Neurophysiology	S. Besnard	ADAPTATION - Vital sign monitoring during Christian Clot's expedition in the Valley of Death
Université de Montpellier	Institut Charles Gerhardt	N. Frety	Thermoelectric Materials
Université de Neuchâtel	Complex Systems Group	V. Schiavoni	Usage of Trusted Execution Environments for cloud computation (IntelSGX) and IoT protocols (ARM's TrustZone)
University Hospital Inselspital Bern	Department ENT Surgery	M. Caversaccio	Image-guided micro surgery for hearing aid implantation
University Hospital of Bern (Inselspital)	Department of Neurology	O. Baud	Validation of the use of chronic portable EEG recordings to better monitor epilepsy
University Hospital of Bern (Inselspital)	Department of Pneumology	T. Geiser, S. Ott	Validation of non-invasive miniature optical sensors for scoring of sleep stages: a prospective concept study
University Hospital of Bern (Inselspital)	Department of Neurosurgery	A. Raabe	Evaluation of an in-vivo study to assess the performance of a sensor-based robotic approach to spinal surgery
University Hospital of Bern (Inselspital)	Department of Cardiovascular Surgery	D. Reineke	Clinical study on non-invasive blood pressure monitoring in 40 patients carrying a left ventricular assist device

University	Institute	Professor	Field of collaboration
University Hospital of Bern (Inselspital)	Department of Cardiology and Clinical Research	E. Rexhaj	Clinical study on 24h ambulatory blood pressure monitoring in 70 hypertensive patients using wrist-located optical sensors
University Hospital of Bern (Inselspital)	Department of Cardiology and Clinical Research	S. Rimoldi	Clinical validation of a PAP sensor against non-invasive medical gold standard
University Hospital of Bern (Inselspital)	Department of intensive Care Medicine	J. Schefold, D. Reinecke	Validation of the extended AVA product with the non-invasive measure of the blood pressure in reference to the medical gold standard and with a 40-patient cohort (pregnant women)
University Hospital Zürich	Biomedical optics research laboratory	M. Wolf	Newborn vital signs monitoring based on multiple vision sensors
University of Applied Sciences and Arts Northwestern Switzerland (FHNW)	Institut für Nanotechnische Kunststoffanwendungen	M. Kristiansen	Micro and nano structuring
University of Applied Sciences and Arts Northwestern Switzerland (FHNW)	Institute of Product and Production Engineering	B. Resan	Lasers
University of Applied Sciences and Arts Northwestern Switzerland (FHNW)	Chemistry and Bioanalytics	L. Suter-Dick	Microtissues
University of Applied Sciences and Arts of Southern Switzerland (SUPSI)	Energy Systems Sector	M. Caccivio	Metrology
University of Applied Sciences and Arts of Southern Switzerland (SUPSI)	IDSIA Dalle Molle Institute for Artificial Intelligence	L. M. Gambardella	Machine Learning
University of Applied Sciences and Arts, Lucerne (HSLU)	CC Fluid Mechanics and Hydro-Machines	E. Casartelli	Digital twin
University of Applied Sciences and Arts, Lucerne (HSLU)	CC Aerospace biomedical science & technology	M. Egli	Cell viability check, Bioreactor for space
University of Basel	Psychiatry Hospital / Center for Chronobiology	C. Cajochen	Human Centric Lighting / Chronobiology
University of Bern	ARTORG Center for Biomedical Engineering	S. Weber	Image-guided micro surgery for hearing aid implantation
University of Bristol, United Kingdom	Department of Computer Science	A. Roy	Cryptography & Security

University	Institute	Professor	Field of collaboration
University of Essex, Colchester, United Kingdom	School of Computer Science and Electronic Engineering	L. Citi	Point-process and machine-learning-based neuro-muscular decoding/control algorithms
University of Geneva	Institute of Chemistry	T. Buergi	Microstructural study of nano particles
University of Gothenburg, Sweden	Department of Orthopaedics	J. Wessberg	Sensory feedback
University of Lausanne	Information Security and Privacy Lab	K. Huguenin	Privacy mechanisms for mHealth data
University of Lorraine, France	Laboratoire lorrain de Recherche en Informatique et ses Applications	V. Lallemand	Cryptography & Security
University of Neuchâtel	Institut de Biologie	F. Kessler, P. Junier	Ultrastructural investigation
University of Sherbrooke	Neonatology	E. Fortin-Pelerin	Evaluation of PAP measurement accuracy in sheep
University of Zürich	Institute of Neuroinformatics	T. Delbrück	On-chip convolutional neural network for visual scene processing, Development of embedded neural networks in microcontrollers
Vienna University	Department of Physical Chemistry	P. Lieberzeit	Chemical Sensor
Wyss Center	Bio and Neuro Engineering	C. Clément	Integrated circuits for brain implants

Teaching

	Title of lecture	Context	Location
F. Cosandier	Metrology	Redefinition of SI units	
M. Dadras	Microscopy	Applictaion of micrpscopy for ultrastructural studies	University of Neuchâtel
M. Despont	Packaging and hybridization, the valorization of MEMS technologies	Micro- 534 Advanced MEMS 2019 (D. Briand)	EPF Lausanne
A. Hutter	Battery Modeling with Application to High Energy Density Systems	EPFL summer school	BFH Biel
N. Marjanovic	Introduction to Flexible Electronic	FSRM course	Fribourg (Swiss ePrint event)
N. Marjanovic, F. Zanella	Organic and Printed Electronics	Master course MICRO-505	EPF Lausanne
D. Schmid	Smart body sensors	SATW TecDay & TecNight	Kantonsschule Heerbrugg
	Smart body sensors	SATW TecDay	Kantonsschule Sursee
O. Sereda	X-ray Powder Diffraction	CCMX advanced course: Powder Characterisation and Dispersion	EPF Lausanne
	Thin Film analysis: Microstructure and Residual Stress	Microelectronics	HE-Arc

Theses

PhD Degrees Awarded in 2019

Name	University	Title
G. Quaranta	EPF Lausanne	Resonant waveguide gratings for color-selective diffraction
F. Sorba	EPF Lausanne	Elastomer-based pneumatic device to measure the mechanical properties of cell monolayers

CSEM Employees carrying out a PhD & PhD Funded by CSEM

Name	Professor / University	Theme / CSEM Unit	Start year
T. Aderneuer	C. Cajochen / University of Basel	Free form micro optics for human centric lighting / Center Muttenz	2017
C. Aguet	P. Frossard / EPF Lausanne	Generate realistic synthetic PPG data using Generative adversarial networks / Systems	2019
M. Auchlin	V. Gass / EPF Lausanne	Electrical engineering topic / Micro&Nano Systems	2017
L. Biggio	T. Hofmann / ETH Zürich	Center Alpnach	2019
B. Bonnal	C. Dehollain / EPF Lausanne	Cooperative sensors / Systems	2019
G. Borque Gallego	Y. Perriard / EPF Lausanne	Mignature magnetic bearing reaction wheel / Systems	2017
T. C. Müller	A. P. Burg / EPF Lausanne	Variation-aware digital design / Integrated and Wireless Systems	2016
S. Cerida Rengifo	C. C. Enz / EPF Lausanne	FMCW Radar Front-End / Integrated and Wireless Systems	2018
F. Chicco	C. C. Enz / EPF Lausanne	Frequency Synthesis for FMCW Radar. / Integrated and Wireless Systems	2017
L. Driencourt	E. Constable / University of Basel	Plasmon-enhanced water splitting / Center Muttenz	2017
M. Dussouillez	C. Ballif / EPF Lausanne	Perovskite stability / Photovoltaics	2019
Y. El-Zein	K. Huguenin / University of Lausanne	mHealth data privacy / Systems	2019
T. Frei	V. Gass / EPF Lausanne	Thermal management of microsystem in harsh environment // Microheat pipe / Micro&Nano Systems	2017
E. Genzoni	J. M. Vesin / EPF Lausanne	Exploring full content of optical signals to enhance cardiac arrhythmia screening / Systems	2019
Z. A. Halvorsen	A. De Mello / ETH Zürich	Miniaturized fluid sample preparation for water quality monitoring / Center Alpnach	2017
D. Honzàtko	P. Fua / EPF Lausanne	Defect detection using deep learning / Integrated and Wireless Systems	2018
P. Iurilli	V. Wood / ETH Zürich	State-of-health modeling for batteries / Photovoltaics	2018
S. Jafari	S. Sturla / ETH Zürich	Aptamer-based assays for food safety / Centre Landquart	2017
P. Jokic	L. Benini / ETH Zürich	Embedded Machine Learning / Integrated and Wireless Systems	2017
L. Komini	K. Wegener / ETH Zürich	Topology optimization for compliant mechanisms / Systems	2019

Name	Professor / University	Theme / CSEM Unit	Start year
E. Ntavelis	L. van Gool / ETH Zürich	Multimodal Learning & Generation: Utilizing diverse inputs to generate & manipulate images / Center Alpnach	2019
E. Obrzud	F. Pepe / University of Geneva	Optical frequency comb for spectrograph calibration / Systems	2016
P. Scharnhorst	C. Jones / EPF Lausanne	Reinforcement learning for building and grid control / Photovoltaics	2019
L.-L. Senaud	C. Ballif / EPF Lausanne	Silicon Heterojunction Solar Cells / Photovoltaics	2017
J. Simeunovic	P. Frossard / EPF Lausanne	Graph signal processing for energy grids / Photovoltaics	2019
Y. Tang	O. Guenat / University of Bern	Applications of cellulose-based materials to electrochemical sensing / Centre Landquart	2017
A. M. Tuomiranta	C. Ballif / EPF Lausanne	Optimal design and operations of photovoltaic power plants / Photovoltaics	2015
T. Voumard	T. Südmeyer / University of Neuchâtel	Astronomical spectrometers calibration light / Systems	2019

Commissions and Committees

P.-J. Alet	INTERSOLAR EUROPE Conference Committee, committee chairman
F. Amez-Droz	CSEM Representative, Swiss Association of Science Journalism
C. Bosshard	BaselArea.Swiss: Technology Field Leader Micro, Nano & Materials DayOne: Member of Core Team Managing Director of the Swissphotonics NTN Member of the Board of EPIC (European Photonics Industry Consortium) Member of the Board of Stakeholders of Photonics21 Member of the University Council of the University of Basel
P. Dallemagne	Secretary and Swiss representative of Technical Committee 5 "Information Technology Applications", International Federation for Information Processing (IFIP)
J.-D. Decotignie	International Advisory Committee, Workshop on Factory Communication Systems, Sundsvall, Sweden ISO TC 65 Swiss Committee ISO TC 65C, WG16 convenor, Wireless Industrial Communication Standardization
R. Delgado-Gonzalo	Expert Group in Digital Health in the Swiss Alliance for Data-Intensive Services
M. Despeisse	n-PV workshop committee, EUPVSEC topic organizer, SolarPower Europe.
M. Despont	Board Member of the International Micro and Nano Engineering Society - iMNEs Board member of the Swiss-MNT network Chairman of the International Steering Committee of IEEE International Conference on Micro ElectroMechanical Systems (MEMS) CSEM and HTA representative at the Micro- and Nano- Technology Workgroup, European Spatial Agency (ESA) Member of the editorial board of Microelectronic Engineering Journal (Elsevier) Member of the Industrial Advisory Board, Nanotechnology Program, Prof H. Bahaskaran, Oxford University, UK Regional Program Chair of the 21st International Conference on Solid-State Sensors, Actuators and Microsystems (Transducers 2021)

L. A. Dunbar	Academic co-Lead of Machine Learning Clinic in the Swiss Alliance for Data-Intensive Services Academic co-Lead Swiss Alliance for Data-Intensive Services Member of Technical Subcommittee of IES in the IEEE
M. El-Khoury	CNCI Chambre Neuchâteloise du Commerce et de l'Industrie, Neuchâtel Concours International de Chronométrie, Le Locle, Membre du Comité d'honneur Member of the Swiss Academy of Engineering Sciences SATW
S. Emery	Member of the Technical Committee of the IEEE SOI-3D-Subthreshold (S3S) Conference
O. Fernandez	Member of SciPiL (the Scientific Partnership in Lighting by Luger Research)
R. Ferrini	Chair of the Swissphotonics Solid State Lighting - (SSSL) Swiss National Laboratory for Solid State Lighting Member of SciPiL (the Scientific Partnership in Lighting by Luger Research)
S. Fricke	Member of the Organising Committee, Swiss ePrint 2019
E. Györvary	Core team member of Team Finland in Switzerland Extended Board Member of CSEM Brasil Extended Board Member of the Heterogeneous Technology Alliance (alliance federating the Fraunhofer (microelectronics), VTT, CEA-Tech, and CSEM) Member & CSEM representative of EARTO Working Group on Emerging Technologies for Healthcare Member of the Finnish Chamber of Commerce Member of the Latin American Chamber of Commerce Steering board member of Innovation Group Digitalization at Swiss Food Research
A. Hutter	Commission des énergies et de l'eau de la ville de Neuchâtel Innosuisse expert
R. Jose James	Chairman Swiss Chapter IEEE Electronic Packaging Society
C. Julia-Schmutz	Communication Coordinator within the Heterogeneous Technology Alliance (HTA) CSEM Representative, BioAlps
H. F. Knapp	Board member for NTN INARTIS Board of Directors member for cluster initiative Toolpoint for Lab Science Executive Board member of biotechnet, Switzerland Jury member for Zinno Ideenscheck Pre-jury member for Swiss Technology Award
G. Kotrotsios	IEEE Subcommittee on Human-Machine in Manufacturing Environment Member of Microcity Consultancy Committee Member of the Board of AM-TTC (Advanced Manufacturing Technology Transfer Centers) Initiative Member of the Board of the Heterogeneous Technology Alliance (alliance federating the Fraunhofer (microelectronics), VTT, CEA-Tech and CSEM) Member of the Executive Board of EREA (the European Association of Aeronautics Research Centers) Member of the Steering Committee of the SATW Advanced Manufacturing Research Alliance Member of the Swiss Academy of Engineering Sciences SATW Micronarc, member of the Group of Experts Vice Chairman of the Board of Directors of CSEM Brasil

M. Krieger	CSEM Representative Expert Workgroup Data driven Business Models, Swiss Alliance Data intensive services CSEM Representative Greater Zürich Area (GZA) CSEM Representative Innovation Expert Group Food Packaging at Swiss Food Research CSEM Representative SEMI global semiconductor industry association CSEM Representative Smart Card Forum Switzerland (SCF) CSEM Representative Zürcher Handelskammer (ZHK) CSEM Representative, Advanced Factory Automation workgroup of Swissmem (AFA)
F. Kurth	Local organizing committee, International Conference on Miniaturized Systems for Chemistry and Life Sciences (μ TAS 2019), Basel, CH, 2019 Technical program committee, International Conference on Miniaturized Systems for Chemistry and Life Sciences (μ TAS 2019), 2019
M. Lemay	Board Member, Swiss Society for Biomedical Engineering
A. Madrigal	Chair of the Advisory Board of the Space exhibition of the Museum of Transport of Lucerne Chair of the EARTO Working Group Space Research CSEM Representative, General Forum Clean Sky CSEM Representative, Swiss Aeronautics Security and Defense Division of Swissmem (Swiss ASD) CSEM Representative, Swiss Space Industries Group of Swissmem (SSIG) Expert for the evaluation of H2020 proposals in the Space Work Programme of the European Commission Member of the General Assembly of EREA (Association of European Establishments in Aeronautics) and CSEM Delegate in the Aviation Research Groups of the Association Member of the Steering Committee of the Swiss Space Center Member of the Strategic Committee of the Swiss Aeropole
N. Marjanovic	Member of the Organising Committee, Swiss ePrint 2019
S. Mohrdiek	Member of Phonotics21 Work Group 6 – Design and Manufacturing of Components and Systems Member of Review Panel for Irish Photonic Integration Center Member of Swissmem Fachgruppe Photonics Swissphotonics, Head of Swiss Photonic Packaging Laboratory (SPPL)
J.-L. Nagel	Member of the Editorial Board of the “Journal of Low Power Electronics” (JOLPE)
R. Pugin	Member of the Expert Committee of the Association NTN Innovative Surfaces Member of the Scientific Committee of the 2017 World Congress on Micro and Nano Manufacturing Member of the Scientific Committee of the 4M Micro-Nano Manufacturing Association
J. R. Farserotu	Chair and Research Co-ordinator The Hermes Partnership Chair of ETSI Technical Committee Smart Body Area Networks (TC SmartBAN) Program Committee Member, BodyNets 2019, Florence, Italy
D. Ruffieux	Member of the International Technical Program Committee of the European Solid-state Circuit Conference (ESSCIRC) in the RF and mmWave Building Blocks
E. Schaller	Member of the Executive Board of sensors.ch, Switzerland
P. Schmid	CSEM Representative Swiss Mechatronics Cluster
O. Sereda	Chair, Additive Manufacturing session, Euromat 2019
P. Steiert	Advisory Board Member for Institute für Chemistry and Biological Chemistry at the ZHAW Advisory Council for cluster initiative Toolpoint for Lab Science Member of the Executive Board for Verein Startup Pilatus
A. Steinecker	CSEM Representative EPoSS and Member of Working Group Robotics CSEM Representative IVAM

Prizes and Awards

- June 2019 David Schmid received the Best Poster Award at SwissNano Convention for the ACEnano project poster "Sample preparation for solubility of nanomaterials risk assessment" (Lausanne, CH).
- June 2019 Luc Driencourt won the prize for the best poster award at SwissNano Convention for his work on "Study of Plasmon-enhanced water splitting in a hematite photoanode" (Lausanne, CH).
- June 2019 Best poster award presented to Benjamin Gallinet at SwissNano Convention for his work on "Plasmonic nanoscale retarder controlled with liquid crystals" (Lausanne, CH).
- July 2019 Fabian Braun was presented with the award for the best young investigator's paper in the category Applications at the 20th International Conference on Biomedical Applications of Electrical Impedance Tomography, EIT 2019 (London, UK).
- September 2019 Tobias Herr was awarded one of the European Research Council's prestigious ERC Starting Grants, for his proposal "STARSHIP - Microphotonics-based frequency combs for habitable exoplanet detection".
- September 2019 Amir Ghadimi is the recipient of the 2019 Swiss Physical Society's (SPS) award for exceptional research by a young researcher in the field of computational physics. (Zürich, CH).
- September 2019 Sylvain Karlen has been awarded this year's Prix OMEGA scientific for his PhD thesis entitled "Fabrication and characterization of MEMS alkali vapor cells used in chip-scale atomic clocks and other atomic devices" (Montreux, CH).
- November 2019 Best poster award presented to Davide Migliorelli, Safiye Jafari, Silvia Generelli, and co-authors for their work entitled "Carbon black modified screen printed electrodes and magnetic beads for mass production compatible point of site detection of domoic acid in shellfish", at the Recent Advances in Food Analysis (RAFA) Conference (Prague, CZ).

CSEM SA

Jaquet-Droz 1
CH-2002 Neuchâtel

CENTER ALPNACH

Untere Gründlstrasse 1
CH-6055 Alpnach

CENTER LANDQUART

Bahnhofstrasse 1
CH-7302 Landquart

CENTER MUTTENZ

Tramstrasse 99
CH-4132 Muttenz

ZÜRICH OFFICE

Technoparkstrasse 1
CH-8005 Zurich

**CONTACT**

www.csem.ch
info@csem.ch
jobs@csem.ch